Research Group Biomedical Imaging Physics
Chair of Biomedical Physics
Department of Physics
School of Natural Sciences
Technical University of Munich

Towards Clinical Spectral and Phase-Contrast Breast Computed Tomography

June 2022

Lisa Heck
PhD Thesis

Supervisor:
Prof. Dr. Julia Herzen

Technische Universität München
Fakultät für Physik

Towards Clinical Spectral and Phase-Contrast Breast Computed Tomography

Lisa Heck

Vollständiger Abdruck der von der Fakultät für Physik der Technischen Universität München zur Erlangung des akademischen Grades einer

Doktorin der Naturwissenschaften (Dr. rer. nat.)

genehmigten Dissertation.

Vorsitzender:	Prof. Dr. Ulrich Gerland
Prüfer der Dissertation:	1. Prof. Dr. Julia Herzen
	2. Prof. Dr. Dimitrios Karampinos

Die Dissertation wurde am 09.06.2022 bei der Technischen Universität München eingereicht und durch die Fakultät für Physik am 08.07.2022 angenommen.

Abstract

Mammography as a widespread, common screening procedure is nowadays a valuable clinical tool for the early detection of breast cancer. Improvements of the sensitivity, specificity and also the mortality rate have been observed since the introduction of the corresponding screening programs. Nevertheless, attenuation-based mammography suffers from inherently low contrast of soft tissue, which results in failure to detect microcalcifications or cancerous lesions distinctly, leading to high recall rates. To overcome the superposition of diagnostically relevant anatomical tissue structures, another limitation of projection-based mammography, the community focused on the clinical implementation of three-dimensional attenuation-based breast computed tomography (BCT) in the past years. One technology that strongly evolved over the last decades in the field of preclinical research is grating-based phase-contrast imaging with a Talbot-Lau interferometer. It has been demonstrated that this promising approach can provide improved diagnostic image content due to increased lesion detection using the phase information or through the classification of microcalcifications using the dark-field signal. By combining this technology with energy-resolving single-photon-counting detectors, spectral differential phase contrast (SDPC) X-ray imaging can be performed which further exploits the advantages of grating interferometry. Like attenuation-based spectral X-ray imaging, SDPC provides material-selective and quantitative images, but with a decreased background noise level.

One major component of this work is the first experimental investigation of grating-based phase-contrast BCT to simultaneously benefit from their respective strengths. Due to the radiation sensitivity of the female breast, this was first conducted at the Munich Compact Light Source (MuCLS), a quasi-monochromatic laboratory-size inverse Compton X-ray source. In this study, a dose-compatible attenuation-based and grating-based phase-contrast BCT for breast phantoms of different sizes as well as for a freshly dissected fibroadenoma was achieved. In a second step, a simulation study for SDPC X-ray mammography and BCT was performed: First quasi-monochromatic using a dual-energy approach, followed by a polychromatic X-ray source with a detector-based spectral separation. The simulations showed contrast enhancement and noise reduction in a dose-compatible range, especially for the polychromatic mammography. This offers the possibility to lower the mean glandular dose (MGD) or reduce the amount of contrast agent injected without compromising image quality.

Zusammenfassung

Die Mammographie als weit verbreitetes, gängiges Screening-Verfahren ist heute ein wertvolles klinisches Instrument zur Früherkennung von Brustkrebs. Seit der Einführung der entsprechenden Screening-Programme sind Verbesserungen der Sensitivität, Spezifität und auch der Sterblichkeitsrate zu beobachten. Dennoch leidet die absorptionsbasierte Mammographie unter dem inhärent geringen Kontrast des Weichgewebes, was dazu führt, dass Mikroverkalkungen oder kanzeröse Läsionen nicht eindeutig erkannt werden können und es somit hohe Rückrufraten gibt. Um die Überlagerung diagnostisch relevanter anatomischer Gewebestrukturen, eine weitere Einschränkung der Mammographie, zu überwinden, konzentrierte sich die Fachwelt in den letzten Jahren auf der klinischen Umsetzung der dreidimensionalen absorptionsbasierten Brust Computertomographie (BCT). Eine Technologie, die sich in den letzten Jahrzehnten auf dem Gebiet der präklinischen Forschung stark weiterentwickelt hat, ist die gitterbasierte Phasenkontrast-Bildgebung mit einem Talbot-Lau Interferometer. Es hat sich gezeigt, dass dieser vielversprechende Ansatz einen verbesserten diagnostischen Bildgehalt durch eine verstärkte Erkennung von Läsionen anhand der Phaseninformation oder durch die Klassifizierung von Mikroverkalkungen anhand des Dunkelfeldsignals liefern kann. Durch die Kombination dieser Technologie mit energieauflösenden, photonenzählenden Detektoren kann die spektrale differentielle Phasenkontrast (SDPC) Röntgenbildgebung durchgeführt werden, wodurch die Vorteile der Gitterinterferometrie noch stärker genutzt werden können. Wie die spektrale Röntgenbildgebung auf Absorptionsbasis liefert SDPC materialselektive und quantitative Bilder, jedoch mit einem geringeren Hintergrundrauschen.
Ein Hauptbestandteil dieser Arbeit ist die erste experimentelle Untersuchung des gitterbasierten Phasenkontrast-BCT, um gleichzeitig von ihren jeweiligen Stärken zu profitieren. Aufgrund der Strahlungsempfindlichkeit der Brust wurde dies zunächst an der Munich Compact Light Source (MuCLS) durchgeführt, einer quasi-monochromatischen inversen Compton Röntgenquelle. In dieser Studie wurde ein dosisverträglich absorptions- und gitterbasiertes Phasenkontrast-BCT für Brustphantome unterschiedlicher Größe sowie für ein frisches Fibroadenom erzielt. In einem zweiten Schritt wurde eine Simulationsstudie für SDPC-Röntgenmammographie und BCT zunächst quasi-monochromatisch mit einem Zwei-Energien-Ansatz durchgeführt, anschließend für eine polychromatische Röntgenquelle mit einer detektorbasierten spektralen Trennung. Die Simulationen zeigen eine Kontrastverbesserung und Rauschreduzierung in einem dosisverträglichen Bereich, insbesondere für die polychromatische Mammographie. Dies bietet die Möglichkeit, die mittlere Drüsendosis (MGD) zu senken oder die Menge eines injizierten Kontrastmittels zu reduzieren, ohne die Bildqualität zu beeinträchtigen.

Publications and Scientific Presentations

Publications as First Author

L. Heck, M. Dierolf, C. Jud, E. Eggl, T. Sellerer, K. Mechlem, B. Günther, K. Achterhold, B. Gleich, S. Metz, D. Pfeiffer & J. Herzen. Contrast-enhanced spectral mammography with a compact synchrotron source. *PLOS ONE* **14**(10):e0222816 (2019).

L. Heck, E. Eggl, S. Grandl, M. Dierolf, C. Jud, B. Günther, K. Achterhold, D. Mayr, B. Gleich, K. Hellerhoff, F. Pfeiffer & J. Herzen. Dose and spatial resolution analysis of grating-based phase-contrast mammography using an inverse Compton X-ray source. *Journal of Medical Imaging* **7**(2):023505 (2020).

L. Heck & J. Herzen. Recent advances in X-ray imaging of breast tissue: From two- to three-dimensional imaging. *Physica Medica* **79**:69-79 (2020).

L. Heck, R. Klaar, K. Mechlem, T. Sellerer, C. Schmid, K.Taphorn, F. Pfeiffer & J. Herzen. Spectral Differential Phase Contrast X-ray Mammography. *Submitted* (2022).

Publications as Co-Author

E. Eggl, S. Grandl, A. Sztrókay-Gaul, M. Dierolf, C. Jud, **L. Heck**, K. Burger, B. Günther, K. Achterhold, D. Mayr, J. Wilkens, S. Auweter, B. Gleich, K. Hellerhoff, M. Reiser, F. Pfeiffer & J. Herzen. Dose-compatible grating-based phase-contrast mammography on mastectomy specimens using a compact synchrotron source. *Scientific Reports* **8**(1):15700 (2018).

J. Scholz, C. Petrich, M. Riedel, **L. Heck**, L. Birnbacher, S. Gkoumas, T. Sellerer, K. Achterhold, & J. Herzen. Biomedical x-ray imaging with a GaAs photon-counting detector: A comparative study. *Applied Physics Letters Photonics* **5**(10):106108 (2020).

S. Grandl, W. Gottwald, D. Berthe, **L. Heck**, S. Resch, D. John, J. Herzen & K. Hellerhoff. Grating-based phase contrast mammography: Assessing complemen-

tary diagnostic information of Dark Field Breast Imaging. An ex-vivo set-up. *To be submitted* (2022).

Conference Proceedings

L. Heck, E. Eggl, S. Grandl, M. Dierolf, C. Jud, B. Günther, K. Achterhold, D. Mayr, B. Gleich, K. Hellerhoff, F. Pfeiffer & J. Herzen. Dose and spatial resolution analysis of grating-based phase-contrast mammography using an inverse Compton X-ray source. *Proceedings of SPIE 11113, Developments in X-ray Tomography XII* **111130M** (2019).

Conference Proceedings as Co-Author

B. Günther, R. Gradl, C. Jud, E. Eggl, S. Kulpe, E. Braig, **L. Heck**, J. Brantl, K. Achterhold, B. Gleich, M. Dierolf & F. Pfeiffer. Evaluation and optimization of multimodal x-ray imaging techniques for inverse Compton x-ray sources. *Proceedings of SPIE 11110, Advances in Laboratory-based X-Ray Sources, Optics, and Applications VII* **1111008** (2019).

Oral Presentations

Review of the latest Developments in Grating-based Phase-Contrast Mammography. *International Symposium on Biomedical Applications of X-ray Phase-Contrast Imaging (IMXP), Munich, Germany, January 2020.*

Contrast-Enhanced Spectral Mammography with a Compact Synchrotron Source. *Annual Meeting of the Radiological Society of North America (RSNA), Chicago, USA, December 2019.*

Dose and spatial resolution analysis of grating-based phase-contrast mammography using an inverse Compton X-ray source. *SPIE Optics and Photonics, San Diego, USA, August 2019.*

Dose-compatible grating-based phase-contrast mammography on mastectomy specimens using a compact synchrotron source. *European Congress of Radiology (ECR), Vienna, Austria, August 2019.*

Poster Presentations

Dose-compatible grating-based phase-contrast mammography on mastectomy specimens using a compact synchrotron source. *International Workshop on X-ray and Neutron Phase Imaging with Gratings (XNPIG), Sendai, Japan, October 2019.*

Dose-compatible grating-based phase-contrast mammography on mastectomy specimens using a compact synchrotron source. *International Symposium on Biomedical Applications of X-ray Phase-Contrast Imaging (IMXP), Garmisch-Partenkirchen, Germany, January 2019.*

Contents

1 Introduction to Breast Imaging

The first chapter is an introductory part that serves to motivate the background of the work carried out in this thesis. In this context, the current state of the art for imaging the female breast in a clinical environment is initially explained, followed by the current state of research. Furthermore, an outline of the contents of the following chapters is provided. Please note that parts of this chapter have recently been summarized in the review article on recent advances in X-ray breast imaging by Heck and Herzen [Heck, 2020].

1.1 Clinical State of the Art

Breast cancer is the most common type of cancer worldwide and the leading cause of death in women under 60 [WHO, 2020b]. It is estimated that approximately 15 % of all cancer deaths in women in 2018 were due to breast cancer [WHO, 2020a]. For this reason, early detection of this disease is nowadays inevitable. Mammography, ultrasound (US) and magnetic resonance imaging (MRI) are the standard imaging modalities used for this purpose in clinical practice to date. Among them, the former is established as a screening program. Although the introduction of these programs successfully demonstrate a reduced mortality rate (38-58 %) in the USA and in Europe [Taylor, 2004; Paap, 2011; Paci, 2014; Paap, 2014; Sankatsing, 2017; Hendrick, 2019], measures such as the sensitivity between 69 % and 94 %, the specificity between 78 % and 95 % [Stout, 2014], and the positive predictive value between 7 % and 13 % [Venkatesan, 2009] remain unsatisfactory. In case of females with dense breast tissue, the sensitivity even drops to 30-48 % [Mandelson, 2000; Destounis, 2017]. Detection of suspicious findings or palpable masses such as cancerous lesions or cysts is sometimes not possible in two-dimensional radiography due to intrinsically low soft tissue contrast. Therefore, overlapping breast tissue structures with diagnostically relevant abnormalities and thus obtaining clinically useful images remains a challenge in mammography. These points emphasize the need to further improve the diagnostic content in female breast imaging. Without the use of radiation, US and MRI are two imaging modalities that provide an alternative to mammography and thus also support early breast cancer

detection. In most cases, US is used as supporting tool in addition to mammography to ensure a more reliable image evaluation and to obtain a final diagnosis. There are two groups that mainly benefit from US imaging: First, women with dense breast tissue and second, young women [Clevert, 2007]. Another possibility is the combination of US with MRI. While this combination leads to a higher sensitivity it also leads to an increased number of false positive diagnoses. The resulting overdiagnosis can affect more than 20% of the detected breast cancers [Berg, 2008]. For MRI alone, the sensitivity is very promising at 90 %. However, specificity needs improvement due to its wide range between 37 % and 97 % [Kuhl, 1999; Orel, 1999]. For several reasons, MRI is not appropriate as a breast cancer screening program: MRI suffers from a low resolution of the images, the need for an imaging expert and is neither very cost- nor time-efficient. In addition, the specificity of MRI can only be improved by the injection of a contrast agent and is therefore is not suitable for people with contraindications such as contrast agent side effects. Furthermore, MRI can not be used by women with claustrophobia or pacemakers. One second-level examination that is clinically used is contrast-enhanced spectral mammography (CESM) and relies on dual-energy K-edge subtraction imaging. Iodine-containing contrast agent is injected, which accumulates in the newly formed blood vessels that result from the neo-angiogenesis of a tumor [Carmeliet, 2000]. In case of uncertain mammography results, CESM is used as check-up as it overcomes limitations of conventional mammography since it reveals lesions that are previously not detected. Nevertheless, CESM is – like MRI – not an ideal imaging method because of the toxicity of the contrast agent [Lusic, 2013] and additionally due to applied MGD that is higher compared to standard mammography (3.0 mGy vs. 2.1 mGy) [James, 2017]. The demand for extending two-dimensional mammography to three dimensions is met by digital breast tomosynthesis (DBT). This technique retrieves a depth resolution with a confined extend by combining multiple projections of the compressed breast across a limited angular range. Consequently, the detrimental effect of superposition of breast tissue in mammography can be mitigated. Although there are several advantages when comparing DBT to standard mammography, there is still interest in developing BCT as it would provide an unrestricted view of the female breast. In the 1970s, Chang et al. performed first studies about attenuation-based BCT [Chang, 1977; Chang, 1978; Chang, 1980]. Over the past decades, several groups have resumed research on BCT and have greatly advanced the development of this technique towards clinical application [Kalender, 2012; Kalender, 2017; ABCT, 2020; Boone, 2001; Boone, 2006; Lindfors, 2008; Prionas, 2010; Koning, 2019; Kuzmiak, 2016]. Some of these studies show that an average MGD for BCT comparable to that of two-view mammography can be achieved. Due to the radiation sensitivity of the glandular cells within the female breast and the rule that the dose should be as low as reasonably achievable (ALARA principle), this is a very important and successful progress for BCT. The foundation of two companies – *AB-CT - Advanced Breast-*

CT GmbH (Erlangen, Germany) and *Koning Corporation* (Norcross, Georgia, USA) [ABCT, 2020; Koning, 2019] – working to bring BCT into clinical practice underscores the clinical relevance of BCT. Both companies have developed commercial imaging devices that are now installed in several hospitals. Results of the first clinical *in vivo* images from the nu:view system from *AB-CT* were recently published with and without the usage of contrast media [Berger, 2019b; Berger, 2019a; Shim, 2020; Berger, 2022]. These results highlight the clinical capability of a dedicated BCT system especially due to its low radiation dose (between 4.4 and 5.7 mGy) and the additionally improved patient comfort, as no breast compression is required [Berger, 2019b]. However, just as with mammography, the image quality or more precisely the weak soft tissue contrast still needs improvement, which is again the reason for the injection of iodine-containing contrast medium [Berger, 2022]. A brief overview of all dedicated BCT systems is given by Sarno et al [Sarno, 2015]. In summary, these results and efforts underline the great potential for this promising imaging alternative for women whose mammography is not very meaningful due to the dense tissue structures and who do not want undergo MRI. Although recent developments and the techniques described above have improved early detection of breast cancer leading to a reduction in mortality, attenuation-based breast imaging still suffers from the inherently low soft tissue contrast. This makes tissue discrimination and in consequence diagnosis difficult. Therefore, the need for more reliable imaging techniques remains very high.

1.2 Current State of Research

The current state of research in X-ray-based breast imaging can mainly be split into two parts: It addresses novel imaging approaches that have evolved in recent decades such as phase-contrast and spectral imaging taking technical advances like energy-resolving single-photon-counting detectors into account.
Using the additional refraction and scattering properties of X-ray photons is one possibility to overcome the limitation of the intrinsically low soft tissue contrast which can until now only be enhanced by the use of contrast agent. These properties are thus of great relevance and interest for mammography and BCT. Phase-sensitive techniques such as propagation- [Gureyev, 2009; Wu, 2014; Krenkel, 2016] and grating-based phase-contrast [Pfeiffer, 2006; Weitkamp, 2005; Momose, 2003] imaging have developed in recent years and evaluated for breast imaging. The propagation-based approach has actively been researched at the Synchrotron Radiation for Medical Physics (SYRMEP) beamline at the Elettra Synchrotron (Trieste, Italy) and at the Imaging and Medical beamline (IMBL) of the Australian Synchrotron (Monash, Australia) both for mammography first [Arfelli, 2000; Olivo, 2009; Castelli, 2011; Longo, 2014; Olivo, 2014] and finally for BCT [Longo, 2016; Tromba, 2016; Taba, 2018; Pacilè, 2018; Brombal, 2018a;

Brombal, 2018b; Brombal, 2018c; Lewis, 2018; Brombal, 2019; Piai, 2019; Longo, 2019; Pacilè, 2019; Delogu, 2019; Longo, 2020]. For both applications, improved delineation of breast abnormalities in a clinical dose range was ultimately achieved, resulting in fundamentally improved diagnostic image content. Due to the lack of clinical feasibility of propagation-based imaging meaning that scanning women *in vivo* in clinical daily routine remains unlikely with such an X-ray source due to the high costs, availability and space requirements of synchrotron facilities, imaging with grating-based phase-contrast has gained importance [Pfeiffer, 2006; Pfeiffer, 2007; Pfeiffer, 2008]. This approach allows to additionally retrieve the so-called dark-field signal that corresponds to ultra-small-angle scattering [Pfeiffer, 2008]. Since microcalcifications scatter differently depending on their size and composition and can already be sign for breast cancer [OGrady, 2018], this extra signal is another benefit of this approach. This leads to a better detection, discrimination and classification of them based on the analysis of their micromophology with the dark-field signal [Wang, 2014; Scherer, 2016; Rauch, 2020]. In addition, further work on this topic demonstrated that the grating-based approach also provides promising results regarding for example the improved cancerous lesion or cysts detection [Stampanoni, 2011; Scherer, 2014; Grandl, 2015; Hauser, 2014; Auweter, 2014; Grandl, 2022]. The clinical relevance is emphasized by the fact that this approach has been conducted in a dose-compatible range [Scherer, 2015] and that it was successfully implemented into commercial mammography system [Koehler, 2015; Arboleda, 2019]. As consequence, an extension to BCT has also been conducted first at synchrotron sources [Sztrókay, 2013; Auweter, 2014] before starting experiments at clinically relevant conventional X-ray sources [Grandl, 2013; Grandl, 2014; Hellerhoff, 2019; Willner, 2016]. These studies deal with the quantitative breast tissue characterization [Willner, 2016] and the examination of intraductal carcinoma *in situ* [Hellerhoff, 2019] and fibroadenomas [Grandl, 2014] resulting in an improved visibility of those lesions. The potential of this method is underlined by the foundation of the company *GratXray AG* (Villigen, Switzerland), which aims at developing a commercial grating-based phase-contrast BCT system [GratXray, 2022]. Nevertheless, and especially in contrast to the results obtained with monochromatic radiation, these studies have no clinical relevance so far, as the MGD exceeds the proposed dose limit of 5 mGy, which needs to be investigated in further research. In order to address this issue, this work aims for a low-dose grating-based phase-contrast BCT. To first establish a proof of principle, this is performed at the MuCLS, an inverse Compton X-ray source that delivers quasi-monochromatic X-ray photons instead of measuring directly at a conventional X-ray source. This should serve as a preliminary work, the results of which should subsequently be transferred to polychromatic X-ray sources. Initial studies have already proven breast imaging at the MuCLS [Eggl, 2016b; Eggl, 2018; Heck, 2019].
However, spectral imaging has recently also become more important. As introduced in the previous section, CESM is a growing clinical check-up procedure used for fi-

nal diagnosis. In contrast to that dual-energy approach, multi-energy imaging can nowadays also be performed via detector-based spectral separation using the energy-resolving single-photon-counting detector technology [Schlomka, 2008; Flohr, 2020]. These detectors separate X-ray spectra in only one exposure resulting in spatially and temporally perfectly registered images circumventing motion artifacts and a potentially higher MGD due to the acquisition of multiple images. In a comparison of conventional and spectral CT, Shikhaliez and Fritz proposed that spectral imaging could be a potential application for dedicated BCT [Shikhaliev, 2011]. In addition, the clinical BCT from *AB-CT* is already equipped with such a detector but does not yet use the possibility of spectral imaging in clinical imaging [ABCT, 2020]. One first study has been published so far, in which the spectral performance was investigated in a phantom study [Ruth, 2020]. Based on the energy-dependent attenuation, material decompositions can be performed and basis material images can be generated, which help to distinguish tissue structures. Although several clinical studies successfully worked out the benefit of attenuation-based spectral imaging for e.g. coronary angiography or mammography [Ehn, 2017; Sellerer, 2017; Mechlem, 2018b; Mechlem, 2018a; Heck, 2019], this approach suffers from strong noise amplification leading to a reduced contrast-to-noise ratio (CNR) especially in the low-dose range. This is particularly problematic for mammography, where the detection of microcalcifications is important, but would be lost in noise within an attenuation-based material decomposition. By combining the two previously presented approaches, namely grating-based phase contrast and spectral imaging using a photon-counting detector or a dual-energy approach, SDPC imaging can be realized. This was originally performed in numerical simulations for thorax radiography [Mechlem, 2020]. One benefits from the strengths of both imaging approaches by using both phase and spectral information simultaneously while the respective restrictions, such as phase wrapping and beam hardening, are mitigated. In addition to the quantitative and material-selective images obtained with a decreased noise level compared to attenuation-based spectral imaging, a third dark-field basis material image is generated [Mechlem, 2020]. As side effect of grating-based phase-contrast imaging, SDPC mammography and BCT is the second objective which will be pursued in this work. To obtain a ground truth of the potential benefits, simulations for the attenuation- and SDPC-based material decompositions are first performed with a quasi-monochromatic X-ray source [Heck, 2022]. Based on the obtained results, the simulations will be extended to the more clinically realistic conventional X-ray tube [Heck, 2022].

Outline

This work gives an overview of the recent developments in spectral and phase-contrast imaging for the medical application of BCT. In Ch. 2, the theoretical background, on which this work is based, is introduced focusing on X-ray generation and detection, grating interferometry and fundamentals of computed tomography (CT). Ch. 3 contains a description of the methods which are used and applied in this work. This includes different processing approaches, the basics of spectral imaging, the estimation of the MGD, image evaluation measures and the background of detector characterization. The experimental results of this thesis mainly comprise two projects and are therefore divided into two chapters. First, Ch. 4 deals with the realization of low-dose attenuation-only and grating-based phase-contrast BCT at the MuCLS preferably in a clinical dose-tolerant limit to provide preliminary work for this approach at polychromatic X-ray sources. Second, in Ch. 5, the results of SDPC representing a beneficial combination of the two aforementioned approaches are given. Simulations for a quasi-mono- and polychromatic X-ray spectrum are conducted for projection-based mammography imaging as well as for BCT. Ultimately, Ch. 6 summarizes the results of this thesis in a final conclusion together with a brief summary of the prior discussed outlook for prospective research on this topic.

Theoretical Background 2

This chapter mainly explains the basic theoretical background the work is based on including the definition, the generation and the detection of X-ray photons. First, the wave-particle dualism of X-ray photons, their interaction with matter as well as the complex refractive index are introduced. This is followed by the definition of the brilliance as figure of merit for X-ray sources. Among those, a conventional X-ray tube and the compact light source are both described here. Besides this, the direct and indirect detection process of flat-panel detectors as well as the single-photon-counting detector technology are presented. Then, phase-contrast imaging with a Talbot-Lau grating interferometer and the corresponding signal extraction process is explained. Last, the principles for the reconstruction of three-dimensional computed tomography (CT) data including filtered backprojection (FBP) and statistical iterative reconstruction (SIR) are presented. Unless otherwise indicated, the literature mainly used for the explanations in this chapter is [Kak, 1988; Spieler, 2006; Attwood, 2007; Buzug, 2008; AlsNielsen, 2011; Podgorsak, 2010; Willmott, 2011; Russo, 2017]

2.1 Definition of X-rays

X-ray photons are one part of the continuous electromagnetic spectrum drawn in Fig. 2.1 and located between the ultraviolet spectrum and the gamma rays. X-ray photons and gamma rays are not differentiated according to their photon energy, but according to their radiation origin. In general, the properties of electromagnetic radiation can be explained in two different ways. First, by the classical model in which X-rays are represented as waves with wavelengths ranging from approximately 1 nm to 1 pm. Another common unit for the wavelength of X-ray waves is 1 Ångström (10^{-10} m). This wavelength regime corresponds to an energy range between keV and MeV. One discriminates between soft and hard X-rays where the former are mainly used for X-ray microscopy. Hard X-rays with an energy of more than 5-10 keV are utilized for X-ray crystallography or for medical imaging due to their high penetration depth in opaque objects compared to soft X-rays. In the quantum mechanical view, however, X-rays are considered to be quantized into photons which are defined by a distinct photon

energy E that is generally calculated by

$$E = \frac{hc}{\lambda} = \hbar\omega\,, \tag{2.1}$$

with the Planck's constant $h = 4.136 \cdot 10^{-15}$ eVs, the speed of light in vacuum with $c = 2.9979 \cdot 10^{8}$ m/s, the wavelength λ and the radiation frequency $\omega = 2\pi f$. Both concepts are important to understand the behavior of X-rays. On an atomic scale, the particle picture may be the most intuitive, while on a macroscopic scale, the wave picture may be beneficial for the description of the following interaction processes.

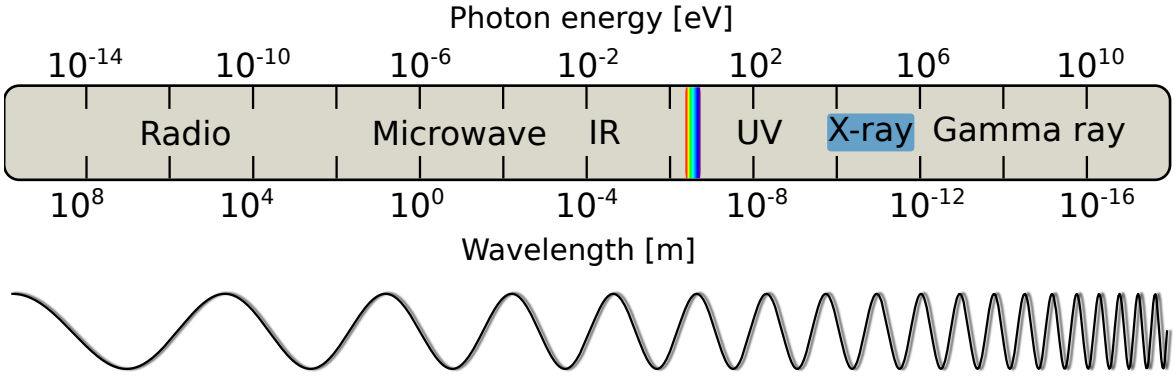

Figure 2.1: Overview of the electromagnetic spectrum. The continuous spectrum includes long-wave radio waves, microwaves, infrared light, visible light, ultraviolet light, X-rays and very short-wave gamma rays. The X-ray spectrum is marked with blue and located between the ultraviolet spectrum and the gamma rays with wavelength of around 10^{-10} m.

2.1.1 X-ray Interactions with Matter

Here, the main processes of the X-ray interaction with matter are introduced. In the energy range of X-rays, the photons mainly interact with electrons. This includes the photoelectric absorption as well as scattering processes such as elastic (Thomson/Rayleigh) and inelastic (Compton) scattering. There are also other interaction processes that are neglected here: On the one hand, pair production also as a primary interaction process since it is not relevant to the clinically used energy range. On the other hand, secondary processes like X-ray fluorescence and Auger electron emission.

Photoelectric Effect

An incident X-ray photon can be fully absorbed by an electron bound to an atom, if the photon's energy exceeds the electron's binding energy. The energy of the X-ray

photon is transferred to the electron which is subsequently released from the atom. This process is called photoelectric absorption. An electron from the outer shell can fill the resulting vacancy. In consequence, a so-called fluorescence photon or Auger electron is emitted with an energy corresponding to the energy difference between the two atomic shells or the energy difference between the two atomic shells minus the Auger electrons binding energy.

Elastic Scattering

Thomson or Rayleigh scattering are elastic scattering processes. They take place when the wavelength of the X-ray photon is longer than the atomic radius, i.e. only at small photon energies. While the wavelength, the X-ray energy and the absolute value of the momentum remain the same after the interaction, the propagation direction of the scattered X-ray photon changes.

Inelastic Scattering

Compton scattering is an inelastic and incoherent scattering process. An X-ray photon hits a weakly bound orbital electron with a binding energy lower than the photon's energy. The incoming photon transfers a part of its momentum to the electron. After the collision, the electron moves with an energy E_k that corresponds to the energy the incoming photon lost. This results in a photon with a smaller X-ray energy, another propagation direction and a longer wavelength. By the conservation of total energy and momentum conversation [Podgorsak, 2010], the wavelength shift $\Delta\lambda$ is calculated as

$$\Delta\lambda = \lambda' - \lambda_0 = \lambda_\mathrm{C}(1 - \cos\theta)\,, \tag{2.2}$$

with λ' and λ_0 denoting the wavelength of the scattered and the incident photon, $\lambda_\mathrm{C} = h/m_\mathrm{e}c$ the Compton wavelength and θ as scattering angle between the incoming and the scattered photon.

2.1.2 Complex Refractive Index

On a more macroscopic rather than the atomic level, X-ray refraction, reflection and absorption at the interface between different media can be characterized based on their respective refractive index n. This complex refractive index n is defined as follows

$$n = 1 - \delta + i\beta\,, \tag{2.3}$$

with δ and β as refractive index decrement and the absorption index, respectively. The δ value is in order of 10^{-5} in solids and 10^{-8} in air. However, β is much smaller than that. Both quantities depend on the X-ray energy and the material of the medium.
An X-ray photon can be expressed as electromagnetic wave $\Psi(\vec{r}, t)$ in the wave optical model at time point t and position $\vec{r} = (0, 0, 0)^{\mathrm{T}}$ as follows:

$$\Psi(\vec{r}, t) = \Psi_0 e^{i(\vec{k}\cdot\vec{r}-\omega t)}\,, \tag{2.4}$$

where Ψ_0 is the initial amplitude of the wave, $\vec{k}$ the wave vector with $|\vec{k}| = 2\pi/\lambda$ and ω the angular frequency. For a wave propagating in a medium, its complex refractive index n has to be considered in Eq. (2.4). When it is additionally assumed that the wave only propagates in z-direction, also the position vector changes to $\vec{r} = (0, 0, z)^{\mathrm{T}}$. This results in a modification of Eq. (2.4):

$$\Psi(z, t) = \Psi_0 \cdot e^{i(nkz-\omega t)} = \Psi_0 \underbrace{e^{i(kz-\omega t)}}_{\text{propagation}} \cdot \underbrace{e^{-\beta kz}}_{\text{attenuation}} \cdot \underbrace{e^{-i\delta kz}}_{\text{phase shift}}\,. \tag{2.5}$$

By splitting the general equation in three parts, the first one denotes the propagation, the second the attenuation and the last one the phase shifting term. The propagation of a wave front through a medium and the impact of these three effects on this wave are schematically visualized in Fig. 2.2.

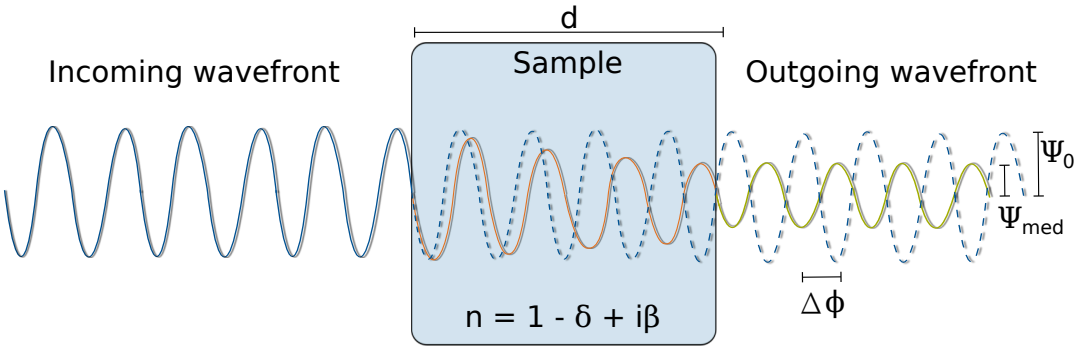

Figure 2.2: Interaction of a monochromatic X-ray wavefront with a sample. The incoming X-ray wavefront is drawn in blue on the left side of the sample and the outgoing wavefront behind the sample is shown in green. The wave transversing the sample, characterized by its refractive index n, is depicted in orange. Compared to the undisturbed wavefront shown as a blue dotted line for comparison, the wavefront's amplitude is reduced from Ψ_0 to Ψ_{med} and the phase is shifted by $\Delta\phi$ by the sample.

Attenuation and Beer-Lambert law

The interaction of X-rays with matter modifies the original wave, e.g. in terms of a reduced amplitude. This effect is related to the attenuating part in Eq. (2.5). The intensity that is measured after the X-rays crossed the object is defined as $|\Psi|^2 = \Psi\Psi^*$. Thus, the intensity $I(z)$ after a certain propagation distance z becomes

$$I(z) = |\Psi_0 \cdot e^{i(kz-\omega t)} \cdot e^{-\beta kz} \cdot e^{-i\delta kz}|^2 = \Psi_0^2 e^{-2\beta kz}, \tag{2.6}$$

where Ψ_0^2 equals to the initial intensity I_0 of the incoming X-ray wavefront. From this equation follows the definition of the linear attenuation coefficient with $\mu = 2\beta k$. In the simplified case, this leads to the so-called Beer-Lambert law

$$I(z) = I_0 \cdot e^{-\mu z}, \tag{2.7}$$

with a monoenergetic attenuation coefficient μ for a homogeneous object of thickness z and an initial intensity I_0. For a polychromatic X-ray source and a heterogeneous object, the Beer-Lambert law changes to

$$I(z) = \int_{E_{\min}}^{E_{\max}} I_0(E) e^{-\int_0^z \mu(E,Z,z')\mathrm{d}z'} \mathrm{d}E. \tag{2.8}$$

The linear attenuation coefficient depends on the X-ray energy E (decreases with increasing photon energy, $\mu \sim E^{-3}$) and on the atomic number Z ($\mu \sim Z^4$). Consequently, the attenuation coefficient is element-specific. Furthermore, the linear attenuation coefficient can be expressed as

$$\mu(E, Z) = \left(\frac{\rho N_\mathrm{A}}{A}\right) \sigma_\mathrm{tot}(E, Z)\,, \tag{2.9}$$

where ρ denotes the mass density, N_A the Avogadro's constant, A the atomic mass and $\sigma_\mathrm{tot}(E, Z)$ the total scattering cross section. For a molecule consisting of N atoms, however, the total attenuation coefficient is calculated as the weighted sum of the individual elements attenuation coefficient $\mu_i(E)$.

$$\mu(E) = \sum_i^N w_i \mu_i(E)\,, \tag{2.10}$$

where w_i is the mass fraction of the respective element i in the molecule.

X-ray phase shift

In addition to the attenuating part, a phase shift $\Delta\phi$ can be added to the incoming wavefront as visualized in Fig. 2.2 and shown in Eq. (2.5). Extracted from the exponent of this equation, the phase shift $\Delta\phi$ for a homogeneous object of thickness z is defined as

$$\Delta\phi = \delta k z = \delta \frac{2\pi}{\lambda} z. \tag{2.11}$$

Comparing the projection approximation for a wave field with the results obtained for the first Born approximation [Spieler, 2006], which are both not further elaborated here, the refractive index decrement δ is

$$\delta = \frac{2\pi r_0 \rho_e}{k^2}\,, \tag{2.12}$$

with r_0 being the classical electron radius. For a polychromatic X-ray source and a heterogeneous object, the generalized phase shift can be expressed as

$$\Delta\phi = k \int_0^z \delta(z')\mathrm{d}z'\,. \tag{2.13}$$

For a phase shift inducing object such as a wedge, the incoming wavefront and its propagation direction is deflected by an angle α after passing the sample. This refraction is just in the order of micro radians. Through geometrical considerations and for small phase gradients where the small-angle approximation ($\tan\alpha = \alpha$) can be applied, the refraction angle is approximated by [Davis, 1995; Spieler, 2006]

$$\alpha \approx \frac{1}{k}\frac{\partial\phi}{\partial x} = \frac{\lambda}{2\pi}\frac{\partial\phi}{\partial x}\,. \tag{2.14}$$

2.2 X-ray Sources

Over the last century, different types of X-ray sources were developed, ranging from large synchrotron facilities to conventional X-ray tubes, which generate X-ray photons in different ways. The quality of their X-ray beam can be expressed with a figure of merit called brilliance. It takes the key properties of the X-ray source into account: The bandwidth $\Delta E/E$, the photon flux Φ, the source size area ΔA and the beam collimation described in terms of the solid angle $\Delta\Omega$ into which the X-rays are emitted. The brilliance is defined by combining these properties into a single equation:

$$\text{Brilliance} = \frac{\Phi}{\Delta\Omega \cdot \Delta A \cdot \Delta E/E} = \frac{\text{Photons/second}}{(\text{mrad})^2(\text{source area in mm}^2)(0.1\,\%\,\text{BW})}\,. \quad (2.15)$$

Compared to conventional X-ray tubes ($< 10^{10}$), synchrotron sources can typically reach at least an up to ten orders of magnitude higher brilliance ($\sim 10^{20}$). Then, by following the experiments performed in this work, the basic principle of a conventional X-ray tube used for clinical X-ray diagnostics as well as the working principle of the Compact Light Source (CLS), a compact inverse Compton X-ray source (brilliance $\sim 10^{10}$), are described in the following sections.

2.2.1 Conventional X-ray Tube

The basic principle of a conventional X-ray tube relies on the interaction of electrons with the material of the anode. Free electrons are thermally emitted from the cathode by heating up its filament. Subsequently, they are accelerated towards the anode by an electric field. Once the electrons hit the target material, two interactions predominantly form the polychromatic spectrum emitted by an X-ray tube. The broad, continuous part originates from electrons which are decelerated by the electric field of the metallic anode's material. The resulting radiation is called Bremsstrahlung. The high-energy cut-off of the X-ray spectrum corresponds to the applied tube voltage. In addition, sharp, so-called characteristic lines indicated by the two arrows in Fig. 2.3 (B) superimpose the continuous spectrum. They are formed by incoming electrons which remove an atomic electron from the inner shell. This results in a vacancy that is filled by an electron from an outer shell. As a consequence, an X-ray fluorescence photon is emitted with a specific energy corresponding to the energy difference between the two respective shells. The schematic drawing of a conventional X-ray tube (Coolidge side-window tube) is provided in Fig. 2.3 (A) and an example of an X-ray source spectrum in (B). In order to increase the total power and the photon flux of an X-ray tube, rotating anode generators have been introduced. In these devices, the anode is rotated effectively distributing the heat produced during the electron-matter interactions over a larger area.

2.2.2 Munich Compact Light Source

The MuCLS hosts an inverse Compton X-ray source and a beamline with two experimental end-stations. The inverse Compton Source, the Lyncean Compact Light Source, was developed by *Lyncean Technologies Inc.* (Fremont, USA) [Lyncean, 2022], while the two experimental end-stations were designed in-house at TUM. A schematic

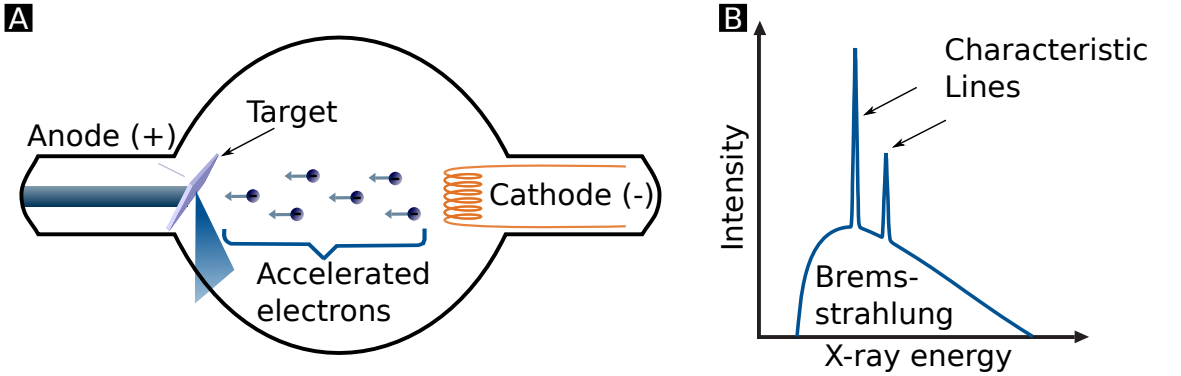

Figure 2.3: Conventional X-ray tube and polychromatic X-ray spectrum. (A) Schematic drawing of a conventional X-ray tube. Free electrons are thermally emitted from the cathode by heating up its filament and travel towards the anode where X-ray photons are generated through the interaction of electrons with the anode material. (B) Example of a polychromatic X-ray spectrum including the characteristic emission lines and the continuous spectrum.

drawing of the X-ray source itself is presented on the left side of Fig. 2.4 (A). The grating interferometer used for the experiments in this thesis is schematically depicted on the right. In the following, the working principle of the compact inverse Compton source is described while the grating-based experimental setup will be presented later in Sec. 4.2.

The MuCLS X-ray photons are generated through inverse Compton scattering during the collision of laser photons and accelerated electrons. In general, the working principle of this can be described in two different ways: In the particle picture, the photon is Compton scattered in the rest frame of the highly relativistic electron. Thus, the backscattered photon is promoted to the X-ray regime in the laboratory frame. In the wave picture, the highly relativistic electron is wiggled in the electromagnetic field of the laser, comparable to X-ray generation with a classical undulator at synchrotrons. Due to the scope of this work, this is not explained more in detail here, but can be found in [Günther, 2021]. The explanations in this section are mainly based on [Eggl, 2016a; Gradl, 2019; Günther, 2020; Günther, 2021].

The CLS contains two major subsystems, the electron system and the laser. In the electron system, electrons are generated in a photo-cathode radio-frequency gun and then accelerated to relativistic energies between 29 and 45 MeV in a 5 m long electron linear accelerator. Then, they are injected and stored in a miniature electron storage ring that has a circumference of 4.6 m and in which the electron bunch revolves at a repetition rate of 65 MHz. In order to ensure a high quality of the X-ray beam, the circulating electron bunch is replaced at a rate of 25 Hz which equals 2.6 million turns. The storage ring is designed such that the electron beam is focused in both

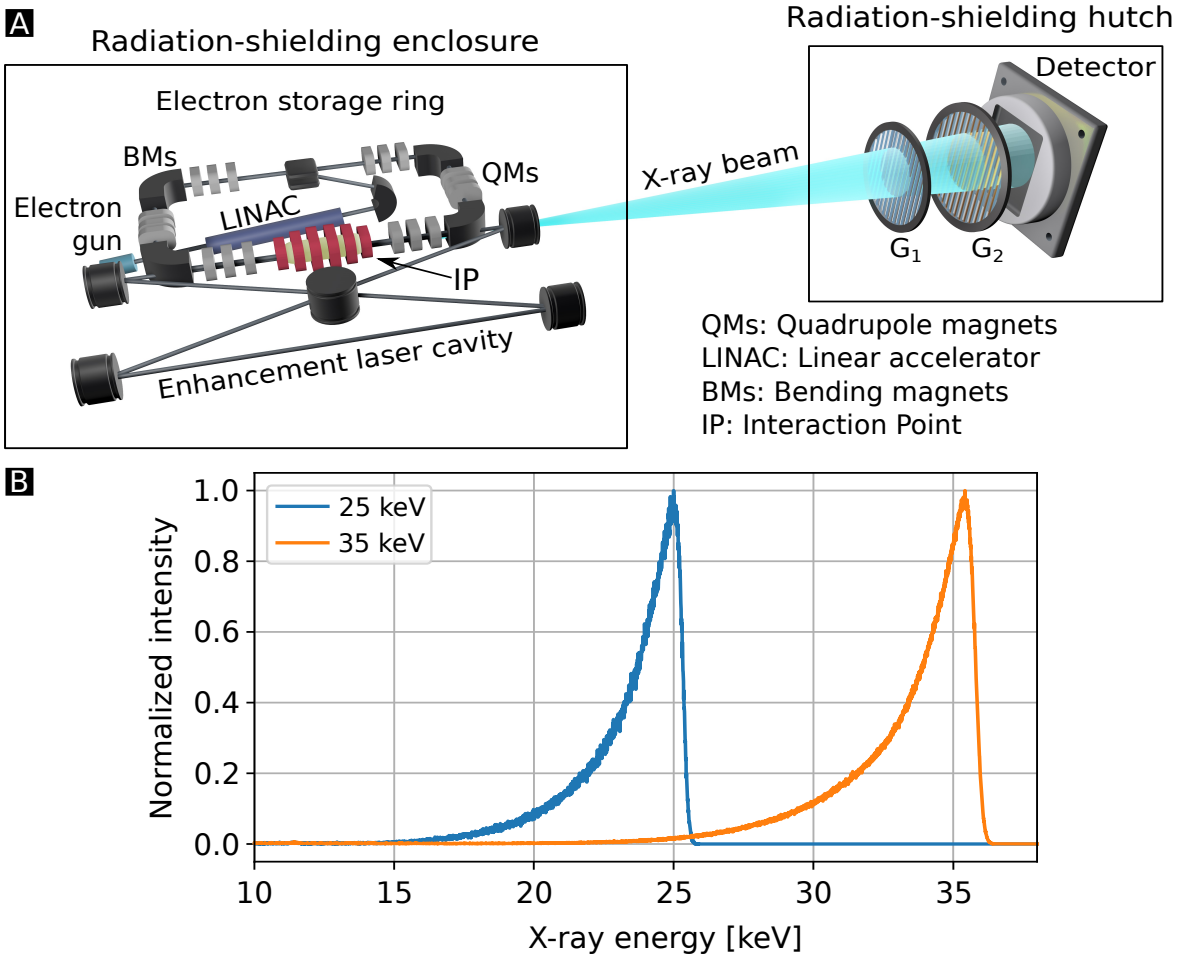

Figure 2.4: Schematic drawing and X-ray source spectrum of the CLS. (A) Electrons are produced in a radiofrequency cathode, accelerated towards relativistic energies and stored in the electron storage ring. In the interaction point, they collide head-on with the infrared laser pulse which is stored in the enhancement laser cavity. This interaction generates quasi-monochromatic X-rays photons. The produced X-rays are collimated to an opening angle of 4 mrad by an aperture. An evacuated beam pipe guides the X-ray photons to the experimental hutches. Here, only one is exemplary shown although two hutches are available for experiments. (B) X-ray source spectrum shown for 25 keV and 35 keV.

transverse directions in the straight section of the storage ring in which the interaction with the laser takes place. The key component of the laser system is a high-finesse bow-tie enhancement laser cavity with a total length of 9.2 m. It increases the power delivered by the Nd:YAG laser (wavelength 1064 nm) from ~25 kW to ~350 kW. Since the laser's repetition rate is 65 MHz as well, two laser pulses are circulating inside the enhancement cavity at the same time. Consequently, its effective repetition rate at the

interaction point (IP) inside the aforementioned shared straight section is the same as the one of the electron bunch. The enhancement cavity is designed such that the laser beam is focused at the same position like the electron bunch. There, the electron bunch collides head-on with the laser pulse. Quasi-monochromatic X-ray photons are generated in this collision via the so-called inverse Compton scattering. The resulting X-ray energy E_x is calculated by

$$E_\mathrm{x} = \frac{(1 - \beta \cdot \cos\theta_\mathrm{i}) \cdot E_\mathrm{L}}{1 - \beta \cdot \cos\theta_\mathrm{f} + (E_\mathrm{L}/E_\mathrm{e})(1 - \cos(\theta_\mathrm{f} - \theta_\mathrm{i}))}\,, \tag{2.16}$$

where E_L denotes the laser photon energy, $\beta = v/c$, θ_i and θ_f the incoming and afterwards scattering angles and E_e the electron energy. Equation (2.16) simplifies to

$$E_\mathrm{x} \approx \frac{E_\mathrm{e}(1+\beta)^2 E_\mathrm{L}}{E_\mathrm{e}/\gamma^2} \approx 4\gamma^2 E_\mathrm{L}\,, \tag{2.17}$$

for a head-on collision of laser photon and electron bunch in the case of backscattering with $\gamma = E_\mathrm{e}/E_0$ and $E_0 = 511\,\mathrm{keV}$ as electron rest energy. Since the wavelength of the laser is fixed, the electron energy is adjusted to tune the X-ray energy. The generated X-rays are confined to an opening angle of 4 mrad by an aperture. This X-ray beam propagates to the experimental set-ups via an evacuated beam pipe. The currently possible X-ray energy operation range is between 15 and 35 keV. The X-ray source spectra for 25 keV and 35 keV are shown in Fig. 2.4 (B). Additional operation parameters currently used and characteristics such as X-ray brilliance, bandwidth, source size are shortly summarized in Tab. 2.1.

2.3 X-ray Detection

While classical techniques such as photographic films were used to detect the disturbed X-ray wavefront in the past, digital detectors are preferred nowadays. In the following, both the working principle of flat-panel detectors as well as the direct detection principle of photon-counting detectors are introduced. Unless otherwise indicated, the first subsection is mainly based on the explanations in [Spahn, 2005; Seibert, 2006] while for the second subsection the following references are used [Spieler, 2006; Ballabriga, 2007; Ballabriga, 2013; Pennicard, 2013; Ballabriga, 2016; Sellerer, 2016].

2.3.1 Flat-panel Detector

Two types of flat-panel detectors exist which can be divided into an indirect or direct detection method. In the first case of the indirect detection principle, the scintilla-

Revolution frequency	65 MHz
Electron energy	29 to 45 MeV
Laser wavelength	1064 nm
Laser power	350 kW
X-ray energy	15 to 35 keV
X-ray flux	Up to 1.5 $\times 10^{10}$ photons/s (15 keV)
	Up to 4.5 $\times 10^{10}$ photons/s (35 keV)
X-ray divergence	4 mrad
X-ray source size	~50 µm (σ-value)
X-ray bandwidth	3 % (15 keV) to 5 % (35 keV)
X-ray brilliance	1.2 $\times 10^{10}$ photons/(s (0.1 % bandwidth) mm^{2}mrad^2)

Table 2.1: Overview of the current operation parameters of the CLS. It includes the characteristics about the X-ray source and beam as well as the parameter of the laser and the electron bunch [Günther, 2020].

tion crystal, the impinging X-ray photons are absorbed and converted to visible light. Usually gadolinium oxysulfide (GadOx) or caesium iodide (CsI) are employed as scintillator material due to their high quantum efficiency and high light yield which originates from their high atomic numbers. Afterwards, an electronic signal is produced which is arranged by the following process: Every detector element called pixel consists of a thin-film-transistor (TFT) and a photo diode that works as a capacitor deposited on the TFT. The photo diode is initially charged by a bias voltage. Electron-hole pairs are produced in the semiconductor of the photo diode by the absorption of visible light photons. As a consequence, this discharges the photo diode. When the TFT is switched on by the gate line, the charge flows to the photo diode until the initial bias voltage is restored. The total charge is proportional to the energy and the number of X-rays hitting the detector. This is measured by the coupled readout electronics. After one so-called readout cycle and once the photo diode has reached the initial bias voltage, the next acquisition can be performed. With those indirect detecting flat-panel detectors, the information about the energy of the incoming X-ray is lost since the total charge is integrated during one readout cycle of the detector. During the readout process, there is dark current of and thermal noise in the photo diode and electronic noise. The offset

induced by the dark current must be corrected while noise contributions from thermal and electronic noise are added to Poisson noise. Therefore, an additional dark current correction is necessary when such detectors are used.
In direct converting detectors, a photo conductor is utilized instead of a scintillator and a photo diode. Electron-hole pairs are produced by the incoming X-ray photons in an amorphous Selenium-based layer. By applying an electric field to the layer, the generated charge carriers travel to the electrodes at which they are stored. The readout electronics are the same like the ones for an indirectly converting detector and also the readout noise is similar. In this case, the energetic resolution is lost as well. Although the detector's point spread function (PSF) is superior with its nearly box-like behavior than the one in the indirect detection scheme, spatial blur slightly exists since part of the generated charge cloud spreads on its way to the storage electrode. Thus, the charge cloud is not completely collected in the pixel that is directly under the location in which the X-ray photon was originally absorbed. With the exception of few prototypes, flat-panel detectors are by far the most commonly used detector types for medical imaging.

2.3.2 Photon-counting Detector

In contrast to the scintillator-based integrating detector technology, photon-counting detectors employ a direct detection principle. The main difference is that each incident X-ray photon is measured energy-selectively and individually from others. It is possible to discriminate between several energy intervals simultaneously, so that the signal is split into different energy bins and thus the energy information is not completely lost. Photon-counting detectors are single-pulse processing detectors and consist of an active semiconductor sensor layer in which the incoming X-ray photons are converted into electron-hole pairs. Therefore, silicon (Si), gallium arsenide (GaAs) and cadmium telluride (CdTe) are common sensor materials. The amount of generated charge carriers determining the signal pulse height is proportional to the energy of the incoming photon. By applying a bias voltage U_{bias}, an electric field is induced, which separates the produced charge carriers. The electrodes of the sensor layer are connected to an individual pixel electronic circuit via so-called bump-bonds. A pulse-processing architecture is realized by those pixel-wise read-out circuits realized by an application specific integrated circuit (ASIC). As presented in Fig. 2.5, such a circuit mainly consists of a pre-amplifier, a shaper, several energy discriminators and the corresponding counters. The collected signal is first amplified before it is fed to the shaper, which acts as a bandpass filter and suppresses noise while maintaining the signal. The height of the shaped signal is proportional to the number of charge carriers collected and in turn to the absorbed X-ray energy of the impinging photon. The output of the shaper is then compared to several energy thresholds (THLs) (here: two) in the dis-

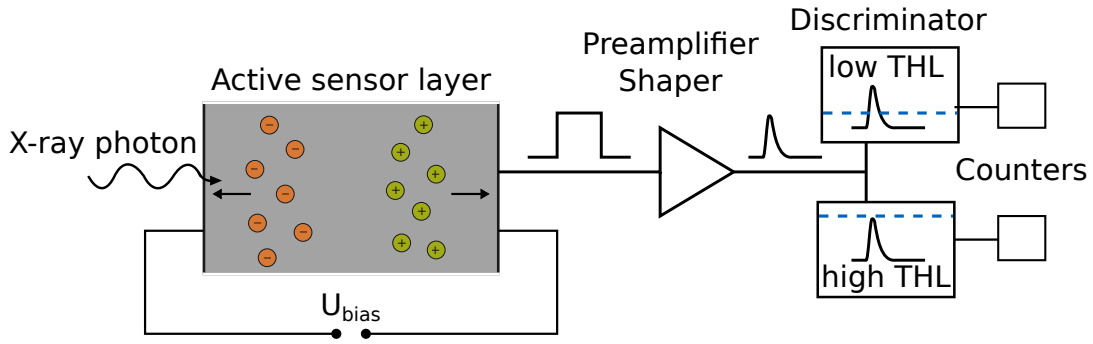

Figure 2.5: Pixel electronics of a two THL-based photon-counting detector. The absorbed X-ray photon creates electron-hole pairs in the active sensor layer. They are separated by the applied bias voltage U_{bias}. The resulting signal is pre-amplified, shaped and finally compared to the adjusted THLs in the discriminator before stored in the corresponding counters. Spatial and temporal registration of spectral data is obtained without losing energy information completely, while thermal and electronic noise are effectively eliminated.

criminator. A logical signal is sent to the corresponding counter as soon as the signal exceeds the corresponding energy THL so that the incident X-ray photon is detected. Finally, the amount of stored counts is read-out and sent to a field programmable gate array (FPGA). It is used to store the count data obtained during an acquisition. This technology achieves spatial and temporal registration of spectral data within one measurement.

Nevertheless, some sensor-related effects affect the spectral resolution of photon-counting detectors shown in Fig. 2.6. In the ideal detection case (A), the whole energy of the incoming X-ray photon is absorbed by photoelectric absorption and the created charge cloud is read-out by only one pixel. In contrast, when a photon hits the detector close to the boundary of two pixels, the charge cloud could spread out across the pixel's border and be detected in both pixels. This decreases the signal strength for the pixel in which the photon originally hit the detector. In addition, when the spread-out charge cloud induced a signal that exceeds the THL in another pixel, a signal is falsely detected with a lower energy. This effect is called charge-sharing and affects the spectral as well as the spatial resolution and is depicted in (B). Some detectors additionally have a charge-sharing correction implemented. It either compares the charge cloud collected by neighbouring pixels and just counts the one with the highest signal or corrects the signal strength. Furthermore, the X-ray photon can get scattered within the sensor material as well. Although the energy of an X-ray photon absorbed after coherent scattering (C) is the same, the photon may travel to a neighboring pixel, affecting spatial resolution. Compton scattering (D) has a similar effect as charge-sharing since the X-ray photon loses some of its energy and partial charge

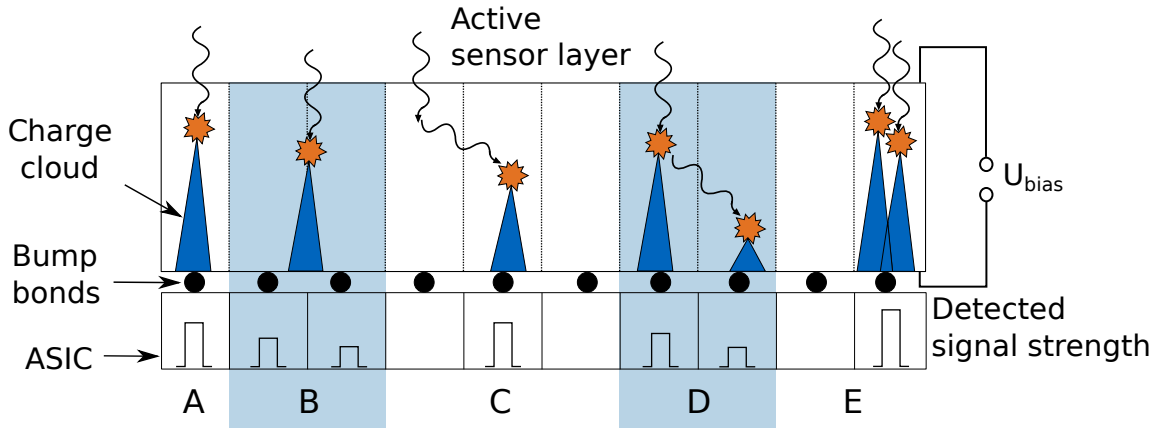

Figure 2.6: Sensor-related effects of photon-counting detectors. (A) The ideal case where the whole X-ray energy is detected in one pixel. (B) The charge-sharing effect where the charge cloud spreads across several pixels and more than one pixel detects a signal. (C) Coherent scattering where the charge cloud is created in a neighbouring pixel and falsely detected. (D) The Compton scattering effect, where the energy resolution is additionally affected. (E) Pulse pile-up takes place when two or more photons are simultaneously detected since they can not be distinguished temporally. As a consequence, they are detected as one photon with a higher X-ray energy. Figure is adapted from [Ehn, 2017].

deposition can occur in multiple pixels allowing more than one pixel to detect a signal. The last effect called signal pulse pile-up is shown in subfigure (E). This happens when two or more X-ray photons hit the detector pixel in a period of time that is smaller than the temporal resolution of the detector. In this case, they cannot be distinguished and are detected as one photon with a higher X-ray energy since their signal strengths overlap.

2.4 Grating-based Interferometry

In the field of X-ray imaging, one way to enhance the contrast of soft tissue is to use the wave properties of X-ray photons such as the phase and ultra-small-angle scattering information. Over the last decades, phase-sensitive X-ray imaging methods such as crystal interferometry [Bonse, 1965; Momose, 2003], analyzer-based imaging [Davis, 1995; Ingal, 1995] and free-space propagation [Snigirev, 1995; Wilkins, 1996; Cloetens, 1999] have been established. They require high spatial coherence and a high photon flux as provided by large-scale synchrotron facilities. With regard to medical applications and diagnostic imaging, the most promising approach for retrieving phase-contrast and dark-field information with a conventional, laboratory-based and low-brilliance X-ray

source is grating-based interferometry [David, 2002; Weitkamp, 2005; Pfeiffer, 2007]. This technique is used in this work and is therefore introduced and explained in the following in more detail.

2.4.1 Talbot Effect

In 1836, Henry Fox Talbot discovered the effect which was named after him during his experimental investigations. He placed periodic structures in the beam path of visible light and observed that the periodic structure is reproduced as a self-image behind the so-called grating after a certain propagation distance [Talbot, 1836]. The distance is called Talbot distance d_T and defined as

$$d_{\mathrm{T}} = \frac{1}{\eta^2}\frac{np^2}{2\lambda}\,. \tag{2.18}$$

It depends on the grating period p and the wavelength λ of the electromagnetic wave [Weitkamp, 2006]. It works for both attenuating as well as phase shifting periodic structures. The Talbot order n is an odd number ($n = 1, 3, 5, ...$) for phase gratings and an even number ($n = 0, 2, 4, ...$) for absorption gratings . A further difference between $\pi/2$-phase or absorption grating and the π-shifting phase grating is given by the factor η as follows

$$\eta = \begin{cases} 1 & \text{for a } \pi/2\text{-phase grating or absorption grating,} \\ 2 & \text{for a } \pi\text{-phase grating.} \end{cases} \tag{2.19}$$

The simulated interference patterns or so-called Talbot carpets of an absorption, a π- and a $\pi/2$-shifting phase grating for a monochromatic X-ray source are illustrated in Fig 2.7. Wit an absorption grating in (A) the self image occurs after half of the Talbot distance. For the $\pi/2$- and the π-phase grating, however, the periodical structure reappears after odd multiples of 1/4 or 1/16 of the Talbot distance, respectively. It has to be noted that the period of the modulation pattern behind the $\pi/2$-shifting phase grating is half the period of the grating.

2.4.2 X-ray Grating Interferometry

X-ray grating interferometry, also known as Talbot interferometry, was first introduced at synchrotron sources. An essential basis of this approach is the aforementioned Talbot self-imaging effect (cf. Sec. 2.4.1) [Talbot, 1836]. The interferometer uses at least two optical gratings to obtain the phase information of an X-ray wavefront. These gratings

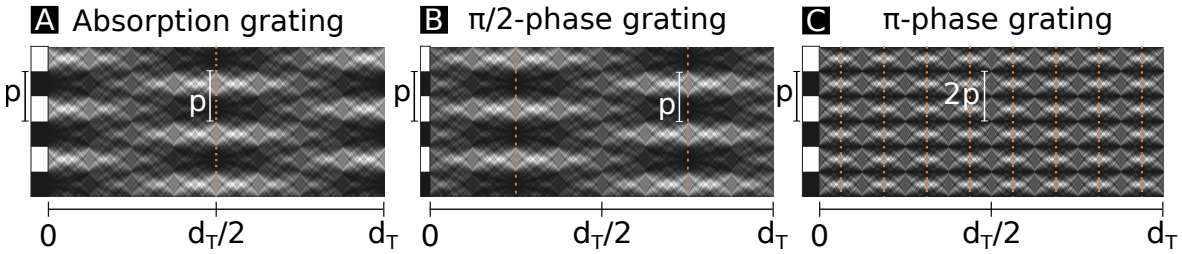

Figure 2.7: Simulated Talbot carpets for different grating types. The interference patterns are displayed for (A) the absorption grating, (B) the π-phase grating and (C) the $\pi/2$-phase grating for a full Talbot distance d_T simulated with monochromatic parallel beam geometry. While the self images, indicated by dotted orange lines, of the absorption grating appear after a distance of $d_T/2$, the $\pi/2$- and π-phase gratings repeats itself after odd multiples of 1/4 or 1/16 of the Talbot distance, respectively.

act either absorbing or phase-shifting on X-ray photons and consist of periodically arranged thin bars [Weitkamp, 2006]. The first grating G_1 is a phase-shifting grating that imposes a periodic spatial modulation on the X-ray wavefront's amplitude and is therefore also known as beam splitter or reference grating. With this grating, the so-called Talbot carpet is created. The grating periods are only a few micrometres in size so that the length of the experimental setup is not very long due to the Talbot spacing. By placing a sample in the beam path, the Talbot carpet is distorted so that lateral displacements have to be detected. Since most detectors have pixel sizes larger than the period of the intensity modulation, they can not directly resolve the intensity pattern so the pattern is invisible for regular detectors. This is why a second grating G_2 called analyzer grating is required to resolve the modulations. It is mounted directly in front of the detector with a distance to the reference grating corresponding to one of the fractional Talbot distances (cf. Eq.(2.18)). In contrast to G_1, the analyzer grating is an absorption grating with higher grating bars for complete X-ray attenuation. The grating period p_2 of the analyzer grating is proportional to the period p_1 of the reference grating G_1 and calculated as

$$p_2 = M\frac{p_1}{\eta}\,. \tag{2.20}$$

It additionally considers the magnification factor M which is defined as quotient of the source-to-G_2 and the source-to-G_1 distance.
For imaging with a laboratory X-ray source with an extended source size, an additional source grating G_0 is necessary in order to accomplish the transverse coherence required for grating interferometry [Pfeiffer, 2006; Pfeiffer, 2007; Pfeiffer, 2008]. The initial X-ray beam is split by this absorption grating into an array of smaller, individually

coherent but mutually incoherent line sources [Pfeiffer, 2006]. An X-ray wavefront with increased effective spatial coherence is obtained, so that the Talbot-Lau interferometer allows the same image modality extraction as with synchrotron facilities [Pfeiffer, 2006; Pfeiffer, 2008]. Depending on the inter-grating distances, the grating period of the source grating p_0 is

$$p_0 = p_2 \frac{l}{d}, \tag{2.21}$$

with l as distance between G_0 and G_1 and d as distance between G_1 and G_2 [Pfeiffer, 2006]. If you choose p_0 and the distance correctly, the interference patterns of each slit will match each other individually. The working principle of a Talbot-Lau interferometer for a three-grating interferometer is illustrated in the first row in Fig. 2.8 for three different samples representing (A) the attenuating, (B) the phase-shifting and (C) the scattering case. In the real case, however, a sample consists of a combination of the three modalities. The procedure to sample the interference pattern by moving one of the gratings relative to the others is called phase stepping and will be described in the following section.

2.4.3 Phase Stepping and Image Extraction

The interference pattern is distorted when placing a sample in the beam path. Three complimentary imaging modalities can be extracted with grating interferometry: The attenuation, the differential phase and the dark-field (small-angle scattering) contrast. The attenuation decreases the mean intensity of the stepping curve when a sample absorbs X-ray photons (A). In the phase-shifting case (B), the interference pattern is shifted so that also the stepping curve is moved laterally. Small-angle scattering reduces the amplitude of the stepping curve referring to a reduction of the interference pattern's intensity (C). In the first row of Fig. 2.8, the effect of inserting a sample in the beam path is visualized.
In order to retrieve the three signals, one of the gratings is shifted in lateral direction perpendicular to the grating bars over one grating period during the phase stepping procedure to resolve the interference pattern. The measured intensity that is recorded for each detector pixel follows a sinusoidal curve and depends on the relative grating position x_g. This curve is called phase stepping curve. A reference phase stepping curve is recorded without a sample in the beam path so that the sample stepping curve and the changes affecting it can be examined. The effect on the after passing the sample is visualized in the second row of Fig. 2.8.
Several approaches exist to finally obtain the three signals by comparing the reference and the sample stepping curve. The Fourier decomposition where the description is based on a Fourier series is a fast and simple way. In order to calculate the sinusoidal

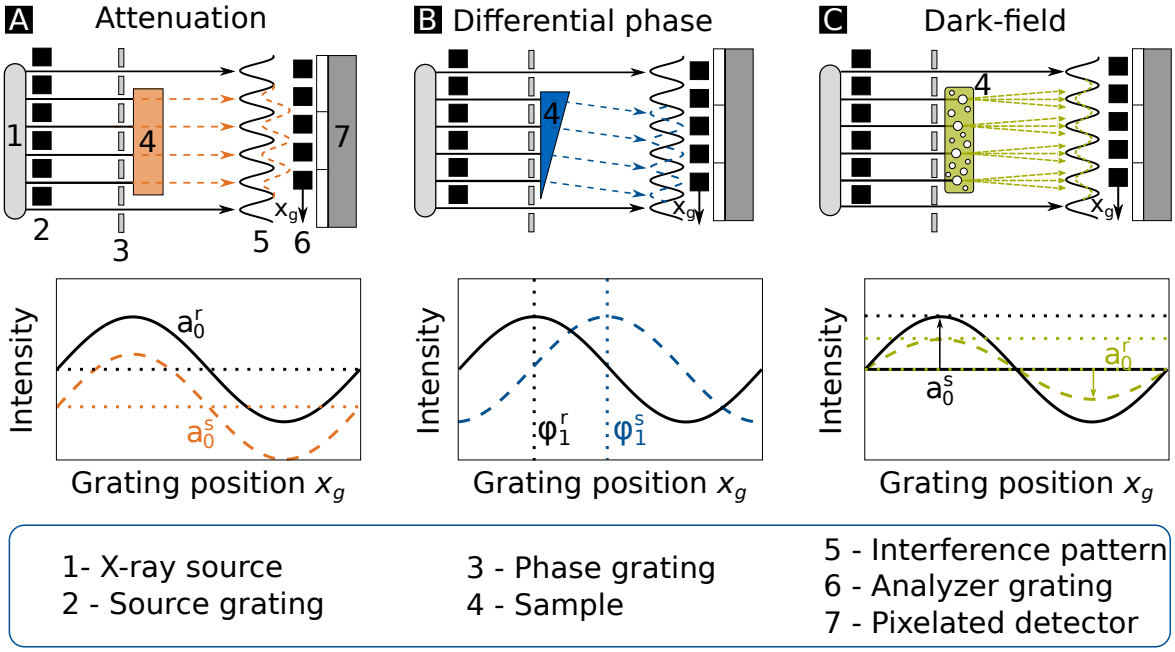

Figure 2.8: Working principle of a Talbot-Lau grating interferometer. (A) The absorption-contrast induced by a purely attenuating sample reduces the measured mean intensity a_0 of the stepping curve. (B) The phase-contrast signal refers to the lateral phase shift of the interference pattern caused by the refraction of a sample. (C) The dark-field signal corresponds to ultra-small-angle scattering of a sample resulting in a reduced amplitude a_1 of the stepping curve. The reference curve is illustrated by the black line whereas the sample curve is indicated by the dashed, colored line.

stepping curve, the measured intensity $I(x, y, x_g)$ in one detector pixel for a grating position x_g is modelled as

$$I(x, y, x_g) = \sum_{i}^{M} a_i(x, y) \sin\left(2\pi i \frac{x_g}{p} - \varphi_i(x, y)\right) , \tag{2.22}$$

for a total of M phase steps. In the first order, the Fourier series can be approximated as follows

$$I(x, y, x_g) = a_0(x, y) + a_1(x, y) \sin\left(2\pi \frac{x_g}{p} + \varphi_1(x, y)\right) , \tag{2.23}$$

where all terms above the first order are neglected when moderate coherence with a visibility below 50 % is assumed [Bech, 2009]. Here, a_0 denotes the average measured intensity, a_1 the modulation amplitude and φ_1 the phase shift. After measuring one full

stepping curve with (denoted with superscript s) and without (denoted with superscript r) sample in the beam path, the three imaging signals (absorption, refraction and scattering) can then be retrieved:

Transmission

The pixelwise transmission signal can be extracted from the measured intensities I and I_0 or rather from the average intensity a_0 from the stepping curve with (s) and without (r) sample in the beam path

$$T = \frac{a_0^{\mathrm{s}}(x,y)}{a_0^{\mathrm{r}}(x,y)} = \frac{I(x,y)}{I_0(x,y)} = e^{-\int \mu(x,y,z)dz}\,. \tag{2.24}$$

Referring to the Beer-Lambert law (cf. Eq.(2.7)), the transmission directly correlates with the linear mass attenuation coefficient μ. In clinical daily routine and practice, images are mostly evaluated regarding the negative logarithmic form of the transmission signal.

Differential Phase Contrast

The phase shift can be calculated by pixelwise subtracting the phases of the two stepping curves yielding the differential phase-contrast signal:

$$\Delta\varphi(x,y) = \varphi_1^{\mathrm{s}}(x,y) - \varphi_1^{\mathrm{r}}(x,y). \tag{2.25}$$

Dark-Field Contrast

The reference flat-field visibility V is measured without any sample in the beam path and is calculated by connecting the average intensity a_0 and the amplitude a_1 of the stepping curve as follows

$$V^{\mathrm{r}}(x,y) = \frac{I_{\max} - I_{\min}}{I_{\max} + I_{\min}} = \frac{a_1^{\mathrm{r}}(x,y)}{a_0^{\mathrm{r}}(x,y)}. \tag{2.26}$$

It is an important parameter that is often used for the assessment of the quality of an interferometer. The visibility reduction induced by a scattering sample is commonly known as dark-field signal and calculated by the quotient of the visibilities with and without sample in the beam path

$$D(x,y) = \frac{V^s(x,y)}{V^r(x,y)} = \frac{a_1^{\mathrm{s}} a_0^{\mathrm{r}}}{a_1^{\mathrm{r}} a_0^{\mathrm{s}}} \,. \tag{2.27}$$

2.5 Principles of Computed Tomography

CT is a widely spread imaging approach for clinical, but also non-destructive X-ray imaging that is able to provide three-dimensional information of the inside of a sample or patient. For that, a set of angular projection images are taken which are then reconstructed to obtain the volumetric information of the sample. Two different approaches are used to reconstruct the measured data, referred to as FBP and iterative reconstruction. FBP is a fast, analytically well-described and common clinically used method. The SIR algorithm, however, is one way of iterative reconstruction that is more complex and computationally expensive and as the name suggests, statistical information is required. Unless otherwise indicated, the explanations in this section are based on [Radon, 1986; Kak, 1988; Hsieh, 2003; Buzug, 2008; Hahn, 2014].

2.5.1 Radon Transform

Although CT devices nowadays use fan- or cone-beam geometry, parallel-beam geometry is assumed for the following theoretical explanations for simplicity. This geometry assumption implies that there are a several parallel lines travelling through the sample which together form one CT slice. Instead of using a conventional Cartesian coordinate system (x, y) fixed for the sample position, a rotating coordinate system (s, t), is defined. A visualization of the connection between both coordinate systems is drawn on the left sketch in Fig. 2.9. The measured projection $p(\theta, s)$ of an inhomogeneous sample in the rotating coordinate system (s, t) under the projection angle θ is given by the following integral

$$p_\theta(s) = \int_0^d \mu(s,t)\mathrm{d}t \,, \tag{2.28}$$

representing the Radon transform. Here, s is the width of the detector and t the beam direction. In clinical CT imaging, however, one is rather interested in the spatial object information meaning the spatial distribution of the attenuation coefficients in the fixed coordinate system of the sample (x, y) rather than in the one of the rotating coordinate system (s, r). The geometrical connection between the variables of the two coordinate systems can be written in the following notation by using unit vectors

$$\begin{pmatrix} s \\ t \end{pmatrix} = \begin{pmatrix} \cos\theta & \sin\theta \\ -\sin\theta & \cos\theta \end{pmatrix} \begin{pmatrix} x \\ y \end{pmatrix} . \tag{2.29}$$

This enables to transfer any point from one coordinate system to the other. Consequently, the attenuation coefficient from Eq. (2.28) can also be expressed as

$$f(x,y) = \mu(s(x,y), t(x,y)) . \tag{2.30}$$

Since in the rotating coordinate system, the X-ray source is stepwise shifted and thus reflects a sampling process, a δ-function can be used for the description. Using Eq. (2.29), the projection integral may in consequence be written as

$$\begin{aligned} p_\theta(s) &= \int_0^d f(s,t)\mathrm{d}t \\ &= \int_{-\infty}^{\infty} f(x,y)\delta(x\cos\theta + y\sin\theta - s)\mathrm{d}x\mathrm{d}y . \end{aligned} \tag{2.31}$$

The two-dimensional Radon transform of the sample is taken to transform a function $f(x,y)$ into its angular projections. Therefore the following notation is usually utilized

$$p_\theta(s) = \mathcal{R}_2\{f(x,y)\} . \tag{2.32}$$

Since the direct inversion of the Radon transform to obtain the objection function is not computationally feasible, the data is reconstructed using the Fourier Slice theorem and FBP or SIR which will be explained in the next section.

2.5.2 Fourier Slice Theorem

In contrast to the inverse Radon transform, the Fourier Slice theorem connects the one-dimensional Fourier transform of the projection to the two-dimensional Fourier transform of the objection function. This is schematically depicted in Fig. 2.9. All in all, the procedure of the Fourier Slice theorem is split into three parts. First, the one-dimensional Fourier transform of $p_\theta(x) = \int f(x)\mathrm{d}y$ is calculated. This is described by

$$P_\theta(u) = \mathcal{F}\{p_\theta(x)\} = \int_{-\infty}^{\infty} p_\theta(x) e^{-2\pi i x u}\mathrm{d}x . \tag{2.33}$$

The two-dimensional Fourier transform of the object function $f(x, y)$, however, is defined as

$$F(u, v) = \mathcal{F}\{f(x, y)\} = \iint_{-\infty}^{\infty} f(x, y) e^{-2\pi i(xu+yv)} \mathrm{d}x\mathrm{d}y \,. \tag{2.34}$$

Regarding the Fourier transform along a line at $v = 0$, $F(u, v)$ is simplified and one slice through $F(u, v)$ is given by

$$\begin{aligned} F(u, 0) &= \int_{-\infty}^{\infty} \int_{-\infty}^{\infty} f(x, y) e^{-2\pi i x u} \mathrm{d}x\mathrm{d}y \\ &= \int_{-\infty}^{\infty} \left(\int_{-\infty}^{\infty} f(x, y) \mathrm{d}y \right) e^{-2\pi i x u} \mathrm{d}x. \end{aligned} \tag{2.35}$$

In the second row, the equation is divided into two parts where the exponential factor does no longer depend on the variable y. The comparison of the integral in the brackets of this equation with Eq. (2.28) by assuming that the attenuation coefficient $\mu(s, t)$ corresponds to the object function $f(x, y)$ shows that it equals a projection under angle zero. By submitting Eq. (2.28), it follows

$$F(u, 0) = \int_{-\infty}^{\infty} p_\theta(x) e^{-2\pi i x u} \mathrm{d}x = P(u, \theta) \,, \tag{2.36}$$

which equals Eq. (2.33) and reflects the basic idea of the Fourier slice theorem. Translating the mathematical formulations into words, the theorem states that the one-dimensional Fourier transform $P_\theta(u)$ of a parallel projection $p_\theta(x)$ recorded under an angle θ equals a radial line through the two-dimensional Fourier transform of the object function $f(x, y)$ taken at the same angle θ. Please note that, as indicated by the centered sketch of Fig. 2.9, two problems arise when following this approach. On the one hand, the data points are radially distributed in Fourier space meaning over a polar instead of a rectangular grid so that an interpolation is required. On the other hand, since the sampling becomes sparser with increasing distance from the center, this results in lower sampling for higher frequencies, which leads to a deterioration of the image quality.

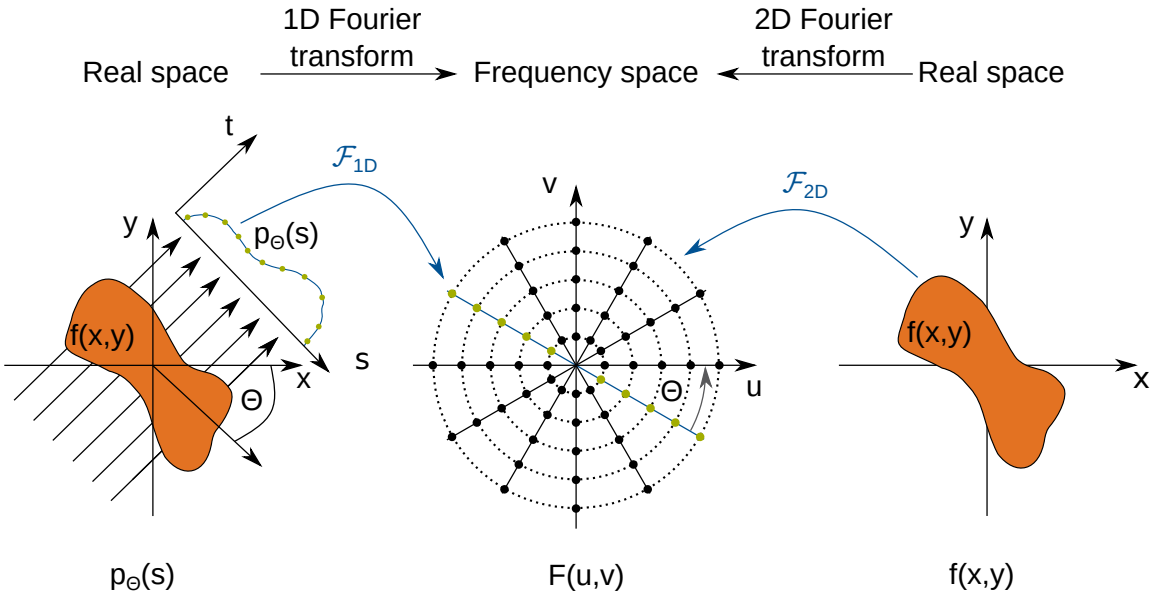

Figure 2.9: Visualization of the Fourier slice theorem. The one-dimensional Fourier transform of a parallel projection $p_\theta(s)$ of $f(x, y)$ obtained at an angle θ equals a radial line of the two-dimensional Fourier transform of $f(x, y)$ taken at the same angle. In the centered sketch, the unequal angular sampling in Fourier space is illustrated showing the sparser sampling the higher the distance from the center.

2.5.3 Filtered Backprojection

The aforementioned unequal sampling in the Fourier domain can be compensated by weighting the data in the frequency space before they are back projected. This algorithm is called FBP and mathematically shortly introduced in the following. A more comprehensive description about the mathematical background is summarized in [Kak, 1988; Buzug, 2008]. With the Fourier slice theorem, the object function can be derived with the two-dimensional Fourier transform:

$$f(x,y) = \frac{1}{2\pi} \int_{-\infty}^{\infty} \int_{-\infty}^{\infty} F(u,v) e^{2\pi i(xu+yv)} \mathrm{d}u\mathrm{d}v \,. \tag{2.37}$$

The data is transferred from a rectangular (u, v) to a polar coordinate system (ω, θ) by changing $u = \omega cos\theta$ and $v = \omega sin\theta$. The Jacobian determinant is considered to substitute the differentials with $\mathrm{d}u\mathrm{d}v = |\omega|\mathrm{d}\omega\mathrm{d}\theta$. Thus, Eq. (2.37) results in

$$f(x,y) = \frac{1}{2\pi} \int_{0}^{2\pi} \int_{-\infty}^{\infty} F(\omega\cos\theta, \omega\sin\theta) e^{2\pi i\omega(x\cos\theta + y\sin\theta)} \omega \mathrm{d}\omega\mathrm{d}\theta \,, \tag{2.38}$$

using the transformations from above. By applying now the knowledge about the Fourier slice theorem from Sec. 2.5.2, one can rewrite the two-dimensional Fourier transform $F(\omega\cos\theta, \omega\sin\theta) = F(u, v)$ with the Fourier transform of a projection under an angle θ as follows

$$f(x,y) = \frac{1}{2\pi}\int_0^{2\pi}\int_{-\infty}^{\infty} P_\theta(\omega) e^{2\pi i\omega(x\cos\theta + y\sin\theta)}\omega \mathrm{d}\omega \mathrm{d}\theta \tag{2.39}$$

$$= \frac{1}{2\pi}\int_0^{\pi} \underbrace{\int_{-\infty}^{\infty} P_\theta(\omega) e^{2\pi i\omega s}|\omega|\mathrm{d}\omega}_{h_\theta(s)-\text{filtered projection}} \mathrm{d}\theta\,. \tag{2.40}$$

The inner integral, indicated by $h_\theta(s)$, reflects the projections filtered with a high-pass filter in Fourier space. The higher frequencies are weighted more which is required due to the sparse sampling in the outer regions. Depending on the application and in addition to the linear ramp $|\omega|$ introduced above (also known as Ram-Lak filter [Ramachandran, 1971]), various filters can be used, which should generally ensure a balance between edge sharpening or preservation of edges and noise reduction. Examples therefore the Shepp-Logan or the Hamming filter. The outer integral is responsible for the backprojection of the prior filtered projections. For every angular position θ, they are smeared out along s. The imaginary Hilbert filter is used for the reconstruction of differential data. The Hilbert filter equals an integration of differential data in real space. This filter is defined by a sign-function (sgn) as follows [Pfeiffer, 2007]

$$H(\omega) = \frac{1}{2\pi i \mathrm{sgn}(\omega)}\,. \tag{2.41}$$

In order to fulfill the angular sampling requirements for CT reconstruction and to avoid undersampling, the Nyquist theorem has to be considered. It ensures sufficient data sampling in the Fourier space for artifact-free reconstruction with FBP. It is stated that the maximum frequency in the data spectrum has to be less than half of the sampling rate. Taking the number of pixels $\mathcal{N}_{\mathrm{pix}}$ in horizontal direction into account, the minimum number of projection angles $\mathcal{N}_{\mathrm{proj}}$ can be estimated as follows [Kak, 1988; Natterer, 1986]

$$\mathcal{N}_{\mathrm{proj}} \geqslant \frac{\pi}{2}\mathcal{N}_{\mathrm{pix}}\,. \tag{2.42}$$

2.5.4 Statistical Iterative Reconstruction

SIR is another method for the reconstruction of three-dimensional data. This approach utilizes a statistical noise model together with iterative reconstruction. Compared to FBP, it is less prone to missing data, angular undersampling and complex geometry leading in consequence to an improve image quality. Further noise reduction is enabled by the usage of a regularization term that incorporates prior knowledge about the sample. The computational effort, however, is more challenging than the analytical approaches such as the FBP and thus more time-consuming. Generally, the SIR approach is composed of five individual parts:

1. Data noise model
2. Forward model for calculating the expected photon counts
3. Regularization term
4. Optimization algorithm to solve the log-likelihood function

Each part is shortly explained in the following. For a more detailed description, see [Hsieh, 2003; Hahn, 2014]. To find a final image $\vec{\mu}_f$ is the main goal of this approach. This can be obtained by maximizing the probability of the measured data $\vec{y}$ in due consideration of the current estimate $\vec{\mu}$. Mathematically it is expressed as follows

$$\vec{\mu}_{\mathrm{f}} = \arg\max_{\vec{\mu}} P(\vec{\mu}|\vec{y})\,, \tag{2.43}$$

with $P(\vec{\mu}|\vec{y})$ as probability function where several noise models can be employed for the measurements. The Bayes' theorem [Bayes, 1763] is an important rule that will be used for the derivations in the following and is defined as

$$P(\vec{\mu}|\vec{y}) = \frac{P(\vec{y}|\vec{\mu})P(\vec{\mu})}{P(\vec{y})}\,. \tag{2.44}$$

Two commonly used **data noise models** are the Poisson or the Gaussian distribution. Since detecting X-ray photons is a counting process and the individual events are independent of each other, a Poisson distribution is assumed for the detected counts. For the expected photon counts $\hat{y}_i(\vec{\mu})$ from the i-th of totally N measurements, the probability of the measured data is defined as

$$P(\vec{y}|\hat{\mu}) = \prod_{i=1}^{N} \frac{\hat{y}_i(\vec{\mu})^{y_i}}{y_i!} e^{-\hat{y}_i(\vec{\mu})}\,, \tag{2.45}$$

when assuming statistical independence of the measurements. The Poisson model turns into a Gaussian distribution for a higher amount of detected photon counts. Thus, the probability is approximated by

$$P(\vec{y}|\hat{\mu}) = \prod_{i=1}^{N} \frac{1}{\sqrt{2\pi}\sigma_i} \exp\left(-\frac{(y_i - \hat{y}_i(\vec{\mu}))^2}{2\sigma_i^2}\right), \tag{2.46}$$

with σ_i denoting the standard deviation of the i-th measurement. The discretization, a finite parametrization of the spatially distributed attenuation coefficients μ is required and a **forward model** is established. According to the Radon transform, the forward projection in a discretized form is expressed as

$$l_i = \sum_j a_{ij}\mu_j \,, \tag{2.47}$$

representing the line "integrals" l_i and information about voxel j for pixel i are contained in the matrix a_{ij}. It includes forward projections and the Beer-Lambert law in order to express the expected number of photon counts $\hat{y}_i$ for a reference number of photon counts during flat-field acquisition $y_{r,i}$ as

$$\hat{y}_i = y_{r,i} \exp\left(-\sum_j a_{ij}\mu_j\right). \tag{2.48}$$

The last point deals with the **optimization algorithm** and for this, Eq. (2.43) can be rewritten as follows

$$\begin{aligned}
\arg\max_{\vec{\mu}} P(\vec{\mu}|\vec{y}) &= \arg\max_{\vec{\mu}} \big(P(\vec{y}|\vec{\mu})P(\vec{\mu})\big) && (2.49)\\
&= \arg\min_{\vec{\mu}} \big(-\ln P(\vec{y}|\vec{\mu}) - \ln P(\vec{\mu})\big) && (2.50)\\
&\approx \arg\min_{\vec{\mu}} \big(-\ln P(\vec{y}|\vec{\mu}) + \lambda\mathcal{R}(\vec{\mu})\big)\,, && (2.51)
\end{aligned}$$

while applying that $P(\vec{y})$ is not depending on $\vec{\mu}$. The first summand equals the log-likelihood function $L(\vec{\mu})$ and the second one corresponds to the **regularization** where λ denotes the regularization strength. For nearest-neighbour-based regularizers which is an established way to obtain a prior knowledge, the regularization term is defined as

$$\mathcal{R} = \sum_i \sum_{j\in\mathcal{N}_i} w_{ij}\Psi(|\mu_i - \mu_j|)\,, \tag{2.52}$$

where large variations between adjacent voxels i and j are penalized with the potential function $\Psi(\cdot)$. $\mathcal{N}_i$ and ω_{ij} denote a set of voxel indices and the weights for penalization, respectively. The Huber regularization term combines a linear and a quadratic function and is used since a pure quadratic penalty would smooth the edges too much. This

regularization penalizes in two different ways. It is quadratic if below a certain threshold γ the deviations between adjacent pixels is small and thus most likely correspond to noise. However, when detecting edges, where the difference is consequently larger, it is linear. Mathematically written, this is described by the following equation:

$$\mathcal{R}_H = \sum_i \sum_{j \in \mathcal{N}_i} w_{ij} \begin{cases} \frac{(\mu_i - \mu_j)^2}{2\gamma^2} & \text{for } |\mu_i - \mu_j| \leqslant \gamma\,, \\ \frac{|\mu_i - \mu_j| - \gamma/2}{\gamma} & \text{for } |\mu_i - \mu_j| > \gamma. \end{cases} \tag{2.53}$$

The final image quality strongly depends on the choice of the parameters used for the reconstruction. Smaller structures can become blurred so that they are no longer detected in case of over-regularization. In contrast, too little regularisation leads to increased noise due to over-fitting.

Methods 3

This chapter comprises the methodological background that is used to generate the simulated and experimental results in this work. Primarily, advanced processing techniques such as patchwise phase retrieval and a material decomposition into lipid, water and protein. In addition, the principles about conventional spectral attenuation-based and SDPC X-ray imaging are introduced. The estimation of the MGD for the experimental measurements is then explained before the image evaluation parameters are presented, which are used for the final evaluation of the results. The parameters include the calculation of the CNR, the assessment of the image sharpness and an introduction to a theoretical noise analysis. Finally, the background of detector characterization including PSF, modulation transfer function (MTF) and line spread function (LSF) is described.

3.1 Patchwise Phase Retrieval

For applications like dose-compatible BCT where the MGD of every single projection is ultra low and only a few photons are detected, accurately extracting the phase information from the stepping curve becomes challenging. Higher statistics would be required to circumvent this problem. One simple way to reduce noise in an image is achieved by pixel binning, what means that the detector counts of neighbouring pixels are summed up to one larger pixel. The drawback is that resolution gets lost. With patchwise phase retrieval, however, it is possible to reduce the noise level while maintaining the spatial resolution but at the expense of image sharpness (cf. Sec. 3.5.2). The approach is illustrated in a schematic drawing in Fig. 3.1. One image is shifted to all neighboring pixel directions. The 4N-patchwise phase retrieval considers four additional pixels (up, down, left and right). In 8N-patchwise phase retrieval the diagonal pixels are also included. Thus, four or eight data points are additionally obtained for one stepping position which in consequence facilitates least squares fitting of the sinusoidal stepping curve which is performed by an expectation maximization algorithm. It has to be noted that a large moiré pattern is required to avoid strong outliers in the stepping curve.

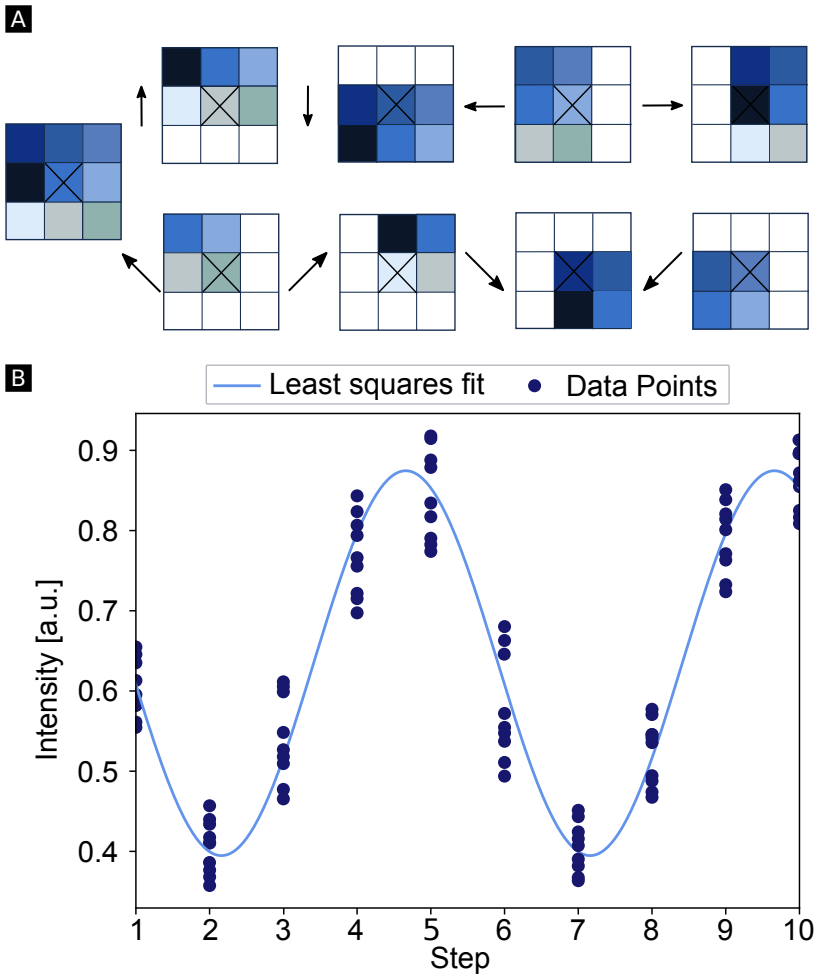

Figure 3.1: Illustration of patchwise phase retrieval. (A) Schematic drawing of an image patch which is shifted to all adjacent pixels. This is possible by using four (up, down, left right) or eight (additionally including the diagonals) neighbouring pixels. (B) In the stepping curve, every stepping position has, depending on the number of included neighbouring pixels, different intensity values. Thus, the least squares fit for the stepping curve is improved. This figure is adapted and extended from [Resch, 2021].

3.2 Material Decomposition into Lipid, Water and Protein

Recently published work demonstrated the feasibility of material-selective image calculation with grating-based phase-contrast X-ray imaging [Willner, 2016; Braig, 2018]. Willner et al. presented the material decomposition into lipid, protein and water

[Willner, 2016], whereas Braig et al. calculated iodine and virtual-non-contrast images [Braig, 2018]. Especially the results of the first publication emphasizes the potential for breast imaging since the tissue composition differs between normal and malignant tissue. The water content of tumors is higher and the lipid content of tumors is lower than in normal tissue [Tromberg, 2005]. Furthermore, the amount of the protein collagen [Haka, 2005] of abnormal breast tissue is also increased compared to normal breast tissue. This approach could serve as a new supporting analysis tool for reliable breast cancer detection. The linear material decomposition into lipid, water and protein explained in the following is based on the assumptions from Willner et al. [Willner, 2016]. The linear attenuation coefficient μ_{mix} of a mixture containing various different chemical elements i is expressed by

$$\mu_{\text{mix}} = \rho_{\text{mix}} \cdot \sum_i w_i \cdot \frac{\mu_i}{\rho_i}\,, \tag{3.1}$$

using ρ_{mix} as mixture's density, ω_i as weighting factor representing the fraction of each element in the sample and ρ_i as element's density of the i-th element. The refractive index decrement of the mixture δ_{mix}, encoded in the phase information, is derived by

$$\delta_{\text{mix}} = \frac{r_e h^2 c^2}{2\pi E^2} \cdot \rho_{\text{mix}} \cdot \sum_i \left(\frac{w_i \cdot N_{\text{A}}}{A_i} \right) \cdot Z_i\,, \tag{3.2}$$

with r_e being the electron radius, h Planck's constant, c the speed of light, E the effective X-ray energy, N_{A} the Avogadro constant, A_i the atomic mass and Z_i the atomic number [Herzen, 2009]. The density of the given mixture ρ_{mix} is written as follows

$$\rho_{\text{mix}} = p \cdot \rho_p + l \cdot \rho_l + w \cdot \rho_w\,, \tag{3.3}$$

where p, l and w are the volume fractions of protein, lipid and water, respectively. With this knowledge, it is possible to calculate the Hounsfield Unit (HU) and the phase-contrast Hounsfield Unit (HUp), which are standard measures in clinical CT imaging, in the following way

$$\begin{aligned} \text{HU} &= \frac{\mu_{\text{tissue}} - \mu_{\text{water}}}{\mu_{\text{water}} - \mu_{\text{air}}} \cdot 1000\,, \\ \text{HUp} &= \frac{\delta_{\text{tissue}} - \delta_{\text{water}}}{\delta_{\text{water}} - \delta_{\text{air}}} \cdot 1000\,. \end{aligned} \tag{3.4}$$

For this purpose, the linear mass attenuation coefficients μ_{tissue}, μ_{water}, μ_{air} and the refractive index decrements δ_{tissue}, δ_{water}, δ_{air} of tissue, water and air are required. Using

the assumption that the volume fractions of protein, lipid and water are summed up to one

$$p + l + w = 1\,, \tag{3.5}$$

the HU-HUp pair for every arbitrary mixture is described by the following vector notation:

$$\begin{pmatrix} \text{HUp} \\ \text{HU} \end{pmatrix} = \vec{w} + p \cdot (\vec{p} - \vec{w}) + l \cdot (\vec{l} - \vec{w})\ . \tag{3.6}$$

Here, the 100 % water, 100 % protein and 100 % lipid HU-HUp pairs are given by $\vec{w}$, $\vec{p}$ and $\vec{l}$, respectively. By solving this linear system of equations for p and l, the amount of the protein and the lipid fraction is derived. With the definition from Eq. (3.5), the missing water fraction is finally calculated by

$$w = 1 - p - l. \tag{3.7}$$

Since water has per definition 0 HU and 0 HUp, the LPW-triangle is spanned by the protein $\vec{p}$ and lipid $\vec{l}$ vector starting from the origin which corresponds to water. This approach enables the depiction of every HU-HUp-pair of different mixtures by simple vector addition and thus the analysis of the sample composition and the partial fractions of water, lipid or protein in it.

3.3 Principles of Spectral Differential Phase-Contrast Imaging

Although a material decomposition generally allows for a successful discrimination of materials in one object, attenuation-based spectral imaging with a polychromatic X-ray source suffers from a high amount of background noise after the decomposition compared to the attenuation images. With the extension to the recently developed spectral differential phase-contrast X-ray imaging approach, which benefits from the strengths from both spectral and phase-contrast imaging, one can overcome this limitation. In this chapter, the principles that lead to the SDPC algorithm are introduced. This includes conventional attenuation-based spectral imaging (cf. Sec. 3.3.1), differential phase-contrast imaging (cf. Sec 3.3.2) and finally the SDPC approach (cf. Sec 3.3.3) representing a combination of the two aforementioned methods.

3.3.1 Conventional Attenuation-based Spectral Imaging

For the absence of absorption K-edges, the energy-dependent linear mass attenuation coefficient can be described by a linear combination of two arbitrary basis materials

$$\mu(E) = A_1 f_1(E) + A_2 f_2(E)\,, \tag{3.8}$$

where A_α represents the line integrals of the respective basis material α and $f_\alpha(E)$ the energy dependency of the attenuation caused by those materials [Alvarez, 1976]. Since the contribution of Rayleigh scattering to the total attenuation cross-section is small compared to the one of the photoelectric and Compton effect, only these two interaction processes are relevant for medical imaging in the range of 20 keV to 140 keV. Based on this, the attenuation caused by an object can be modeled by only two basis materials, which can be obtained by a material decomposition. It has to be noted that Eq. (3.8) can theoretically be extended to more than two basis materials, e.g. by materials with K-edge discontinuities in the relevant energy range and decomposition into three or more basis-materials could be transformed. In order to implement this, however, more than two source energies or energy bins are required to avoid an underdetermined set of equations. A direct quantitative evaluation of the samples internal structures in terms of calculating electron density and effective number maps can be realized by the photoelectric/Compton decomposition. Since this no electron density maps are shown in this work, see [Ehn, 2017] for further information about its calculation.
The attenuation-based conventional spectral imaging approach is based on a forward model. Using the Beer-Lambert law and the assumption from Eq. (3.8), the expected number of photon counts $\hat{y}_i^s$ registered in detector pixel i for spectrum s and two basis materials is expressed as follows

$$\hat{y}_i^s = \int_0^\infty S^s(E) \cdot R^s(E) e^{-A_1^i f_1(E) - A_2^i f_2(E)} \mathrm{d}E\,, \tag{3.9}$$

with $S^s(E)$ denoting the source spectrum and $R^s(E)$ the spectral bin sensitivity of the detector being the probability that a photon with an X-ray energy E is detected in energy bin s [Mechlem, 2019b]. Since a dual-energy approach with two different interferometers and source spectra (low- and high-energy spectrum) is simulated for a quasi-monochromatic X-ray source, it has to be noted that in contrast to the assumptions made by [Mechlem, 2020], the source spectrum $S^s(E)$ differs from each other for the different X-ray energies ($\mathrm{s} = 1, 2$). The realistic detector energy response function (considering charge sharing and K-escape photons) and the quantum efficiency for the pixel-wise effective spectra been considered in a tool simulating the behaviour of photon-counting detectors based on the assumptions by [Schlomka, 2008]. Assuming uncorrelated Poisson statistics for the individual bin and pixel data, the model param-

eters of the forward model in Eq. (3.9) (here the basis material line integrals A_α) are determined with a maximum-likelihood estimator. This is performed by minimizing the following negative log-likelihood function in detector pixel i of totally N pixels [Roessl, 2007; Long, 2014; Mechlem, 2018b]:

$$-L(\vec{A}_1, \vec{A}_2) = \sum_{s=1}^{S} \hat{y}_i^s - y_i^s \ln \hat{y}_i^s \,, \tag{3.10}$$

in order to obtain the two basis material line integrals $\vec{A}_1$ and $\vec{A}_2$ for all pixels with y_i^s being the measured photon counts. This optimization problem is solved for each detector pixel individually for conventional attenuation-based spectral imaging because they are not correlated which in turn facilitates the optimization.

3.3.2 Differential Phase-Contrast Imaging

As described before (cf. Sec. 2.4), the image acquisition in differential phase-contrast imaging can be conducted by grating interferometry. Neglecting the polychromaticity of an X-ray spectrum, the expected number of photon counts at the detector $\hat{y}_i^r$ for every stepping position r is given by [Mechlem, 2019b]

$$\hat{y}_i^r = b \cdot e^{-\mu_i} (1 + V e^{-\epsilon_i} \cos(\phi_r + \Delta\phi_i)) \,. \tag{3.11}$$

The three modalities extracted by grating-based phase-contrast imaging, namely attenuation, phase shift and visibility reduction (corresponding to the dark-field signal) are denoted by μ_i, $\Delta\phi_i$ and ϵ_i. The reference intensity, reference phase and reference visibility of the stepping curve are expressed by b, ϕ_r and V, respectively. To obtain the three aforementioned modalities (μ_i, $\Delta\phi_i$, ϵ_i), Fourier processing, least-squares fitting or expectation-maximization processing can be utilized. Here, it is performed by minimizing a negative log-likelihood function of the measured data as follows

$$-L(\vec{\mu}, \Delta\vec{\phi}, \vec{\epsilon}) = \sum_{r=1}^{R} \hat{y}_i^r - y_i^r \ln \hat{y}_i^r \,, \tag{3.12}$$

where y_i^r indicates the measured number of photon counts for each detector pixel i and stepping position r of R stepping positions in total [Mechlem, 2019b]. Again, this optimization problem is solvable for every detector pixel individually.

3.3.3 Spectral Differential Phase-Contrast X-ray Imaging

Starting from the simultaneous acquisition of energy-resolved phase stepping curves in grating-based phase-contrast X-ray imaging, the SDPC forward model is derived combining the two forward models presented above (cf. Eq. (3.9) and (3.11)). It expresses the expected number of photon counts $\hat{y}_i^{rs}$ as follows [Mechlem, 2019b]

$$\begin{aligned}\hat{y}_i^{rs} = \int_0^\infty S^s(E) R^s(E) e^{-A_1^i f_1(E) - A_2^i f_2(E)} \cdot \\ \left[1 + V^s(E) e^{-d_\epsilon^i f_\epsilon^s(E)} \cos\left(\phi^{s,r}(E) + \Delta\phi_i^s(E)\right)\right] dE\,.\end{aligned} \tag{3.13}$$

Here, an additional third basis material that is responsible for the stepping curve's visibility reduction is introduced and called "dark-field basis material". The additional term in the exponent compared to the forward model in Eq. (3.11) energy-dependent visibility reduction per unit length $f_\epsilon(E)$ and is explained in more detail by Mechlem et al. in [Mechlem, 2019b]. However, this is not further explained here due to the lack of relevance for this work. Please refer to [Mechlem, 2019b; Mechlem, 2020] for additional information concerning this topic.
A dual-energy approach with two different interferometers and source spectra (low- and high-energy spectrum) is simulated in the quasi-monochromatic case. Therefore, it has to be noted that in contrast to the assumptions made by [Mechlem, 2020], several parameters (source spectrum $S^s(E)$, visibility $V^s(E)$, reference phase Φ_r^s and phase shift $\Delta\phi_i^s(E)$) differ from each other for the different spectral acquisitions ($\mathrm{s} = 1, 2$). These parameters are therefore denoted with an additional index s which is omitted in the case of polychromatic imaging where only one source spectrum ($\mathrm{s} = 1$) is used. In the latter case, the spectral separation is detector-based.
The differential phase shift $\Delta\phi$ is proportional to the the gradient of the projected electron density (PED) $\frac{\partial}{\partial x}\tilde{\rho}_e(x_i, y_i)$ with x_i and y_i as spatial coordinates for every detector pixel i in the detector plane, is perpendicular to the grating bars and can be calculated as follows [Birnbacher, 2018; Qi, 2010]

$$\Delta\phi_i^s(E) = \frac{q^s}{E^2} \frac{\partial}{\partial x} \tilde{\rho}_e(x_i, y_i)\,, \tag{3.14}$$

with a proportionality factor q which is defined as

$$q^s = \frac{M r_e h^2 c^2 d^s_{\mathrm{G}_1,\mathrm{G}_2}}{p_2^s} \cdot g\,, \tag{3.15}$$

where r_e the classical electron radius, $d_{\mathrm{G}_1,\mathrm{G}_2}$ the inter-grating distance between G_1 and G_2 and p_2 the G_2 grating period. For the quasi-monochromatic dual-energy simulation

case where two interferometers are modelled, the inter-grating distance $d_{\mathrm{G_1,G_2}}$ or the $\mathrm{G_2}$ grating period is changed so that they match with the design energy. Therefore, these two parameters are also marked with the index s. Since the measured electron density profile is magnified, the magnification M is additionally considered. The sensitivity reduction factor g depends on the position of the sample [Donath, 2009]. It corrects for the fact that the sample is not directly located at the $\mathrm{G_1}$ grating position. It is differentiated between the following two cases

$$g = \begin{cases} 1 - \frac{d_{\mathrm{sample,G_1}}}{d_{\mathrm{source,G_1}}} & \text{for sample between X−ray source spot/G}_0 \text{ and G}_1\,, \\ 1 - \frac{d_{\mathrm{sample,G_1}}}{d_{\mathrm{G_1,G_2}}} & \text{for sample between G}_1 \text{ and G}_2\,. \end{cases} \tag{3.16}$$

Here, $d_{\mathrm{sample,G_1}}$ and $d_{\mathrm{source,G_1}}$ denote the distances between sample to $\mathrm{G_1}$ and between source or $\mathrm{G_0}$ to $\mathrm{G_1}$, respectively. The phase shift $\Delta\phi_i$ is proportional to the gradient of the PED which is perpendicular to the grating bars.
The (projected) electron density can be determined by both conventional attenuation-based and phase-contrast imaging and is therefore the connecting parameter between grating-based phase-contrast and spectral imaging for SDPC. Instead of obtaining the PED $\tilde{\rho}_e^i = \tilde{\rho}_e(x_i, y_i)$ by the integration of the three-dimensional electron density distribution $\rho_e(x, y, z)$ along the projection direction (z-direction) with

$$\tilde{\rho}_e(x, y) = \int \rho_e(x, y, z)\mathrm{d}z\,, \tag{3.17}$$

the idea is to express the PED as sum of the PEDs of the respective basis materials M_i in order to eliminate the PED as additional optimization variable:

$$\tilde{\rho}_\mathrm{e}^i = A_1^i \rho_\mathrm{e}(M_1) + A_2^i \rho_\mathrm{e}(M_2)\,, \tag{3.18}$$

with $\rho_e(M_i)$ denoting the electron densities of the respective basis materials. As in conventional attenuation-based spectral imaging, this assumption works well for the relevant energy range of medical imaging from 20 to 140 keV.
Analogous to spectral imaging, the optimization problem is solved by minimizing the negative log-likelihood function to obtain the two basis material $\vec{A_1}$ and $\vec{A_2}$ as well as the thickness of the dark-field generating material $\vec{d_\epsilon}$ as follows

$$-L(\vec{A_1}, \vec{A_2}, \vec{d_\epsilon}) = \sum_{i=1}^{N} \sum_{s=1}^{S} \sum_{r=1}^{R} \hat{y}_i^{rs} - y_i^{rs} \ln \hat{y}_i^{rs}\,. \tag{3.19}$$

In contrast to conventional attenuation-based spectral imaging and due to the statistical coupling of adjacent pixels by the electron density gradient, the SDPC optimization

problem is not separable for each detector pixel individually. As a consequence, it is conducted for every detector row perpendicular to the grating bars. Local optima are introduced by the cosine term in the SDPC forward model (cf. Eq. (3.13)). Instead of a computationally intensive global optimization strategy, a gradient-based optimization strategy is fed with a sufficiently close initial guess. The initial guess used for the SDPC optimization is the result of the conventional material decomposition and smoothed with a 2D Gaussian with $\sigma = 2.0$.

3.4 Estimation of the Mean Glandular Dose

Dosimetry is one of the most important tasks in medical X-ray imaging. Since glandular tissue in the female breast is the most radiation-sensitive organ of the human body, dose monitoring is very crucial to minimize the probability of radiation-induced detriment. An extensive review about dosimetry in breast imaging is given in [Dance, 2016]. In this section, a brief introduction into different general dosimetric quantities is given before the detailed calculation of the MGD at the MuCLS is explained.

Dosimetric Measures

In general, dosimetry discriminates between the absorbed dose D and the kinetic energy released per unit mass (kerma) K which are the two most important quantities. While the absorbed dose refers to the locally absorbed mean energy $\mathrm{d}\bar{\epsilon}$ per unit mass $\mathrm{d}m$ as follows [Nenot, 2009]

$$D = \frac{\mathrm{d}\bar{\epsilon}}{\mathrm{d}m}\,, \tag{3.20}$$

the kerma, however, considers the kinetic energy E_{tr} transferred to charged secondary particles of the first generation by indirect ionizing radiation [Krieger, 2012]. The kerma is defined as the mean sum of this kinetic energy $\mathrm{d}E_{\mathrm{tr}}$ per unit mass $\mathrm{d}m$ [PetoussiHenss, 2010]

$$K = \frac{\mathrm{d}E_{\mathrm{tr}}}{\mathrm{d}m}\,. \tag{3.21}$$

The unit of kerma is joule per kilogram which is defined as gray (1 J/kg = 1 Gy). To consider the energy fluence $\Phi(E)$ of the uncharged particles for every energy bin E, kerma can also be calculated as follows

$$K = \int \Phi(E) \cdot E \cdot \frac{\mu_{\mathrm{tr}}(E)}{\rho} \mathrm{d}E \,. \tag{3.22}$$

with $\frac{\mu_{\mathrm{tr}}(E)}{\rho}$ as material-depending mass energy transfer coefficient. Thereby, the product $\left[E \cdot \frac{\mu_{\mathrm{tr}}(E)}{\rho}\right]$ is also known as kerma factor. The total kerma K is composed of two parts, the collision kerma K_{col} and the radiative kerma K_{rad} [Attix, 1979]

$$K = K_{\mathrm{col}} + K_{\mathrm{rad}} \,. \tag{3.23}$$

The collison kerma includes the part of the transferred kinetic energy which is converted into ionizations and excitations by the secondary electrons. The radiative kerma refers to the part which is converted back into photon energy (e.g. bremsstrahlung, annihilation radiation of positrons or fluorescence radiation). Since the radiative kerma is related to the bremsstrahlung whose amount is negligible compared to the one of collision kerma for low X-ray energies and air ($K_{\mathrm{rad}} \approx 0$), the air kerma is used as follows [Schlegel, 1999]

$$K_{\mathrm{air}} = \int \Phi(E) \cdot E \cdot \left(\frac{\mu_{\mathrm{en}}(E)}{\rho}\right)_{\mathrm{air}} \mathrm{d}E \,, \tag{3.24}$$

with $\left(\frac{\mu_{\mathrm{en}}(E)}{\rho}\right)_{\mathrm{air}}$ as energy-dependent mass energy absorption coefficient of air for uncharged particles. The International Atomic Energy Agency (IAEA) recommends air kerma as the main measure in dosimetry [IAEA, 2007]. Additionally, (air) kerma can be used for the calibration of ionization chambers in dose monitoring protocols. Another quantity, now obsolete but still used in US papers, is exposure X. It should represent the ionization in air based on ionizing radiation like X-ray photons. This quantity has commonly been used for ionization chambers filled with air, so that the exposure is defined as the electric charge freed divided by the mass of the air [Schlegel, 1999]

$$X = \frac{\mathrm{d}Q}{\mathrm{d}m} \,, \tag{3.25}$$

where $\mathrm{d}Q$ represents the number of charge of ions which are produced in the air of the mass element $\mathrm{d}m$. The unit of the exposure is defined as [X] = R. To convert between the two dosimetric measures (air kerma and exposure), the conversion $1\,\mathrm{R} = 8.7\,\mathrm{Gy}$ is used.

Mean Glandular Dose Calculation at the Munich Compact Light Source

One way to obtain the effective dose of an entire organ is to measure the equivalent or absorbed dose and calculate the effective dose by using tissue and radiation weighting factors [Harrison, 2015]. Since the air kerma is measurable, but not the specific dose applied to an organ, an approximating calculation is required. Therefore, conversion factors usually provided by Monte Carlo simulations are used to convert air kerma into dose (in this case: MGD). A detailed comparison of the existing dose calculation models is summarized in [Eggl, 2017] including a comparison between the model of Dance et al. [Dance, 1990; Dance, 1999; Dance, 2000], Wu et al. [Wu, 1991; Wu, 1994] and Boone et al. [Boone, 1999; Boone, 2002]. The disadvantage of most of the models for breast imaging at the MuCLS is that the conversion factors are just listed for specific X-ray spectra [Dance, 1990; Dance, 1999; Dance, 2000; Wu, 1991; Wu, 1994]. In contrast, the SIERRA Monte Carlo simulation-based model developed by Boone et al. tabulates monoenergetic normalized glandular dose coefficients, the DgN values [Boone, 2002]. They are compatible with arbitrary X-ray spectra, e.g. with those produced by the MuCLS. The DgN values are provided by fit equations for energies between 8 keV and 50 keV, for breast thicknesses between 2 cm and 9 cm and different percentages of glandular tissue (0 %, 50 % and 100 %) for a given sample. The energy-dependent normalized glandular dose coefficients are exemplary plotted for a glandularity distribution of 50 % in Fig. 3.2. Based on the assumptions by [Boone, 2002] and [Nosratieh, 2015] explained in [Eggl, 2017], the MGD at the MuCLS is calculated with

$$\mathrm{MGD} = \sum_{E=E_{\min}}^{E_{\max}} K(E)[\mathrm{mGy}] \cdot \kappa \left[\frac{\mathrm{R}}{\mathrm{mGy}}\right] \cdot \left(\mathrm{DgN}(E,t,g)\left[\frac{\mathrm{mGy}}{\mathrm{R}}\right]\right) , \tag{3.26}$$

where κ is the conversion factor from air kerma to exposure with $\kappa = 0.114\,\mathrm{R/mGy}$, t the breast thickness and g the amount of glandularity (0 %, 50 % or 100 %). The respective units are given in square brackets. For a CT scan, the MGD values of N projections are summed up to the total MGD. For the sake of simplicity and since the photon flux is not stable over the time at the MuCLS, the air kerma is not measured during every beam time, but calculated using the following equation

$$K_{\mathrm{MuCLS}}(E) = E \cdot \Phi(E) \cdot \left(\frac{\mu_{\mathrm{en}}}{\rho}(E)\right)_{\mathrm{air}} . \tag{3.27}$$

For this equation, the tabulated values from Buhr et al. are used for the mass energy attenuation coefficient of air [Buhr, 2012]. In addition, the X-ray spectrum is measured

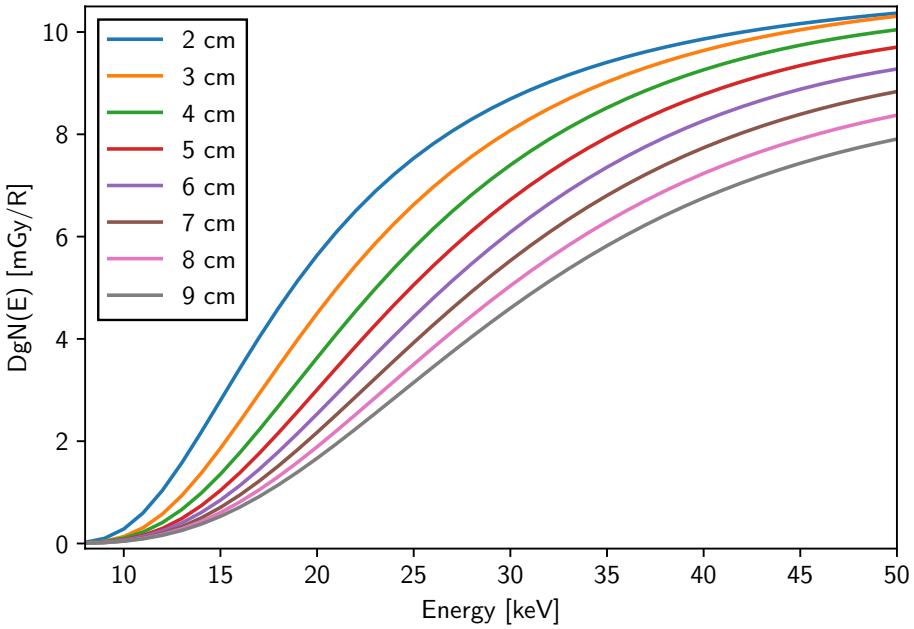

Figure 3.2: Energy-dependent normalized glandular dose coefficients DgN(E). Since the air kerma depends on the mass where the energy is deposited, the values are plotted for different sample thicknesses ranging from 2 cm to 9 cm and for a glandularity of 50 %.

using an energy-dispersive detector (Amptek X-123, *Amptek Inc.*, USA). The spectrum is corrected for the absorption of air and the efficiency of the detector. The flux is measured with the SANTIS 0808 GaAs 75 µm prototype detector (*DECTRIS AG*, Baden-Daettwil, Switzerland) in an additional scan without any sample or gratings in the beam path. The scintibloc counts are simultaneously recorded during this scan since the photon flux is not stable at the MuCLS. Previous measurements show that the behaviour is linear to each other [Cont, 2016]. In order to finally estimate the photon flux, the following steps are performed: The photon flux at the sample position is obtained by averaging the photon counts over an arbitrary region of interest (ROI) and correcting for the pixel size yielding the photon flux per square millimeter at the sample position. To obtain the relevant photon flux at the sample instead of the detector position, a geometrical correction is conducted. For this, the following equation of the transmitted intensity

$$T = \frac{\sum_{E=E_{\min}}^{E_{\max}} S(E) \cdot \exp\left(-\frac{\mu}{\rho} \cdot \rho \cdot d\right)}{\sum_{E=E_{\min}}^{E_{\max}} S(E)}\,, \tag{3.28}$$

with $S(E)$ as normalized intensity per energy bin E of the spectrum, d as thickness of the absorbed material, μ/ρ as mass attenuation coefficient and ρ as density of the respective material, is used to correct for the absorption of air between detector and sample and the water bath (including polymethyl methacrylate (PMMA) and water). The transmitted intensity T is also utilized to calculate the detector's quantum efficiency $\mathrm{QE}_{\mathrm{Santis}}$ which is expressed as follows

$$\mathrm{QE}_{\mathrm{Santis}} = 1 - T_{\mathrm{GaAs}} \,. \tag{3.29}$$

All in all, the initially measured flux is finally corrected for the air gap between detector and sample position T_{air}, for the PMMA of the walls of the water bath T_{PMMA} and the water within the water bath T_{water} to obtain the corrected photon flux at the sample position:

$$\Phi_{\mathrm{cor}} = \frac{\Phi}{\mathrm{QE}_{\mathrm{Santis}} \cdot T_{\mathrm{air}} \cdot T_{\mathrm{PMMA}} \cdot T_{\mathrm{water}}} \,. \tag{3.30}$$

Through the multiplication of the normalized spectrum $S_{\mathrm{norm}}(E)$ and the corrected flux Φ_{cor}, the corrected flux per energy bin $\Phi(E)$ is obtained

$$\Phi(E) = \frac{S_{\mathrm{norm}}(E)}{\sum_{E=E_{\mathrm{min}}}^{E_{\mathrm{max}}} S_{\mathrm{norm}}(E)} \cdot \Phi_{\mathrm{cor}} \,. \tag{3.31}$$

3.5 Image Evaluation

The results presented in this work are assessed in different ways. The image quality is evaluated based on the CNR, the edge sharpness and a theoretical noise analysis taking into account the applied MGD. All approaches are explained in the following subsections.

3.5.1 Contrast-to-noise Ratio

The CNR is a measure to quantify noise in combination with the contrast in an image. The contrast is defined by the difference between two average signals $\overline{S_1}$ and $\overline{S_2}$ in two different ROIs. The contrast, divided by the standard deviation σ_{BG} within a larger ROI of a background region, represents the CNR:

$$\mathrm{CNR} = \frac{\overline{S_1} - \overline{S_2}}{\sigma_{\mathrm{BG}}} \,. \tag{3.32}$$

The standard deviation is defined as

$$\sigma = \sqrt{\frac{1}{N}\sum_{i=1}^{N}(x_i - \bar{x})^2}\,, \tag{3.33}$$

where N is the total number of pixels of the selected ROI, x_i is the intensity of the given pixel and $\overline{x}$ is the average of the intensity in all pixels. Noise is generally separated in random and structural components. Random noise arises based on the quantum mottle and can be decreased by imaging with more X-ray photons. Structural components, however, are given by fixed structures of every sample.

3.5.2 Assessment of Edge Sharpness

In addition to the quantification of contrast and noise, it is also important to take the resolution or sharpness of an image into account. The analysis of strongly attenuating or phase-shifting edges is suitable to investigate the latter. At an edge, intensity values gradually de- or increase such that the slope of its intensity curve can be used as sharpness measure. While blurred edges correspond to a rather lower resolution, sharp edges result in low to high (or the other way round) intensity values very quickly. The intensity values along one line across the edge are fitted using a logistic fit function $f(x)$ which is adapted and slightly modified from Ahmad et al. [Ahmad, 2015] and defined as

$$f(x) = \frac{L}{1 + e^{k(x_0 - x)}} + c\,, \tag{3.34}$$

with L as amplitude, c as vertical offset, x_0 as horizontal offset of the logistic fit and k as measure for the slope of the curve. For the analysis of the edge sharpness, the k-value is the relevant parameter and is therefore used as measure. The higher the k-value, the better the sharpness, and the lower the k-value, the blurrier the edge corresponding to a lower resolution. For a CT scan, the line is averaged over several slices to increase image statistics and make it less prone to background noise. At straight edges, it is also possible to average over several neighbouring pixels. In Fig. 3.3, one exemplary CT slice with a zoom-in section of the PMMA rod ROI which is used for edge sharpness analysis is presented in (A) while in (B), the plotted original values and the corresponding logistic fit are shown.

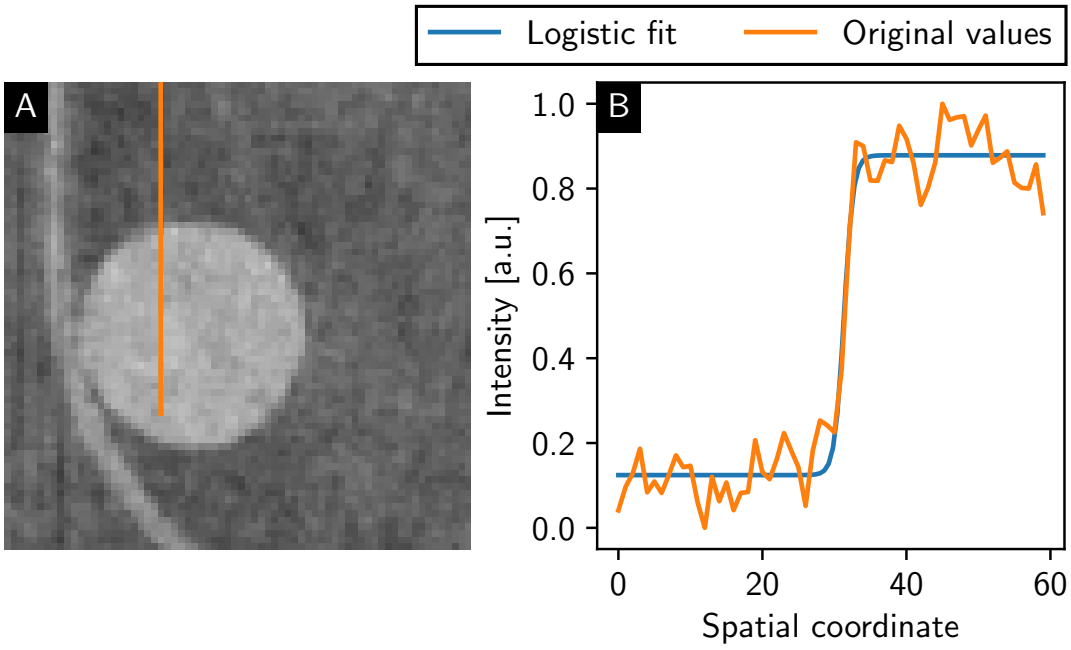

Figure 3.3: Visualization of the edge sharpness measure. (A) Exemplary slice of a CT scan including the edge of a PMMA rod. The orange line indicates the line along which the k-value is calculated. (B) The original values of the orange line are plotted and the logistic fit whose slope is a measure for the edge sharpness is added.

3.5.3 Theoretical Noise Analysis

One way to evaluate the image quality and to compare the different imaging modalities is a noise analysis initially proposed by [Mechlem, 2020] and among others used for the estimation of optimum imaging parameters. It is based on the Cramér–Rao lower bound (CRLB) from estimation theory and predicts the variance of the PED in order to quantify the noise in the generated images.
For an unbiased estimator (like the maximum-likelihood estimator), it predicts the lower bound of the minimal variance. For a given vector parameter $\mathbf{a}$, the covariance matrix $\mathbf{C}(\mathbf{a})$ is stated as [Kay, 1997]

$$\mathbf{C}(\mathbf{a}) - [\mathbf{F}(\mathbf{a})]^{-1} \geqslant 0\,. \tag{3.35}$$

This means that the $\mathbf{C}(\mathbf{a}) - [\mathbf{F}(\mathbf{a})]^{-1}$ matrix is positive semidefinite. The Fisher information matrix $\mathbf{F}(\mathbf{a})$ is defined by

$$\mathbf{F}_{uv} = E\left[-\frac{\partial^2 L(\mathbf{a})}{\partial a_u \partial a_v}\right], \tag{3.36}$$

where E represents the expectation value of the curvature of the negative log-likelihood function $L(\mathbf{a})$ and u and v as indices of the given vector $\mathbf{a}$. The covariance matrix $\mathbf{C}(\mathbf{a})$ of vector $\mathbf{a}$ is

$$\mathbf{C}_{uv} = E[(a_u - E(a_u))\,(a_v - E\,(a_v))]\,. \tag{3.37}$$

Based on the assumptions/knowledge of Eq. (3.35), the lower bound of the squared variances of the estimated parameters $\sigma^2(a_u)$ is

$$\mathbf{C}_{uu} = \sigma^2(a_u) \geqslant \left(\mathbf{F}^{-1}\right)_{uu}. \tag{3.38}$$

Since Eq. (3.35) is semidefinite, the diagonal matrix elements of the $\mathbf{C}(\mathbf{a}) - [\mathbf{F}(\mathbf{a})]$ matrix are non-negative. In consequence, the estimated parameter's squared variance $\sigma^2(a_u)$ can only be larger than or equal to the diagonal elements of the inverse Fisher information matrix. As derived by and shown in [Mechlem, 2020], the CRLB approach can be used for the prediction of the noise levels of the three imaging modalities described above and enables a quantitative image comparison. Here, only the prediction for the conventional spectral and the SDPC imaging are introduced. Please refer to [Mechlem, 2020] for a more detailed derivation of this approach especially of the Fisher matrix for differential phase-contrast imaging.
By utilizing the negative log-likelihood functions from Eq. (3.10) and (3.19) together with Eq. (3.36), the corresponding Fisher matrix $\mathbf{F}_{uv}$ can be calculated. The Fisher information matrix for conventional attenuation-based spectral imaging is derived as follows [Roessl, 2009]

$$\mathbf{F}_{uv} = \sum_{s=1}^{S} \frac{1}{\hat{y}^s} \frac{\partial \hat{y}^s}{\partial A_u} \frac{\partial \hat{y}^s}{\partial A_v}, \tag{3.39}$$

with $\hat{y}^s$ as expected number of photon counts for source spectrum s, and A_u and A_v as line integrals of the basis materials u and v. Due to simplicity reasons, it has been dispensed to include the pixel dependency with index i in this case, since this optimization problem is separable for every pixel individually and since there is no correlation between neighbouring pixels. Thus, the Fisher matrix for spectral imaging with two basis materials is reduced to a 2×2 matrix. To calculate the lower bound or in this case the theoretically lowest basis material variances $\sigma^2(A_{u,v})$ using Eq. (3.38), the Fisher information matrix from Eq. (3.39) is inverted with the 2×2 matrix inversion formula.

As mentioned in Sec. 3.3.3, for SDPC imaging, however, the optimization problem can not be solved for every pixel individually. In contrast to spectral imaging, the Fisher matrix is extended to three optimization variables for all pixels N with a vector $\mathbf{a} = (A_1^1, ..., A_1^N, A_2^1, ..., A_2^N, d_\epsilon^1, ...d_\epsilon^N)$. Thus, the resulting 3N×3N Fisher information matrix is calculated for every stepping position r of totally R stepping positions by

$$\mathbf{F}_{uv} = \sum_{i=1}^{N} \sum_{s=1}^{S} \sum_{r=1}^{R} \frac{1}{\hat{y}^{rs}} \frac{\partial \hat{y}^{rs}}{\partial a_u} \frac{\partial \hat{y}^{rs}}{\partial a_v} \,. \tag{3.40}$$

Since the differential phase shift only couples neighboring pixels, most of the matrix elements become zero. Again, the inverse Fisher matrix is calculated in order to use its elements for the estimation of the line integral's covariance:

$$\mathrm{Cov}(a^u, a^v) \approx \mathbf{F}_{uv}^{-1} \,. \tag{3.41}$$

For the material decompositions (conventional and SDPC), the PED variance $\sigma^2(\rho_e)$ given in [cm^{-4}] is calculated by standard error propagation from the variances of the respective basis material thicknesses for one pixel as follows

$$\sigma^2(\rho_e) = \rho_e^V(M_1)^2\sigma^2(A_1) + \rho_e^V(M_2)^2\sigma^2(A_2) + 2 \cdot \rho_e^V(M_1)\rho_e^V(M_2)\mathrm{Cov}(A_1, A_2) \,, \tag{3.42}$$

where $\rho_\mathrm{e}^\mathrm{V}(\mathrm{M}_1)$ and $\rho_\mathrm{e}^\mathrm{V}(\mathrm{M}_2)$ represent the volume electron densities of the two basis materials, $\sigma^2(\mathrm{A}_1)$ and $\sigma^2(\mathrm{A}_2)$ the basis material variances and $\mathrm{Cov}(\mathrm{A}_1, \mathrm{A}_2)$ the covariance of the two basis material thicknesses approximated by $(F^{-1})_{12}$.

3.6 Detector Characterization

The characterization of an imaging system can be conducted by measuring the spatial resolution including measures such as the MTF, the PSF and the LSF measured either with a knife edge or a Siemens star. The PSF depicts the intensity distribution obtained with an infinitesimal small pin hole and source spot. The MTF represents a spatial frequency dependent loss in amplitude of intensity modulations. The LSF, however, is the intensity distribution obtained with an infinitesimal small slit which equals a line of the MTF. In the following two sections, two common approaches to calculate these measures using an absorbing sample of known shape are presented, both experimentally and mathematically. They are useful to get access to the spatial resolution of an imaging detector by placing the test pattern as close as possible to the detector so that other influencing parameter can be minimized. The explanations in this section

are based on and further information giving a comprehensive overview can be found in [Boreman, 2001; Buzug, 2008; Behling, 2015; Russo, 2017].

3.6.1 Knife Edge Approach

Overall, the resulting MTF of an imaging system is composed of the respective MTFs of all components such as the X-ray source, the detector, the pixel electronics and the geometry [Buzug, 2008]

$$\mathrm{MTF}_{\mathrm{system}} = \mathrm{MTF}_{\mathrm{source}} \cdot \mathrm{MTF}_{\mathrm{detector}} \cdot \mathrm{MTF}_{\mathrm{electronics}} \cdot \mathrm{MTF}_{\mathrm{geometry}} \cdot \ldots \tag{3.43}$$

One possibility to obtain the MTF of the system is using a straight, sharp and highly absorbing knife edge. Experimentally, the edge spread function (ESF) is derived by plotting the normalized pixel values of the transmission image perpendicular to the edge depending on the distance to the edge. In order to avoid sparse sampling of the ESF, the edge has to be placed with a small inclination angle into the beam path a subpixel accurate ESF. A linear combination of three error functions is used for fitting the ESF. An one-dimensional Heaviside-function $\Theta(x)$ can be used to model the produced intensity pattern of such an edge resulting in the so-called ESF. Mathematically written, the ESF is defined as

$$\mathrm{ESF}(x) = \int_{-\infty}^{\infty} \int_{-\infty}^{\infty} \mathrm{PSF}(u,v)\Theta(x-u)\mathrm{d}u\mathrm{d}v\,, \tag{3.44}$$

where v is parallel and x and y perpendicular to the edge. The angular properties of the PSF could be obtained step by step through measurements at different inclination angles. From Eq. (3.44), the LSF as derivative of the ESF can be accessed via

$$\mathrm{ESF}(x) = \int_{-\infty}^{\infty} \mathrm{LSF}(u)\Theta(x-u)\mathrm{d}u \Leftrightarrow \mathrm{LSF}(x) = \frac{\mathrm{d}}{\mathrm{d}x}\mathrm{ESF}(x)\,. \tag{3.45}$$

Taking the real part of the Fourier transform of the LSF into account, the MTF can be calculated as follows

$$\mathrm{MTF} = \Re\{\mathcal{F}\{\mathrm{LSF}\}\}\,. \tag{3.46}$$

The 10 % value of the MTF is commonly a measure for the spatial resolution of an optical imaging system given in line pairs per millimeter. In an ideal imaging case, one is able to discriminate two neighbouring black and white line pairs.

3.6.2 Siemens Star Approach

The second approach uses a Siemens star which is an absorbing test pattern consisting of alternating, radially equidistant rays. The spatial frequency increases towards the center of the plate. Experimentally, the radius- or rather the spatial frequency-dependent contrast between the different rays is analyzed. Although the analysis is more complex than with the edge approach, it is possible to obtain the two-dimensional PSF with a Siemens star directly from the measured MTF within one measurement. Different steps have to be conducted which are explained in the following:
Since this method is limited by the center plate of the Siemens star, whose size depends on the respective production of the test pattern, this center plate of the Siemens star has to be identified first. For this, a region growth segmentation is used starting with a user-selected seed placed in the center region. This results in a radial mask from which the center of mass and thus also the center of the Siemens star is computed. This is followed by an analysis of the radial line plots resulting in the generation of the MTF. A radius-dependent frequency modulation is induced by the alternating non- and high-absorbing rays for the pixels on a circle around the center plate. An additional angle-dependent modulation superimposes this fixed frequency modulation (the enveloping of it) and finally defines the edge sharpness measure. In contrast to the determination of the ESF, which usually only refers to a line plot perpendicular to the sharp edge, the intensity difference between the minima and maxima of neighbouring pixels that resembles a loss of contrast is of interest for the Siemens star approach. For this, an upper $U_\mathrm{e}(\alpha, r)$ and lower $L_\mathrm{e}(\alpha, r)$ envelope function is calculated and plotted to the high frequency intensity modulation, so that the contrast c between the alternating intensities results from their ratio as follows

$$c(\alpha, r) = \frac{U_\mathrm{e}(\alpha, r)}{L_\mathrm{e}(\alpha, r)}\,. \tag{3.47}$$

Here, r denotes radius and is directly related to the spatial frequencies. The angle-dependent MTF is finally generated by combining all analyzed radial line plots for each radius. A discretizied two-dimensional Gaussian function is assumed for the PSF to fill missing values in the MTF. Finally, the results of the MTF are transformed into a Cartesian coordinate system. The resulting intensity maximum is located around the center and is either round- or elliptical-shaped. The data can be Fourier transformed which then leads to the PSF:

$$\mathrm{PSF} = |\mathcal{F}\{\mathrm{MTF}\}|\,. \tag{3.48}$$

An ideal imaging system would yield in a point-like PSF meaning that there is full contrast for all of the MTF's spatial frequencies.

Breast Computed Tomography at the Munich Compact Light Source 4

In this chapter, first attempts towards grating-based phase-contrast BCT with a quasi-monochromatic X-ray source are presented. This chapter initially includes a description of the experimental setup of the second hutch of the MuCLS at which all projection images of the samples have been acquired. Since achieving a low MGD for BCT is the main goal and biggest challenge of this project, dose considerations were made in advance to determine optimized exposure times. To find the most suitable detector for this application, an evaluation and comparison of them was also conducted. Finally, first BCT results with samples fitting into the field of view (FOV) are presented followed by an off-axis scan for a larger breast-like phantom. Please note that parts of the results in this chapter were produced in collaboration with a master's thesis [Resch, 2021]. Some clinical images used for a visual comparison of the image quality of the laboratory results obtained were provided by Magda Marcon. They were also published in "Recent advances in X-ray imaging of breast tissue: From two- to three-dimensional imaging" so that subfigures may appear identical to the publication [Heck, 2020].

4.1 Motivation

Although the breast imaging community already focused on the development of attenuation-based BCT a few decades ago, [Chang, 1977; Chang, 1978; Chang, 1980], the mile stones towards the clinical implementation of this technology have mainly been achieved during the last two decades [Boone, 2001; Boone, 2006; Lindfors, 2008; Prionas, 2010; Kalender, 2012; Kuzmiak, 2016; Kalender, 2017; Koning, 2019; ABCT, 2020]. The examination with BCT offers an unrestricted three-dimensional view of the female breast without the patient feeling disturbed by the compression of the breast. The results of several studies as well as efforts of researchers and manufacturers show the great potential of this promising imaging alternative for women whose mammography is not very meaningful and who do not want to or are not allowed to undergo MRI. Ten reasons for the necessity of BCT are listed in [OConnell, 2017]. Among others, this technique provides shorter performance time and better resolution than MRI, benefits for dense breasts, it overcomes limitations of mammography and reduces false positive

or negative diagnoses.
However, the problem of low soft tissue contrast, which is due to the weak absorption in biomedical samples, remains as with mammography. An example for *in vivo* attenuation-based BCT is presented in Fig. 4.1 (A) and (C) for a coronal and sagittal view, respectively. The multricentric invasive ductal carcinoma indicated by the orange arrows was better visible after the administration of iodine-containing contrast agent in (B, D). This example underlines the demand for an imaging technique providing higher soft tissue contrast without the need of injecting a contrast agent. While the X-rays traverse matter, they are attenuated, refracted as well as scattered. Exploiting the latter two by imaging with phase-sensitive techniques such as propagation-, analyzer- or grating-based phase-contrast imaging could help to overcome the aforementioned limitation [Momose, 2003; Weitkamp, 2005; Pfeiffer, 2006; Gureyev, 2009; Wu, 2014; Krenkel, 2016].
First studies for propagation-based phase-contrast mammography have been performed at the Synchrotron Radiation for Medical Physics (SYRMEP) beamline in Trieste [Arfelli, 2000; Olivo, 2009; Castelli, 2011; Longo, 2014; Olivo, 2014]. Due to the monochromaticity of such an X-ray source, the photon energy can be perfectly adjusted for each application leading to an optimized contrast-to-dose-ratio. Improved detection of breast cancer was successfully observed in initial proof-of-principle studies and finally in a clinical trial with more than 70 patients. [Arfelli, 2000; Olivo, 2009; Castelli, 2011; Longo, 2014; Olivo, 2014]. However, the clinical feasibility of this method remains unlikely due to the high costs, limited availability, high spatial requirements and remoteness of synchrotrons with respect to clinics.
In contrast, grating-based phase-contrast imaging is the most promising approach with regard to the clinical implementation at a polychromatic X-ray source [Pfeiffer, 2006; Pfeiffer, 2007; Pfeiffer, 2008]. This technique additionally retrieves information about the ultra-small-angle scattering that is related to the dark-field signal. Besides the enhanced delineation of breast cancer features using the phase information, an improved detection and classification of microcalcifications using the scattering information can be achieved [Stampanoni, 2011; Scherer, 2014; Scherer, 2016; Grandl, 2015; Hauser, 2014; Auweter, 2014]. However, the applied MGD of the previous studies using grating interferometry still exceed the allowed limit of 2.5 mGy per view [Perry, 2006]. Thus, subsequent studies demonstrated the feasibility of this technique in a dose-compatible range at a laboratory setup using a polychromatic X-ray source and even at a clinical mammography device [Koehler, 2015; Scherer, 2015; Arboleda, 2019].
For early breast cancer detection, both approaches showed fundamental advances which were encouraging for researchers to try to extend these results to BCT. Several experiments for the evaluation of BCT have been performed in different ways including analyzer-based [Keyriläinen, 2008; Sztrókay, 2012], grating-based [Sztrókay, 2013; Grandl, 2014; Hellerhoff, 2019; Willner, 2016] and propagation-based [Longo, 2016;

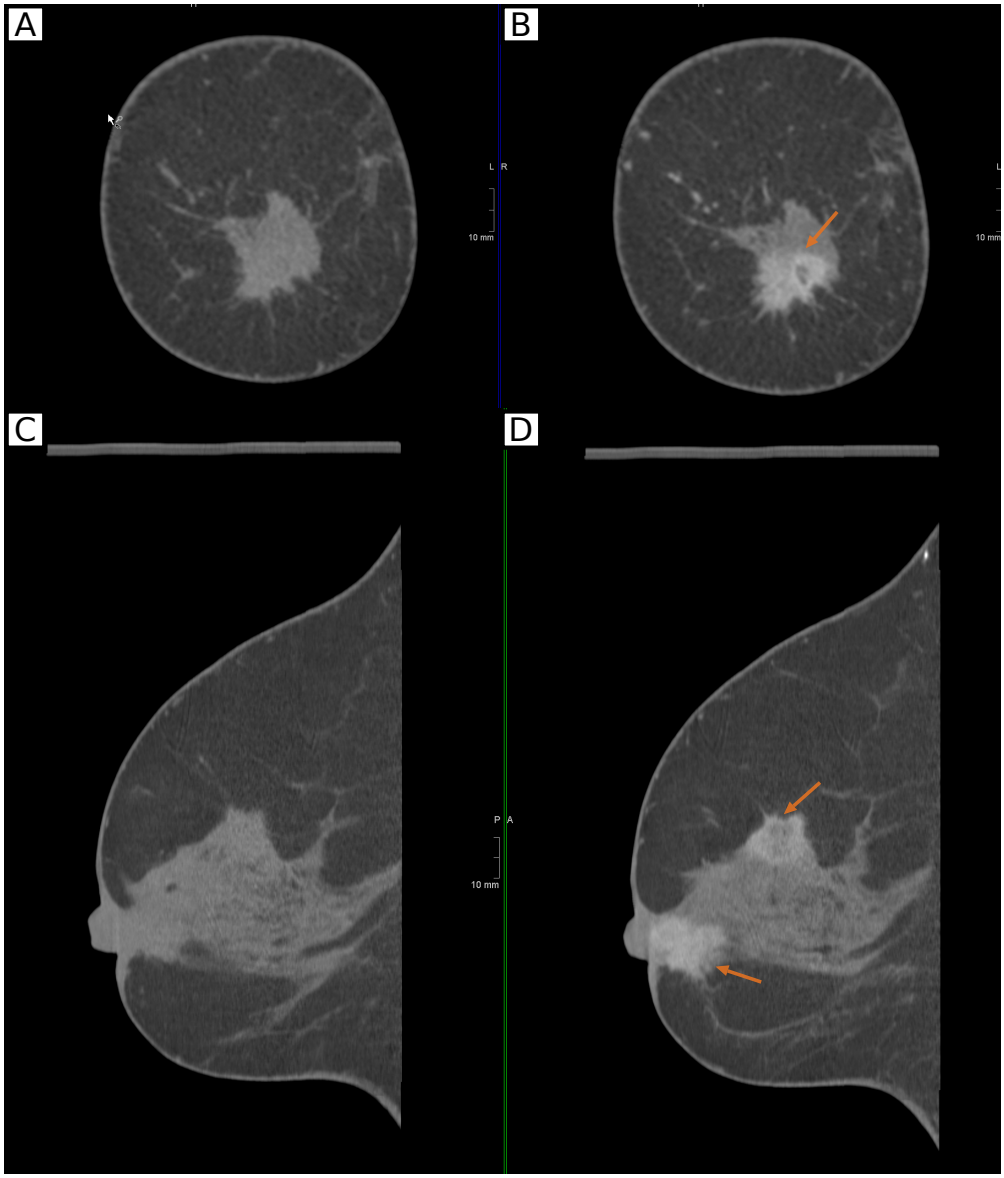

Figure 4.1: Example of *in vivo* attenuation-contrast breast computed tomography. The (A, B) coronal and (C, D) sagittal views of the uncompressed breast is presented. In contrast to the images in the left column, the images in the right column contain iodinated contrast agent. The patient has a nipple retraction and multicentric invasive ductal carcinoma and was diagnosed with a retroareolar lesion (invasive ductal carcinoma) which is better visible after contrast agent administration. In the sagittal view an additional lesion is detected in the upper quadrants of the breast. Images were provided by Magda Marcon and published in [Heck, 2020].

Tromba, 2016; Taba, 2018; Pacilè, 2018; Brombal, 2018c; Brombal, 2018a; Brombal, 2018b; Lewis, 2018; Brombal, 2019; Piai, 2019; Longo, 2019; Pacilè, 2019; Delogu, 2019; Longo, 2020] phase-contrast imaging techniques with different imaging settings. All studies reveal advantages of three-dimensional imaging in combination with phase contrast in terms of an improved detection of cancerous lesions and abnormalities in the breast. Although the synchrotron-based results at Elettra and the Australian synchrotron were obtained at a dose within the limit for mammography, scanning women clinically *in vivo* is rather unlikely at such X-ray sources due to aforementioned limitations. Consequently, this approach would be challenging to implement in clinical daily routine.
The overall aim of this project is the development of low-dose grating-based phase-contrast BCT. Instead of measuring directly at a conventional, clinically used polychromatic X-ray source, initial experiments are conducted at the MuCLS, the world's first commercial installation of an inverse Compton source, due to the radiation sensitivity of the female breast. The X-ray source provides quasi-monochromatic X-ray photons meaning that photons that only contribute to the applied MGD, but not to image contrast are eliminated. Several studies have already been accomplished on dose-compatible mammography, CESM and DBT at the CLS which should now be extended to BCT [Eggl, 2016b; Eggl, 2018; Heck, 2019]. A first attempt deals with an attenuation-only BCT without any gratings in the beam path. Afterwards, this is extended to grating-based phase contrast performed with a smaller breast phantom and a freshly dissected fibroadenoma. Finally, a larger breast phantom is measured with an off-axis CT scan.

4.2 Experimental Setup

A photograph of the experimental setup of the MuCLS's second hutch is shown in Fig. 4.2. Through an evacuated beam pipe, the generated X-ray photons travel to the experimental hutch. Two sample stages are available in this experimental hutch called "mammo" stage for projection-based measurements and the "combi" stage for CT scans. In this work, the sample is placed on the "combi" stage 14.93 m downstream the IP of the accelerated electrons and the laser pulse. The sample hangs in a 30 mm thick water bath during the measurement to avoid phase wrapping. A two-grating interferometer including a phase grating G_1 (made of nickel (Ni)) and an analyzer grating G_2 (made of gold (Au)) is utilized and installed behind the sample stage. The FOV is 70 mm at the sample position and matches the size of the G_2. Depending on the design energy of the grating interferometer, the phase grating is replaced and in consequence also the inter-grating distance is adjusted. The detailed grating specifications are listed in Tab. 4.1. Please note that the G_1 grating is inclined by 6.33 degree

resulting in an effective period of 4.89 µm. On average, approximate visibilities of 50 % and 35 % are obtained for 25 keV and 35 keV, respectively. For attenuation-based CT scans, the grating interferometer is moved out of the beam path. A movable stage with different detectors is mounted 16.05 m away from the IP directly behind the G_2. The individual detectors including the Dexela 1512, one flat-panel detector, and three photon-counting detectors (XC-Thor, Santis GaAs 75 µm and 150 µm) are delineated in the following in more detail. Depending on the geometrical arrangement and the physical pixel size, the effective pixel size of the detectors is calculated as follows

$$\text{Effective pixel size} = \frac{\text{physical pixel size}}{M}\,, \tag{4.1}$$

where the magnification M is defined as

$$M = \frac{\text{SDD}}{\text{SSD}}\,, \tag{4.2}$$

with SDD being the source-to-detector and SSD the source-to-sample distance. For our experimental setup, this results in a magnification of 1.075 at the sample position on the combi stage.

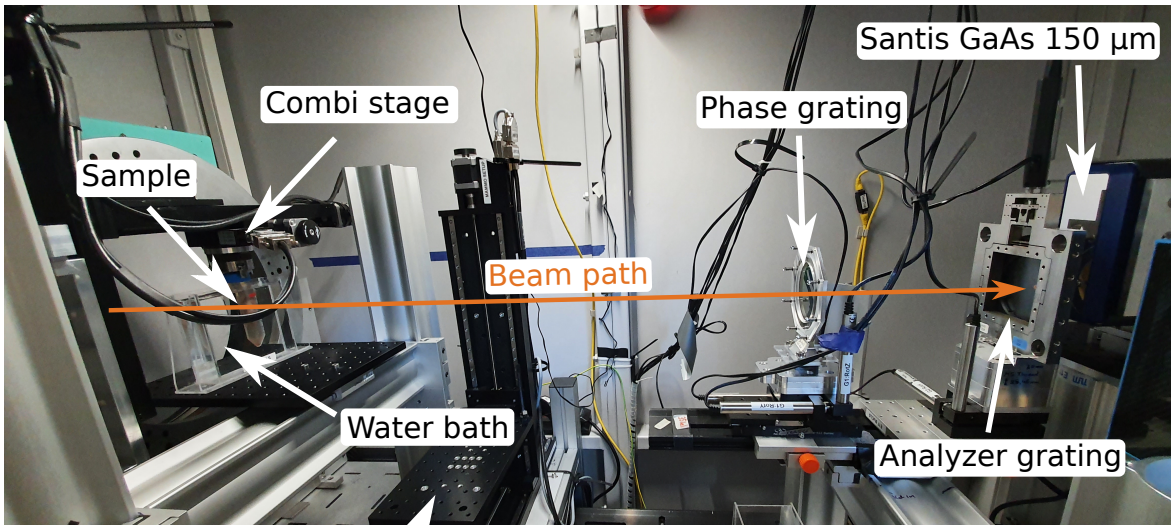

Figure 4.2: Photograph of the experimental setup of the second hutch at the MuCLS. This setup is used for attenuation-only and grating-based phase-contrast BCT. The sample is mounted hanging into a 3 cm thick water bath in front of the grating interferometer including phase and analyzer grating. The X-ray beam comes from the left side out of the evacuated beam pipe. The detectors are mounted on a movable stage directly behind the analyzer grating on the right side.

	G_1	G_1	G_2
Design Energy [keV]	25.00	35.00	both
Material	Ni	Ni	Au
Substrate	Si 525 µm	Si 525 µm	Si 525 µm
Height [µm]	4.39	6.15	70.00
Period [µm]	4.92	4.92	5.00
Duty cycle	0.50	0.50	0.50
Inter-grating distance d_G [cm]	24.80	34.50	-

Table 4.1: Specifications of the gratings at the MuCLS. The individual characteristics of the gratings used in this work for 25 keV and 35 keV are presented. The G_2 is the same for both X-ray energies. The two G_1 gratings have a phase shift of $\pi/2$. The inter-grating distance is adjusted for the respective design energy.

PerkinElmer Dexela 1512

The Dexela 1512 from *PerkinElmer* (Waltham, Massachusetts, USA) is a flat-panel detector with a physical pixel size of 74.8 µm resulting in an effective pixel size of 69.6 µm for the geometry at the combi stage. The detector has a GadOx scintillator with a thickness of 150 µm. The active area is limited to 1536 × 1944 pixels or 145.4 mm × 114.9 mm [Elmer, 2012]. The maximum frame rate of this detector is 26 fps corresponding to a minimum exposure time of 38.50 ms. In the following work, this detector will be referred to simply as Dexela.

SANTIS GaAs 75 µm

The SANTIS 0808 GaAs 75 µm is a prototype detector provided by *DECTRIS AG* (Baden-Daettwil, Switzerland). It is a photon-counting detector consisting of two modules both equipped with a 500 µm thick GaAs sensor and separated by a gap of 36 pixels. The detector's active area is 77.25 mm × 77.20 mm or 1030 pixel × 1028 pixels. In order to use the spectral ability of this detector, it is possible to set two different energy THLs per pixel [DECTRIS, 2019]. At the MuCLS, the physical pixel size of 75.0 µm results in an effective pixel size of 69.8 µm. The maximum frame rate for this detector is tabulated as 100 fps resulting in a lowest achievable exposure time of 10 ms. In the following work, this detector will be referred to simply as Santis 75 µm.

SANTIS GaAs 150 µm

The SANTIS 0808 GaAs 150 µm is a prototype photon-counting detector provided by *DECTRIS AG* (Baden-Daettwil, Switzerland). The detector is equipped with two modules of different sizes which are separated by a horizontal gap of five pixels. The first module has a 500 µm and the second one a 750 µm thick GaAs sensor. An active area of 154.20 mm × 38.55 mm or 1035 × 257 pixels can be used. The adjustment of four energy THLs is possible for this device. Due to the small magnification, the effective pixel size of this detector is 139.5 µm at the MuCLS. In burst mode, a maximum frame rate of 200 Hz corresponding to a minimum exposure time of 5 ms is possible. In the following work, this detector will be referred to simply as Santis 150 µm.

XCounter XC-Thor FX10

The XC-Thor FX10 from *Direct Conversion AB* (Danderyd, Sweden) is a single photon-counting hybrid-pixel array detector equipped with a 750 µm thick CdTe sensor. The physical pixel size is 100 µm resulting in an effective pixel size of 93.0 µm for the experimental setup used in this work. The total FOV meaning the active sensor area is limited to 100 mm x 50 mm. For spectral imaging, it is possible to adjust two energy THLs. The maximum frame rate for this detector is tabulated as 300 fps resulting in a minimum possible exposure time of 3.33 ms. In the following work, this detector will be referred to simply as XC-Thor.

4.3 Samples

The two samples described in the following sections are used to realize the first attempts towards dose-compatible attenuation-only and grating-based phase-contrast BCT at the MuCLS. The first one is a self-created breast-like phantom (cf. Sec. 4.3.1) and the second one is a freshly dissected breast specimen including a fibroadenoma (cf. Sec. 4.3.2).

4.3.1 Breast Phantom

For the preliminary work of attenuation-only and grating-based phase-contrast BCT, a breast-like phantom is created. A piece of pork neck is used which should represent the female breast as both mostly consist of adipose tissue. The female breast is additionally composed of glandular tissue which is difficult to mimic in a biological phantom and thus neglected here. Iodinated contrast agent and calcifications made of hydroxyapatite and tissue glue are inserted. IMERON 400 MCT (*Bracco Imaging Deutschland GmbH*,

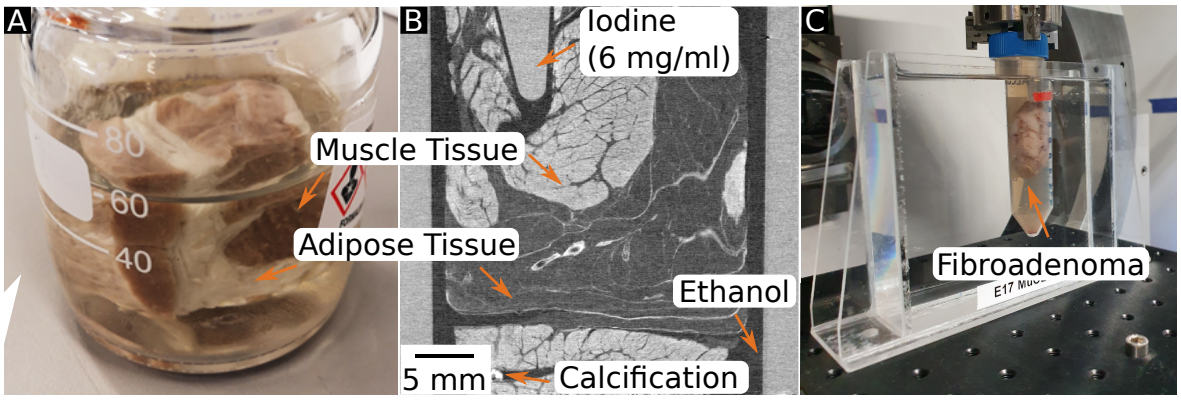

Figure 4.3: Samples used for grating-based phase-contrast BCT at the MuCLS. (A) Photograph of a piece of pork neck which consists of a high amount of adipose tissue representing the breast phantom. It contains additional calcifications made of hydroxyapatite and tissue glue and an Eppendorf tube with iodinated contrast agent in a clinical concentration of 6 mg/ml. (B) Sagittal slice of a phase-contrast CT image of the breast phantom used for orientation. (C) Photograph of a 2.5 cm thick fibroadenoma.

Germany) is selected as commonly clinically used contrast agent. Injecting the contrast agent in a concentration of 400 mg/ml at a standard dose of 1.5 ml/kg per body weight of the woman, leads to a concentration of 6 mg/ml in the patient's blood vessels with a body weight of 80 kg and a blood volume of 66 ml/kg [Wadsworth, 1954]. Thus, an iodine concentration of 6 mg/ml is chosen for the breast phantom. A photograph of the sample is depicted in Fig. 4.3 (A) and a corresponding sagittal slice of a phase-contrast CT image is additionally shown in (B) to enable a better orientation. The sample is 2.5 × 2.5 × 4 cm^3 large and chosen to fit in the FOV of the experimental setup. The sample is first fixed in 4 % formaldehyde before it is added into a 70 % solution of ethanol in the Falcon tube. This preparation allows the sample to be reused at any time for prospective measurements. For subsequent work on this topic, the same sample was recreated only with a larger diameter of approximately 6 cm to investigate the difficulty of a dose-compatible off-axis CT scan (cf. Sec. 4.5.5).

4.3.2 Fibroadenoma

For the first evaluation of the experimental parameter settings initially investigated with the breast phantom, the Red Cross Hospital Munich provided us with freshly dissected fibroadenomas as first human breast specimens. The study was conducted in accordance with the Declaration of Helsinki and approved by the local ethics committee (Ethik-Kommission der Bayerischen Landesärztekammer (BLAEK), number 19063, date of permission 30/09/2019). The 2.5 cm thick samples are embedded in

4 % formaldehyde and an additional PMMA rod is inserted in the Falcon tube for energy calibration. This human breast sample is chosen since it fits in the experimental FOV in contrast to large-scale mastectomy specimens. Fibroadenomas are the most common benign breast lesions. They are benign fibroepithelial tumors that usually occur in young women and in approximately 10 % of the female population worldwide [Ajmal, 2021]. They are solid, not fluid-filled, usually unilateral with regular or lobulated borders, often differ in size between a few millimeters and several centimeters and originate from stromal and epithelial connective tissue cells which contain progesterone and estrogen [Ajmal, 2021]. The growth of fibroadenomas is related to reproductive hormones so that - due to the high amount of female reproductive hormones during pregnancy - they may proliferate and the connective tissues increase [Ajmal, 2021].

4.4 Dose Considerations and Choice of Exposure Time

Based on the two-view standard mammography screening, the published dose values for the conventional attenuation-based BCT are proposed to a total MGD of 5 mGy [Kalender, 2012; Kalender, 2017]. Thus, to acquire knowledge about the relevant exposure time range, dose considerations must first be performed before starting experimental work at the MuCLS. Therefore, MGD and the corresponding photon flux values from previously conducted mammography studies are taken for a comparison [Eggl, 2018; Heck, 2019]. Measuring for example with a photon energy of 35 keV at a flux of $2.8 \cdot 10^{10}$ photons/seconds results in a MGD of 0.278 mGy per second. Consequently, a total exposure time of 18 s is the upper limit for a 5 mGy-based BCT measurement. Assuming an off-axis CT scan for large mastectomy samples with 1340 angles and 5 phase steps, the exposure times for each projection and phase step would be very short with 13.4 ms and 2.7 ms, respectively. For such low-dose CT scans, the demands on the detectors, which have to deal with short exposure times, are very high. In Sec. 4.2, the maximum frame rates of the given detectors are presented. Comparing the flat-panel detector with the photon-counting detectors, it is noticeable that the lowest achievable exposure times are provided by the photon-counting detectors and their high maximum frame rates. The low frame rate of the Dexela, a standard mammography detector, is not compatible with the high requirement of short exposure times needed for BCT. Therefore, it is generally preferred measuring with photon-counting detectors.
In this work, we aim for a grating-based phase-contrast BCT where three signals are obtained simultaneously. Therefore, we propose this method rather as a check-up examination than as a screening method. Thus, a higher MGD than the 5 mGy proposed for the attenuation-based BCT would also be reasonable. For first investigations in this

direction we assumed a MGD of e.g. 20 mGy and a smaller sample. This requires only 650 angular projections for the CT scan resulting in an exposure time per projection and stepping position of 22 ms. Based on the aforementioned assumptions as well as taking pre-processing like binning, angle reduction and advanced reconstruction techniques into account which additionally lower the MGD, higher exposure times would be feasible. Please note that in addition to that, the daily varying photon flux of the CLS must be taken into account so that the exposure times are adjusted accordingly. Most of the measurements performed in this work have been conducted with a lower photon flux than previously mentioned. In consequence, the measurements presented in the following sections are generally conducted such that low and high dose measurements ranging from exposure times with 40 ms up to 500 ms are obtained.

4.5 Experimental Results

The experimental results of this section are divided into different parts. After an initial analysis of the spatial resolution of different detectors (cf. Sec. 4.5.1), attenuation-only (cf. Sec. 4.5.2) and grating-based phase-contrast breast computed tomography are investigated. Therefore, a small breast-like phantom (cf. Sec. 4.5.3) and a fibroadenoma representing a freshly dissected breast specimen are used for demonstration (cf. Sec. 4.5.4) Finally, a larger breast-like phantom is created to examine the potential of an off-axis CT scan (cf. Sec. 4.5.5).

4.5.1 Detector Comparison based on the Spatial Resolution

In this section, the Dexela and the Santis 75 µm detector as well as the two times binned Santis 75 µm and the unbinned Santis 150 µm are compared regarding their spatial resolution. Therefore, measurements with a tungsten knife edge in horizontal and vertical direction and with a Siemens star are conducted. The measurements with the edge are performed with a slight inclination of a few degrees compared to the pixelated detector to obtain a dense sampling of the edge and thus an over-sampled ESF. They are evaluated regarding their MTF, PSF and LSF. All measurements are performed with an X-ray energy of 35 keV. The energy THLs of the two photon-counting detectors are set to 55 % of the X-ray energy. In order to generate enough statistics, 100 images with an exposure time of 5 s are recorded and finally averaged for the two Santis detectors. Due to the comparably fast saturation of the Dexela flat-panel detector, more images (500) with a smaller exposure time (0.1 s) are taken. For the comparison between the Dexela and the Santis 75 µm, measurements are conducted at the detector and the sample ("mammo" stage) position. The position of the detector is additionally analyzed, as close to the detector surface any contribution from the X-ray

source spot is eliminated. Thus, the detector's MTF is exclusively measured. Since the position-dependent results do not differ very much in case of this X-ray source, it has been dispensed to measure at both positions for the two times binned Santis 75 µm and the unbinned Santis 150 µm.

Comparison between Dexela and Santis 75 µm

The MTFs for the Dexela (blue and orange) and the Santis 75 µm (red and green) detector at sample and detector position measured in horizontal ((h) in solid lines) and vertical ((v) in dashed lines) direction with the knife edge are presented in Fig. 4.4. The Nyquist limit for the detector and the sample position is indicated by a dashed, grey line while the 10% MTF limit is shown by a dashed, black line. The MTF of the Santis 75 µm detector shortly stagnates at the beginning before it slowly decreases. It is noteworthy that the MTF does not fall below neither the 50 % nor the 10 % limit within the Nyquist limit. The MTF drops to the 10% limit at a spatial frequency of more than 12 lp/mm. In contrast, the Dexela's MTF has a steep drop at first, i.e. it drops much faster with increasing spatial frequency than the MTF of the Santis 75 µm. Based on these observations, it is obvious that the MTF of the Santis 75 µm is significantly higher than the one of the Dexela. Although the MTF and the Nyquist limit are very close for the Dexela measurements, none of the given MTFs falls below the 10 % threshold within the Nyquist limit. The PSFs which are extracted from the Siemens star measurement are depicted in Fig. 4.5. The ones of the Dexela are shown in the first row (A and B) and for the Santis 75 µm in the second row (C and D). The results measured at the detector position are visible in the left column (A and C) and the results of the sample position measurement are visible on the right (B and D). While all PSFs exhibit a symmetric behavior, it is obvious that the PSF of the Santis 75 µm detector is distributed over fewer pixels and thus smaller. By then integrating the data of the PSFs along the x- and y-axis, the LSFs are obtained in horizontal and vertical direction, respectively. These results are presented in Fig. 4.6 and the corresponding full width half maximum (FWHM) values are listed in Tab. 4.2. While for the Santis 75 µm, the width of the fitted Gaussian in Fig. 4.6 does not differ much comparing sample and detector positions, there is a significant difference for the Dexela. The LSF at the detector position is broader which indicates the stronger influence of the source blur for a flat-panel detector. This is also underlined by the respective FWHM where the values are 41 % higher for the Dexela and only 10 % or 22 % for the Santis 75 µm comparing detector and sample position.

The strong difference for the behavior of the MTF, PSF and LSF between the Dexela and the Santis 75 µm described above are mainly caused by the fact that two fundamentally different detector technologies are compared. Generally, there is a strong influence of shared light for the Dexela flat-panel detector in the scintillation-based layer which

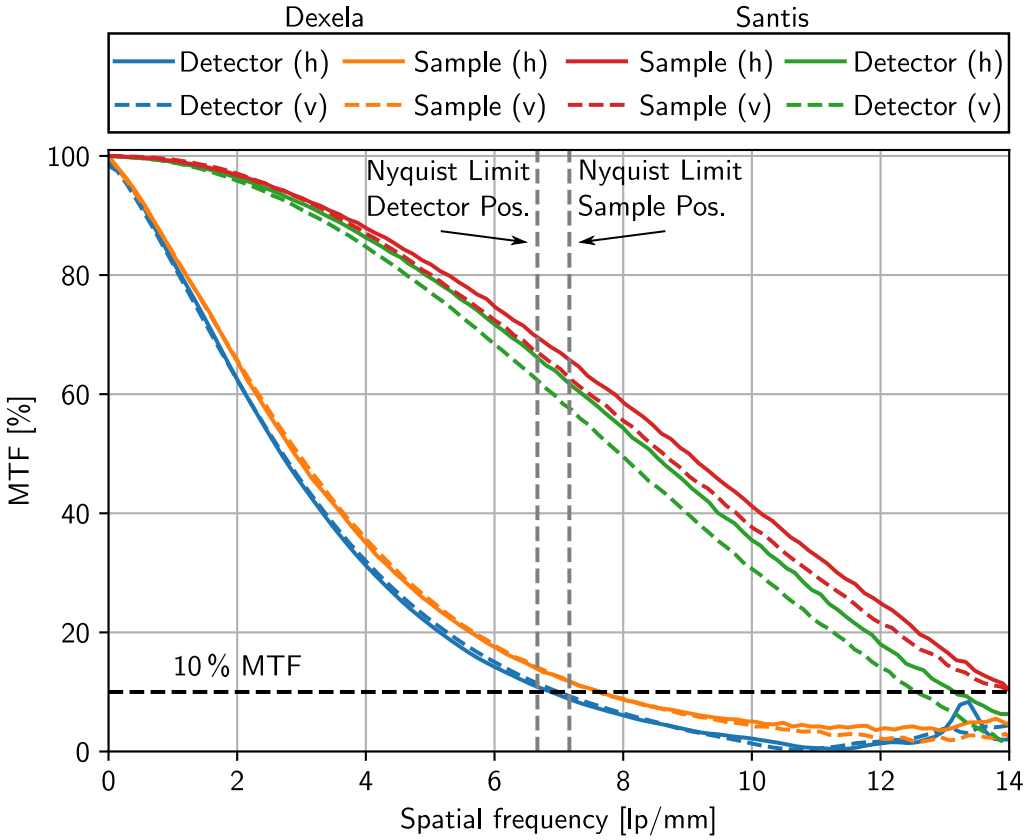

Figure 4.4: Comparison of the MTFs for the Dexela and the Santis 75 µm detector. It includes the MTFs at the sample and the detector position in horizontal and vertical direction for both detectors. It is clearly visible that the MTFs only differ slightly comparing horizontal (h) and vertical (v) direction as well as detector and sample position. In contrast, the achievable resolution is significantly higher for the Santis 75 µm than for the Dexela.

	Dexela	Santis 75 µm	Dexela	Santis 75 µm
	Detector		**Sample**	
σ_x [µm]	68.73	36.79	48.64	30.17
σ_y [µm]	68.52	35.38	48.52	32.19

Table 4.2: FWHM values for the Dexela and the Santis 75 µm. It is clearly visible that the values for the Dexela are higher than for the Santis 75 µm. The FWHM values at the sample position are lower than at the detector position for both detectors.

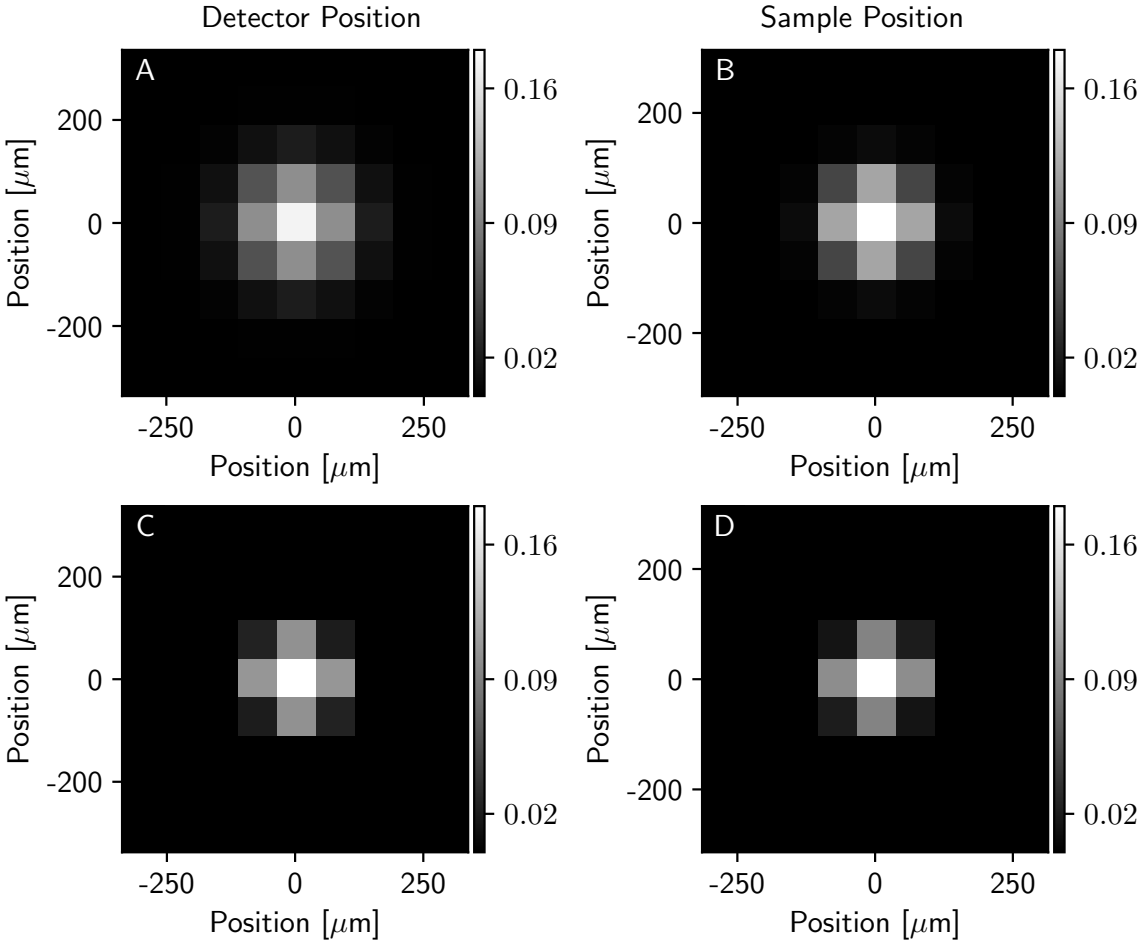

Figure 4.5: Comparison of the PSFs of the Dexela and the Santis 75 µm detector. The Dexela's PSF are shown in (A) and (B) while the one of the Santis are presented in (C) and (D). For every detector, the results measured at the detector position are in the left column and for sample position in the right column. It becomes clear that the Dexela smears out over more pixels than the Santis 75 µm resulting in a sharper image and higher resolution.

results in lower measures than for the Santis 75 µm. The Dexela smears out over a few pixels resulting in an slightly blurred image and a worse spatial resolution. This blurring becomes visible in the PSFs in Fig. 4.5 (A) and (B) where the contribution ranges over four pixels for the Dexela instead of two pixels for the Santis 75 µm. Although the results for the photon-counting-based Santis 75 µm detector appear promising and indicate that with this detector, a measurement with higher resolution would be achieved, they differ from an ideal detector system since they are not point-like. It is likely that ideal figure of merits can not be reached here due to the crosstalk between neighbor-

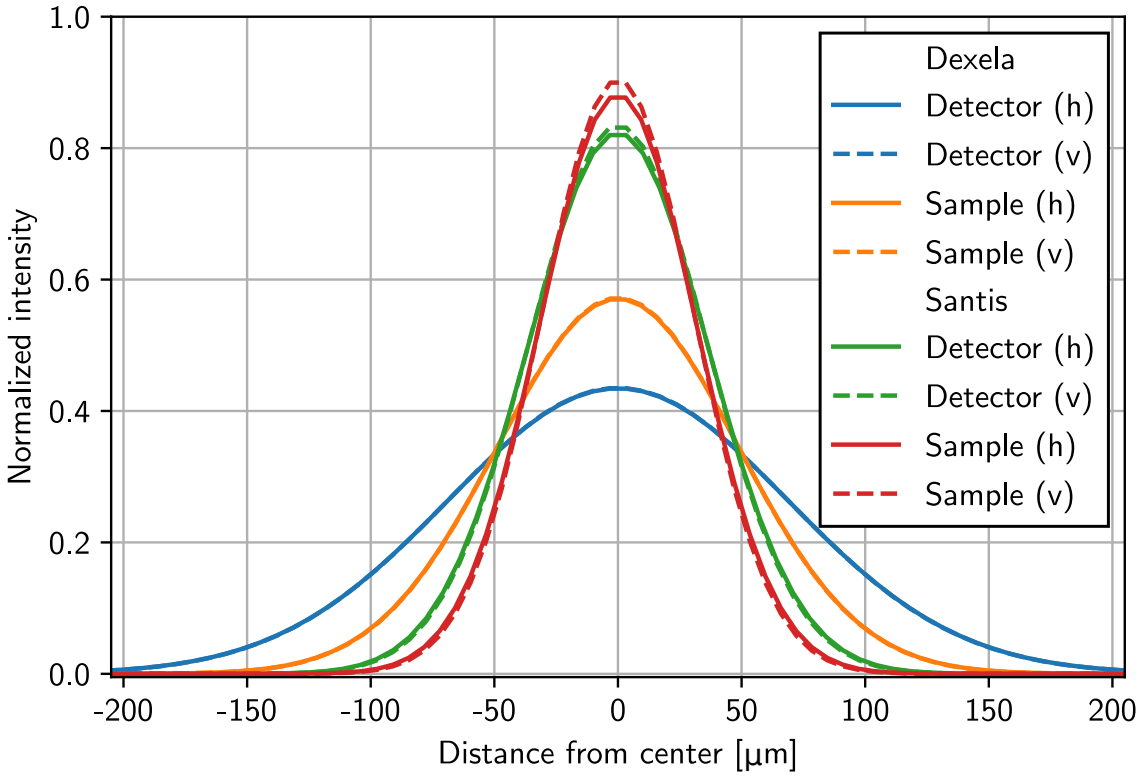

Figure 4.6: Comparison of the LSFs of the Dexela and the Santis 75 µm detector. It includes the LSF at the sample and the detector position in horizontal (h) and vertical (v) direction. While the directional influence is comparatively small, the LSF differ between sample and detector position and especially between the two detectors. The LSF of the Santis 75 µm is significantly higher than of the Dexela.

ing pixels. In summary, one benefits from the photon-counting detector in terms of a higher spatial resolution in addition to the aforementioned shorter possible exposure times (cf. Sec. 4.4).

Comparison between Santis 150 µm and Santis 75 µm

In Fig. 4.7, the MTFs for the Santis 75 µm and 150 µm detector oriented in horizontal (h) and vertical (v) direction are presented and plotted in solid and dashed lines, respectively. As initially indicated, the knife edge and the Siemens star have only been measured at the sample position due to the high similarity of the results between detector and sample position and since the results of the sample position are of particular interest for BCT measurements. Here again, the MTFs of both detectors do

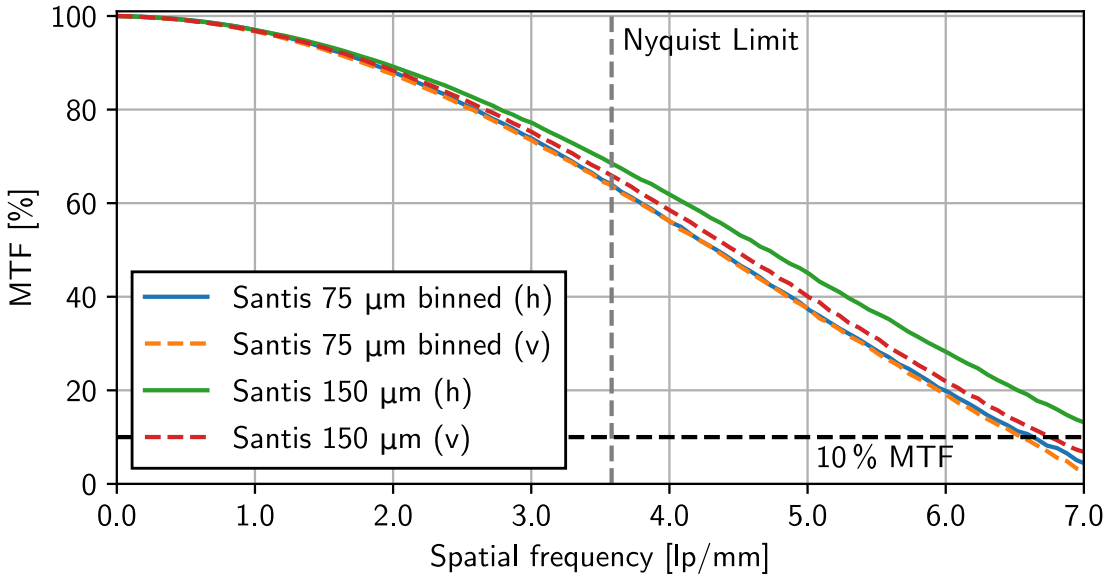

Figure 4.7: Comparison of the MTFs for the Santis 75 µm binned and the Santis 150 µm. It includes both the horizontal and the vertical direction and shows that the Santis 150 µm detector has a slightly higher achievable resolution. To better distinguish the results of the Santis 75 µm, the vertically and horizontally oriented measurements are plotted in dashed and solid lines, respectively.

not fall below either the 50 % or the 10 % limit within the Nyquist limit (marked with a vertical, grey, dotted line). The PSFs are depicted in Fig. 4.8 for the Santis 75 µm two times binned (A) and the Santis 150 µm (B). There, only a small difference can be observed: It appears that the PSF of the two times binned 75 µm detector is slightly broader especially regarding the diagonals than the PSF of the 150 µm. Extracting now the LSF from the PSF results in the plots presented in Fig. 4.9. The corresponding FWHM values are listed in Tab. 4.3 and underline the visual observations. As far as FWHM values are concerned, the Santis 150 µm achieves again the best values by a small margin. Although both have the same effective pixel size after binning the Santis 75 µm by a factor of two, the MTF-based resolution is a bit higher for the detector with the physical pixel size of 150 µm. This can be explained by taking the sensor-related effects of a photon-counting detector presented in Fig. 2.6 into account. For smaller pixel sizes, it is more likely that the incoming X-ray photon is falsely detected due to charge-sharing or being detected at the inter-pixel edge and the energy information is completely lost. In general, the probability of this effect decreases with increasing pixel sizes as here for the Santis 150 µm. These results indicate that binning after conducting the measurement is not beneficial and thus that measurements with a detector with an intrinsically higher physical pixel size is preferred.

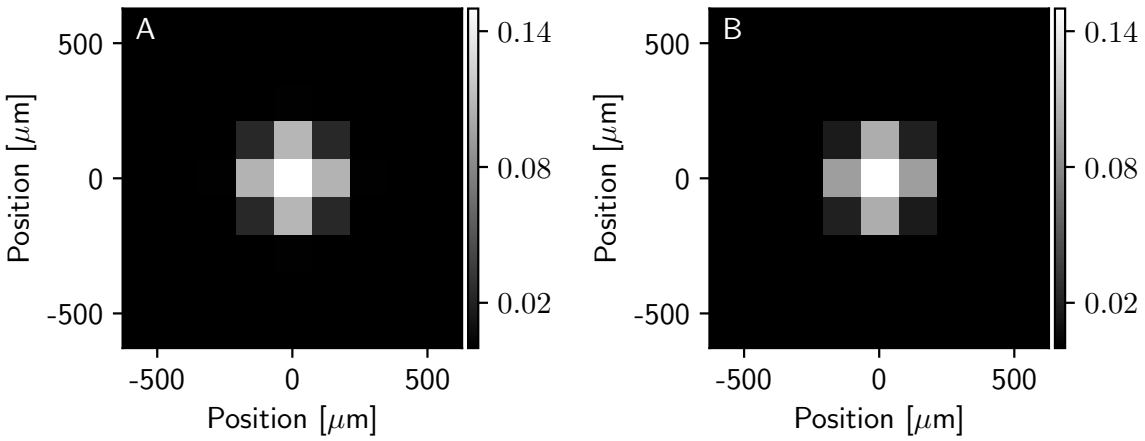

Figure 4.8: Comparison of the PSFs for the Santis 75 µm binned and the Santis 150 µm. The PSF of the two times binned Santis 75 µm in (A) is slightly broader especially in diagonal direction than the one of the Santis 150 µm in (B).

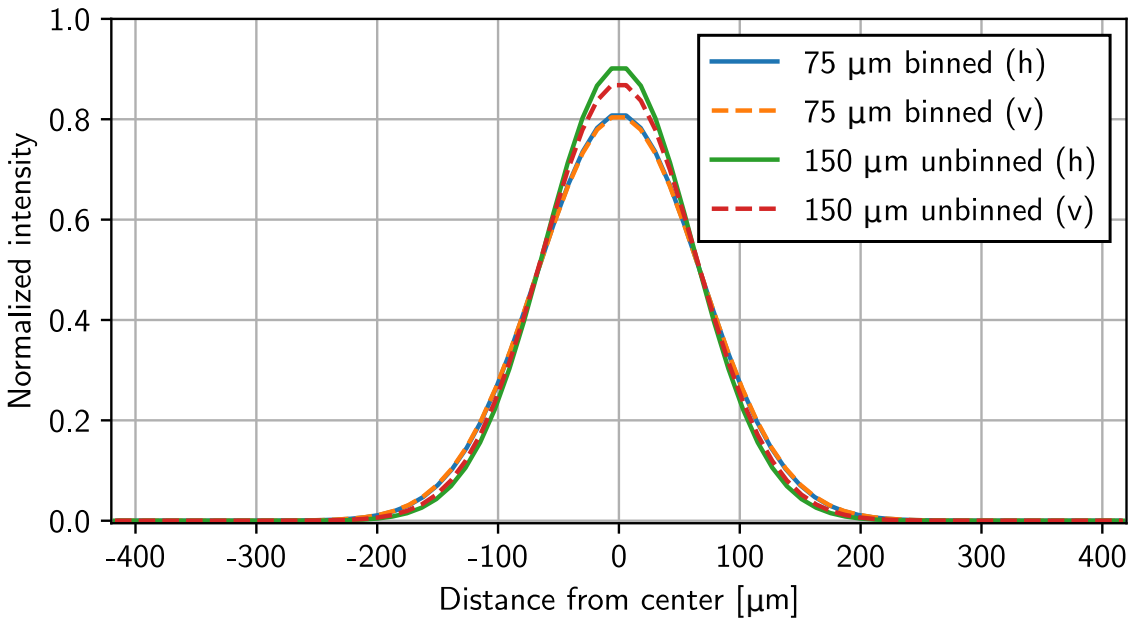

Figure 4.9: Comparison of the LSFs for the Santis 75 µm binned and the Santis 150 µm. It shows that the LSF of the detector with an unbinned physical pixel size of 150 µm is slightly higher in both directions compared to the Santis 75 µm detector that is binned to a pixel size of 150 µm. To better distinguish the results of the Santis 75 µm, the vertically and horizontally oriented measurements are plotted in dashed and solid lines, respectively.

	Santis 150 µm	Santis 75 µm binned
σ_x [µm]	60.79	67.91
σ_y [µm]	63.15	68.23

Table 4.3: FWHM values for the two times binned Santis 75 µm and 150 µm. The values indicate that the Santis 150 µm has a slightly narrower LSF. For the Santis 150 µm, the values in x- and y-direction differ a bit while they are nearly the same for the two times binned Santis 75 µm

4.5.2 Attenuation-based Breast Computed Tomography

Before starting with grating-based phase-contrast BCT, the first work of this project deals with achieving a low-dose and clinically comparable attenuation-based BCT at the MuCLS. Therefore, the breast phantom described in Sec. 4.3.1 was measured without any gratings in the beam path while being submerged in a water bath during the scan. At the time of these measurements, the preferred Santis 150 µm prototype detector was not yet available. This is why – based on the knowledge from the previous sections – the images were recorded with the GaAs-based photon-counting detector Santis 75 µm with binning afterwards instead. After pixel binning, resulting in a detector width of 515 pixels and taking the sample thickness into account, 650 projections were acquired over one full rotation according to the Nyquist theorem (cf. Eq. (2.42)). There are several possibilities to obtain reconstructions with different MGDs depending on the combination of exposure time, binning and angle reduction. To cover both low- and high-dose measurements, several exposure times of 40 ms, 70 ms and 500 ms were taken for each projection angle for this study. In the work of Sandra Resch, this data has been analyzed comparing different binning factors to reduce the required number of projections and thus the MGD [Resch, 2021]. The analysis shows that the two times binned images with an effective pixel size of 139.6 µm visually reveals the best results for the high dose measurement (106.43 mGy) while maintaining a balance between MGD and resolution. Nevertheless, three times binning is necessary to further reduce the number of angles used for reconstruction and thus the MGD towards the low-dose regime. Hence, the images presented in this section are three times binned and have an effective pixel size of 209.4 µm. The pixel size is higher compared to standard mammography, but this is reasonable since the first industrial and clinically available BCT *nu:view* from *AB-CT - Advanced Breast-CT GmbH* (Erlangen, Germany) uses similar sized pixels (100 µm physical pixel size) resulting in voxel sizes of 150 µm^3 [ABCT, 2020]. Flat fields with a longer exposure time than for the projection images are taken in the beginning and at the end of the measurement to obtain better statistics and to improve the image quality of the flat field corrected projection images [Allner, 2022].

A typewriter detector shift with a maximum shift of 10 pixels in both directions was set to avoid ring artifacts in the reconstruction. To achieve a dose-compatible BCT, an exposure time of 40 ms per phase step was chosen. For the whole scan, this results in a MGD of 8.5 mGy. To meet the clinically suggested BCT dose limit of no more than 5 mGy [Kalender, 2012; Kalender, 2017; Berger, 2019b], the number of angles is halved which satisfies the Nyquist criterion due to binning.
The results for the attenuation-based BCT taken at the MuCLS are presented in Fig. 4.10 and are reconstructed with SIR. One axial (A) and one sagittal (B) slice containing the iodinated contrast agent are shown and reconstructed with a MGD of 4.25 mGy and 325 angles in total. Please note that the slices presented here are only exemplary representatives of the whole volume. Larger structures like muscle and adipose tissue are still discernible from each other, but smaller fiber structures get lost in the background noise. Nevertheless, tiny muscle and adipose tissue structures are still discernible as indicated by the orange arrows in (B). While the soft tissue contrast in the attenuation images is intrinsically quite low, the iodine-containing contrast agent (blue arrows in (A) and (B)) is very clearly visible which underlines why it is often used in the clinic to generate more contrast. Since the images are reconstructed with SIR using regularization, the images appear slightly blurred compared to a conventional FBP but also less noisy. In subfigure (C), a clinical *in vivo* BCT slice taken with the *nu:view* system and a total MGD of approximately 5 mGy is depicted for comparison. The green arrow indicates an invasive ductal carcinoma also highlighted by the injection of iodinated contrast agent. By visually comparing the images, it becomes clear that the laboratory results can successfully compete with the clinical low-dose BCT. Since these results are quite promising, the emphasis of the next sections is on phase-contrast imaging to further improve soft tissue contrast without the usage of contrast agents.

4.5.3 Investigation of Grating-based Phase-contrast Breast Computed Tomography with a Breast Phantom

Since it is possible to obtain attenuation-based BCT images in a dose-compatible range (cf. Sec. 4.5.2), the investigation of BCT is extended to grating-based phase-contrast BCT. The topic was mainly dealt with in the context of the master thesis of Sandra Resch [Resch, 2021]. This includes among others the comparison of different detectors, of various denoising approaches and of several reconstruction techniques. Since parts of the results presented in this work here are based on the earlier obtained knowledge, the results are briefly summarized in the following.

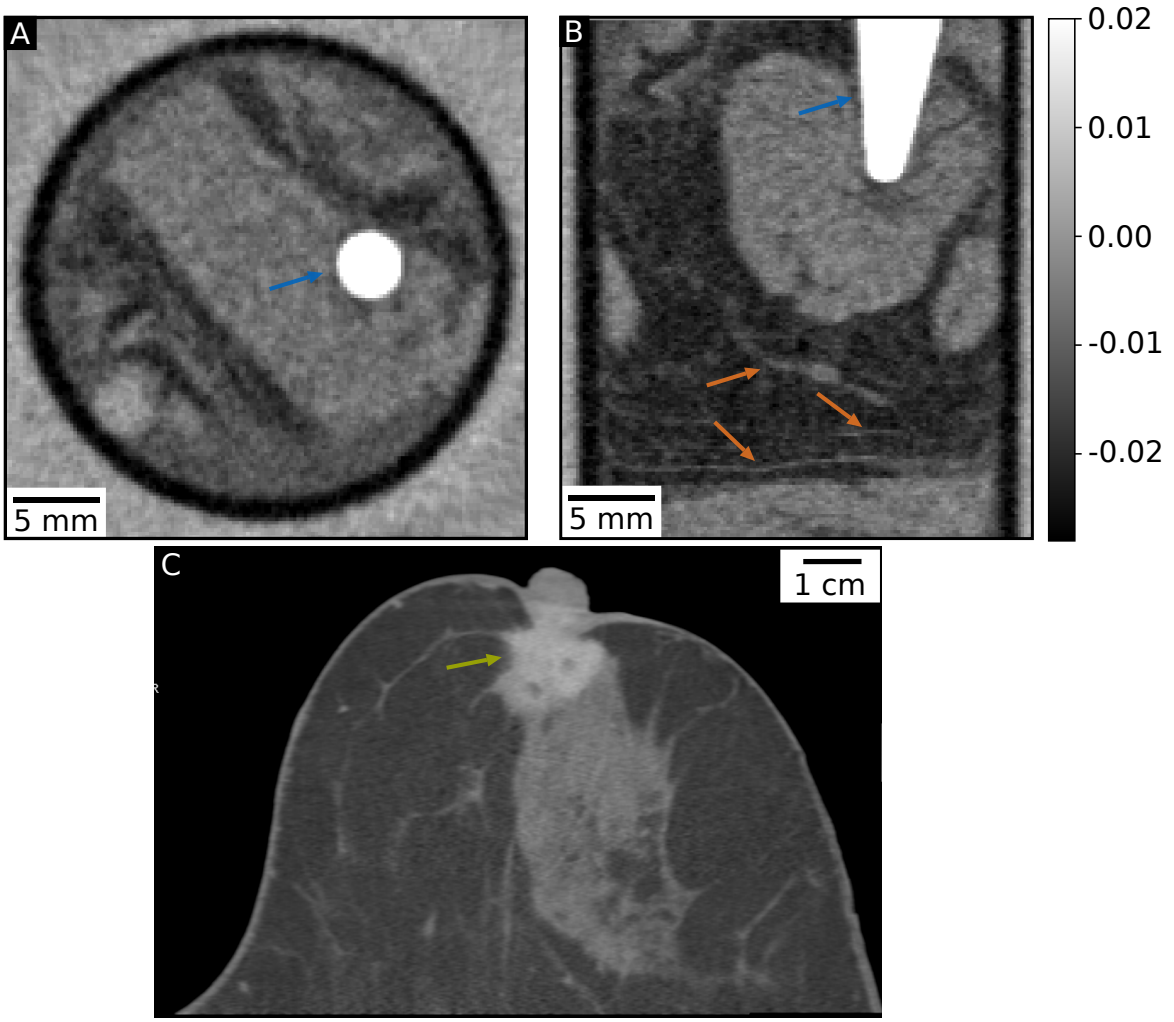

Figure 4.10: Comparison of attenuation-based BCT. SIR reconstructed BCT scans taken at the MuCLS showing (A) the axial and (B) the sagittal view are presented. The MGD is 4.25 mGy for an exposure time of 40 ms per projection. Iodinated contrast agent is indicated by blue arrows while smaller structures are highlighted by the orange arrows in (B). (C) Clinical *in vivo* attenuation-contrast BCT is additionally shown for visual comparison. The injected iodine containing contrast agent is highlighted by the green arrow and shows the invasive ductal carcinoma. The image in subfigure (C) is provided by Magda Macron and published by [Heck, 2020].

Detector Comparison

A visual and CNR-based comparison with the breast phantom (cf. Sec. 4.3.1) for attenuation-only as well as phase-contrast images was conducted. The comparison

includes the Santis 75 µm unbinned and two times binned, the Santis 150 µm and the Dexela detector. First, the analysis of the influence of the physical pixel size of the two Santis detectors turns out that although the reconstructions with the two times binned Santis 75 µm seem to be slightly sharper, the calculation of the spatial resolution by Fourier analysis is a bit better for the unbinned Santis 150 µm. Second, by taking the spectral performance of this technology into account, which would be necessary for spectral measurements at a polychromatic X-ray source, a detector with a higher physical pixel would be better. There, the probability of charge sharing is decreased and thus the spectral resolution is higher [Berthe, 2021]. In case of the Santis 150 µm, the 500 µm module would then be preferred since the charge cloud is not able to further spread over several detector pixels as it would be the case for the 800 µm module [Berthe, 2021]. Although there are already photon-counting detectors with charge-sharing correction that could ensure better spectral resolution even for detectors with smaller pixel sizes, a detector with a larger pixel size remains more interesting for BCT because the dose limit must be maintained and a high spatial resolution is not absolutely necessary. Nevertheless, photon-counting detectors can handle both very short and long exposure times and generate sharper images in contrast to the integrating flat-panel detectors. There, fast saturation and low detector frame rates limit the measurements. Furthermore, small sample details are better observed in the Santis images than in the comparably blurry images of the Dexela detector which smears over several pixel due to the broader PSF of the Dexela (cf. Sec. 4.5.1). As consequence of Sandra Resch's work, a more detailed detector comparison based on measurements with a knife edge and a Siemens star are already provided in Sec. 4.5.1. The observations of both comparisons are in agreement to each other. Photon-counting detectors with larger detector pixels are the recommended detector technology that should be used for low-dose BCT imaging.

Denoising Techniques

For low-dose BCT imaging, projections with less image statistic are recorded and thus a higher background noise level is present. Therefore, denoising or rather improving the statistics of a single projection is an important issue to generate useful BCT images with a low MGD. A comparison of pixel binning, patchwise phase retrieval and dictionary-based denoising is performed with the Santis 75 µm. Binning is a very easy way to obtain more image statistics with the consequence that one looses spatial resolution and smaller structures potentially get lost. In contrast, patchwise phase retrieval is a simple way to on the one hand increase image statistics while on the other hand maintaining most of the spatial resolution of the image but at the expense of edge sharpness. Combining both approaches is a promising and easy way to generate images with sufficient image quality while reducing the MGD to a clinically and dose-compatible

range. Dictionary denoising, however, introduces artifacts especially for the low-dose results, is comparatively very time-consuming, requires more computing power and is not easy to handle in terms of estimating the best denoising parameters. For this reason, this approach was not pursued further for the following reconstructions.

Single-shot Computed Tomography

As alternative to grating-based phase-contrast imaging using the phase stepping approach, a single-shot CT is investigated to avoid time-consuming stepping and to thus potentially reduce the MGD. For this approach, the G_1 grating is rotated in z-direction to induce a misalignment between the G_1 and the G_2 grating. In consequence, the Moiré effect creates a small periodic intensity pattern. The three imaging modalities are extracted with Fourier space phase retrieval based on the assumptions in [Bevins, 2011] which are not further explained here. The images have a resolution in axial plane corresponding to the effective pixel size of 69.7 µm, but in y-direction the resolution is with 279.8 µm four times higher. These values lead to the problem that the resolution is too high for BCT in axial plane, but slightly to low in y-direction. In addition, the minimal refraction angle for the stepping approach is lower than for the single-shot one which means that the sensitivity is higher for grating-based phase-contrast imaging with stepping. The loss in sensitivity for the single-shot scan is mainly caused by the significantly reduced visibility during the single-shot scan due to the strong G_1 rotation and the small fringes. One problem is that the resolution in the y-direction would be increased by further rotating the G_1, but this would result in a lower sensitivity in return. It is therefore a challenge to find a balance between these two parameters. In summary, despite the generally shorter scanning time due to the skipping of the classical stepping procedure, the single-shot method is not a promising alternative for the application of low-dose phase-contrast BCT because image quality is not significantly improved, additional artifacts occur and the expected dose reduction due to the omission of phase stepping fails to materialize.

Low-dose Grating-based Phase-Contrast Breast Computed Tomography

Finally, a grating-based low-dose phase-contrast BCT measurement was conducted with the Santis 75 µm detector at an X-ray energy of 35 keV. Five phase steps were taken where the exposure time for one stepping position was 40 ms. In accordance to the Nyquist theorem, 650 projections are totally taken over 360° resulting in a MGD of 40.67 mGy for the whole scan. Based on the knowledge described above, the images are processed with patchwise phase retrieval and two times binned so that an effective pixel size of 139.6 µm is obtained. The images shown in Fig. 4.11 are reconstructed with FBP. The attenuation-contrast images are presented in the left column (A, C)

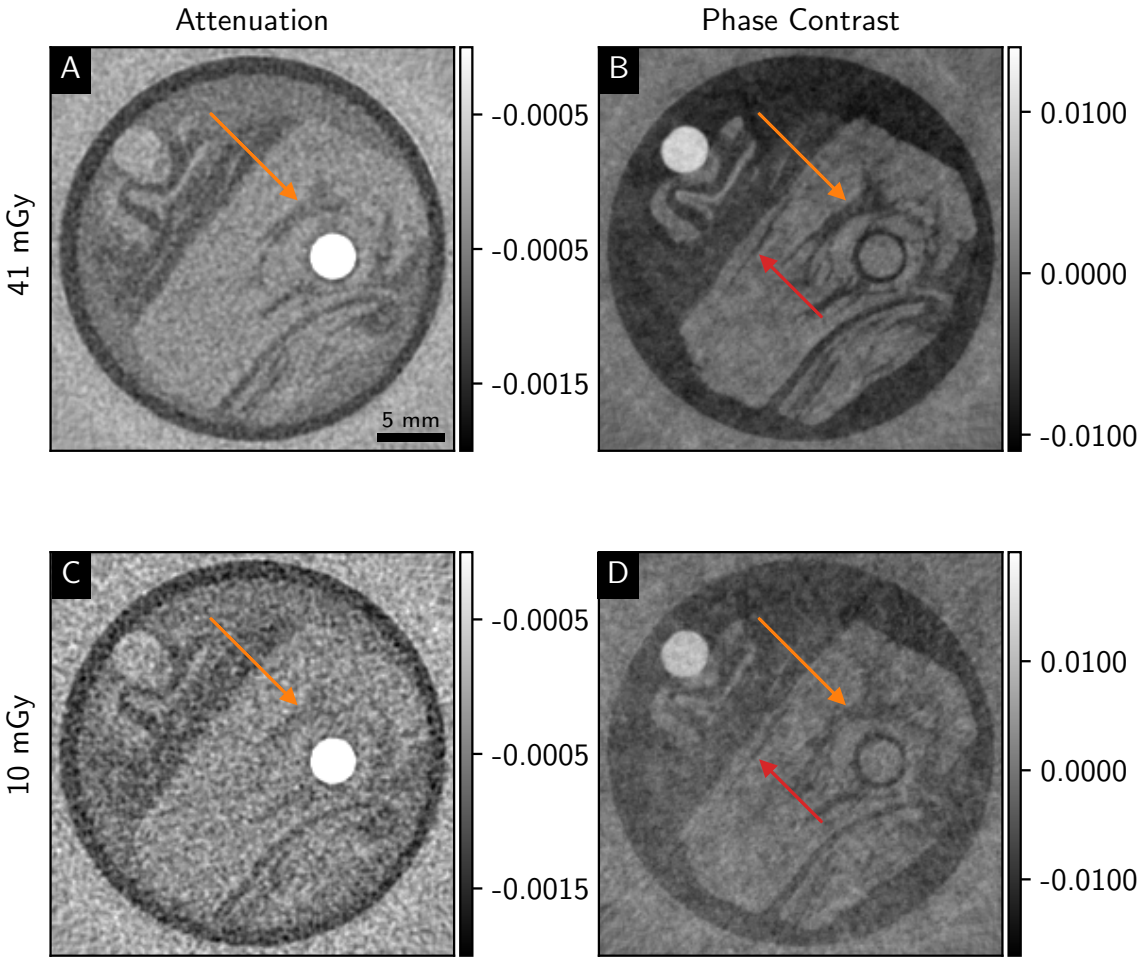

Figure 4.11: Low-dose grating-based phase-contrast BCT with a breast phantom. (A, C) Attenuation-contrast and (B, D) phase-contrast FBP measured with a MGD of 40.68 mGy (A, B) and 10.17 mGy (C, D), respectively. The images are scaled for maximum detail visibility. The reconstructions reveal an enhanced contrast in the phase-contrast image compared to the attenuation-based image. More smaller structures can be identified in (B) and (D) indicated by the red arrows.

and the phase-contrast images in the right column (B, D). Here, a distinction is made between the reconstructions with a higher dose of 40.68 mGy in the first row (A, B) and the low-dose images (C, D) with a MGD of 10.17 mGy in the second row. For the latter, only every fourth angle (163 angles totally) is used for reconstruction. The reconstructions reveal an enhanced contrast in the phase-contrast images compared to the attenuation images for both presented dose regimes. It becomes visible that one benefits from the phase-contrast information especially in the low-dose image (D) as

indicated by the orange arrow. While the small structure is still detectable in the higher dose attenuation image in (A), it is hard to recognize it in the low-dose image in (C) and could also be just noise. However, in the low-dose phase-contrast image in (D), it is possible to distinguish the adipose from the muscle tissue, so that this structure is still well perceptible. Furthermore, the thin structure indicated by the red arrow in the phase-contrast images is visually discernible despite the dose reduction, whereas it is not visible in either the higher or the low-dose attenuation-contrast images. With a MGD of 10.17 mGy, the achieved dose is only by a factor of two higher than the MGD of the commercially used BCT device in the clinics [ABCT, 2020]. For phase-contrast imaging, a higher dose can be justified by the further information obtained through the additional imaging signals. It has to be noted, that the focus in this work was rather on the evaluation of the phase-contrast images and pushing this towards a low-dose regime. The dark-field image was neglected in this work and not presented here, but would also provide further information especially regarding the detection and classification of microcalcifications [Wang, 2014; Scherer, 2016] as well as the discrimination of benign and malignant cysts [Grandl, 2022]. All in all, these results show that grating-based phase-contrast BCT is feasible to be conducted with a low MGD at a quasi-monochromatic X-ray source, while the image quality is adequate for this dose regime and one additionally benefits from the phase-contrast information.

4.5.4 Breast Computed Tomography of a Freshly Dissected Fibroadenoma

The radiologists from the Red Cross Hospital provided us with a freshly dissected fibroadenoma for a more realistic investigation of grating-based phase-contrast BCT. The sample is described in Sec. 4.3.2. Several fibroadenomas are measured within this study, but only one result is exemplary depicted here. In daily clinical routine, it is challenging to diagnose fibroadenoma or more generally to differentiate between benign and malignant lesions. Most of these patients present with palpable findings. The clinical images of the fibroadenoma are shown in Fig. 4.12. In the mammographic image of the whole breast (A), a 3.6 cm large lesion is detected in the upper left marked by a blue circle. It is clearly discernible that there is a lesion, but with this imaging method, it is not possible to discriminate whether it is a benign fibroadenoma or a malignant carcinoma. Although a dark, black region is visible in the additional US examination in (B), a punch biopsy is required to make a final diagnosis. Only the final histopathological analysis confirms a benign fibroadenoma shown in (C) and (D). The fibroadenoma was measured at the MuCLS at an X-ray energy of 35 keV with 400 projections over 360° with 5 steps per angle. To cover the lower and the high MGD range, multiple exposure times of 500 ms and 60 ms are taken resulting in MGDs of 216 mGy and 26 mGy, respectively. The measurements are performed with the Santis

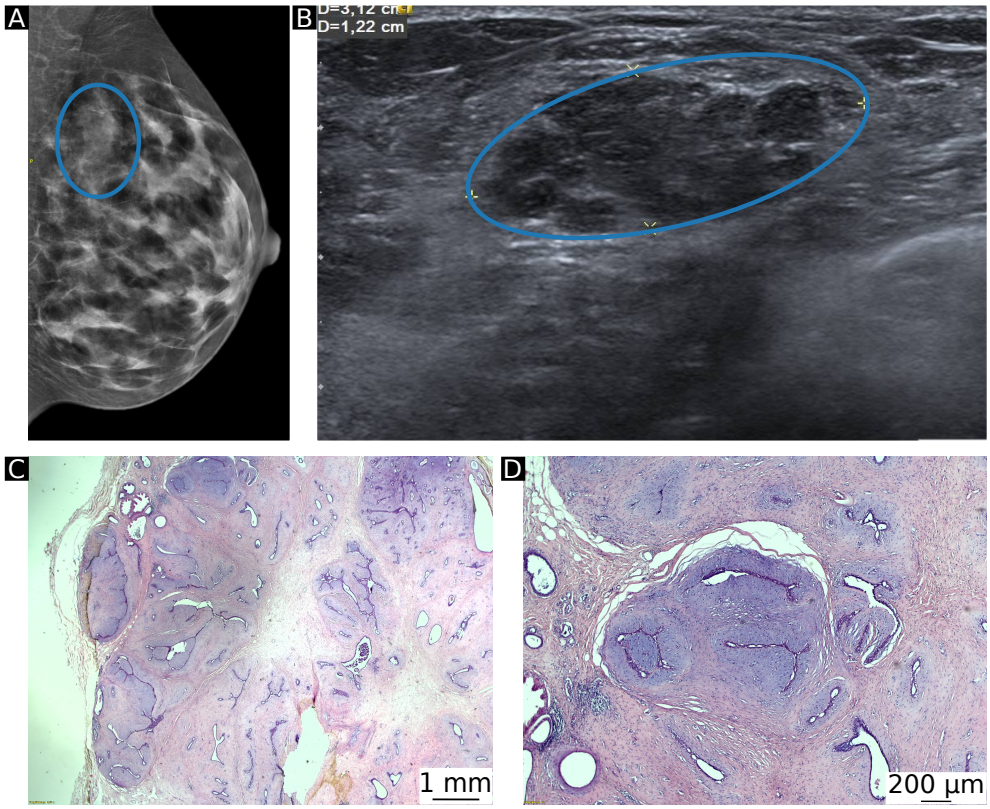

Figure 4.12: Clinical diagnostic of the fibroadenoma. A 3.6 cm large palpable lesion is clinically imaged for better clarification. But (A) the mammographic and also (B) the US image both can not distinguish between a benign fibroadenoma or a malignant carcinoma. After a punch biopsy, a reliable diagnosis can be made during (C, D) the histopathological analysis. The images were kindly provided by the Red Cross Hospital.

GaAs 150 µm with an effective pixel size of 139.6 µm. The data is not additionally binned. The SIR reconstructed results are depicted in Fig. 4.13. Axial slices of the attenuation-contrast images are shown in the left column and phase-contrast images in the right column. The rows are sorted in dose ascending order starting with the measurement of the highest dose. The MGD from the low-dose measurement (60 ms, 26 mGy) has been further decreased by reducing the number of angles used for the reconstructions. In this way, almost a clinically comparable MGD of 9 mGy (E, F) was achieved. The high dose measurement is used as a ground truth to see how many and which structures have probably been lost during the dose reduction process. With the exception of the darker area on the right side corresponding to adipose tissue, there is nearly no contrast within the fibroadenoma in the attenuation-contrast images at any of the three MGDs. In the phase-contrast image, however, finer structures

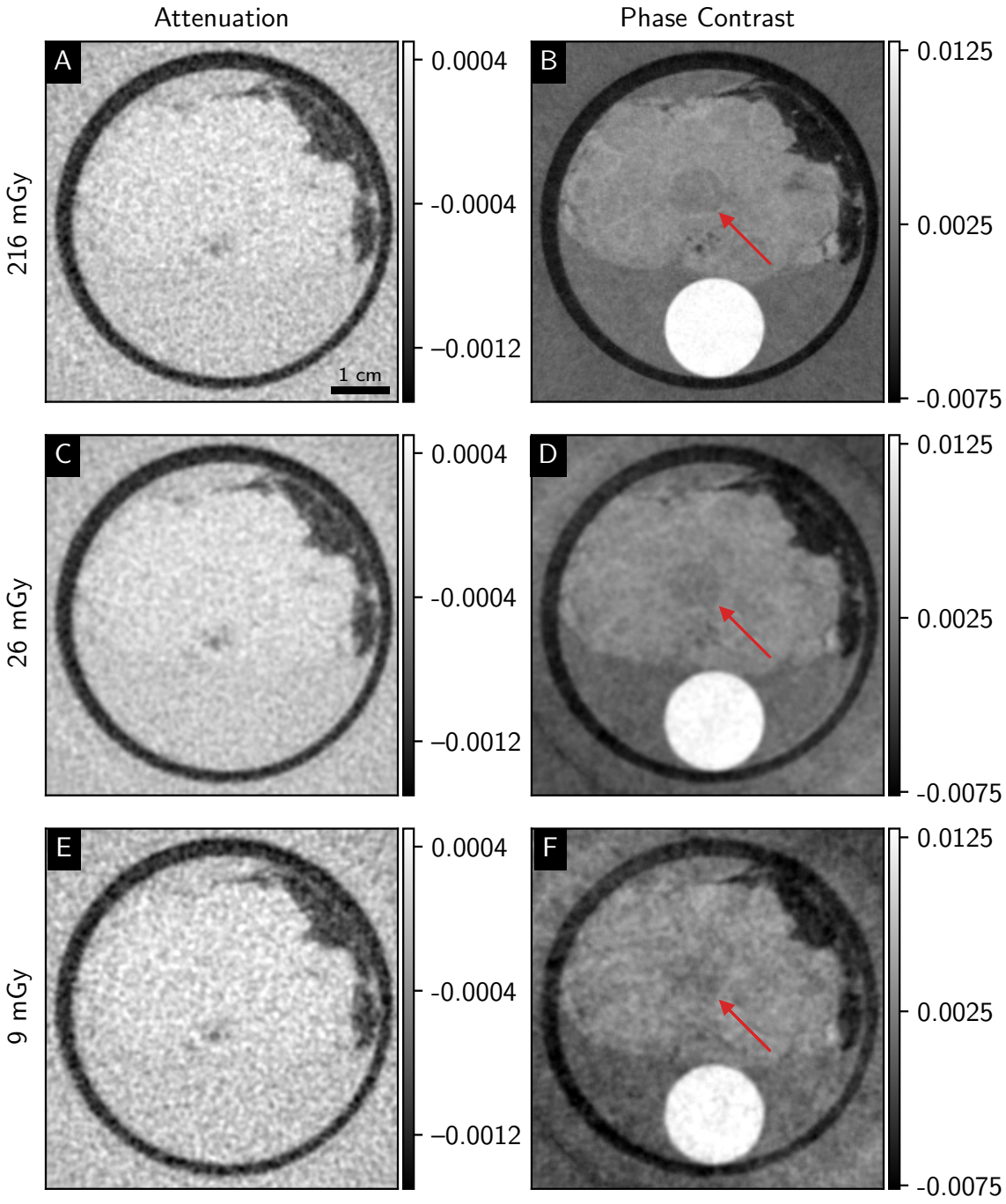

Figure 4.13: Dose-dependent comparison of the fibroadenoma's BCT scan. The reconstructions are conducted with (A, B) 216 mGy, (C, D) 26 mGy and (E, F) 9 mGy. The attenuation-contrast images are depicted in the left column and the phase-contrast images in the right column. The MGD was subsequently decreased by reducing the amount of angles used for reconstruction.

Modality	216 mGy	26 mGy	9 mGy
Attenuation	0.31	0.26	0.13
Phase Contrast	3.18	3.31	1.91

Table 4.4: CNR analysis for the fibroadenoma. The values reveal that there is nearly no contrast for the attenuation-based images compared to the phase-contrast images for the cell-rich region in the center of the fibroadenoma.

called connective tissue strands appear. They get more and more lost in background noise by the dose reduction. The darker area in the center of the fibroadenoma also stands out which could probably be a very cell-rich region. Although this region loses more contrast when the dose is reduced, it is still better detectable in the low-dose phase-contrast image in (F) than in the high-dose attenuation-contrast image in (A). An analysis of the CNR for this region presented in Tab. 4.4 emphasizes this visual impression. While the values for the attenuation-contrast image are below one and thus indicate that this is just noise, the CNR for the phase-contrast images are more than ten times higher. The only striking point here is that the CNR slightly increases from 3.18 to 3.31 for the CTs reconstructed with a MGD of 216 mGy and 26 mGy. This can be explained by the fact that the advantage of patchwise phase retrieval becomes more apparent in the low-dose regime while for such high doses, a saturation occurs. Moreover, these two MGDs result from two measurement with different exposure times which can also influence this result.
A material decomposition into lipid, protein and water (cf. Sec. 3.2) is additionally performed to analyze the internal structure of the sample. This can especially be of interest for the early breast cancer detection since the water content of tumors is higher and its lipid content is lower than in normal tissue [Tromberg, 2005]. Furthermore, also the amount of the protein collagen [Haka, 2005] of abnormal breast tissue is increased compared to normal breast tissue. Consequently, this approach could serve as new supporting analysis tool for a more reliable breast cancer detection. For effective energy calibration of the polychromatic X-ray spectrum, a PMMA rod is added to the sample. The results of this decomposition are presented in Fig. 4.14. The MGD of these images is 26 mGy. The decomposed images are extracted from the reconstructed attenuation- and phase-contrast images in Fig. 4.13 (C) and (D). The electron density map shown in Fig. 4.14 (D) is required for the material decomposition. The unit of the colorbar is electrons per nm^3. The mean value of the electron density of the PMMA rod is $387.00 \pm 3.46\,e/nm^3$. Since this is consistent with the theoretical value ($386.4\,e/nm^3$) of PMMA, a quantitative analysis is ensured. It is clearly visible that the discrimination of the three different materials generally works. The surrounding structure of the fibroadenoma is adipose tissue (A). The fibroadenoma itself is mainly

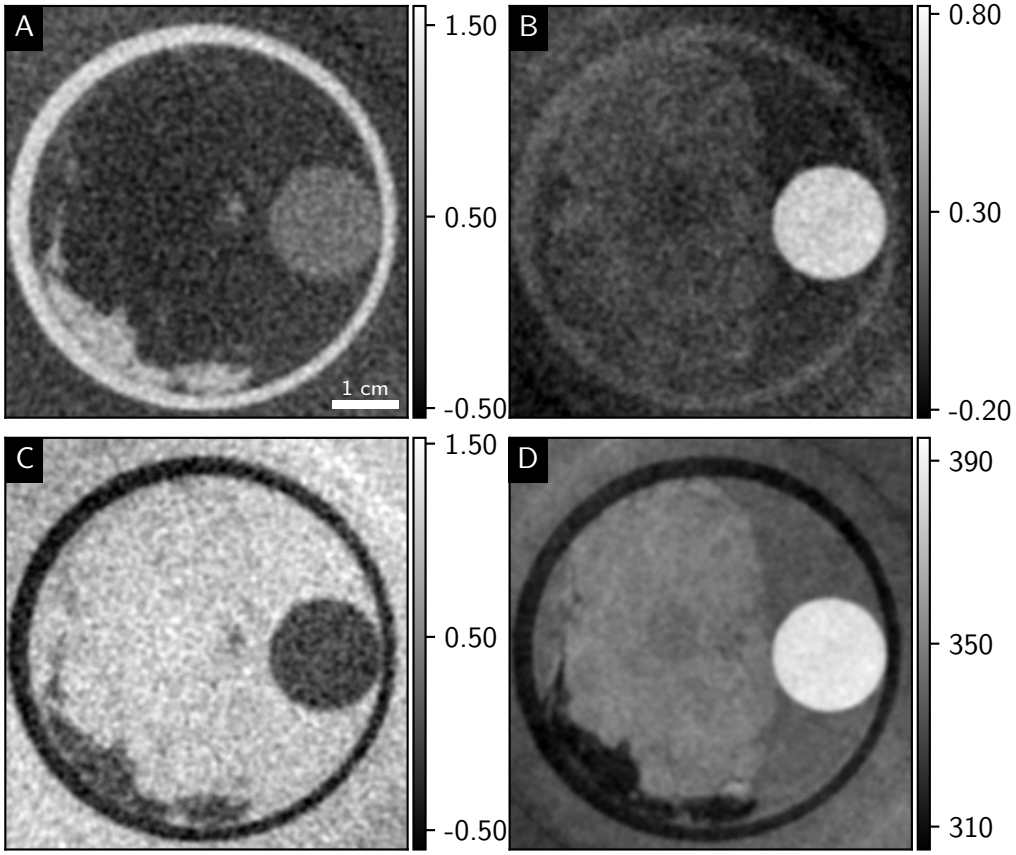

Figure 4.14: Material decomposition into lipid, protein and water of a fibroadenoma. The (A) lipid image shows that the surrounding structure is adipose tissue whereas the fibroadenoma itself is mainly composed of (B) protein and (C) water. (D) The electron density map is given in the unit electrons per nm^3. These images are obtained with a MGD of 26 mGy.

composed of protein (B) and formalin where the sample was stored in so that the sample is consequently soaked with this liquid and thus appears in the water image in (C). Although this material decomposition generally works, it is difficult to lower the MGD further, as noise would then predominate.

4.5.5 Off-axis Computed Tomography of a Breast Phantom

The samples presented in the previous sections are limited to a maximal diameter of 2.5 cm. For clinical imaging, the maximal sample size has to be extended so that larger samples (e.g. freshly dissected mastectomy specimens) can be measured. Since the

FOV is limited by several factors such as the size of the gratings, the detector and the focal spot, a so-called off-axis BCT is conducted to artificially enlarge the FOV. Therefore, the technique proposed by Wang et al. has been used [Wang, 2002]. A displacement of the detector by maximum 50 % or of the sample is required such that the FOV can arbitrarily be adjusted depending on the sample size. For the reconstruction, a data weighting scheme is applied for the redundant region in the center of the measured sample and can be used in combination with FBP. For more information about the weighting function see [Wang, 2002]. For this measurement, a new breast-like phantom is created which resembles the sample in Fig. 4.3 (A). The only difference is the size with 7 cm in diameter instead. The measurement is conducted with the XC-Thor photon-counting detector with an X-ray energy of 35 keV at the MuCLS. To cover a full range from low to high MGDs, 14 frames with 100 ms each are recorded for every of the five stepping position and all of the 1339 angles. The MGD for the full BCT with one frame and all angles used for reconstruction is 149 mGy. The raw data was two times binned yielding to a clinically relevant effective pixel size of 192 µm and reconstructed with FBP. The number of angles used for the reconstructions is reduced to 226 to lower the MGD to 25 mGy. The results of the off-axis BCT are depicted in Fig. 4.15 showing the attenuation- (left column) and the phase-contrast (right column) images. A comparison between normal (A, B), 4N- (C, D) and 8N- (E, F) patchwise processing is additionally provided. Visual comparison of the images shows that the background noise is significantly reduced in the 8N-patchwise processing results, while smaller sample features are still preserved. The image evaluation parameters including the CNR, the background noise σ_{BG} and the k-value are listed in Tab. 4.5. They underline the aforementioned observations: The background noise σ_{bg} is halved for both imaging modalities which consequently results in higher CNR values. Although the k-vlaue slightly decreases from normal to 8N-patchwise processing, structures visually do not get lost in the presented images. Nevertheless, the balance between the contrast and the sharpness or resolution of the images is still acceptable for clinical diagnostic imaging. Although streaking artifacts appear from undersampling despite pixel binning, these results are quite promising for future work on this topic.

4.6 Discussion and Outlook

Besides the successful achievements regarding the attenuation-based BCT with 4.25 mGy in Sec. 4.5.2 and the almost clinically dose-compatible grating-based phase-contrast results in Sec. 4.5.3 both conducted with a small breast phantom, some aspects of the experiments are going to be discussed in the following. This should help to develop future direction of BCT research, in particular its translation to larger specimens.
A freshly dissected fibroadenoma was measured in a dose-compatible range of 9 mGy

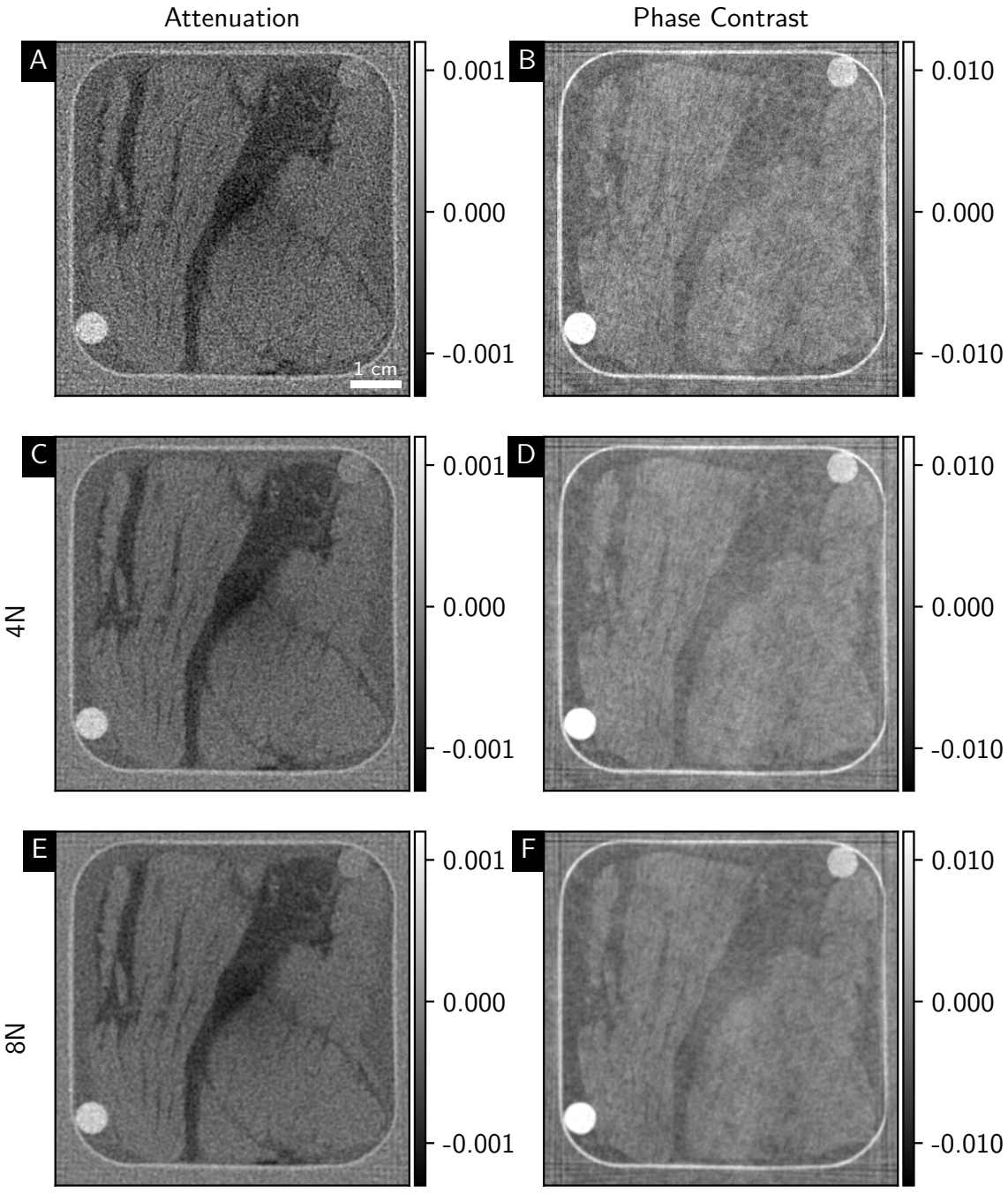

Figure 4.15: Results of the off-axis BCT measurement. Different processing approaches are used for the reconstructions and are finally compared for a MGD of 25 mGy. It is clearly visible that the noise is reduced from conventional to 8N-patchwise processing while the resolution slightly decreases.

	0N	4N	8N
	Attenuation		
CNR	4.75	9.63	12.87
σ_{BG}	$2.0 \cdot 10^{-4}$	$1.0 \cdot 10^{-4}$	$0.8 \cdot 10^{-4}$
k-value	0.39 ± 0.04	0.30 ± 0.02	0.25 ± 0.01
	Phase Contrast		
CNR	9.65	18.06	21.34
σ_{BG}	$1.6 \cdot 10^{-3}$	$0.9 \cdot 10^{-3}$	$0.7 \cdot 10^{-3}$
k-value	0.28 ± 0.03	0.23 ± 0.01	0.20 ± 0.007

Table 4.5: Image evaluation parameters for the off-axis BCT. They include the CNR, the background noise σ_{BG} and the k-value. It becomes visible that the CNR increases while the k-value slightly decreases with patchwise phase retrieval.

applying 8N-patchwise phase retrieval, angle reduction and SIR with the recommended detector, the Santis GaAs 150 µm (cf. Sec. 4.5.1). The clinical examination of this sample including mammography, US and a punch biopsy underlines that the demand for a more reliable imaging approach for early breast cancer detection is very high. Although the results appear very encouraging, some issues remain. The main problem of this specific sample is its intrinsic low soft tissue contrast. Therefore, smaller fiber structures can no longer be distinguished in the low-dose images. However, the soft tissue contrast for a full freshly dissected mastectomy specimen would be higher. Daniel Berthe investigated the feasibility of a fast off-axis BCT scan at a polychromatic X-ray source. In this study, the specimen exhibited an inherently higher soft tissue contrast already in the attenuation-based image [Berthe, 2021]. The contrast enhancement would also show up in the phase information.
The material decomposition into three basis materials generally works for a MGD of 26 mGy. Further reduction of the dose is not performed since the noise would then dominate the resulting images. For this decomposition, the noise level in the low-dose images first would have to be reduced even further, for example by advanced reconstruction methods which will be discussed below. In prospective studies, a change of the basis materials to lipid, fibrous tissue and water would be interesting in order to obtain more meaningful information about the sample's composition. Another problem is that the breast phantom (piece of pork neck) was embedded in formalin for some time. This additionally reduces the contrast as the tissue is soaked with formalin. In

consequence, the long-term aim would be to conduct fast CT scans with a continuous rotation since the measurement of a fresh, non-formalin fixated sample become possible in this case. This in turn would improve the soft tissue contrast.
In addition, an off-axis BCT scan was conducted. Although the MGD for such a large sample could be decreased down to 25 mGy and despite the fact that a higher MGD could generally be justified by the additional information obtained through trimodal imaging, further MGD reduction is necessary to provide the same diagnostic information at a clinically accepted dose range. Therefore, on the one hand, recent work in this field investigates the impact of self-supervised deep learning networks on the image quality with a focus on a potential MGD reduction for polychromatic grating-based phase-contrast BCT [Wirtensohn, 2022]. This study shows that the Noise2Inverse concept denoises the data better allowing an increase of spatial resolution while maintaining the CNR. On the other hand, more advanced reconstruction techniques have to be applied such as the sliding window approach or intensity-based statistical iterative reconstruction (IBSIR) [Zanette, 2012; vTeuffenbach, 2017; Xu, 2022]. The sliding window approach is phase stepping-based and very effective since it requires just one single image per angular position ω. The standard phase stepping at every projection angle can thus be omitted. Three types of the sliding window approach exist: The interlaced phase stepping, the sliding window zigzag and the sliding window interlaced. A comparison of them is presented in Fig. 4.16. In (A), the conventional phase stepping approach is shown in which a full stepping curve is recorded at a fixed angular position ω. For interlaced phase stepping, however, the angular stepping position is slightly different for one stepping scan. As a consequence, this enables the combination of phase stepping with continuous rotation of the sample during the tomography scan. The third technique is called sliding window zigzag and is mainly characterized by recording the images during for- and backward movement of the grating which saves time while acquiring the same information. The interferogram at the inflection point of the grating movement is used twice (orange dot). The sliding window interlaced technique is finally a combination of the both aforementioned approaches. Again both, the angular as well as the grating positions, are continuously moved. Here, only one interferogram is used for only one stepping curve while the others are reused several times. The three imaging modalities are extracted for each method using Fourier analysis, like in the conventional stepping approach. As described by Zanette et al., the number of required interferograms and the applied dose can thus be reduced subsequently [Zanette, 2012]. Especially when combined with a continuous rotation tomography scan, this approach would be promising to improve low-dose grating-based phase-contrast BCT of larger samples further. IBSIR, however, is an iterative reconstruction approach that directly generates the three imaging modalities based on the measured interferograms [vTeuffenbach, 2017]. The intermediate image processing step is omitted since it is included into a SIR-based forward model. In

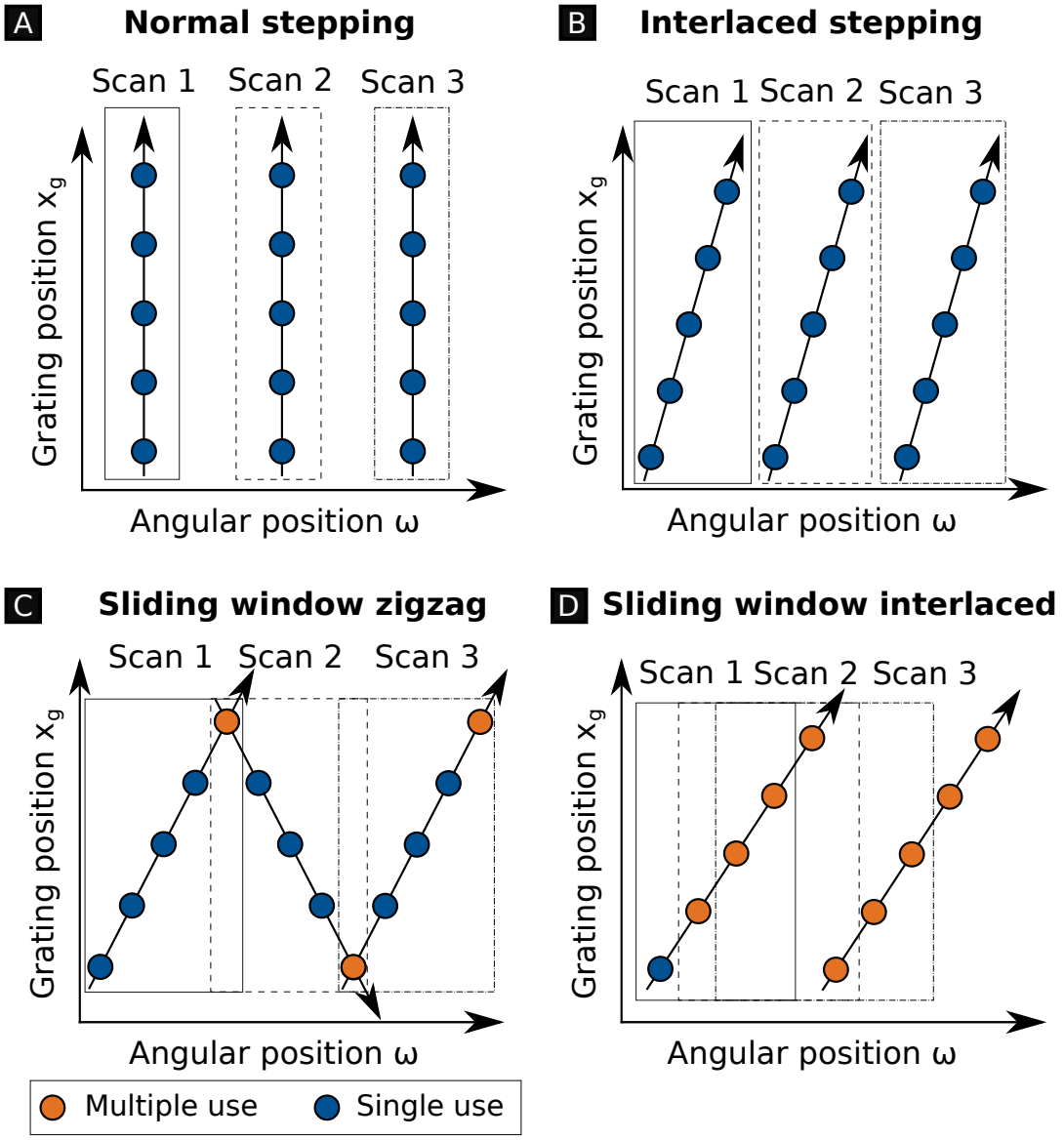

Figure 4.16: Comparison of various stepping approaches. Every dot denotes a detected interferogram. The blue ones are utilized for only one stepping curve while the orange ones are used multiple times. (A) The standard phase stepping procedure where all steps are taken at the same angular position ω. In (B), the so-called interlaced stepping is presented. There, the angular sample position during one stepping curve is slightly different. (C) For the sliding window zigzag technique, projections are taken in both for- and backward movement direction and one interferogram is again utilized in the subsequent scan to save scan time. (D) The sliding window interlaced approach is a combination of the other approaches. Both the angular as well as the grating positions are continuously moved while every interferogram is used several times except the first one [Zanette, 2012].

contrast to sliding window, IBSIR does not require any processed projections since the volume is reconstructed directly from the raw data. Phase retrieval of the projections and interpolations such as fitting the stepping curve is avoided. As a consequence, the reconstruction is less prone to artifacts and thus enhances image quality. IBSIR can be applied to normal phase stepping data, but is especially beneficial for single-shot CT measurements that potentially enable low-dose scans. Another recently published approach is intensity-based iterative reconstruction with helical scanning for grating interferometry [Xu, 2022]. Due to helical scanning, phase stepping can be avoided, yet a simultaneous reconstruction of the image signals is possible. This strategy is of special interest for grating interferometry for BCT as presented by [Xu, 2022].
To summarize, the already promising results presented in this chapter can be further extended and improved with samples intrinsically providing higher soft tissue contrast in combination with more advanced reconstruction techniques.

Spectral Differential Phase-Contrast Imaging 5

In this chapter, numerical simulations of SDPC are presented and finally evaluated for breast imaging as a promising application. This is conducted for a quasi-mono- and a polychromatic X-ray source for mammography as well as quasi-monochromatically for BCT. For every material decomposition task, optimal imaging parameters are previously determined. While the BCT simulations are performed with just one phantom, the mammography simulations are performed with different phantoms, sequentially building on each other. Please note that parts of the results in this chapter have been submitted by Heck et al. [Heck, 2022] and were produced in collaboration with a master's thesis [Klaar, 2021].

5.1 Motivation

Since suspicious abnormalities like cysts or cancerous lesions possibly not being detected during mammography, but sometimes observed during palpation, further follow-up examinations are often required in a clinical environment. One modern clinical check-up procedure to verify uncertain mammography results is CESM [ElSaid, 2014]. An iodinated contrast agent is intravenously injected and a recombined iodine image is calculated using K-edge subtraction imaging. Two radiographs – one below and one above the K-edge of iodine – have to be acquired leading to a higher applied MGD of as in conventional mammography (3.0 mGy vs. 2.1 mGy) [James, 2017]. This approach in consequence increases the detection of lesions and has a higher sensitivity than standard mammography [Fallenberg, 2014; ElSaid, 2014].
Dual-energy-based CESM, however, does not exploit the full potential of spectral imaging since it only uses K-edge subtraction imaging resulting in one so-called "recombined" iodine image. In addition, CESM can - among others - potentially suffer from motion artifacts [Yagil, 2016]. The evolving technique of energy-resolving single-photon-counting detectors, which separate X-ray spectra in only one exposure, can be utilized to perform multi-energy imaging. In contrast to the clinically used CESM approach, the images are temporally and spatially perfectly registered and it is possible to retrieve more information from the acquired spectral data in terms of several basis

material images. This circumvents the acquisition of multiple X-ray images and thus motion artifacts. Several clinical studies have already investigated the advantages of conventional, attenuation-based spectral imaging for medical use [Ehn, 2017; Sellerer, 2017; Mechlem, 2018b; Mechlem, 2018a; Heck, 2019]. Despite the present benefits of this technology and the approach of a basis material decomposition, major problems such as a strong amplification of noise, which leads to a reduction of the CNR, remain [Alvarez, 1976; Kelcz, 1979]. These problems have to be solved for e.g. a reliable detection of microcalcifications in case of breast imaging.
Another actively researched technique providing better soft tissue contrast is grating-based phase-contrast imaging, using the phase information of an X-ray wavefront [Pfeiffer, 2006]. Unlike other phase-contrast techniques that are limited to synchrotron radiation (e.g. propagation-based phase contrast), grating interferometry is clinically more relevant due to its possible implementation with polychromatic, incoherent X-ray sources. Improvements in breast imaging especially regarding the soft tissue contrast using grating-based phase contrast have already been successfully demonstrated [Stampanoni, 2011; Stampanoni, 2013; Scherer, 2014; Auweter, 2014; Hauser, 2014; Scherer, 2015; Grandl, 2015; Koehler, 2015; Eggl, 2018; Arboleda, 2019; Heck, 2020]. In addition to the attenuation and phase information, the so-called dark-field signal introduced by ultra-small-angle scattering is additionally retrieved, providing information about the object's microstructure. This is of particular interest for breast imaging since it facilitates the detection and characterization of microcalcifications [Wang, 2014; Scherer, 2016]. However, grating-based phase-contrast imaging suffers from artifacts such as beam-hardening caused by the polychromatic X-ray source [Chabior, 2011; Yashiro, 2015] and phase wrapping [Haas, 2011].
In order to benefit equally from the strengths of both aforementioned imaging techniques and to overcome their respective limitations, the advantages of combining both modalities in SDPC for its application in standard mammography, CESM and BCT are investigated based on the approach proposed by Mechlem et al. [Mechlem, 2019a; Mechlem, 2019b; Mechlem, 2020]. The PED can be obtained by both techniques and is therefore the connecting quantity between spectral and phase-contrast imaging. By using both the spectral and the phase information simultaneously, quantitative and material-selective basis material images with a reduced noise level can be generated [Mechlem, 2019b; Mechlem, 2020]. Moreover, a third dark-field basis material is obtained which may also be enhanced, but is not examined in detail here.
In the following, numerical simulations with previously determined optimal imaging parameters are conducted using the approach from Mechlem et al. to evaluate the potential of SDPC for mammography and BCT with and without the usage of iodinated contrast agent [Mechlem, 2020]. First, quasi-monochromatic dual-energy-based simulations are performed for the conventional attenuation-based as well as for the SDPC material decomposition to obtain a ground truth of the potential benefits. Fol-

lowing a realistic X-ray source such as the MuCLS, the simulations are performed quasi-monochromatically where the two spectra are completely separated and a spectrum overlap is mostly avoided. Based on this, simulations with a polychromatic X-ray source are also carried out employing a photon-counting detector for the spectral separation to simulate a clinically feasible case in a second step. For both cases, an analysis of the CNR and the PED variance is used to compare the two material decomposition approaches and to finally assess the benefits of this novel imaging approach.

5.2 Setup for the Numerical Simulations

The setups for the mono- and polychromatic simulations are separately introduced in the two subsections presented below. Some characteristics are the same for both cases and are therefore described in advance: For both, the Talbot-Lau interferometer is arranged differently for each optimal design energy resulting in changing grating properties. The source and the analyzer gratings are made of gold and the phase grating is made of nickel. All grating periods and the grating bar height of the phase grating G_1 are optimized to ensure that the design energy of the interferometer ideally matches the source energy. For both cases, a photon-counting detector with a sensor made of CdTe and a thickness of 2.0 mm is used. Based on clinical settings, the physical pixel size is 75 µm for mammography and 150 µm for BCT imaging. The realistic detector energy response function (considering charge sharing, K-escape photons and fluorescence peaks) and the quantum efficiency for the effective spectra for each detector pixel are considered based on the assumptions by [Schlomka, 2008].

Quasi-monochromatic X-ray source

The setup where a quasi-monochromatic X-ray source is used is shown in Fig. 5.1 (A) and mainly inspired by and based on the experimental setup of the second hutch of the MuCLS [Günther, 2020]. The inter-grating distance with 24.795 cm and the height of the analyzer grating G_2 with 90 µm remain the same for all decomposition tasks. The simulation parameters such as the source energies and also the grating specifications are listed in Tab. 5.4 for all decomposition tasks performed for mammography and in Tab. 5.6 for BCT. Two different interferometers depending on the respective low- and high-energy spectrum are used (cf. Tab. 5.4 and Tab. 5.6). The sample is placed in front of the two gratings at a fixed position 1493.3 cm away from the interaction point where quasi-monochromatic X-ray photons are generated. A dual-energy measurement is simulated so that spectral separation is ensured and the spectral separation capability of a photon-counting detector is not used. Only the lower energy THL is adjusted to

10 keV to cut out noise. Due to a small magnification, the effective pixel size results in 74 µm and 148 µm for mammography and BCT, respectively. The X-ray source energy can thus take any value in the relevant energy range of 15 to 35 keV during the parameter optimization process. Using the following function

$$f(E) = A \cdot \frac{\zeta}{2} \cdot \exp\left(\frac{\zeta}{2} \cdot \left(2\kappa + \zeta\tau^2 - 2E\right)\right) \cdot \operatorname{erfc}\left(\frac{1}{\sqrt{2}\tau} \cdot \left(\kappa \cdot \zeta \cdot \tau^2 - E\right)\right), \tag{5.1}$$

which is derived by the exponentially modified Gaussian distribution with A, ζ, κ and τ as fit parameters, a measured 25 keV spectrum is approximated. Neglecting that the shape of the curve changes for measured data meaning an increasing width for higher energy, the peak energy is just shifted to the desired X-ray energy.

Polychromatic X-ray source

A schematic drawing of the interferometer used for the simulation with a polychromatic X-ray source are shown in Fig. 5.1 (B). In contrast to the quasi-monochromatic case, an additional source grating G_0 is placed right behind the X-ray source to ensure coherence. The inter-grating distances with 120 cm and the height of the analyzer grating G_2 with 200 µm are fixed for every decomposition task. The simulation parameters such as tube voltage, design energy, and energy THLs of the detector and also the grating specifications are listed in Tab. 5.4 and 5.5 for all decomposition tasks conducted for mammography. A tungsten X-ray source operated at different acceleration tube voltages for the various decomposition tasks (cf. Tab. 5.5) is assumed. The sample is positioned between G_1 and G_2. The ability of spectral separation by the detector is used, so two energy THLs are set (cf. Tab. 5.5). The lower THL is always fixed to an X-ray energy of 15 keV. The effective pixel size results in 44 µm for mammography and 88 µm for BCT through the geometrical magnification.

5.3 Simulated Breast Phantoms

For the investigation of SDPC X-ray imaging as a potential method for early breast cancer detection, different simulation phantoms are constructed for projection-based mammography imaging and three-dimensional BCT. They are delineated in detail in the following two sections. In addition, the physical properties such as the linear mass attenuation coefficient and the electron density of the considered materials are described.

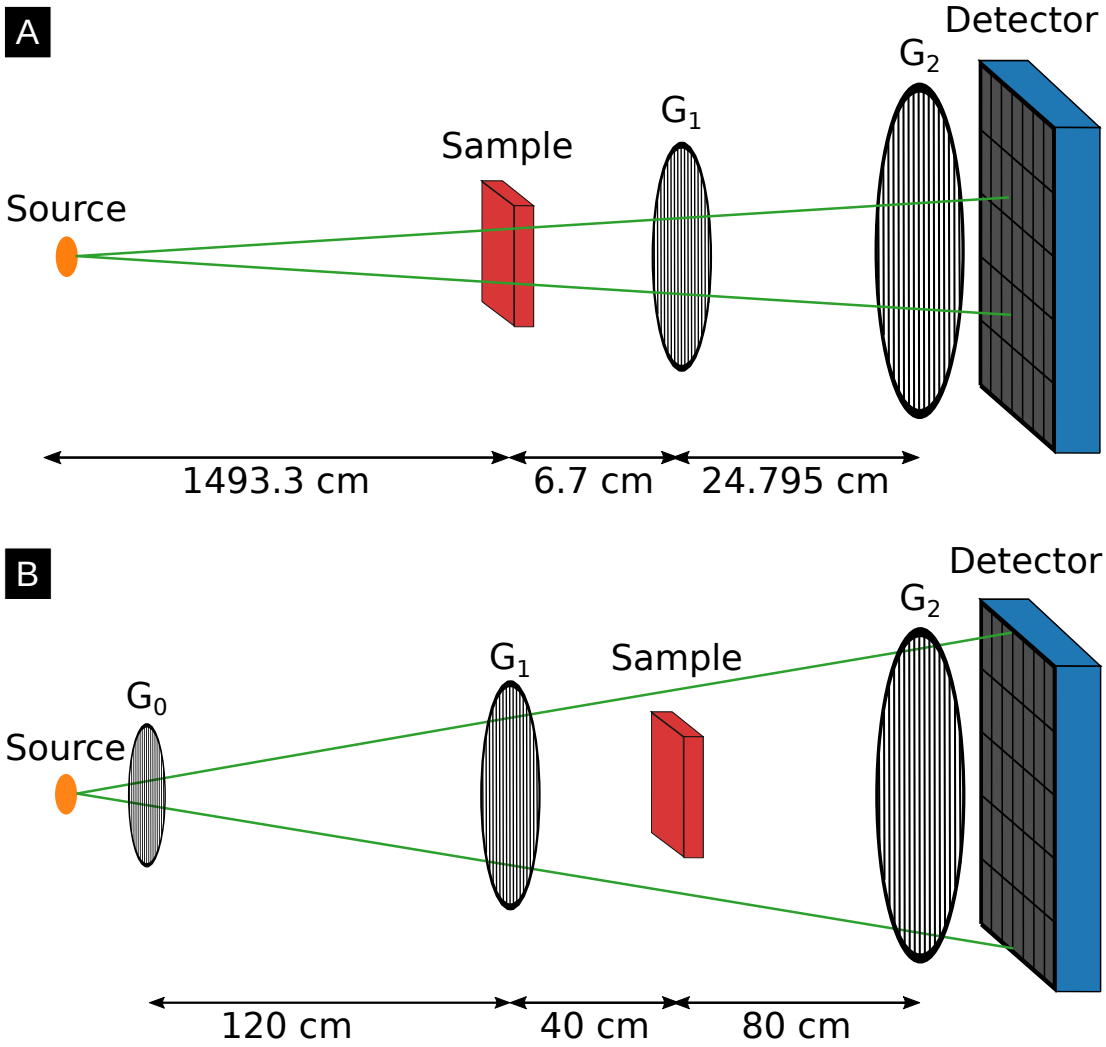

Figure 5.1: Overview of the setup geometry for the numerical SDPC simulations. The two experimental setups using (A) a quasi-monochromatic and (B) a polychromatic X-ray source including a two- or three-grating Talbot-Lau interferometer are respectively presented. Both setups include a reference grating G_1 and an analyzer grating G_2 which is directly mounted in front of the photon-counting detector. In the polychromatic case, an additional source grating G_0 is required. All distances are fixed and only the grating specifications are optimized for the respective decompositions. They are listed in Tab. 5.4 and 5.5 for mammography as well as in Tab. 5.6 for BCT.

5.3.1 Simulated Mammographic Phantom

The phantoms used for the numerical, mammography simulations are mainly inspired and based on the Gammex 156 Mammographic Accreditation Phantom [Gammex,

2015]. In addition to breast tissue as surrounding material, the phantoms contain various structures of interest, such as calcifications, an iodinated contrast agent and tumor masses of different sizes. The calcifications and the tumor masses are spheres and the iohexol structures are rectangular boxes. Different phantoms are created with an increasing number of the aforementioned materials in each case. The first three phantoms in Fig. 5.2 are two-material-based and only consist of breast tissue in the background and tumor masses (A), iohexol structures (B) or calcifications (C). One additional material is inserted in the three-material-based phantoms shown in Fig. 5.3, whereas in Fig. 5.4 all structures are finally embedded. Please note that, the combination of iohexol, calcifications and breast tissue is not included in Fig. 5.3. The thicknesses of the different materials in projection direction are listed in Tab. 5.1. The total thickness of all phantoms is 4.5 cm which is in the range of the mean thickness of a compressed breast in clinical mammography [Helvie, 1994].

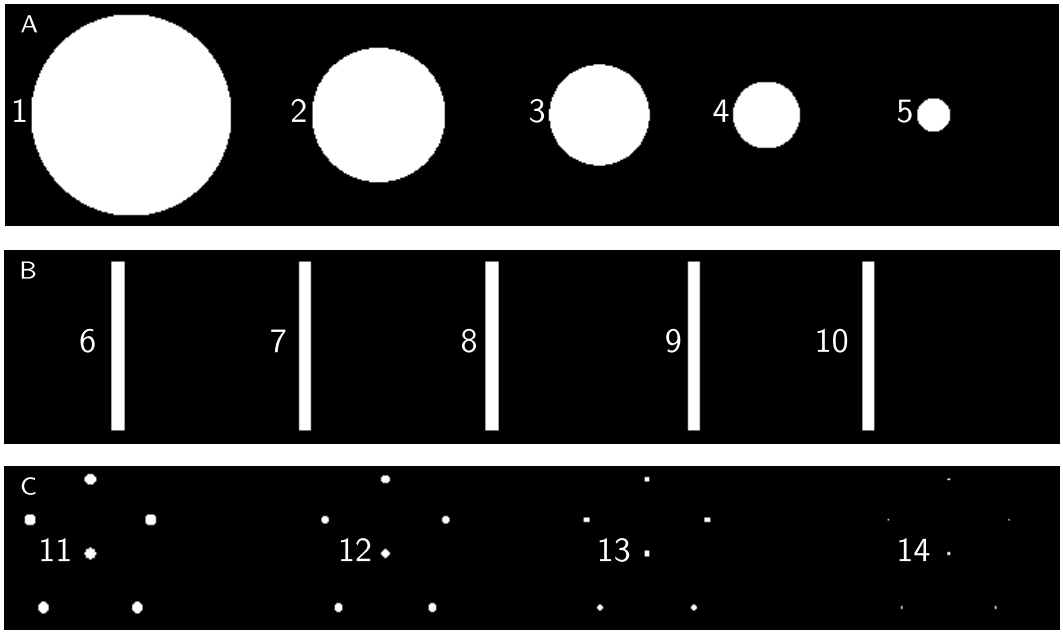

Figure 5.2: Two-material-based mammographic phantoms. These phantoms consist of breast tissue as surrounding material where additionally (A) tumor masses, (B) iohexol structures and (C) calcifications of different sizes are embedded. The total phantom thickness in projection direction is 4.5 cm each.

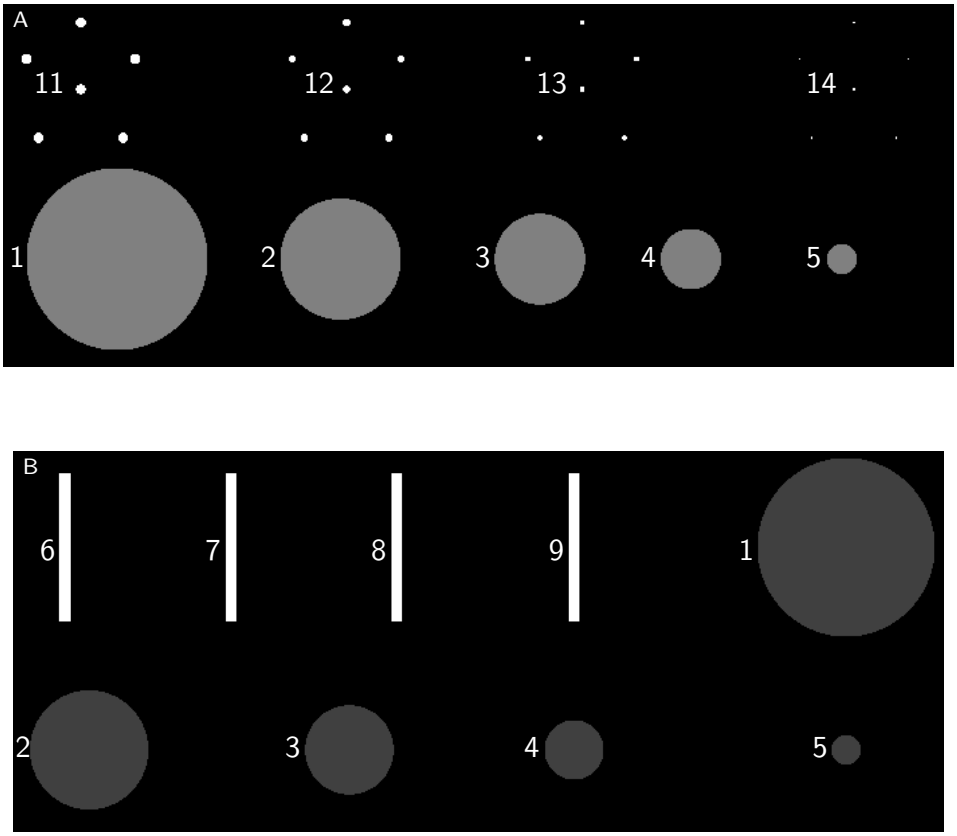

Figure 5.3: Three-material-based mammographic phantoms. Both comprise breast tissue and tumor masses (1-5). In (A), calcifications are additionally inserted (11-14) while in (B), iohexol structures are embedded (6-9). The total phantom thickness in projection direction is 4.5 cm.

Structure	Size 1	Size 2	Size 3	Size 4	Size 5
Tumor (1-5)	14.90	10.00	7.50	4.90	2.40
Iohexol (6-10)	4.00	2.89	2.00	0.89	0.44
Calcium (11-14)	1.11	0.89	0.67	0.44	0.22

Table 5.1: Structural sizes of the mammographic phantoms. Overview of the thicknesses of the individual structures in projection direction embedded in the 4.5 cm thick simulated mammographic phantom. All sizes are given in millimeters.

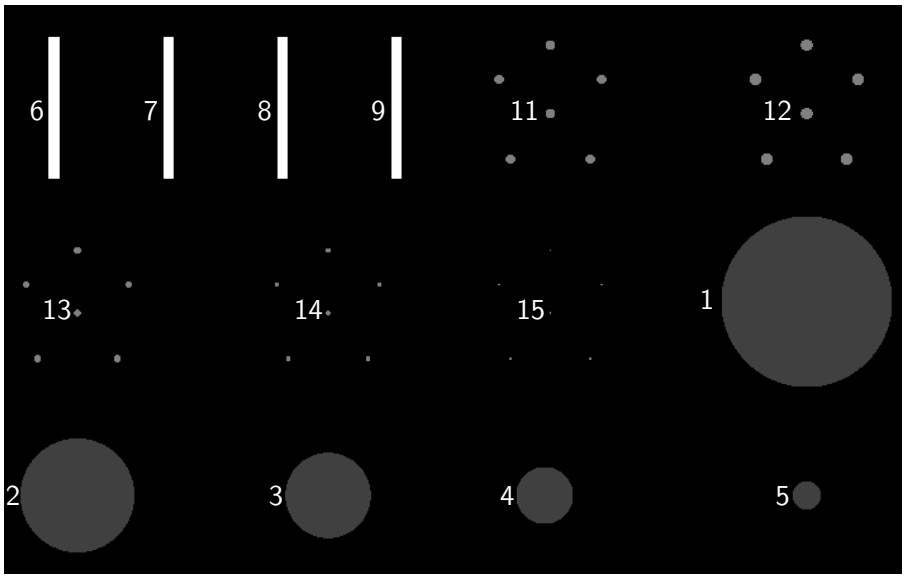

Figure 5.4: Full mammographic phantom. This phantom contains all structures of interest for breast imaging like tumor masses (1-5), iohexol structures (6-9) and calcifications (11-15) with breast tissue as background material. The total phantom thickness is 4.5 cm in projection direction.

5.3.2 Simulated Three-dimensional Breast Phantom

For the BCT simulations, a round-shaped phantom with a diameter of 6 cm and a width of 600 pixels was created. A cluster of microcalcifications (1), six tumor masses (2-7) and five iodine-containing structures (8-10) of different sizes are embedded in breast tissue, which serves as surrounding material. The background material outside of the phantom is air. One exemplary slice of the three-dimensional phantom is presented in Fig. 5.5. The corresponding thicknesses can be taken from Tab. 5.2.

5.3.3 Physical Properties

The calcifications are chosen to be simulated by calcium oxalate ($C_2H_2CaO_5$) as it best mimics microcalcifications *in vivo* [Vedantham, 2013]. The iodinated contrast agent is represented by iohexol because it is the most commonly used clinical contrast agent for CESM [Zanardo, 2019]. The concentration is 6 mg/ml since injecting iohexol in a concentration of 400 mg/ml at a standard dose of 1.5 ml/kg per body weight of the woman, leads to an iohexol concentration of 6 mg/ml in the blood vessels of a patient

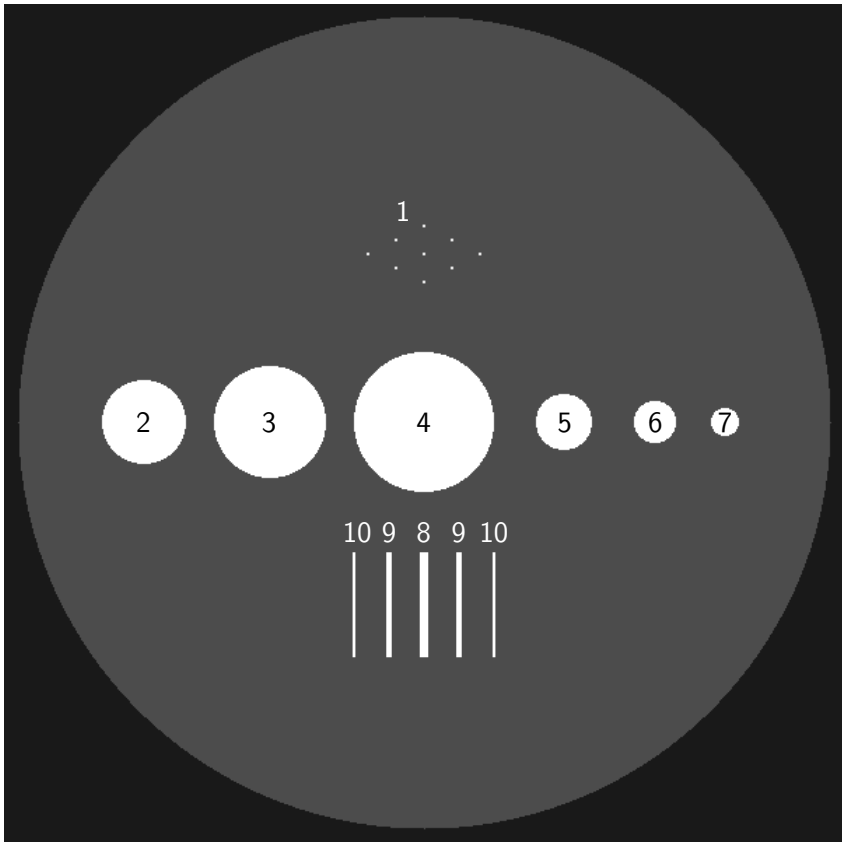

Figure 5.5: Simulated BCT phantom. This phantom includes the structures of interest for BCT like a calcification cluster (1), tumor masses (2-7) and iohexol structures (8-10) embedded in breast tissue. The material outside of the phantom is air. The diameter of the phantom is 6 cm.

Structure	Size 1	Size 2	Size 3	Size 4	Size 5	Size 6
Tumor (2-7)	2.0	3.0	4.0	6.0	10.0	15.0
Iodine (8-10)	0.2	0.4	0.6	-	-	-

Table 5.2: Structural sizes of the simulated BCT phantom. The structures are inserted in a 6 cm thick breast phantom used for the SDPC CT simulations. All sizes are given in centimeter. The diameter of the microcalcifications is 0.6 mm.

with a body weight of 80 kg and a blood volume of 66 ml/kg [Wadsworth, 1954]. The values for the linear attenuation coefficients and the electron densities are taken from various publications [Johns, 1987; Boone, 1996; Schoonjans, 2011; Willner, 2014]. The linear attenuation coefficients of the materials in the clinically relevant energy range of 10-60 keV are plotted in Fig. 5.6. Iohexol in a concentration of 400 mg/ml is additionally plotted since it is later used as a basis material. The corresponding material's electron densities are listed in Tab. 5.3. The electron densities which are not listed in the aforementioned publications are calculated using

$$\rho_e = \rho \cdot N_\mathrm{A} \cdot \frac{\sum_n w_n Z_n}{\sum_n w_n A_n}\,, \tag{5.2}$$

where ρ is the material's density, N_A the Avogadro constant, Z the atomic number and A the atomic mass of element n with the weight fraction w in the respective material.

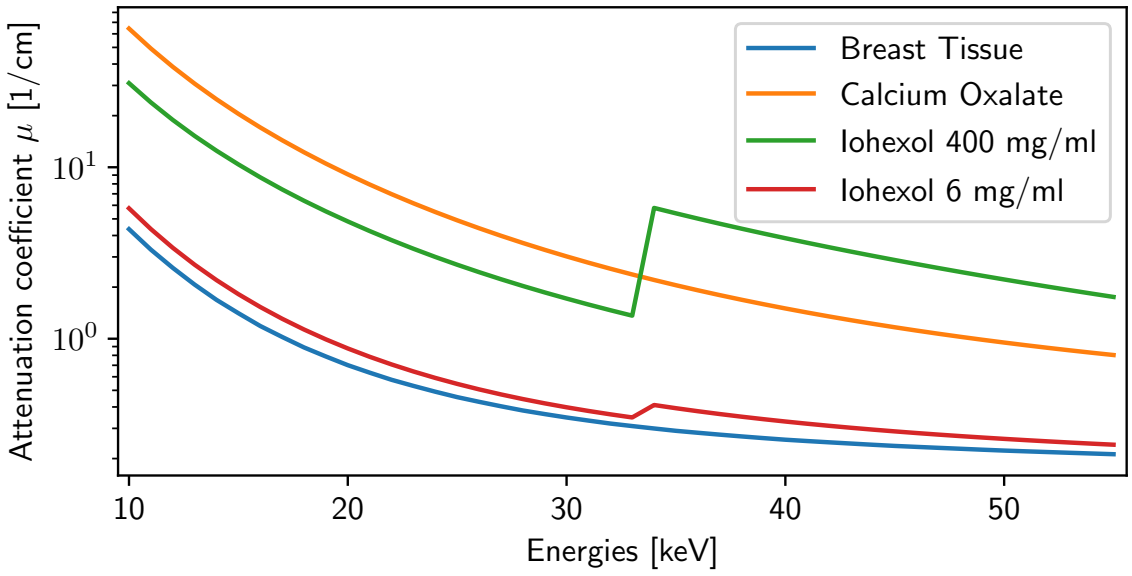

Figure 5.6: Linear attenuation coefficients of the materials used for the simulations. The energy-dependent linear attenuation coefficients for the materials used in the SDPC simulations are plotted. Additionally, the energy-dependent attenuation of iohexol in a concentration of 400 mg/ml is shown as it is later used as basis material.

	Breast Tissue	Tumor Tissue	Calcium Oxalate	Iohexol 400 mg/ml	Iohexol 6 mg/ml
$\rho_e \left[\frac{e}{cm^3}\right]$	$3.39 \cdot 10^{23}$	$3.50 \cdot 10^{23}$	$6.62 \cdot 10^{23}$	$3.38 \cdot 10^{23}$	$3.34 \cdot 10^{23}$

Table 5.3: Volume electron densities used for the simulations. It includes all materials which are embedded in one of the simulated phantoms as well as iohexol in a concentration of 400 mg/ml since it is later used as basis material.

5.4 Estimation of the Optimal Simulation Parameters

In order to achieve the best result of the material decompositions, the determination of the optimal imaging configurations is performed in advance. For each phantom and material decomposition, different basis material combinations and consequently different simulation settings and optimized parameters are determined. The concept is based on the explanations presented in Sec. 3.5.3. The parameters either minimize the PED variance or the basis material line integrals variance for all three imaging methods. In this section, only the parameters that are used for the simulations and that minimize the PED variance based on the CRLB and the noise framework from [Mechlem, 2020] are presented in the following.

5.4.1 Mammography

Corresponding to the given phantoms, the following basis material combinations are used: Breast/tumor tissue, breast tissue/calcium oxalate and breast tissue/iohexol (6 mg/ml)for the two-material-based phantoms as well as tumor tissue/iohexol in a concentration of 6 mg/ml for the three- and multi-material phantom. As mentioned before, the setup parameters are optimized with respect to the lowest PED variance. In the quasi-monochromatic simulations only the source energies are optimized as they correspond to the design energies. For the polychromatic simulations, both the tube voltages and design energies are varied in the parameter optimization. Thus, the specifications of the grating interferometer differ for both X-ray sources and all material combinations to ideally match the respective design energies. The optimal parameters and settings for the numerical simulation are listed in Tab. 5.4 and 5.5 for both cases and all basis material combinations. The corresponding effective X-ray source (A) and the energy-dependent visibility (B) spectra are presented in Fig. 5.7 and 5.8 for the quasi-monochromatic and the polychromatic case, respectively, and for all the performed decomposition tasks. The peak of the visibility spectrum is at the corresponding design energy. For the quasi-monochromatic dual-energy simulation, two X-ray spectra are

Breast and tumor tissue				
	Energy [keV]		G_1	G_2
Low	16.00	Height [µm]	2.81	90.00
		Period [µm]	6.15	6.25
High	28.00	Height [µm]	4.92	90.00
		Period [µm]	4.65	4.72
Breast tissue and calcium oxalate				
	Energy [keV]		G_1	G_2
Low	22.00	Height [µm]	3.86	90.00
		Period [µm]	5.24	5.33
High	35.00	Height [µm]	6.15	90.00
		Period [µm]	4.16	4.23
Breast/tumor tissue and iohexol (6 mg/ml)				
	Energy [keV]		G_1	G_2
Low	30.00	Height [µm]	5.27	90.00
		Period [µm]	4.49	4.56
High	35.00	Height [µm]	6.15	90.00
		Period [µm]	4.16	4.23

Table 5.4: Optimal setup parameters for the numerical mammography simulation for a quasi-monochromatic X-ray source. It contains the source energies which equal the design energies as well as the grating properties like height and period for the different material decompositions.

plotted. In contrast, the effective spectra of the low and the high energy bin are depicted together with the adjusted energy THLs (indicated by the vertical grey lines) for the polychromatic simulation case. The lower THL is always set to a fixed energy of 10 keV and 15 keV for the mono- and the polychromatic case, respectively, to cut out electronic noise. For the decomposition into breast or tumor tissue and iohexol (6 mg/ml), the only striking characteristic is that the optimal energies with 30 keV and

Breast and tumor tissue/calcium oxalate		
Tube voltage [kVp]	40.00	
Design energy [keV]	32.00	
THL low [keV]	15.00	
THL high [keV]	31.00	
	G_0/G_2	G_1
Height [µm]	200.00	5.97
Period [µm]	13.64	6.82
Breast and iohexol (6 mg/ml)		
Tube voltage [kVp]	50.00	
Design energy [keV]	34.00	
THL low [keV]	15.00	
THL high [keV]	33.00	
Height [µm]	200.00	5.62
Period [µm]	13.23	6.62
Tumor tissue and iohexol (6 mg/ml)/calcium oxalate		
Tube voltage [kVp]	50.00	
Design energy [keV]	36.00	
THL low [keV]	15.00	
THL high [keV]	35.00	
Height [µm]	200.00	6.32
Period [µm]	12.86	6.43

Table 5.5: Optimal setup parameters for the numerical mammography simulation for a polychromatic X-ray source. It contains the source energies which equal the design energies as well as the grating properties like height and period for the different material decompositions.

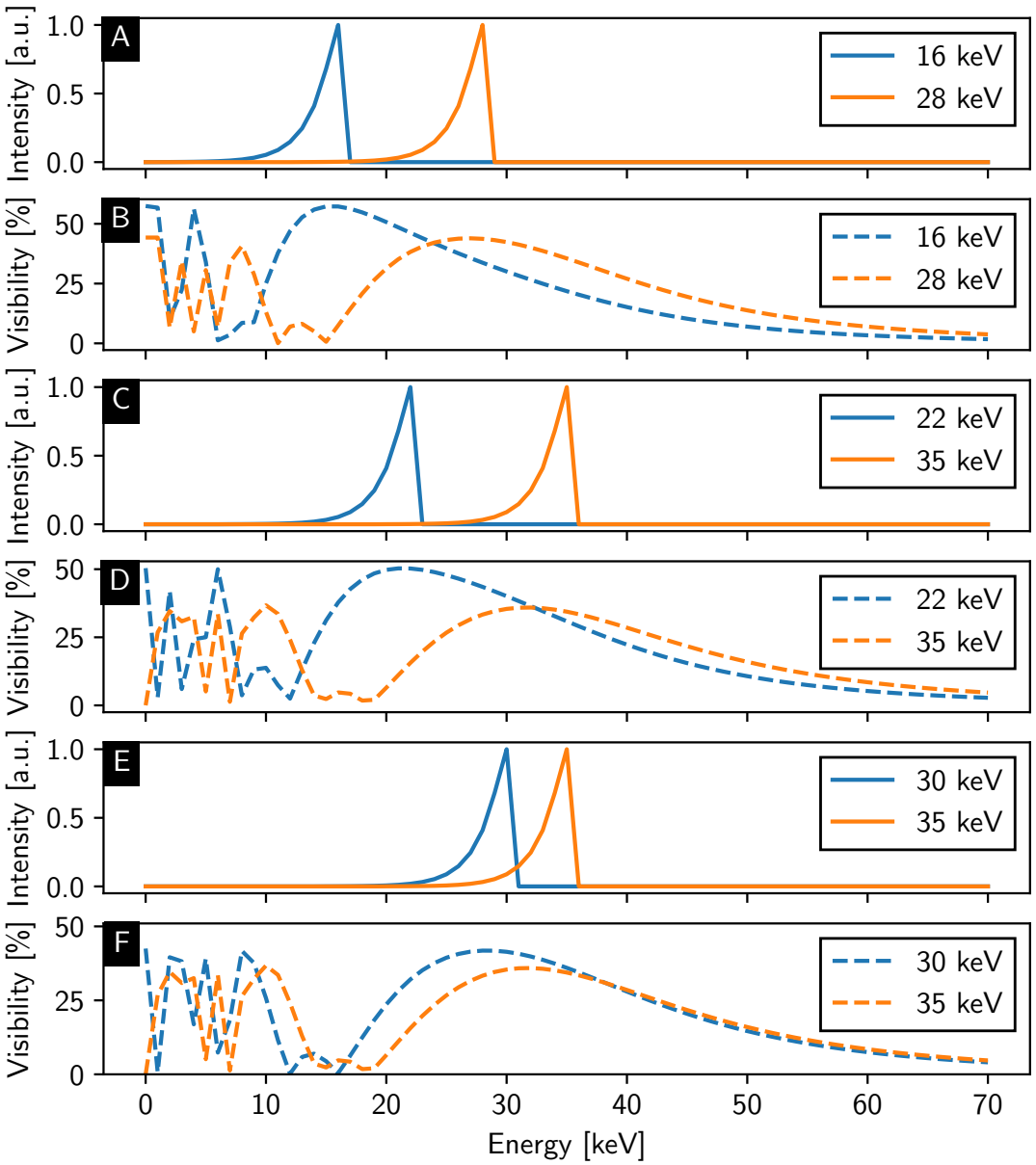

Figure 5.7: Effective quasi-monochromatic X-ray source and visibility spectra for all performed decompositions. The spectra are presented for the decomposition into (A, B) breast and tumor tissue, (C, D) breast tissue and calcium oxalate and (E, F) breast/tumor tissue and iohexol (6 mg/ml). The lower and higher energy spectra are plotted in blue and orange, respectively. The corresponding optimal simulations settings for each plot are listed in Tab. 5.4.

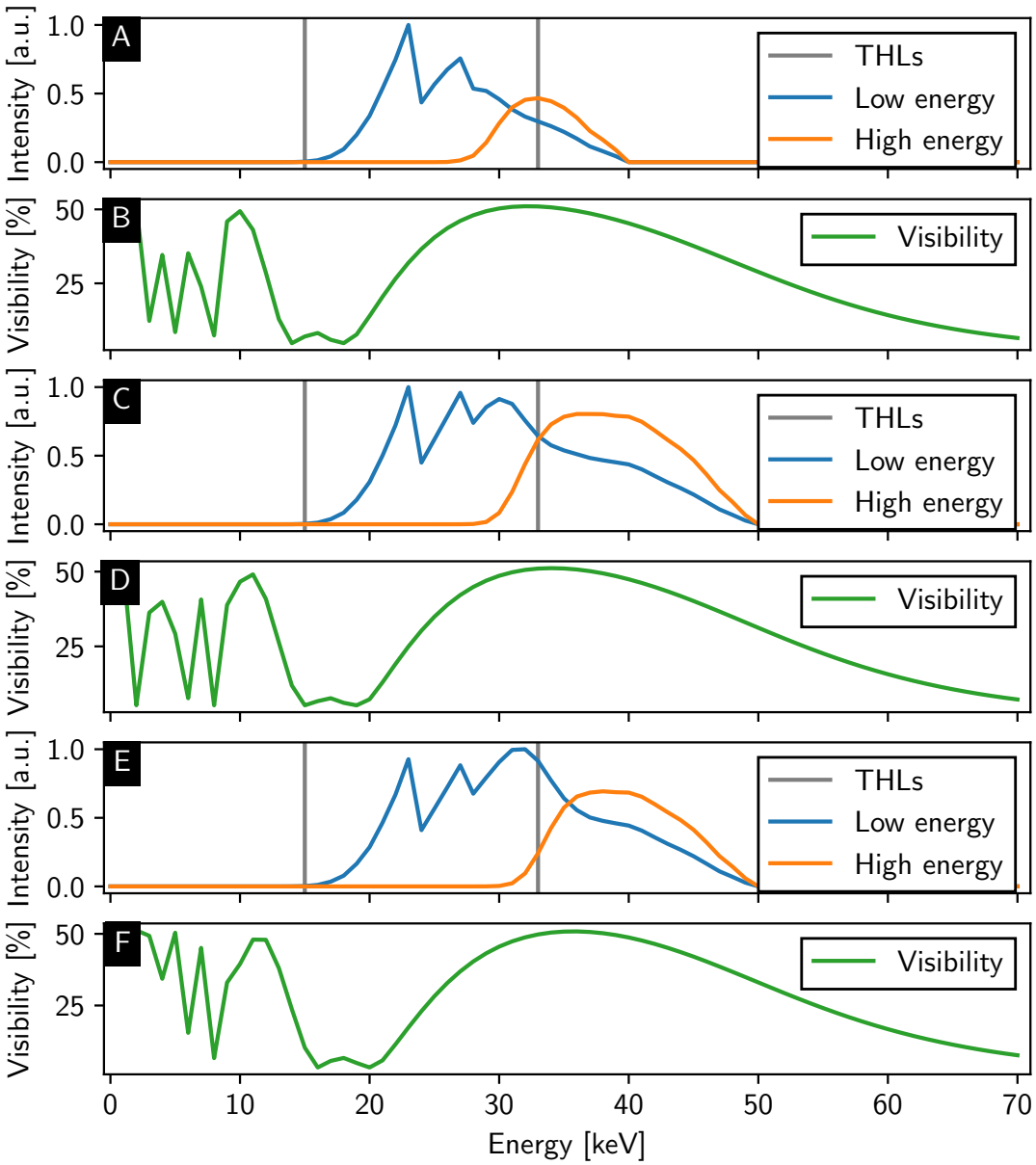

Figure 5.8: Effective polychromatic X-ray source and visibility spectra for all performed decompositions. The spectra are presented for the decomposition into (A, B) breast tissue and tumor tissue/calcium oxalate, (C, D) breast tissue and iohexol (400 mg/ml) and (E, F) tumor tissue and iohexol (6 mg/ml). The peak of the visibility spectrum corresponds to the design energy of the interferometer. The corresponding optimal simulations settings for each plot are listed in Tab. 5.5.

35 keV for the quasi-monochromatic-based decomposition are very close to each other. This indicates the influence of the absorption K-edge of iodine at an energy of 33.2 keV during the parameter optimization process.

5.4.2 Breast Computed Tomography

The parameter optimization is repeated for the SDPC BCT simulations. Therefore, the detector's pixel size is enlarged to 150 µm referring to the commercial BCT device. The assumed sample thickness is extended to 6 cm representing an uncompressed female breast. The three-dimensional phantom is not gradually filled with the various relevant materials as for mammography, so that the number of interesting basis material combinations is reduced. The two sensible basis material combinations for this application are tumor tissue and iohexol (6 mg/ml) as well as into breast tissue and iohexol (400 mg/ml) in order to further enhance the contrast of specific structures as shown later. The optimization results in the same parameters for both basis material combinations. The optimal imaging parameters and grating specifications are summarized in Tab. 5.6 for the quasi-monochromatic X-ray source. The effective X-ray source (A) and energy-dependent visibility (B) spectra are plotted in Fig. 5.9. The absorption K-edge of iodine is indicated by a vertical, green, dashed line. The optimal source energies are very close to the K-edge which underlines the influence of iodine as basis material. By comparing the optimal simulation settings of the BCT with mammography for the same basis material combinations, the two energies appear to be closer together with increasing sample thickness.

5.5 Quasi-monochromatic and Polychromatic Simulation

In this section, the results of all conducted numerical simulations for the quasi-mono- and the polychromatic case are presented. The first part refers to the results performed for two-dimensional mammography imaging (cf. Sec. 5.5.1) followed by the simulations for BCT in the second part (cf. Sec. 5.5.2).

5.5.1 Simulation of Mammography

Two-material-based phantom

The results for the two-material-based phantoms are shown in Fig. 5.10, 5.11 and 5.12 for breast and tumor tissue, breast tissue and calcium oxalate as well as for breast

Tumor tissue and iohexol (6 mg/ml) Breast tissue and iohexol (400 mg/ml)				
	Energy [keV]		G_1	G_2
Low	33.00	Height [µm]	6.15	90
		Period [µm]	4.29	4.35
High	35.00	Height [µm]	5.80	90
		Period [µm]	4.16	4.23

Table 5.6: Optimal setup parameters for the numerical simulation of breast computed tomography for a quasi-monochromatic X-ray source. It contains the source energies which equal the design energies as well as the grating properties like height and period for the decomposition into tumor tissue/iohexol (6 mg/ml) and breast tissue/iohexol (400 mg/ml).

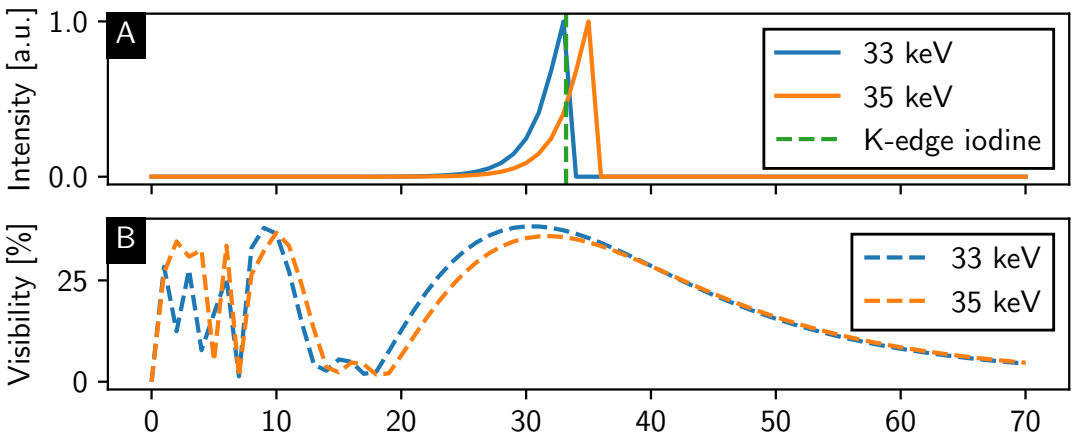

Figure 5.9: Effective quasi-monochromatic X-ray source and visibility spectra for the BCT simulations. The spectra are used for the decomposition into tumor tissue and iohexol (6 mg/ml) as well as into breast tissue and iohexol (400 mg/ml). The lower energy is plotted in blue and the higher one in orange. The absorption K-edge of iodine is indicated by the vertical, green, dashed line at 33.2 keV. The corresponding optimal simulation settings are listed in Tab. 5.6.

tissue and iohexol (6 mg/ml), respectively. The quasi-monochromatic case is always displayed in subfigures (A-D) and the polychromatic case in (E-H). The results for the conventional material decomposition are shown in the left column and the results for

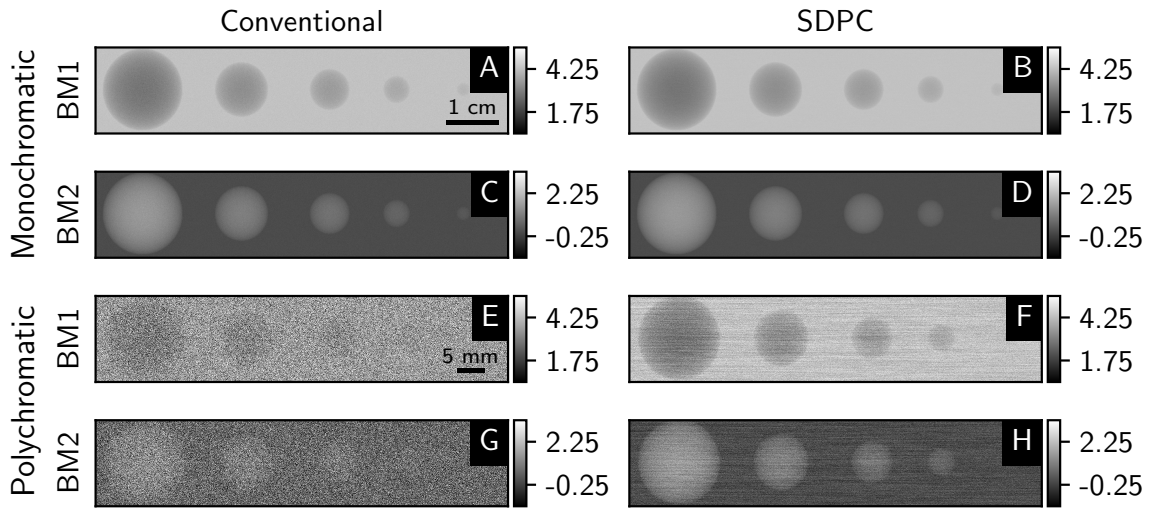

Figure 5.10: Conventional spectral attenuation-based and SDPC material decomposition for (A-D) a quasi-mono- and (E-H) a polychromatic X-ray source for breast tissue (BM1) and tumor tissue (BM2) as phantom and basis materials. Especially in the polychromatic case, the tumor detection is improved in the second basis material image while the background noise level is reduced. Due to the correlation of neighboring pixels, a horizontal noise pattern is introduced in the SDPC-based basis material images in contrast to the conventionally decomposed images. The units for the material decompositions are given by the equivalent projected breast and tumor tissue thicknesses in centimeter. Images are windowed for maximum detail visibility.

the SDPC decomposition in the right one. The first and the second basis material images are denoted with BM1 and BM2, respectively. The total dose for all simulated measurements is 1.25 mGy estimated with the model presented by J. M. Boone and is thus in the relevant dose range for mammography [Boone, 1992; Perry, 2006]. The attenuation and differential phase-contrast images for the three two-material-based phantoms are depicted in the Appendix in Fig. 6.1, 6.2 and 6.3. The noise level for the quasi-monochromatic simulations is generally lower than for the polychromatic ones in all decomposed images of the three two-material based phantoms. Nevertheless, the visual comparison between the conventional and the SDPC material decomposition shows a reduction of the background noise also for the quasi-monochromatic simulations. The decrease is stronger in the polychromatic case where especially the smaller structures become visible after the SDPC material decomposition. The microcalcifications partially get lost in the background noise for the conventional material decomposition (cf. Fig. 5.11 (G)) and are significantly enhanced in the SDPC-based decomposition (cf. Fig. 5.11 (H)). This is also the case for the tumor masses, comparing Fig. 5.10 (G) and (H) and the iohexol structures in Fig. 5.12 (G) and (H). The reason

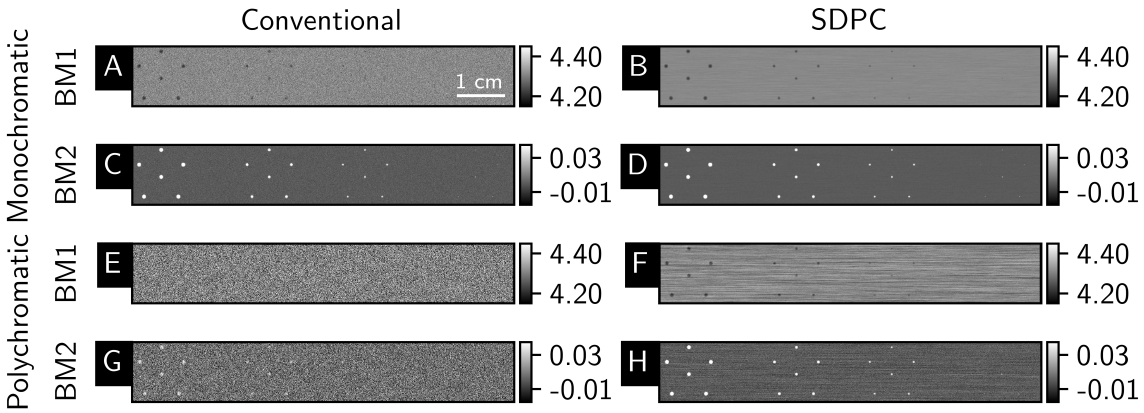

Figure 5.11: Conventional spectral attenuation-based and SDPC material decomposition for (A-D) a quasi-mono- and (E-H) a polychromatic X-ray source for breast tissue (BM1) and calcium oxalate (BM2) as phantom and basis materials. The results reveal an enhanced contrast of the microcalcifications in the SDPC decomposition compared to the conventional one. The improvement is more pronounced in the polychromatic case where the inserts get lost in background noise during the conventional material decomposition. The units for the material decompositions are given by the equivalent projected breast tissue and calcium oxalate thicknesses in centimeter. Images are windowed for maximum detail visibility.

for this is the worse energy separation in the polychromatic case compared to the quasi-monochromatic case which leads to an increased noise level in the conventionally decomposed images. Consequently, the gain of SDPC by the additional phase-contrast information is higher compared to the quasi-monochromatic case where the separation (due to the dual-energy approach) is good. In contrast to the conventional spectral material decomposition whose optimization problem is – as previously mentioned – solved pixelwise, it is not possible to solve the SDPC approach for each pixel separately as the signals from neighboring pixels are correlated. This results in a stripe-like horizontal noise pattern which appears in all SDPC basis material images.
The described visual findings are emphasized by the CNR values and PED variances which are summarized in Tab. 5.7 and 5.8 for both decomposition approaches. Here, the CNR is calculated between one of the structural elements and the surrounding material breast tissue. It should be noted, that the CNR is only calculated for the second basis material image. For the attenuation-based images, the CNR values are listed in the Appendix in Tab. 6.1. For the quasi-monochromatic case, the PED variance is only slightly reduced, but the CNR values show a significant improvement for all structures. For iohexol and the calcifications, the CNR values are approximately three times higher for the SDPC-based material decomposition and also for the tumor masses

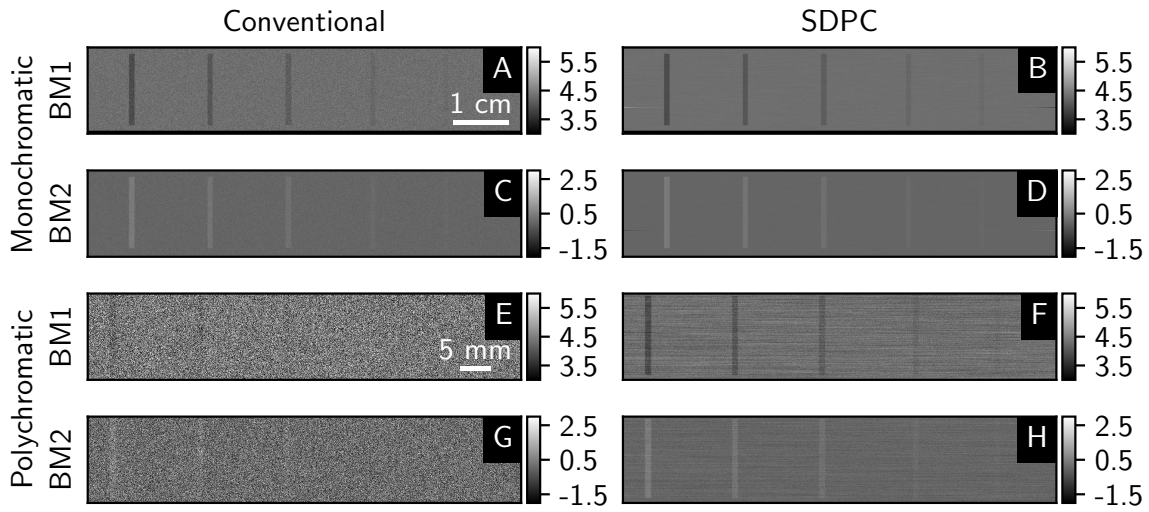

Figure 5.12: Conventional spectral attenuation-based and SDPC material decomposition for (A-D) a quasi-mono- and (E-H) a polychromatic X-ray source for breast tissue (BM1) and iohexol (BM2) in a concentration of 6 mg/ml as phantom and basis materials. The amount of iohexol becomes visible in the second basis material image in both material decompositions. After the SDPC material decomposition, the iohexol structures are remarkably improved in the iohexol basis material image. In the polychromatic case, four instead of only two iohexol structures are detected. The units for the material decompositions are given by the equivalent projected breast tissue and iohexol thicknesses in centimeter. Images are windowed for maximum detail visibility.

an improvement of about 44 % is present. This effect becomes more prominent for the polychromatic simulations where both the PED variances as well as the CNR values are remarkably improved which is clearly emphasized by six- to eight-fold increased CNR values after the SDPC material decomposition.

Since contrast enhancement can also be achieved by applying a filter to the conventional material decomposition results, a comparison based on column-wise summed line plots of the different modalities is presented in Fig. 5.13 with special regard to the resolution/sharpness. This comparison is performed for all decomposition tasks for the two-material-based phantoms exemplary for the polychromatic simulation case. The results are exemplary displayed for the second basis material image. In (A-C), the line plots of the conventional (blue) and the SDPC (orange) material decomposition are presented. It clearly shows that the noise is significantly reduced by SDPC. Furthermore, compared to conventional material decomposition, one tumor mass, two calcification clusters and two iohexol structures are additionally detected in the SDPC approach. Structures get lost in the high background noise and are not observed in the conventionally decomposed images. In (D-F), the SDPC result is compared with

Modality	Size 1	Size 2	Size 3	Size 4	Size 5
	Tumor masses				
Conventional	28.50	18.67	14.09	9.08	4.85
SDPC	41.38	27.09	20.46	13.18	6.91
	PED variance [cm^{-4}]				
Conventional	$6.45 \cdot 10^{41}$				
SDPC	$6.39 \cdot 10^{41}$				
	Calcium oxalate				
Conventional	21.17	17.04	11.88	7.18	–
SDPC	66.43	54.33	37.05	22.11	–
	PED variance [cm^{-4}]				
Conventional	$1.07 \cdot 10^{42}$				
SDPC	$1.06 \cdot 10^{42}$				
	Iohexol 6 mg/ml				
Conventional	3.23	2.30	1.60	0.74	0.39
SDPC	11.80	8.56	5.84	2.64	1.39
	PED variance [cm^{-4}]				
Conventional	$7.18 \cdot 10^{41}$				
SDPC	$7.16 \cdot 10^{41}$				

Table 5.7: CNR values and results of the PED variance for all simulated cases for the two-material phantoms in the quasi-monochromatic simulation case. CNR values for the conventional and the SDPC decomposition for the second basis material image are presented and show a significant improvement for all structural elements from conventional to SDPC decomposition.

the 1D Gaussian filtered conventional material decomposition (green). Although the noise is reduced which in consequence results in higher contrast, resolution gets lost. For the smaller structures pixel 1100 upwards for the tumor masses, from pixel 900 for the calcifications and from 1000 for the iohexol structures, the signal stagnates and the

Modality	Size 1	Size 2	Size 3	Size 4	Size 5
	Tumor masses				
Conventional	0.32	0.23	0.16	0.10	0.12
SDPC	2.14	1.54	1.12	0.78	0.43
	PED variance [cm^{-4}]				
Conventional	$5.92 \cdot 10^{45}$				
SDPC	$1.06 \cdot 10^{43}$				
	Calcium oxalate				
Conventional	1.04	1.10	0.56	0.09	–
SDPC	7.93	7.11	4.44	2.75	–
	PED variance [cm^{-4}]				
Conventional	$8.25 \cdot 10^{44}$				
SDPC	$6.08 \cdot 10^{43}$				
	Iohexol 6 mg/ml				
Conventional	0.21	0.12	0.11	0.02	0.01
SDPC	1.63	1.14	0.81	0.38	0.23
	PED variance [cm^{-4}]				
Conventional	$2.15 \cdot 10^{44}$				
SDPC	$8.47 \cdot 10^{43}$				

Table 5.8: CNR values and results of the PED variance for all simulated cases for the two-material phantoms in the polychromatic simulation case. CNR values for the conventional and the SDPC decomposition for the second basis material image are presented and show a significant improvement for all structural elements from conventional to SDPC decomposition.

structures are no longer distinguishable from the background. Again, only the three largest tumor masses, two calcification clusters and three iohexol structures are observable. Consequently, one gains contrast without losing resolution with SDPC imaging. To emphasize the observations from the line plots, a supplementary analysis of the

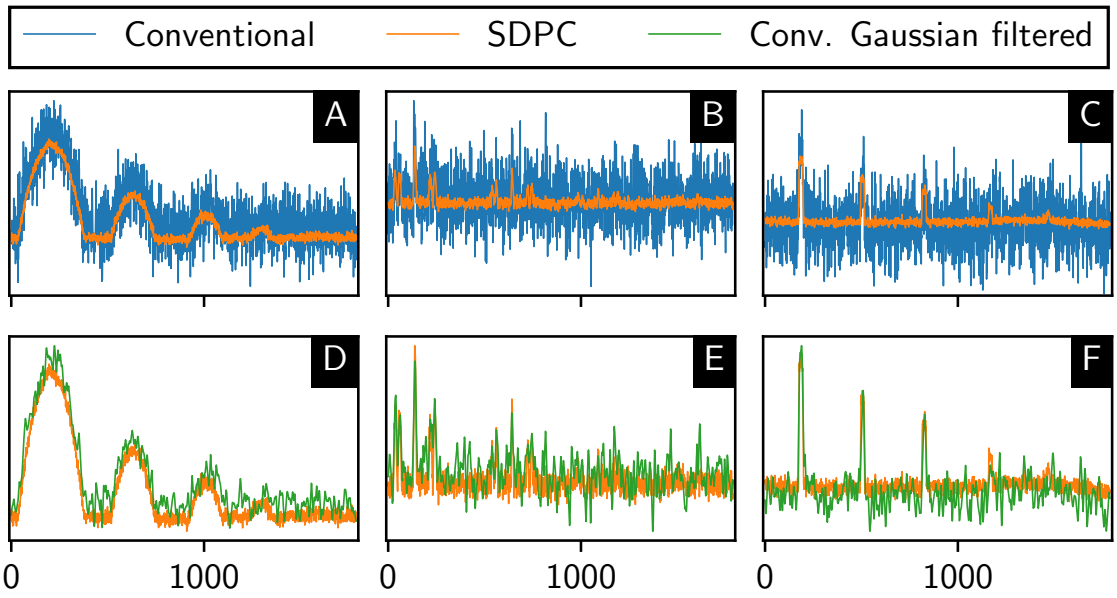

Figure 5.13: Column-wise summed line plots of the different decompositions tasks for the polychromatic simulation case. (A-C) Comparison between the conventional and the SDPC material decomposition for the three two-material-based phantoms. These plots underline the significant noise reduction. (D-F) Comparison between the Gaussian blurred conventional and the SDPC material decomposition showing the loss of resolution through filtering although the noise is reduced. The left column shows the results of the breast/tumor decomposition, the center column the breast/calcium oxalate decomposition and the right column the breast/iohexol (6 mg/ml) decomposition. These results are exemplary displayed for the second basis material image.

CNR, the background noise and the k-value is presented in Tab. 5.9. Since the line plots of the calcification-based phantom are mainly dominated by noise, the analysis is omitted for this phantom. For the k-value calculation, an edge of the largest structural element is respectively used as smaller structures partially get lost in the background noise and thus the k-value would no longer be calculable or useful for comparison. Even though the background noise is the lowest for the Gaussian filtered conventional material decomposition image, the noise in the SDPC image is significantly reduced compared to the unfiltered conventional material decomposition. In addition, the k- and the CNR values underline that the sharpness and the contrast are the highest for the SDPC approach. In conclusion, SDPC imaging outperforms the filtered conventionally decomposed images.

In addition to the two basis material images, an additional dark-field basis material image is generated by the SDPC material decomposition. Since the focus of this work

	Conventional	Conventional Gauss	SDPC
	Tumor		
CNR	0.311	1.813	**2.166**
σ_{BG}	4.133	**0.210**	0.606
k-value	0.111 ± 0.016	0.117 ± 0.006	**0.120 ± 0.003**
	Iohexol 6 mg/ml		
CNR	0.197	1.202	**1.614**
σ_{BG}	2.300	**0.100**	0.252
k-value	0.817 ± 0.644	1.055 ± 0.323	**1.703 ± 0.283**

Table 5.9: Comparison of the image quality measures. The image quality measures include the CNR, the background noise σ_{BG} and the k-value representing the edge sharpness and are calculated for the conventional material decomposition, for the Gaussian filtered one and the SDPC decomposition. This analysis shows that one gains contrast without losing resolution or sharpness with the SDPC approach.

is mainly on the material separation rather than on the physically correct depiction of the ultra-small-angle scattering signal or the improvement of this signal, the dark-field images are not included in the results of the SDPC optimization presented before. For the quasi-monochromatic simulation case and the calcium-based phantom, the results of the dark-field image are exemplary shown in Fig. 5.14. The corresponding CNR values and its percentage improvements are tabulated in Tab. 5.10. Compared to both, the low- and the high-energy dark-field image, a contrast enhancement is discernible which is larger for the low- (between 46 and 111 %) than for the high-energy (between 12 and 17 %) image and depends on the structure size.

Three-material-based phantom

The results of the iohexol-based three-material phantom are presented in Fig. 5.15 using tumor tissue and iohexol (6 mg/ml) as basis materials. A clear separation of the two basis materials is observable. The iohexol structures appear bright only in the second basis material image. For the conventional spectral attenuation-based decomposition, the tumor masses are also very well depicted. This is not the case for the SDPC decomposition where artifacts appear at the edges of the phantom for both simulated X-ray sources. The reason for this is the inconsistency between the attenuation coeffi-

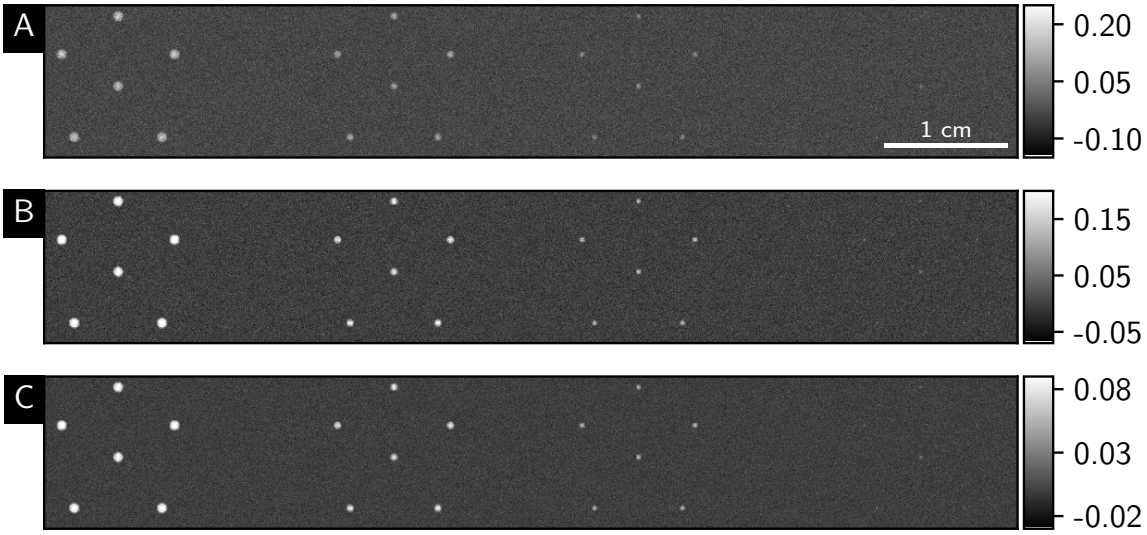

Figure 5.14: Dark-field images of the quasi-monochromatic simulation. It includes the images for (A) the low (22 keV) and (B) the high (35 keV) energy and for (C) the DFI after the SDPC optimization. The unit for the dark-field basis material image is given by the equivalent thickness of a material behaving with $\epsilon(E)$ in centimeters. Please note that the values are not quantitative because the signal strength of the dark field for microcalcifications was not simulated here.

Modality	Size 1	Size 2	Size 3	Size 4
DFI 22 keV	7.98	6.34	5.12	3.21
DFI 35 keV	14.44	11.86	8.29	4.18
DFI SDPC	16.83	13.77	9.75	4.67
Improvement [%]	110.90	117.19	90.43	45.48
	16.55	16.10	17.16	11.72

Table 5.10: CNR values for the conventional and SDPC DFIs. It is exemplary shown for the quasi-monochromatic simulation case for both energies and the SDPC result. It underlines the contrast enhancement after the SDPC optimization which is higher compared to the lower energy, but lower for the higher energy.

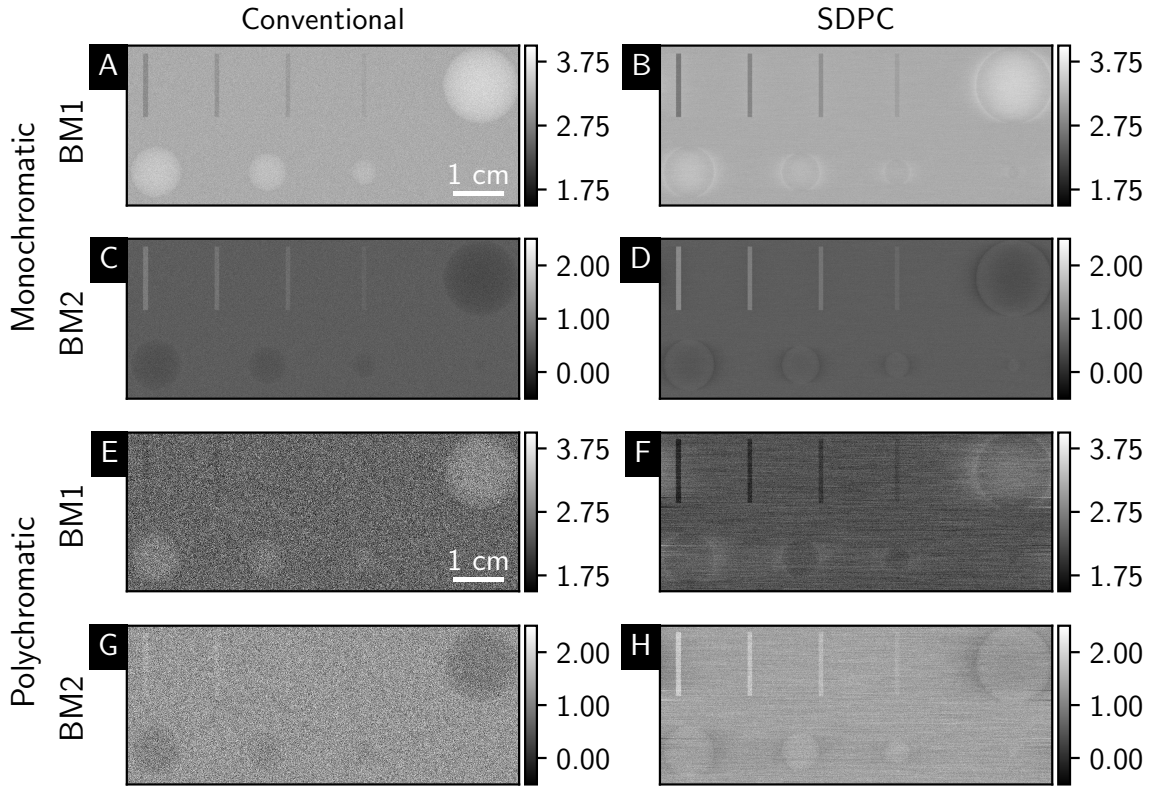

Figure 5.15: Conventional spectral attenuation-based and SDPC material decomposition of the three-material-based phantom for a quasi-mono (A-D) and a polychromatic (E-H) X-ray source into tumor tissue and iohexol with a concentration of 6 mg/ml. It is clearly visible that the iohexol structures are almost perfectly decomposed and separated from the tumor masses. Artifacts appear at the edges of the tumor masses in the images decomposed with the SDPC approach. The reason for this is the inconsistency between the attenuation coefficient and the electron density when a material with K-edge, e.g. iohexol, is present. The units for the material decompositions are given by the equivalent tumor tissue and iohexol thicknesses in centimeter. Images are windowed for maximum detail visibility.

cient and the electron density when a K-edge material, e.g. iohexol, is present within the used X-ray spectra. Additionally, if a phantom containing more materials than available basis materials is used, the physical description of every material individually is challenging. This is especially the case for this particular combination of phantom materials where two soft tissue-like and even one material including a K-absorption edge are present. In this combination, the decomposition with only two basis materials leads to this artifact which is in contrast to the successful and artifact-free material

separation presented before. Furthermore, both soft tissue-like materials (breast and tumor tissue) appear in the same basis material image which totally results in lower contrast for the tumor masses. The results of the CNR and PED variance analysis are summarized in Tab. 5.11. The CNR is only calculated for the second basis material. While the PED variances show an improvement for both simulation cases, the CNRs only demonstrate contrast enhancement for the iohexol structures by up to ten times for the polychromatic case and up to three times for the quasi-monochromatic case. As already visible in the decomposed images in Fig. 5.15, the contrast in terms of CNR for the tumor masses is not increasing. The attenuation and differential phase-contrast images for the two three-material-based phantoms are depicted in the Appendix in Fig. 6.4 and the CNRs for the attenuation images are tabulated in Tab. 6.2.

The second constellation for a three-material-based phantom includes tumor masses and calcifications embedded in breast tissue. In Fig. 5.16 (A) and (B), the results of a polychromatic, high dose and noiseless spectral attenuation-based material decomposition simulation are presented for (A) tumor and (B) calcium oxalate as basis materials. This simulation is carried out with a higher dose and without noise in order to work out possible inconsistencies with regard to the representation of the structures in the respective base materials. While the calcifications correctly pop up only in the second basis material image, it is conspicuous that the tumor masses appear bright in both basis material images. In order to investigate this, line plots through the tumor masses (C) and (D) and also the weight fractions of this decomposition task (E) are additionally plotted. A zoom-in section is provided in (F) to better distinguish between tumor and breast tissue. The line plot in (D) reveals that the tumor masses are modelled with a negative calcium oxalate thickness. However, the values are only negative due to the surrounding breast tissue material causing a negative offset, which is underlined by the plotted theoretical weight fractions in (E) and (F) showing that the breast tissue is modelled with a negative calcium oxalate fraction. When comparing tumor masses and breast tissue, it is still correctly observed that the tumor masses have higher values than breast tissue (D,F). As a result, the tumor masses appear bright due to the offset in the wrong basis material image. Since the separation between tumor mass and calcification is not given even in a high-dose and noise-free simulation, the full results for both X-ray sources and decomposition approaches are not presented here.

Full mammographic phantom

Nevertheless, the extension to a full mammographic phantom is performed to examine the behavior when all four materials are present within one phantom while performing a two-material decomposition. The results of the decompositions for the multi-material phantom are shown in Fig. 5.17 utilizing tumor tissue and iohexol (6 mg/ml) as basis materials. The corresponding attenuation and differential phase-contrast images

Modality	Size 1	Size 2	Size 3	Size 4	Size 5
	Monochromatic				
	Tumor masses				
Conventional	3.37	2.31	1.63	1.13	0.62
SDPC	6.98	3.99	2.08	0.57	0.29
	Iohexol 6 mg/ml				
Conventional	3.33	2.42	1.69	0.73	–
SDPC	10.62	7.84	5.48	2.28	–
	PED variance [cm^{-4}]				
Conventional	$7.18 \cdot 10^{41}$				
SDPC	$7.16 \cdot 10^{41}$				
	Polychromatic				
	Tumor masses				
Conventional	0.37	0.25	0.20	0.12	0.04
SDPC	0.90	0.36	0.06	0.16	0.04
	Iohexol 6 mg/ml				
Conventional	0.17	0.13	0.08	0.03	–
SDPC	1.30	1.13	0.77	0.29	–
	PED variance [cm^{-4}]				
Conventional	$1.61 \cdot 10^{44}$				
SDPC	$3.56 \cdot 10^{43}$				

Table 5.11: CNR values and results of the PED variance for the quasi-mono- and polychromatic simulation for all structures inserted in the iohexol-based three-material phantom. It includes the CNR values for the second basis material image and PED variances for the conventional and the SDPC material decomposition. The PED variance is improved for both simulation cases while for the CNR, there is only an increase of contrast observable for the iohexol structures, but not for the tumor masses. This can be explained by the artifacts that occur and which makes it difficult to visualize the tumor masses resulting in fluctuating CNR values.

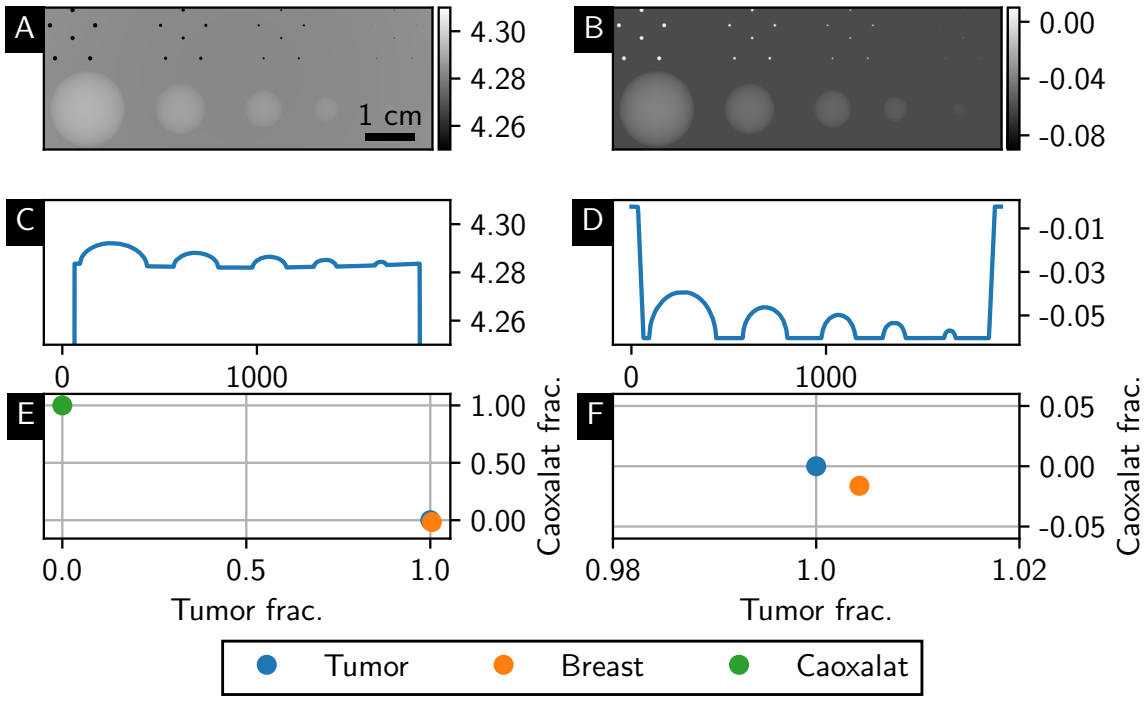

Figure 5.16: Conventional spectral attenuation-based, high dose and noiseless material decomposition into tumor and calcium oxalate. The decomposed images are shown for (A) tumor and (B) calcium oxalate as basis materials. The simulations are conducted for a polychromatic X-ray source. In (C) and (D), the corresponding line plots through the tumor masses are plotted. (E) The weight fractions of this decomposition tasks are presented with (F) a zoom-in section for better visualization. These figures justify why the tumor masses appear bright in both images.

are depicted in the Appendix in Fig. 6.5. In both simulation cases the decrease of background noise is visible in the decomposed images, but it is more obvious for the polychromatic simulation. The outcome of the CNR and the noise analysis is presented in Tab. 5.12 for material decompositions and in the Appendix in Tab. 6.3 for the attenuation images of both simulation cases. It has to be noted that CNR in Tab. 5.12 is only calculated for the second basis material. For the perfectly decomposed iohexol structures, the analysis emphasizes the observed improvement in terms of three to ten times higher CNR values. In addition, lower PED variances for the SDPC decomposition are also calculated for both cases. However, artifacts appear at the other structures. On the one hand, modeling the calcifications is challenging with the chosen basis materials, as their appearance changes in brightness from the conventional to the SDPC decomposition. Furthermore, streaking artifacts appear as blurred edges around the calcifications and the tumor masses in the SDPC decomposed

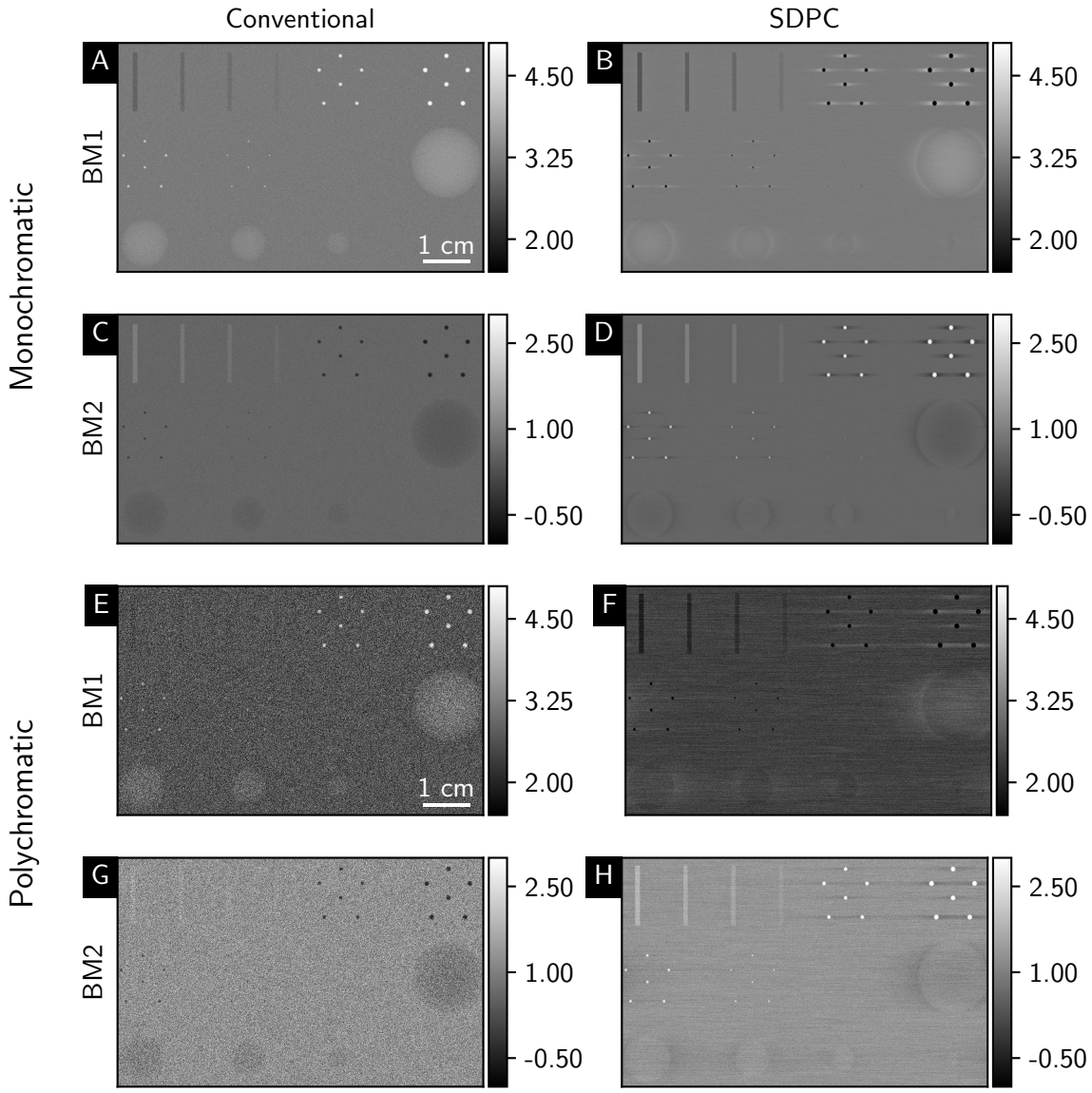

Figure 5.17: Conventional spectral attenuation-based and SDPC material decomposition for (A-D) a quasi-mono- and (E-H) a polychromatic X-ray source into tumor tissue (BM1) and iohexol with a concentration of 6 mg/ml (BM2) as basis materials of the multi-material phantom. While the iohexol structures are almost perfectly decomposed, modeling the calcifications is challenging for the multi-material phantom. Due to the inconsistency between the attenuation coefficient and the electron density when a K-edge material is present, their appearance changes in brightness from the conventional to the SDPC decomposition. The units for the material decompositions are given by the equivalent tumor tissue and iohexol thicknesses in centimeter. Images are windowed for maximum visibility.

Modality	Size 1	Size 2	Size 3	Size 4	Size 5
	Monochromatic				
	Tumor masses				
Conventional	3.21	2.17	1.55	1.09	0.55
SDPC	6.40	3.54	1.84	0.59	0.58
	Iohexol 6 mg/ml				
Conventional	3.34	2.42	1.68	0.74	–
SDPC	10.61	7.72	5.35	2.45	–
	PED variance [cm^{-4}]				
Conventional	$8.61 \cdot 10^{42}$				
SDPC	$8.35 \cdot 10^{42}$				
	Polychromatic				
	Tumor masses				
Conventional	0.31	0.21	0.16	0.14	0.14
SDPC	0.43	0.01	0.09	0.12	0.03
	Iohexol 6 mg/ml				
Conventional	0.16	0.13	0.06	0.05	–
SDPC	1.53	1.09	0.77	0.35	–
	PED variance [cm^{-4}]				
Conventional	$3.19 \cdot 10^{45}$				
SDPC	$8.69 \cdot 10^{44}$				

Table 5.12: CNR values and results of the PED variance for the quasi-mono- and polychromatic simulation for all inserted structures for the multi-material phantom. The analysis includes the CNR values for the conventional and the SDPC material decomposition for the second basis material image. It was omitted for calcium because of the change in brightness in the decomposed images. For the iohexol structures, these values emphasizes the improvement induced by the SDPC approach underlined by the CNR and PED variances.

images. The reason is again the inconsistency between the attenuation coefficient and the electron density when a K-edge material is present. The optimization attempts to find the best possible compromise between the attenuation and the PED. This leads to an inversion of the contrast from conventional to SDPC decomposition. On the other hand, in the case of a phantom including more materials than available basis materials, the physically correct description of every individual material is not possible. The additional materials must be composed as a linear combination of the other two basis materials. Especially in this particular combination of phantom materials where two soft tissue-like, two highly absorbing (calcium oxalate and iohexol) materials and even one material including a K-absorption edge are present. In this combination, the decomposition with only two basis materials leads to these artifacts compared to the successful and artifact-free material separation in Fig. 5.10, 5.11 and 5.12.

5.5.2 Simulation of Computed Tomography

In this section, SDPC BCT is investigated for a quasi-monochromatic X-ray source. As already pointed out in the experimental part about BCT at the MuCLS in Sec. 4, it is challenging to obtain a clinically and dose relevant BCT scan due to the high radiation sensitivity of the female breast. This is why the simulations are again firstly performed with a quasi-monochromatic X-ray source, where X-ray photons that only contribute to dose but not to contrast, are eliminated compared to a polychromatic X-ray source. It has to be noted that the experimental setup at the MuCLS, that is simulated here, is not dose-efficient because the sample is located before the two gratings. To get a ground truth where the final results can be compared with, a high dose simulation is initially performed. According to the Nyquist theorem, the number of required angles is 966 for all simulations and the data is reconstructed with FBP. The decomposition itself is conducted on each projection in image space individually before reconstruction. Again, the Gaussian filtered results of the conventional attenuation-based material decomposition are taken as initial guess for the SDPC optimization based on the nonlinear conjugate gradient algorithm (NLCG).
The material decomposition into tumor tissue and iohexol in a concentration of 6 mg/ml of the CT phantom for a dose of 100 mGy per source energy is presented in Fig. 5.18. The resulting dose per projection is 0.1 mGy. This is referred to as simulation case 1 in the following analysis of CNR and PED variance. In case 2, the MGD is reduced to a more clinically relevant limit of 5 mGy per source energy. This is obtained by reducing the applied dose per projection leading to a target dose per angle of 0.005 mGy. The results of the 5 mGy simulation with the same basis materials mentioned before are shown in Fig. 5.19 and reflect case 2. The decomposition generally reveals similar results as for the mammography simulations presented in Sec. 5.5.1. The tumor masses and the iohexol structures are overall well separated. A shadow around the

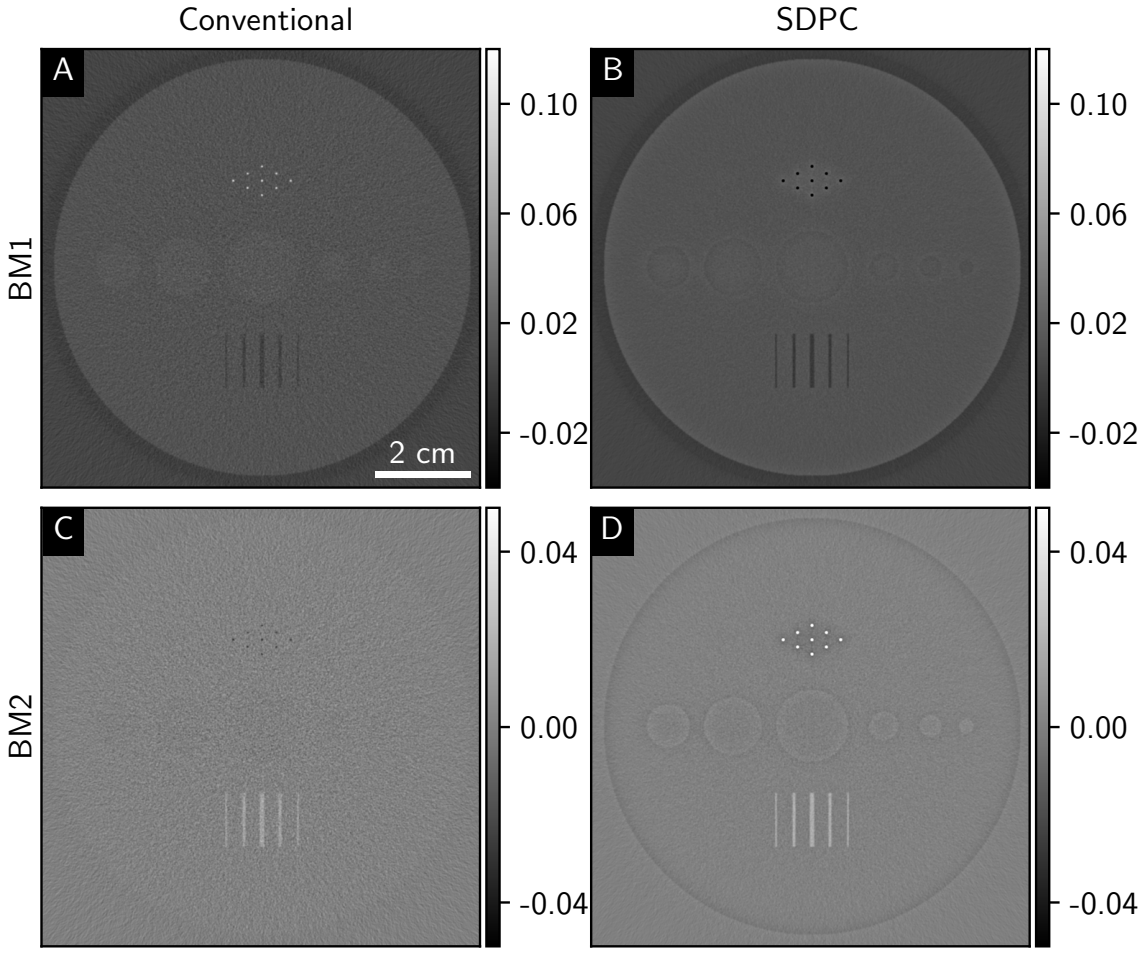

Figure 5.18: Conventional spectral attenuation-based and SDPC material decomposition for a quasi-monochromatic X-ray source for breast computed tomography and a MGD of 100 mGy. Tumor tissue (BM1) and iohexol with a concentration of 6 mg/ml (BM2) are used as basis materials. While the contrast for the iohexol structures is sufficient for detection and enhanced in the SDPC basis material image, the contrast of the tumor masses is barely visible since it appears in the same basis material image like breast tissue. An inversion of contrast occurs for the microcalcifications which can be explained by the inconsistency between the attenuation coefficient and the electron density of iohexol being a K-edge material.

tumor masses is striking in the basis material images of the SDPC decomposition. This effect in the reconstructed three-dimensional volume probably corresponds to the blurred edges visible in the projection images in Fig. 5.17. It is again observable that the calcifications change their brightness from the conventional attenuation-based to

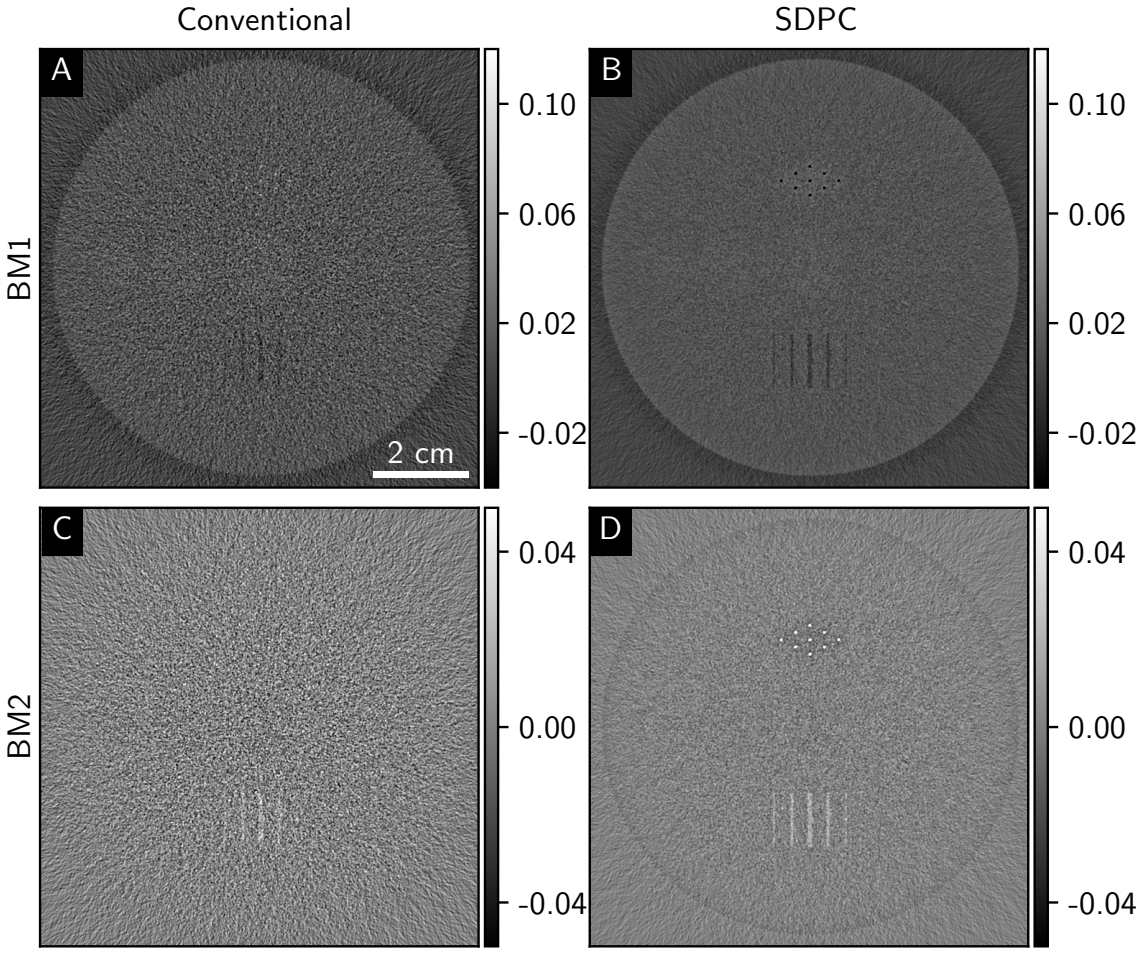

Figure 5.19: Conventional, spectral attenuation-based and spectral differential phase contrast material decomposition for a quasi-monochromatic X-ray source for breast computed tomography and a MGD of 5 mGy. Tumor tissue (BM1) and iohexol with a concentration of 6 mg/ml (BM2) are used as basis materials. While the contrast for the iohexol structures is sufficient for detection and enhanced in the SDPC basis material image, the contrast of the tumor masses is very low since it appears in the same basis material image like breast tissue. An inversion of contrast occurs for the microcalcifications which can be explained by the inconsistency between the attenuation coefficient and the electron density of iohexol as K-edge material.

the SDPC decomposition and show the shadow artifact. All structures are well visible in the higher dose images. In the 5 mGy images, however, some inserts become harder to detect because of the increased noise level. However, the background noise level is clearly reduced in the SDPC decomposition compared to the conventional attenuation-

based decomposition. The contrast of the tumor masses is remarkably decreased and it is challenging to distinguish the smaller iohexol structures and the microcalcifications from the background material in the conventional material decomposition images. In contrast, all iohexol structures and microcalcifications are discernible in the SDPC-based decomposition. These impressions are emphasized by an analysis of the CNR. The results of them are listed in Tab. 5.13 for both simulation cases. The ROIs are defined in only one exemplary slice and not in the whole volume. Generally, the CNRs of the SDPC results outperform the conventional ones by at least a factor of two. The CNR values for the iohexol structures are below one for the conventional simulation case which means that they are no longer detectable. However, they are three times higher after the SDPC material decomposition. The CNR values for calcium and tumor are also increased. By additionally comparing the decomposition of both dose levels, one can also conclude that the lower the dose, the more pronounced is the contrast enhancement provided by the SDPC decomposition. The only lack of these results is the comparatively low contrast of the tumor masses, which needs improvement. Thus, in order to better distinguish between the background material breast tissue and the tumor masses to provide a better contrast, the basis materials in which the phantom is decomposed in are changed into breast tissue and iohexol in a concentration of 400 mg/ml (case 3). The higher concentration is used in order to provide more contrast for the tumor masses because then, more parts of the breast tissue would also be modelled by the other basis material image resulting in better separated breast and tumor tissue. Based on this, an additional low-dose (5 mGy) material decomposition is simulated and its results are displayed in Fig. 5.20. The CNR values of case 3 are also listed in Tab. 5.13. Although the breast tissue basis material image overall appears slightly blurred, the contrast of the tumor masses is significantly improved compared to the previously performed basis material combination. The CNR increases by a factor of seven instead of only two as before. The enhancement of the iohexol structures is comparable to the one of the tumor masses. It is striking that only the iohexol structures are slightly pronounced in the second basis material image of the conventional material decomposition. In addition, the PED variance analysis is performed. Since the parameter optimization in Sec. 5.4 is conducted on only one projection image but not on the whole image volume, the PED variance is here also determined on the decomposed simulated projection images. The results are presented in Tab. 5.14. It revels a slight improvement which becomes with 3.37 % and 7.65 % slightly more prominent for the low-dose simulation cases. The reconstructed attenuation and phase-contrast CT images for 33 keV and 35 keV are presented in the Appendix in Fig. 6.6 and 6.7. For comparison, the corresponding CNR analysis is also given there in Tab. 6.4. The dark-field signal was again neglected in this investigation since the focus is not on the exact determination and subsequent improvement of this signal. It would be helpful to finally identify the microcalcifications due to their change in brightness in the decom-

positions. The general possible improvement is already investigated and presented in Fig. 5.14 and Tab. 5.10 for mammography.

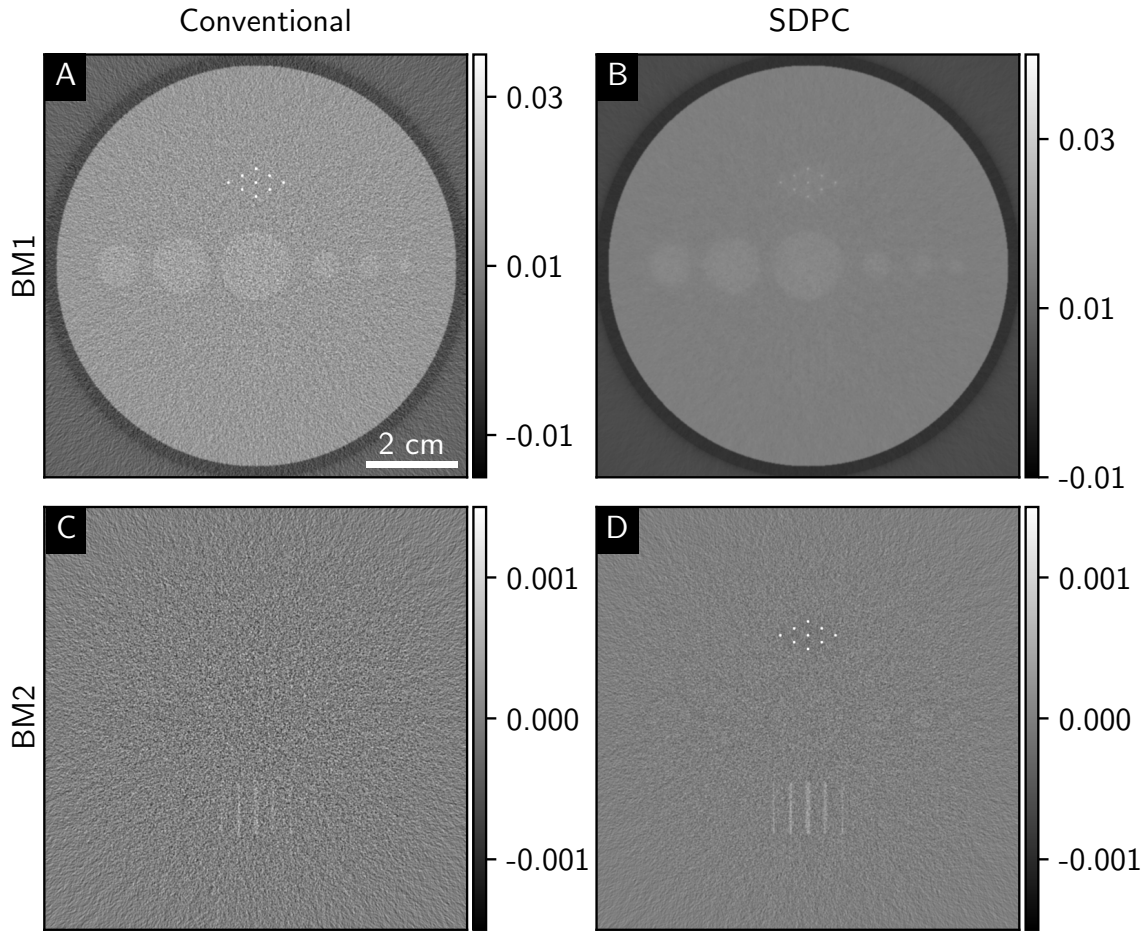

Figure 5.20: Conventional spectral attenuation-based and SDPC material decomposition for a quasi-monochromatic X-ray source for breast computed tomography and a MGD of 5 mGy. Breast tissue (BM1) and iohexol with a concentration of 400 mg/ml (BM2) are used as basis materials. For both, tumor masses and iohexol structures, the contrast is apparent and significantly enhanced after the SDPC decomposition while the background noise is notably decreased.

Structure	Modality	Case 1	Case 2	Case 3
Tumor (BM1)	Conventional	0.74	0.16	0.70
	SDPC	1.55	0.42	5.21
Microcalcification (BM1)	Conventional	15.56	2.92	13.63
	SDPC	74.28	15.89	12.10
Microcalcification (BM2)	Conventional	6.32	0.88	0.97
	SDPC	79.31	17.24	19.26
Iohexol 1 (BM2)	Conventional	3.42	0.76	0.27
	SDPC	10.21	2.26	2.58
Iohexol 2 (BM2)	Conventional	3.91	0.88	0.73
	SDPC	10.12	2.44	2.16
Iohexol 3 (BM2)	Conventional	2.79	0.39	0.70
	SDPC	7.19	1.33	1.62

Table 5.13: CNR analysis for all CT simulations with a quasi-monochromatic X-ray source. The analysis includes the CNR values for the conventional and the SDPC material decomposition. Due to the contrast inversion, the CNR of the microcalcifications is listed for both basis material images, while for tumor tissue and iohexol, it is only given for the corresponding basis material image. The increased CNR values of the iohexol structures underline the contrast improvement after the SDPC decomposition.

Modality	Case 1	Case 2	Case 3
	Monochromatic		
Conventional	$4.31 \cdot 10^{45}$	$9.01 \cdot 10^{46}$	$4.29 \cdot 10^{46}$
SDPC	$4.26 \cdot 10^{45}$	$8.37 \cdot 10^{46}$	$4.15 \cdot 10^{46}$

Table 5.14: Results of the PED variance for the quasi-monochromatic CT simulation. While the value for the high dose SDPC-based material decomposition with approximately 1 % is only slightly lower than for the conventional attenuation-based material decomposition, the improvement for the 5 mGy simulations is between 3.37 % and 7.65 %.

5.6 Discussion and Outlook

The SDPC algorithm, which was initially demonstrated in simulations for thorax radiography in [Mechlem, 2019b], is successfully translated to X-ray breast imaging throughout this chapter. While the decomposition performs well for a two-material-based phantom, horizontal streaking and shadowing artifacts appear for the decomposition of a three-material-based or multi-material phantom when a K-edge material is present (cf. Fig. 5.15 and 5.17). These artifacts are expressed by structures blurred in horizontal direction and should prospectively be prevented. In addition, the separation of tumor masses and microcalcifications in the second three-material phantom (cf. Fig. 5.16) remains challenging. The calcifications appear bright not only in the tumor tissue image, but also in the calcium oxalate image since the surrounding material breast tissue induces a negative offset. For these two reasons, an extension from a two- to a three-material decomposition is proposed for future work. This is firstly shown by Ji et al. by making use of a third source energy, a third energy THL or a dual-energy differential phase-contrast CT measurement [Ji, 2020]. With a third basis material, it would be possible to correctly model all included materials by a linear combination of the basis materials. The optimization would result in three basis material images, so that one could for example decompose into soft tissue (breast or tumour tissue), calcium and iodine. Special cases such as the change in appearance of the microcalcifications in Fig. 5.17 or the bright emergence of structures in the wrong basis material image (cf. Fig. 5.16) could potentially be averted. In particular, problems caused by the K-edge material can be solved.
Another possibility to be able to separate iohexol from the microcalcifications is to make use the dark field. This signal is an additional advantage especially for breast imaging since it helps to diagnose and characterize microcalcifications [Wang, 2014; Scherer, 2016]. Nevertheless, this work was not concerned with the correct depiction of a simulated ultra-small-angle scattering signal and thus its evaluation was generally neglected here. To simulate this signal, either an advanced wave propagation or dedicated dark-field measurements are required to retrieve the energy dependence for microcalcification of different sizes. Then, a parameter optimization could also be performed. Nevertheless, a slightly improved dark-field basis material thickness would be expected after the SDPC decomposition, as it is also implemented in the forward model (cf. Eq. (3.13)) and thus also one of the model parameters determined after minimizing the negative log-likelihood function. The theoretically possible improvement of the dark-field signal by the SDPC framework was exemplary investigated for the quasi-monochromatic simulation case for an arbitrary signal height (cf. Fig. 5.14 and Tab. 5.10). A significant improvement is demonstrated which is reflected in CNR values that are 10-20 % or 45-118 % (depending on the source energy) higher after performing the SDPC material decomposition. In consequence, it would be interesting

to make use of the X-ray dark-field signal in experimental studies where this signal is generated anyway.
In order to fully exploit the potential of the dual-energy SDPC X-ray imaging results, the dose distribution per source energy could be optimized and included in the parameter optimization process. So far, the dose per energy is uniformly distributed to a fixed target dose. With an overall target dose, better image quality would be expected if the dose is optimally distributed over both scans. In addition, one problem with the parameter optimization process is that the optimal imaging settings change for every material decomposition task depending on the selected basis materials, which is not suitable for clinical routine. For this, a decision on imaging settings must be made in advance. However, this should still not be a problem, since these parameters were only optimized for maximum image quality (minimal PED variance) and even with slightly changed parameters for a polychromatic X-ray source, the decomposition would work.
In order to overcome the current limitations of conventional mammography and of the clinically available attenuation-based BCT system [Kalender, 2012; Kalender, 2017; Berger, 2019b; ABCT, 2020], the evaluation of SDPC for three-dimensional breast imaging seems to be another promising approach. With a novel round-shaped phantom created for three-dimensional imaging, SDPC-based BCT imaging is performed and assessed for the quasi-monochromatic X-ray source, various dose levels and different basis material combinations. The BCT simulations with a quasi-monochromatic X-ray source are feasible for both dose levels and reveal enhanced contrast and a material discrimination. For the polychromatic case, it is more challenging to be able to conduct the simulation in a dose-compatible range. In Sec. 4.6, it has already been discussed to extend the reconstruction techniques to more advanced approaches such as sliding window or IBSIR especially with regard to the polychromatic investigation as it was challenging to obtain a grating-based phase-contrast and low-dose off-axis BCT at the MuCLS so far. This would be one possibility to also lower the total target dose for a polychromatic and SDPC-based BCT material decomposition. A first attempt in this direction has already been performed for a phantom study in combination with SIR by Mechlem et al. [Mechlem, 2019a]. The combined SDPC-SIR algorithm is a one-step method meaning that the image reconstruction and the material decomposition is jointly performed. The time-consuming stepping procedure is avoided and an improved image quality would be expected as initially presented in the first preliminary results [Mechlem, 2019a]. In addition, as already addressed in Sec. 4, patchwise phase retrieval or the application of self-supervised deep learning networks would potentially help to realize polychromatic SDPC BCT imaging. Since it makes more sense to incorporate the previously listed improvements first to approach a low-dose, no polychromatic BCT simulation was presented in this work.
As extension of that and based on the simulations, an experimental validation of this technique for mammography and BCT with biomedical samples appears to be use-

ful and should be aimed for. Future experimental studies will then also be able to better deal with the initially mentioned problem of the superposition of diagnostically relevant tissue structures, which has not been addressed by the phantoms of this proof-of-principle study. First attempts towards the experimental investigation of SDPC mammography at the MuCLS have been presented in [Klaar, 2021]. This has to be pursued in further studies not only with self-made breast phantoms, but also with e.g. freshly dissected mastectomy specimens. If the spectral separation of a photon-counting detector does not work sufficiently at a polychromatic X-ray source, it would also be possible to first conduct a dual-energy measurement where the X-ray source spectrum is filtered for the low-energy part in order to eliminate as much of the high-energy X-ray photons as possible. In a first experimental implementation of SDPC mammography at a polychromatic X-ray source where the applied dose was neglected, this approach has already been used to ensure the spectral separation [Breitenhuber, 2020]. Although the decomposition generally works in this study, several issues occur that have to be solved for better accuracy of experimental results of SDPC X-ray imaging. The visibility spectra are simulated and thus assume ideal gratings which lead to an overestimation of the visibility. In addition, the analysis of the data is performed with X-ray spectra that are effectively corrected for position or gratings/filters in the beam path, but not for the energy response of the detector. Since this is one main parameter in the SDPC forward model (cf. Eq. (3.13)), its previous estimation is of great importance, but was not performed in the aforementioned study [Breitenhuber, 2020]. The lack of this quantity can lead to a convergence towards a wrong direction or to an incorrect local minimum in the optimization landscape. It would be best to determine both X-ray spectrum and detector response as well as the visibility spectrum pixelwise to obtain a higher accuracy of the experimental results.
In summary, a significant improvement for the material decomposition with the forward-model-based SDPC algorithm that combines the advantages of dual-energy or spectral energy-resolved imaging with phase-contrast X-ray imaging was obtained. The contrast is enhanced while the noise is reduced for standard mammography and CESM as well as for BCT. These benefits can be used for increasing the contrast while keeping the dose constant, for lowering the dose while maintaining the image quality or for reducing the amount of injected contrast agent. Due to the radiation sensitivity of the female breast, these aspects are of particular interest for breast imaging especially with regard to SDPC BCT.

6 Conclusion

The main findings of this work are given in a final conclusion followed by a brief summary of the outlook for future studies in this research area.

Breast Computed Tomography at the Munich Compact Light Source

Ch. 4 comprises not only the experimental results of BCT at the MuCLS, but also an analysis and comparison of different detectors potentially relevant for X-ray breast imaging. The data for the latter are generated by measurements with a tungsten knife edge and a Siemens star. The results are summarized in Sec. 4.5.1. A comparison between the MTFs, PSFs and LSFs are provided for the Dexela flat-panel detector, the Santis 75 µm and the Santis 150 µm photon-counting detectors. Comparing the Dexela and the Santis 75 µm detectors, which have nearly the same pixel size, reveals the huge advantage of the photon-counting detector technology. Based on the aforementioned measures, the spatial resolution for the Santis 75 µm is significantly higher. In addition to the shorter exposure times that can be achieved with a photon-counting detector, which is an important aspect for low-dose imaging, the recommendation is to use a photon-counting detector for BCT. The difference between the two times binned Santis 75 µm and the unbinned Santis 150 µm is not that large. Nevertheless, since the Santis 150 µm is less susceptible to the charge-sharing effect, it achieves the best results by a small margin. For spectral imaging, one would also benefit from the detector with a larger pixel size since it increases the spectral resolution but at the expense of spatial resolution. But this would be acceptable for BCT since a high spatial resolution is not necessarily required for this application. The results of this work finally lead to the conclusion that a photon-counting detector with a higher pixel size is recommended for BCT.
Experimental studies for BCT are outlined in Sec. 4.5.2 to Sec. 4.5.5. It was successfully shown that an attenuation-based BCT taken at a quasi-monochromatic X-ray source in a clinical dose level (4.25 mGy) is achieved that can visually compete with a clinical

in vivo BCT. Based on this, the grating-based phase-contrast BCT was performed first with a self-build breast phantom and then with a freshly dissected fibroadenoma. For both phantoms, a low MGD of approximately 10 mGy is obtained. The twice as high MGD can be attributed to the analyzer grating being located behind the sample and can be justified by the higher information gain from the additional modalities and the improved soft tissue contrast in phase-contrast imaging. The image data of the fibroadenoma scan was furthermore decomposed into lipid, protein and water. Finally, an off-axis BCT scan was conducted with a more realistic sample size as pre-work for measurements with mastectomy specimens and a MGD of 25 mGy.
Two main aspects have to be improved in future work: First, to better highlight and emphasize the benefit of the phase information for BCT, biomedical samples with inherently more contrast within the samples are required for future studies. Second, further processing and advanced reconstruction techniques are essential in order to also lower the MGD for scans with larger samples sizes. Approaches like self-supervised deep learning networks can denoise the image data, but also reconstruction techniques such as the sliding window approach or IBSIR could potentially help to further decrease the MGD of BCT. A detailed discussion of the results, on which the recommendations of future work are based, can be found in Sec. 4.6. Prospective studies should deal with these aspects to increase the clinical relevance of grating-based phase-contrast BCT.

Spectral Differential Phase-Contrast Imaging

In Ch. 5, the benefits of SDPC for mammography and CESM are firstly investigated in numerical simulations with three two-, two three- and one multi-material phantom for a quasi-mono- and a polychromatic X-ray source at different experimental setups (cf. Sec. 5.5.1). Secondly, iodine containing BCT simulations are conducted for one phantom using a quasi-monochromatic X-ray source (cf. Sec. 5.5.2). For this, the optimal imaging parameters were initially estimated for the various decomposition tasks in Sec. 5.4. While for the two-material-based phantoms, the material discrimination works artifact-free, the three- and multi-material phantoms reveal some artifacts such as blurred edges in horizontal direction, the missing separation of tumor masses and microcalcifications, and the contrast inversion of the microcalcifications. For more information on the detailed discussion of the simulated results, see Sec. 5.6. Nevertheless, all SDPC decompositions show significantly lower noise values and improved contrast when the conventional attenuation-based approach is compared with the SDPC approach. This is also underlined by the analysis of the CNRs and the PED variances (cf. Tabs. 5.7, 5.8, 5.11, 5.12). The CNR values are improved by a factor of three in the quasi-monochromatic case. For the polychromatic X-ray source, the increase in CNR is six to eight times higher which could allow a reduction in the amount

of injected contrast agent by approximately one order of magnitude. In addition to considering contrast and noise in the image evaluation, the behaviour of the resolution is also taken into account. Therefore, a comparison of column-wise summed line plots between the conventional and the SDPC as well as between the conventional and the 1D Gaussian filtered conventional material decomposition was performed. It shows that simply filtering an image reduces noise but at the cost of resolution so that ultimately fewer structures are recognizable. Thus, SDPC imaging benefits from maintaining the resolution and also the edge sharpness. These findings were additionally validated by the k-value. Although the small-angle-scattering signal is not correctly simulated in this work, the theoretical improvement was nevertheless analyzed for the quasi-monochromatic simulation case. It shows a contrast enhancement for both the images of the low and the high X-ray energy. Due to the challenging experimental realization of low-dose BCT at the MuCLS for a larger sample, simulations are only performed with the quasi-monochromatic X-ray source for three different cases. Again, the noise is reduced and contrast enhanced (cf. Tab. 5.13 and 5.14) while contrast inversion of microcalcifications occurs and blurred edges around the spheres appear. Nonetheless, the BCT results are encouraging for prospective work also for polychromatic X-ray source since the dose (5 mGy) was already quite low.
Concluding the discussion of this project, an extension to a three-material decomposition should be the next step for improving the accuracy of SDPC mammography and BCT to avoid artifacts in the decomposed basis material images. For this approach, a third source energy, a third energy THL or a dual-energy differential phase contrast CT measurement is required to extend the SDPC forward model to a third basis material [Ji, 2020]. Moreover, the advanced reconstruction techniques mentioned above are also relevant for prospectively performing polychromatic SDPC BCT simulations such as the use of SDPC-SIR at a reasonable dose [Mechlem, 2019a]. For dual-energy simulations or measurements, one could additionally optimize the dose distribution for the respective scan by adjusting the exposure time to achieve the best possible contrast. Furthermore, an expansion of the experimental validation of SDPC for mammography and BCT with breast phantoms or freshly dissected mastectomy specimens might be very interesting. Such a study would finally enable the evaluation of the clinical relevance of this approach for breast imaging.

Appendix

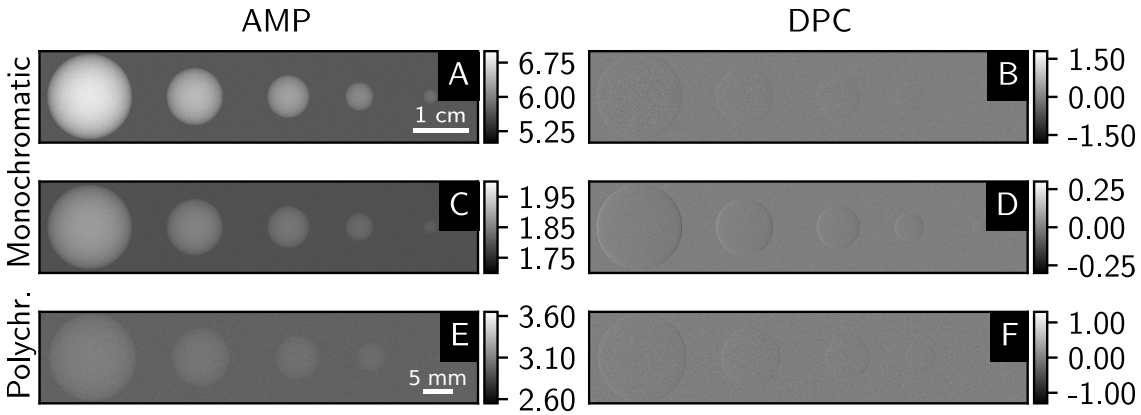

Figure 6.1: Attenuation and differential phase-contrast images for the tumor-based phantom. They are presented for the (A-D) quasi-monochromatic and (E, F) the polychromatic simulation case. The attenuation images are shown in the left column and the differential phase-contrast images in the right column. Images are windowed for maximum detail visibility.

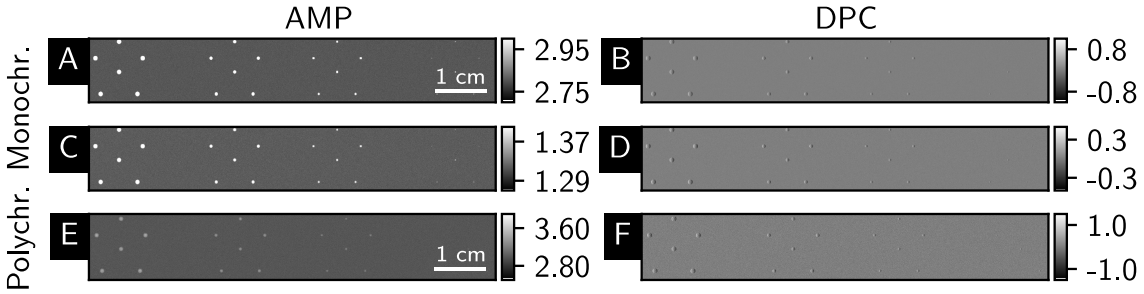

Figure 6.2: Attenuation and differential phase-contrast images for the calcium oxalate-based phantom. They are presented for the (A-D) quasi-monochromatic and (E, F) the polychromatic simulation case. The attenuation images are shown in the left column and the differential phase-contrast images in the right column. Images are windowed for maximum detail visibility.

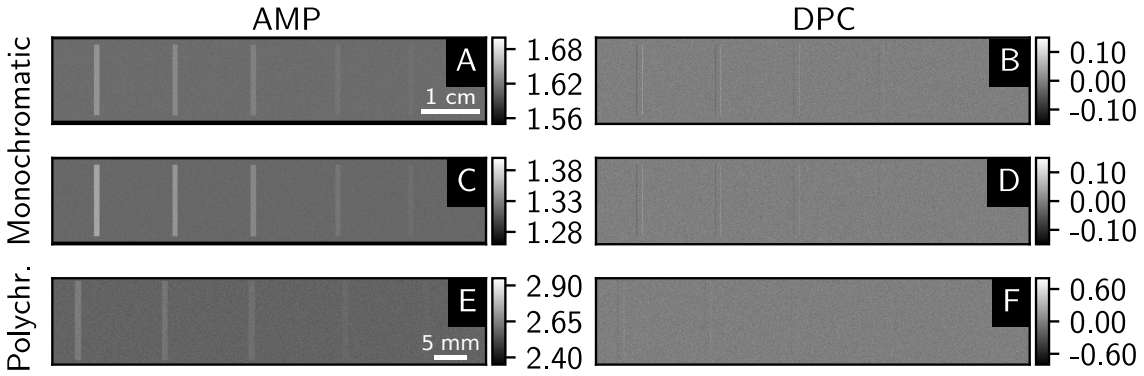

Figure 6.3: Attenuation and differential phase-contrast images for the iohexol-based phantom. They are presented for the (A-D) quasi-monochromatic and (E, F) the polychromatic simulation case. The attenuation images are shown in the left column and the differential phase-contrast images in the right column. Images are windowed for maximum detail visibility.

Modality	Size 1	Size 2	Size 3	Size 4	Size 5
	Monochromatic				
	Tumor masses				
AMP 16 keV	39.07	25.86	19.66	12.78	6.78
AMP 28 keV	20.15	13.18	10.02	6.51	3.32
	Calcium oxalate				
AMP 22 keV	68.83	56.16	38.51	22.78	–
AMP 35 keV	38.68	31.81	21.50	12.47	–
	Iohexol 6 mg/ml				
AMP 30 keV	6.17	4.51	3.07	1.32	0.67
AMP 35 keV	10.36	7.49	5.15	2.29	1.18
	Polychromatic				
	Tumor masses				
AMP	2.75	1.89	1.40	0.99	0.49
	Calcium oxalate				
AMP	8.86	7.33	5.10	2.83	–
	Iohexol 6 mg/ml				
AMP	1.70	1.20	0.84	0.36	0.21

Table 6.1: CNR values for all attenuation-based images for the two-material phantoms in the quasi-mono- and polychromatic simulation case. The CNR values are calculated for the low- and high-energy images in the quasi-monochromatic case.

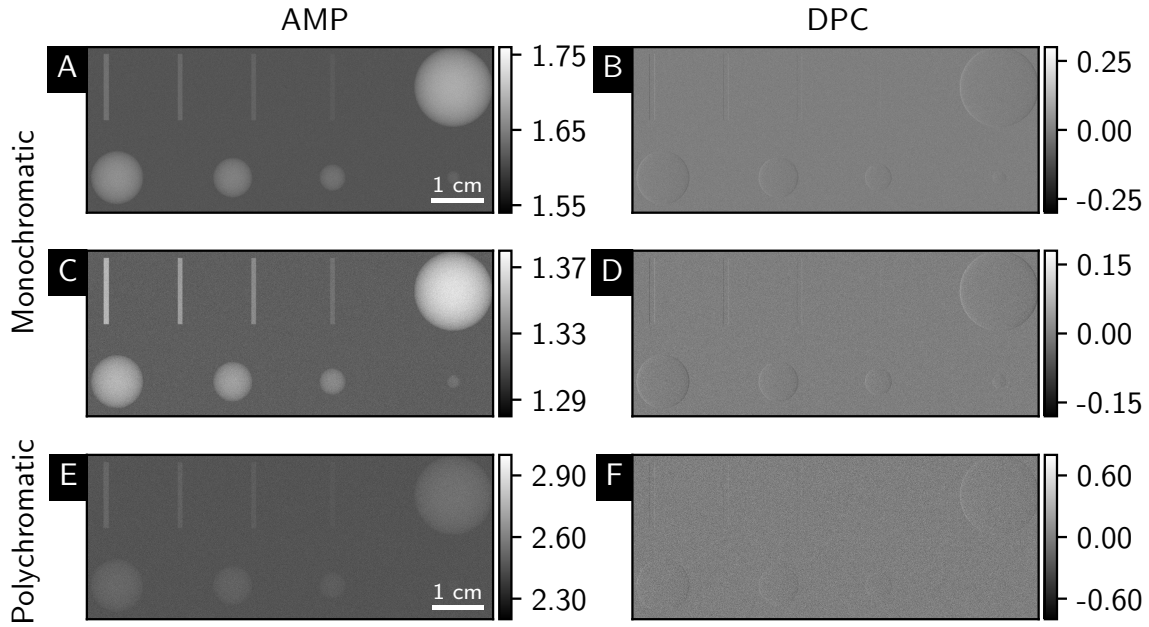

Figure 6.4: Attenuation and differential phase-contrast images for the two-material-based phantom. The images are depicted for (A-D) the quasi-monochromatic and (E, F) the polychromatic simulation case. The attenuation images are shown in the left column and the differential phase-contrast images in the right one. Images are windowed for maximum detail visibility.

Modality	Size 1	Size 2	Size 3	Size 4	Size 5
	Monochromatic				
	Tumor masses				
AMP 30 keV	18.45	12.52	8.94	5.96	2.96
AMP 35 keV	14.78	9.96	7.16	4.71	2.25
	Iohexol 6 mg/ml				
AMP 30 keV	6.19	4.45	3.10	1.36	–
AMP 35 keV	10.44	7.54	5.28	2.30	–
	Polychromatic				
	Tumor masses				
AMP	2.32	1.59	1.21	0.81	0.37
	Iohexol 6 mg/ml				
AMP	1.62	1.60	0.78	0.31	–

Table 6.2: CNR values for all attenuation-based images for the iohexol-based three-material phantom in the quasi-mono- and polychromatic simulation case. The CNR values are calculated for the low- and high-energy images in the quasi-monochromatic case.

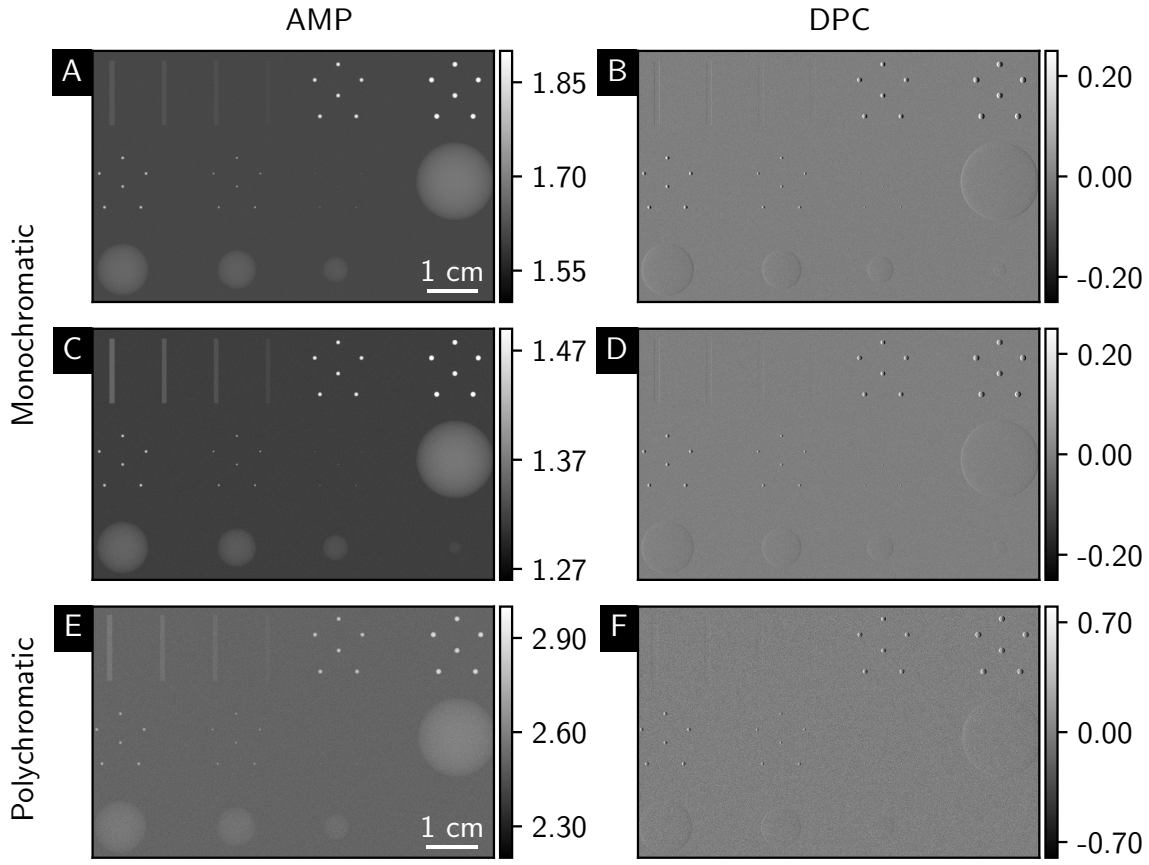

Figure 6.5: Attenuation and differential phase-contrast images for the multi-material-based phantom. The images are shown for (A-D) the quasi-monochromatic and (E, F) the polychromatic simulation case. The attenuation images are shown in the left column and the differential phase-contrast images in the right one. Images are windowed for maximum detail visibility.

Modality	Size 1	Size 2	Size 3	Size 4	Size 5
	Monochromatic				
	Tumor masses				
AMP 30 keV	17.74	11.98	8.52	5.82	3.11
AMP 35 keV	14.20	9.59	6.82	4.62	2.51
	Calcium oxalate				
AMP 30 keV	74.16	66.16	43.46	31.28	15.28
AMP 35 keV	56.75	50.75	32.76	23.47	11.50
	Iohexol 6 mg/ml				
AMP 30 keV	6.14	4.39	3.03	1.40	–
AMP 35 keV	10.40	7.48	5.17	2.34	–
	Polychromatic				
	Tumor masses				
AMP	2.53	1.70	1.25	0.83	0.41
	Calcium oxalate				
AMP	10.10	8.69	5.20	4.45	0.99
	Iohexol 6 mg/ml				
AMP	1.64	1.15	0.80	0.34	–

Table 6.3: CNR values for all attenuation-based images for the multi-material phantom in the quasi-mono- and polychromatic simulation case. The CNR values are calculated for the low- and high-energy images in the quasi-monochromatic case.

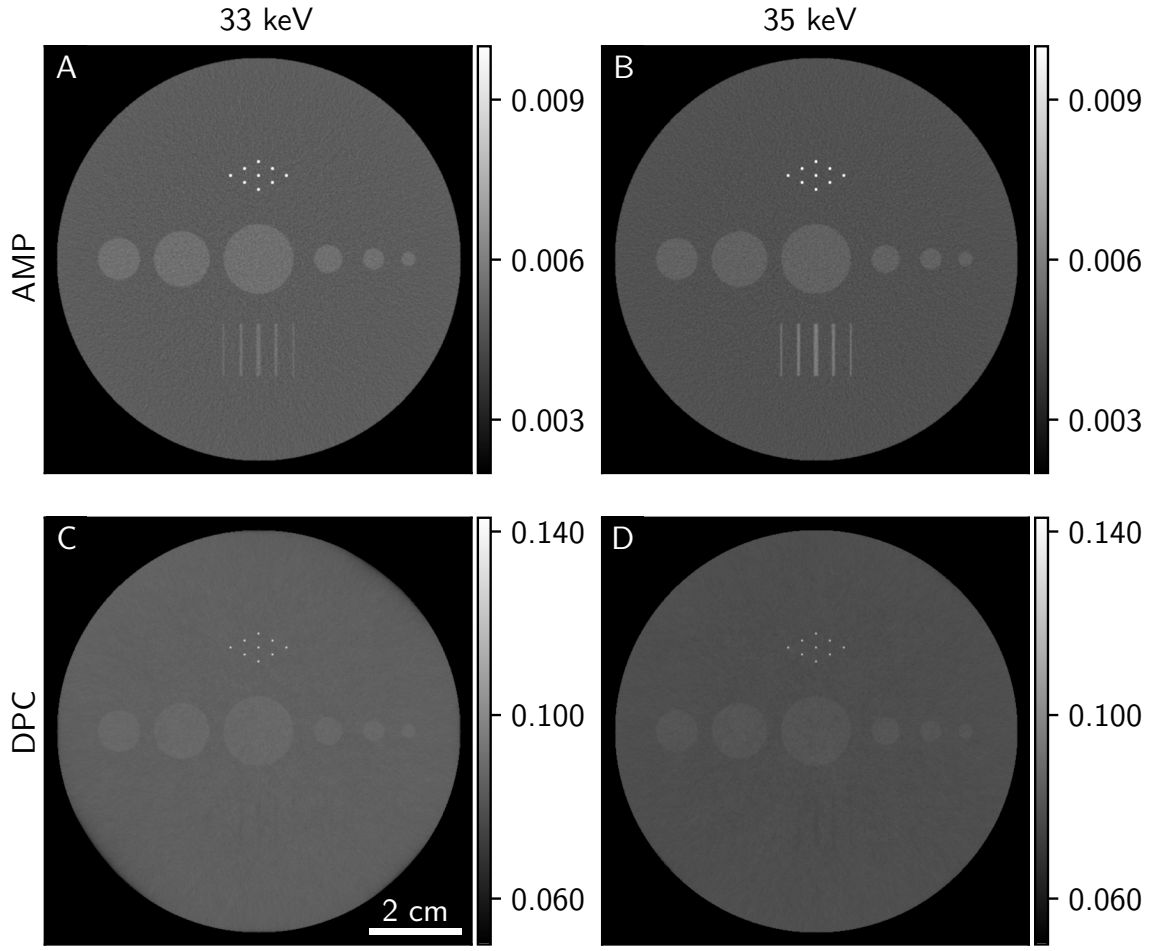

Figure 6.6: Attenuation and differential phase-contrast images for the BCT phantom. The exemplary slices are shown for the (A, B) attenuation and (C, D) the phase-contrast reconstructions for a MGD of 100 mGy. The left column represents the results from the lower (33 keV) and the right one the higher energy (35 keV). Images are windowed for maximum detail visibility.

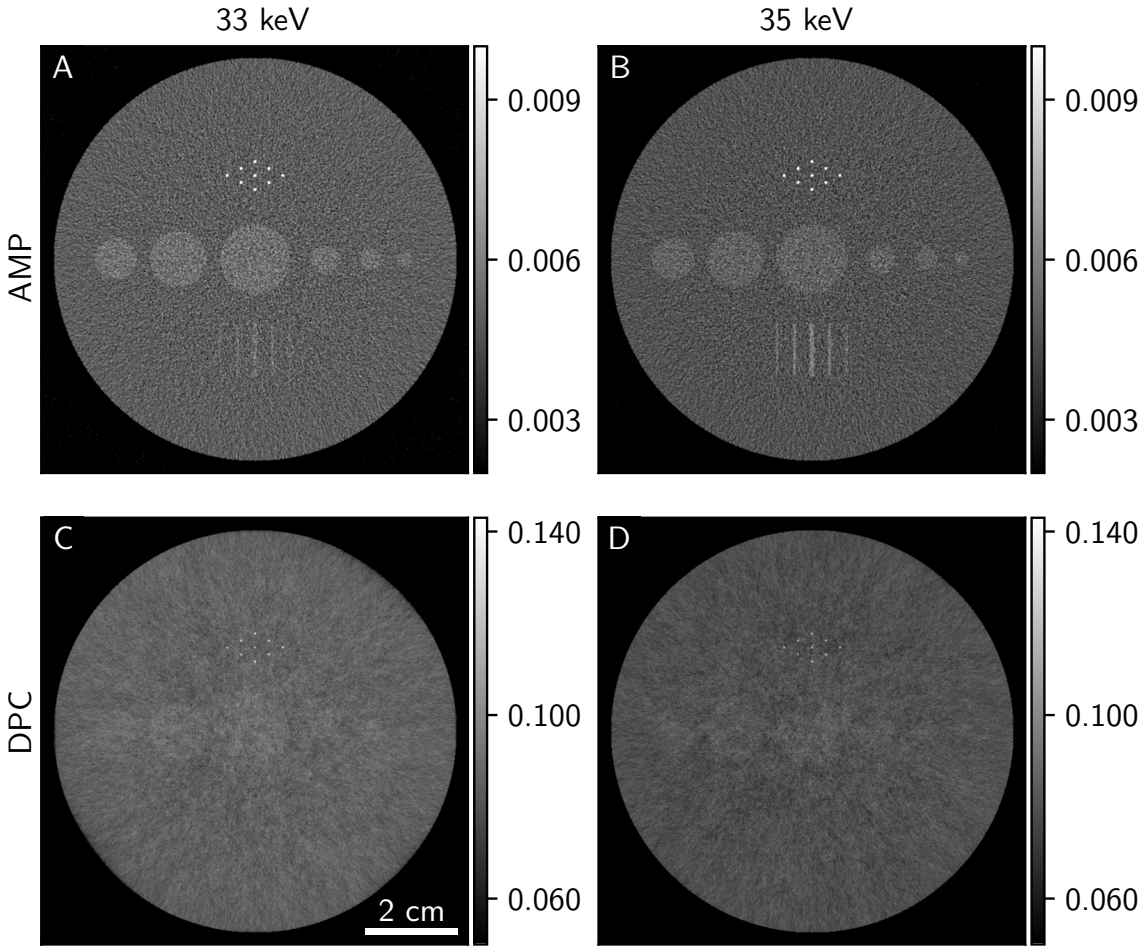

Figure 6.7: Attenuation and differential phase-contrast images for the BCT phantom. The exemplary slices are shown for the (A, B) attenuation and (C, D) the phase-contrast reconstructions for a MGD of 5 mGy. The left column represents the results from the lower (33 keV) and the right one the higher energy (35 keV). Images are windowed for maximum detail visibility.

Structure	AMP low	AMP high	DPC low	DPC high
	100 mGy			
Tumor	4.66	4.26	3.14	2.70
	4.66	4.28	3.36	3.09
	4.82	4.36	3.19	3.31
	4.64	4.29	2.90	3.56
	4.76	4.37	3.31	3.19
	4.53	4.48	3.41	3.08
Microcalcification	96.62	86.91	33.57	33.20
Iohexol	5.17	11.00	1.90	1.24
	5.08	10.45	1.27	1.39
	3.25	7.08	0.80	1.14
	5 mGy			
Tumor	1.00	0.94	1.07	1.01
	1.04	1.01	0.73	0.50
	1.10	0.98	0.77	1.00
	0.95	1.06	0.74	1.06
	1.10	0.99	1.22	1.06
	0.97	1.27	0.95	1.20
Microcalcification	21.17	20.54	5.80	7.17
Iohexol	1.21	2.60	0.21	0.34
	1.21	2.50	0.37	0.63
	0.83	1.41	0.24	0.01

Table 6.4: CNR values for all structures of the reconstructed attenuation and phase-contrast CT images. The values are calculated for the low-energy (33 keV) and the high-energy (35 keV) images.

Bibliography

[Ahmad, 2015] Ahmad, R., Ding, Y. & Simonetti, O. Edge Sharpness Assessment by Parametric Modeling: Application to Magnetic Resonance Imaging. *Concepts in Magnetic Resonance Part A* **44,** 138–149 (2015) (Cited on page 48).

[Ajmal, 2021] Ajmal, M., Khan, M. & van Fossen, K. Breast Fibroadenoma. *StatPearls* (2021) (Cited on page 63).

[Allner, 2022] Allner, S. *Practical Aspects of X-ray Computed Tomography: Preprocessing, Geometry and More.* To be submitted. PhD thesis (Technical University of Munich, 2022) (Cited on page 71).

[AlsNielsen, 2011] Als-Nielsen, J. & McMorrow, D. *Elements of modern X-ray Physics* (John Wiley & Sons, 2011) (Cited on page 7).

[Alvarez, 1976] Alvarez, R. E. & Macovski, A. Energy-selective reconstructions in X-ray computerised tomography. *Physics in Medicine and Biology* **21,** 002 (1976) (Cited on pages 39, 90).

[Arboleda, 2019] Arboleda, C. *et al.* Towards clinical grating-interferometry mammography. *European Radiology* **30,** 1419–1425 (2019) (Cited on pages 4, 56, 90).

[Arfelli, 2000] Arfelli, F. *et al.* Mammography with Synchrotron Radiation: Phase-Detection Techniques. *Radiology* **215,** 286–293 (2000) (Cited on pages 3, 56).

[Attix, 1979] Attix, F. H. Dedicated breast computed tomography: Basic aspects. *Health Physics* **36,** 347–354 (3 1979) (Cited on page 44).

[Attwood, 2007] Attwood, D. *Soft X-Rays and Extreme Ultraviolet Radiation: Principles and Applications* 1st (Cambridge University Press, 2007) (Cited on page 7).

[Auweter, 2014] Auweter, S. D. *et al.* X-ray phase-contrast imaging of the breast—advances towards clinical implementation. *The British Journal of Radiology* **87,** 20130606 (2014) (Cited on pages 4, 56, 90).

[Ballabriga, 2007] Ballabriga, R., Campbell, M., Heijne, E., Llopart, X. & Tlustos, L. The Medipix3 Prototype, a Pixel Readout Chip Working in Single Photon Counting Mode With Improved Spectrometric Performance. *Nuclear Science, IEEE Transactions on* **54,** 1824–1829 (2007) (Cited on page 16).

[Ballabriga, 2013] Ballabriga, R. *et al.* The Medipix3RX: A high resolution, zero dead-time pixel detector readout chip allowing spectroscopic imaging. *Journal of Instrumentation* **8,** C02016 (2013) (Cited on page 16).

[Ballabriga, 2016] Ballabriga, R. *et al.* Review of hybrid pixel detector readout ASICs for spectroscopic X-ray imaging. *Journal of Instrumentation* **11,** P01007–P01007 (2016) (Cited on page 16).

[Bayes, 1763] Bayes, T. An essay towards solving a problem in the doctrine of chances. *Philosophical Transactions of the Royal Society of London* **53,** 370–418 (1763) (Cited on page 31).

[Bech, 2009] Bech, M. *X-ray Imaging with a Grating Interferometer.* PhD thesis (University of Copenhagen, 2009) (Cited on page 24).

[Behling, 2015] Behling, R. *Modern Diagnostic X-Ray Sources: Technology, Manufacturing, Reliability* (2015) (Cited on page 52).

[Berg, 2008] Berg, W. *et al.* Combined Screening With Ultrasound and Mammography vs Mammography Alone in Women With Elevated Risk of Breast Cancer. *JAMA: The journal of the American Medical Association* **299,** 2151–63 (2008) (Cited on page 2).

[Berger, 2019a] Berger, N., Marcon, M., Frauenfelder, T. & Boss, A. Dedicated Spiral Breast Computed Tomography With a Single Photon-Counting Detector: Initial Results of the First 300 Women. *Investigative Radiology* **55,** 68–72 (2019) (Cited on page 3).

[Berger, 2022] Berger, N. *et al.* Contrast Media–Enhanced Breast Computed Tomography With a Photon-Counting Detector: Initial Experiences on In Vivo Image Quality and Correlation to Histology. *Investigative Radiology* **Publish Ahead of Print** (2022) (Cited on page 3).

[Berger, 2019b] Berger, N. *et al.* Dedicated Breast Computed Tomography With a Photon-Counting Detector: Initial Results of Clinical In Vivo Imaging. *Investigative Radiology* **54,** 409–418 (2019) (Cited on pages 3, 72, 127).

[Berthe, 2021] Berthe, D. *Developing a Fast Grating-Based Phase-Contrast Breast-CT with a Polychromatic X-Ray Source* MA thesis (Technical University of Munich, 2021) (Cited on pages 74, 84).

[Bevins, 2011] Bevins, N., Zambelli, J., Li, K., Qi, Z. & Chen, G.-H. Multicontrast x-ray computed tomography imaging using Talbot-Lau interferometry without phase stepping. *Medical Physics* **39,** 424–428 (2011) (Cited on page 75).

[Birnbacher, 2018] Birnbacher, L. *et al.* Accurate effective atomic number determination with polychromatic grating-based phase-contrast computed tomography. *Optics Express* **26,** 15153–15166 (2018) (Cited on page 41).

[Bonse, 1965] Bonse, U. & Hart, M. An X-ray Interferometer. *Applied Physics Letters* **6,** 155–156 (1965) (Cited on page 20).

[Boone, 2002] Boone, J. Normalized glandular dose (DgN) coefficients for arbitrary X-ray spectra in mammography: computer-fit values of Monte Carlo derived data. *Medical Physics* **29,** 869–875 (2002) (Cited on page 45).

[Boone, 1999] Boone, J. M. Glandular Breast Dose for Monoenergetic and High-Energy X-ray Beams: Monte Carlo Assessment. *Radiology* **213,** 23–37 (1999) (Cited on page 45).

[Boone, 1992] Boone, J. M. Parametrized x-ray absorption in diagnostic radiology from Monte Carlo calculations: Implications for x-ray detector design. *Medical Physics* **19,** 1467–1473 (1992) (Cited on page 106).

[Boone, 1996] Boone, J. M. & Chavez, A. E. Comparison of x-ray cross sections for diagnostic and therapeutic medical physics. *Medical Physics* **23,** 1997–2005 (1996) (Cited on page 98).

[Boone, 2001] Boone, J. M., Nelson, T. R., Lindfors, K. K. & Seibert, J. A. Dedicated Breast CT: Radiation Dose and Image Quality Evaluation. *Radiology* **221,** 657–667 (2001) (Cited on pages 2, 55).

[Boone, 2006] Boone, J. M. *et al.* Computed Tomography for Imaging the Breast. *Journal of Mammary Gland Biology and Neoplasia* **11,** 103–111 (2006) (Cited on pages 2, 55).

[Boreman, 2001] Boreman, G. *Modulation Transfer Function in Optical and Electro-optical Systems* (Society of Photo Optical, 2001) (Cited on page 52).

[Braig, 2018] Braig, E. *et al.* Direct quantitative material decomposition employing grating-based X-ray phase-contrast CT. *Scientific Reports* **8,** 16394 (2018) (Cited on pages 36, 37).

[Breitenhuber, 2020] Breitenhuber, G. *Experimental Validation of Dual-Energy Spectral Differential Phase Contrast for Breast Imaging with a Polychromatic X-ray Source* (2020) (Cited on page 128).

[Brombal, 2019] Brombal, L. *et al.* Image quality comparison between a phase-contrast synchrotron radiation breast CT and a clinical breast CT: a phantom based study. *Scientific Reports* **9,** 17778 (2019) (Cited on pages 4, 58).

[Brombal, 2018a] Brombal, L. *et al.* Monochromatic breast computed tomography with synchrotron radiation: phase-contrast and phase-retrieved image comparison and full-volume reconstruction. *Journal of Medical Imaging* **6,** 1–9 (2018) (Cited on pages 3, 58).

[Brombal, 2018b] Brombal, L. *et al. Monochromatic breast CT: absorption and phase-retrieved images* in *Medical Imaging 2018: Physics of Medical Imaging* (SPIE, 2018), 71 (Cited on pages 4, 58).

[Brombal, 2018c] Brombal, L. *et al.* Phase-contrast breast CT: the effect of propagation distance. *Physics in Medicine and Biology* **63,** 24NT03 (2018) (Cited on pages 4, 58).

[Buhr, 2012] Buhr, H., Büermann, L., Gerlach, M., Krumrey, M. & Rabus, H. Measurement of the mass energy-absorption coefficient of air for x-rays in the range from 3 to 60 keV. *Physics in Medicine and Biology* **57,** 8231–8247 (2012) (Cited on page 45).

[Buzug, 2008] Buzug, T. M. *Computed Tomography* (Springer Berlin Heidelberg, 2008) (Cited on pages 7, 26, 29, 52).

[Carmeliet, 2000] Carmeliet, P. & Jain, R. K. Angiogenesis in cancer and other diseases. *Nature* **407,** 249–257 (2000) (Cited on page 2).

[Castelli, 2011] Castelli, E. *et al.* Mammography with Synchrotron Radiation: First Clinical Experience with Phase-Detection Technique. *Radiology* **259,** 684–694 (2011) (Cited on pages 3, 56).

[Chabior, 2011] Chabior, M. *et al.* Beam hardening effects in grating-based x-ray phase-contrast imaging. *Medical physics* **38,** 1189–1195 (2011) (Cited on page 90).

[Chang, 1978] Chang, C. H. J. *et al.* Computed tomographic evaluation of the breast. *American journal of roentgenology* **131,** 459–464 (1978) (Cited on pages 2, 55).

[Chang, 1980] Chang, C. H. J. *et al.* Computed tomography in detection and diagnosis of breast cancer. *Cancer* **46,** 939–946 (1980) (Cited on pages 2, 55).

[Chang, 1977] Chang, C. H. J. *et al.* Computed tomography of the breast. A preliminary report. *Radiology* **124,** 827–829 (1977) (Cited on pages 2, 55).

[Clevert, 2007] Clevert, D. A., Jung, E. M., Jungius, K.-P., Ertan, K. & Kubale, R. Value of tissue harmonic imaging (THI) and contrast harmonic imaging (CHI) in detection and characterisation of breast tumours. *European Radiology* **17,** 1–10 (2007) (Cited on page 2).

[Cloetens, 1999] Cloetens, P. *et al.* HoloTomography: Quantitative Phase Tomography with micrometer resolution using hard Synchrotron Radiation X-rays. *Applied Physics Letters* **75,** 2912–2914 (1999) (Cited on page 20).

[Cont, 2016] Cont, D. *X-Ray Beam Characterization at the Munich Compact Light Source* MA thesis (2016) (Cited on page 46).

[ABCT, 2020] AB-CT. *(Advanced Breast-CT GmbH)* `https://www.ab-ct.com/` (Cited on pages 2, 3, 5, 55, 71, 77, 127).

[Dance, 1990] Dance, D. R. Monte-Carlo calculation of conversion factors for the estimation of mean glandular breast dose. *Physics in Medicine and Biology* **35,** 1211–1220 (1990) (Cited on page 45).

[Dance, 2000] Dance, D. R., Skinner, C. L., Young, K. C., Beckett, J. R. & Kotre, C. J. Additional factors for the estimation of mean glandular breast dose using the UK mammography dosimetry protocol. *Physics in Medicine and Biology* **45,** 3225–3240 (2000) (Cited on page 45).

[Dance, 1999] Dance, D. R., Skinner, C. & Carlsson, G. Breast dosimetry. *Applied Radiation and Isotopes* **50,** 185–203 (1999) (Cited on page 45).

[Dance, 2016] Dance, D. & Sechopoulos, I. Dosimetry in x-ray-based breast imaging. *Physics in Medicine and Biology* **61,** R271–R304 (2016) (Cited on page 43).

[David, 2002] David, C., Nöhammer, B., Solak, H. H. & Ziegler, E. Differential X-ray Phase Contrast Imaging using a Shearing Interferometer. *Applied Physics Letters* **81,** 3287–3289 (2002) (Cited on page 21).

[Davis, 1995] Davis, T., Gao, D., Gureyev, T., Stevenson, A. & Wilkins, S. Phase-Contrast imaging of weakly absorbing materials using hard X-rays. *Nature* **373,** 595–598 (1995) (Cited on pages 12, 20).

[DECTRIS, 2019] DECTRIS. *Technical Specifications SANTIS 0808 GaAs Detector Systems* 2019 (Cited on page 60).

[Delogu, 2019] Delogu, P. *et al.* Optimization of the energy for Breast monochromatic absorption X-ray Computed Tomography. *Scientific Reports* **9,** 13135 (2019) (Cited on pages 4, 58).

[Destounis, 2017] Destounis, S. *et al.* Using Volumetric Breast Density to Quantify the Potential Masking Risk of Mammographic Density. *American Journal of Roentgenology* **208,** 222–227 (2017) (Cited on page 1).

[Donath, 2009] Donath, T. *et al.* Inverse geometry for grating-based x-ray phase-contrast imaging. *Journal of Applied Physics* **106,** 054703–054703 (2009) (Cited on page 42).

[Eggl, 2017] Eggl, E. *Biomedical Imaging At a Compact Synchrotron Source.* PhD thesis (Technical University of Munich, 2017) (Cited on page 45).

[Eggl, 2018] Eggl, E. *et al.* Dose-compatible grating-based phase-contrast mammography on mastectomy specimens using a compact synchrotron source. *Scientific Reports* **8,** 15700 (2018) (Cited on pages 4, 58, 63, 90).

[Eggl, 2016a] Eggl, E. *et al.* The Munich Compact Light Source: initial performance measures. *Journal of Synchrotron Radiation* **23,** 1137–1142 (2016) (Cited on page 14).

[Eggl, 2016b] Eggl, E. *et al.* X-ray phase-contrast tomosynthesis of a human ex vivo breast slice with an inverse Compton x-ray source. *European Physics Letters* **116,** 68003 (2016) (Cited on pages 4, 58).

[Ehn, 2017] Ehn, S. *Photon-counting hybrid-pixel detectors for spectral x-ray imaging applications.* PhD thesis (Technical University of Munich, 2017) (Cited on pages 20, 39).

[Ehn, 2017] Ehn, S. *et al.* Basis material decomposition in spectral CT using a semi-empirical, polychromatic adaption of the Beer–Lambert model. *Physics in Medicine and Biology* **62,** N1–N17 (2017) (Cited on pages 5, 90).

[Elmer, 2012] Elmer, P. *Product Note Flat Panel X-ray Detectors - DEXELA 1207, 1512, 2307, 2315 and 2923.* 2012 (Cited on page 60).

[ElSaid, 2014] ElSaid, N. A. E., Farouk, S., Shetat, O. M. M., Khalifa, N. M. & Nada, O. M. Contrast enhanced digital mammography: Is it useful in detecting lesions in edematous breast? *Egyptian Society of Radiology and Nuclear Medicine* **146,** 371–381 (2014) (Cited on page 89).

[Fallenberg, 2014] Fallenberg, E. *et al.* Contrast-enhanced spectral mammography: Does mammography provide additional clinical benefits or can some radiation exposure be avoided? *Breast Cancer Research and Treatment* **146** (2014) (Cited on page 89).

[Flohr, 2020] Flohr, T., Ulzheimer, S., Petersilka, M. & Schmidt, B. Basic principles and clinical potential of photon-counting detector CT. *Chinese Journal of Academic Radiology* **3,** 19–34 (2020) (Cited on page 5).

[Gammex, 2015] Gammex. *Mammo 156 Phantom* `https://www.sunnuclear.com/documents/datasheets/gammex/156phantom.pdf` (2017) (Cited on page 93).

[Gradl, 2019] Gradl, R. *Dynamic phase-contrast X-ray imaging at an inverse Compton source.* PhD thesis (Technical University of Munich, 2019) (Cited on page 14).

[Grandl, 2013] Grandl, S. *et al.* Evaluation of phase-contrast CT of breast tissue at conventional X-ray sources - presentation of selected findings. *Zeitschrift fur medizinische Physik* **23,** 212–221 (2013) (Cited on page 4).

[Grandl, 2022] Grandl, S. *et al.* Grating-based phase contrast mammography: Assessing complementary diagnostic information of Dark Field Breast Imaging. An ex-vivo set-up. *To be submitted* (2022) (Cited on pages 4, 77).

[Grandl, 2015] Grandl, S. *et al.* Improved visualization of breast cancer features in multifocal carcinoma using phase-contrast and dark-field mammography: an ex vivo study. *European Radiology* **25,** 3659–3668 (2015) (Cited on pages 4, 56, 90).

[Grandl, 2014] Grandl, S. *et al.* Visualizing Typical Features of Breast Fibroadenomas Using Phase-Contrast CT: An Ex-Vivo Study. *PLOS ONE* **9,** e97101 (2014) (Cited on pages 4, 56).

[GratXray, 2022] GratXray. *(GratXray AG)* `https://www.gratxray.com/` (Cited on page 4).

[Günther, 2021] Günther, B. *Stoarge ring-based inverse Compton X-ray sources.* PhD thesis (Technical University of Munich, 2021) (Cited on page 14).

[Günther, 2020] Günther, B. *et al.* The versatile X-ray beamline of the Munich Compact Light Source: Design, instrumentation and applications. *Journal of Synchrotron Radiation* **27,** 1395–1414 (2020) (Cited on pages 14, 17, 91).

[Gureyev, 2009] Gureyev, T. *et al.* Refracting Röntgen's rays: Propagation-based x-ray phase contrast for biomedical imaging. *Journal of Applied Physics* **105,** 102005 (2009) (Cited on pages 3, 56).

[Haas, 2011] Haas, W. *et al. Phase-unwrapping of differential phase-contrast data using attenuation information* in *Medical Imaging 2011: Image Processing* **7962** (SPIE, 2011), 1487–1492 (Cited on page 90).

[Hahn, 2014] Hahn, D. *Statistical IteRative Reconstruction for X-ray Phase-Contrast Computed Tomography.* PhD thesis (Technical University of Munich, 2014) (Cited on pages 26, 31).

[Haka, 2005] Haka, A. S. *et al.* Diagnosing breast cancer by using Raman spectroscopy. *Proceedings of the National Academy of Sciences* **102,** 12371–12376 (2005) (Cited on pages 37, 80).

[Harrison, 2015] Harrison, J. & Lopez, P. Use of effective dose in medicine. *Annals of the ICRP* **44,** 221–228 (2015) (Cited on page 45).

[Hauser, 2014] Hauser, N. *et al.* A Study on Mastectomy Samples to Evaluate Breast Imaging Quality and Potential Clinical Relevance of Differential Phase Contrast Mammography. *Investigative Radiology* **49,** 131–137 (2014) (Cited on pages 4, 56, 90).

[Heck, 2020] Heck, L. & Herzen, J. Recent advances in X-ray imaging of breast tissue: From two- to three-dimensional imaging. *Physica Medica* **79,** 69–79 (2020) (Cited on pages 1, 55, 57, 73, 90).

[Heck, 2019] Heck, L. *et al.* Contrast-enhanced spectral mammography with a compact synchrotron source. *PLOS ONE* **14,** e0222816 (2019) (Cited on pages 4, 5, 58, 63, 90).

[Heck, 2022] Heck, L. *et al.* Spectral Differential Phase Contrast X-ray Mammography. *Submitted* (2022) (Cited on pages 5, 89).

[Hellerhoff, 2019] Hellerhoff, K. *et al.* Assessment of intraductal carcinoma in situ (DCIS) using grating-based X-ray phase-contrast CT at conventional X-ray sources: An experimental ex-vivo study. *PLOS ONE* **14,** e0210291 (2019) (Cited on pages 4, 56).

[Helvie, 1994] Helvie, M., Chan, H.-P., Adler, D. & Boyd, P. Breast thickness in routine mammograms: Effect on image quality and radiation dose. *American Journal of Roentgenology* **163,** 1371–1374 (1994) (Cited on page 94).

[Hendrick, 2019] Hendrick, R. E., Baker, J. A. & Helvie, M. A. Breast cancer deaths averted over 3 decades. *Cancer* **125,** 1482–1488 (2019) (Cited on page 1).

[Herzen, 2009] Herzen, J. *et al.* Quantitative phase-contrast tomography of a liquid phantom using a conventional x-ray tube source. *Optics Express* **17,** 10010–10018 (2009) (Cited on page 37).

[Hsieh, 2003] Hsieh, J. *Computed Tomography: Principles, Design, Artifacts, and recent Advances* (SPIE press, 2003) (Cited on pages 26, 31).

[IAEA, 2007] IAEA. *International Atomic Energy Agency. Dosimetry in Diagnostic Radiology: an International Code of Practice* tech. rep. 457 (International Atomic Energy Agency, Vienna, 2007) (Cited on page 44).

[Ingal, 1995] Ingal, V. & Beliaevskaya, E. X-ray plane-wave Topography Observation of the Phase Contrast from a non-crystalline Object. *Journal of Physics D: Applied Physics* **28,** 2314 (1995) (Cited on page 20).

[James, 2017] James, J., Pavlicek, W., Hanson, J., Boltz, T. & Patel, B. Breast Radiation Dose With CESM Compared With 2D FFDM and 3D Tomosynthesis Mammography. *American Journal of Roentgenology* **208,** 362–372 (2 2017) (Cited on pages 2, 89).

[Ji, 2020] Ji, X., Zhang, R., li ke, k. & Chen, G.-H. Dual Energy Differential Phase Contrast CT (DE-DPC-CT) Imaging. *IEEE Transactions on Medical Imaging* **PP,** 1–1 (2020) (Cited on pages 126, 131).

[Johns, 1987] Johns, P. & Yaffe, M. X-ray characterisation of normal and neoplastic breast tissues. *Physics in Medicine and Biology* **32,** 675–695 (1987) (Cited on page 98).

[Kak, 1988] Kak, A. & Slaney, M. *Principles of Computerized Tomographic Imaging* (IEEE Press, 1988) (Cited on pages 7, 26, 29, 30).

[Kalender, 2012] Kalender, W. A. *et al.* High-resolution spiral CT of the breast at very low dose: concept and feasibility considerations. *European Radiology* **22,** 1–8 (2012) (Cited on pages 2, 55, 63, 72, 127).

[Kalender, 2017] Kalender, W. A. *et al.* Technical feasibility proof for high-resolution low-dose photon-counting CT of the breast. *European Radiology* **27,** 1081–1086 (2017) (Cited on pages 2, 55, 63, 72, 127).

[Kay, 1997] Kay, S. M. *Fundamentals of Statistical Signal Processing: Estimation Theory* (Prentice Hall, 1997) (Cited on page 49).

[Kelcz, 1979] Kelcz, F., Joseph, P. & Hilal, S. Noise considerations in dual energy CT scanning. *Medical physics* **6,** 418–425 (1979) (Cited on page 90).

[Keyriläinen, 2008] Keyriläinen, J. *et al.* Toward High-Contrast Breast CT at Low Radiation Dose. *Radiology* **249,** 321–327 (2008) (Cited on page 56).

[Klaar, 2021] Klaar, R. *Application of Spectral Differential Phase Contrast in Breast Imaging* MA thesis (Technical University of Munich, 2021) (Cited on pages 89, 128).

[Koehler, 2015] Koehler, T. *et al.* Slit-scanning differential x-ray phase-contrast mammography: Proof-of-concept experimental studies. *Medical Physics* **42,** 1959 (2015) (Cited on pages 4, 56, 90).

[Koning, 2019] Koning. *Koning Breast CT (KBCT)* 2019 (Cited on pages 2, 3, 55).

[Krenkel, 2016] Krenkel, M., Töpperwien, M., Dullin, C., Alves, F. & Salditt, T. Propagation-based phase-contrast tomography for high-resolution lung imaging with laboratory sources. *AIP Advances* **6,** 035007 (2016) (Cited on pages 3, 56).

[Krieger, 2012] Krieger, H. *Grundlagen der Strahlungsphysik und des Strahlenschutzes; 4th rev. ed.* (Springer Spektrum, Wiesbaden, 2012) (Cited on page 43).

[Kuhl, 1999] Kuhl, C. *et al.* Dynamic Breast MR Imaging: Are Signal Intensity Time Course Data Useful for Differential Diagnosis of Enhancing Lesions? *Radiology* **211,** 101–110 (1999) (Cited on page 2).

[Kuzmiak, 2016] Kuzmiak, C. M. *et al.* Dedicated Three-dimensional Breast Computed Tomography: Lesion Characteristic Perception by Radiologists. *Journal of Clinical Imaging Science* **6,** 14 (2016) (Cited on pages 2, 55).

[Lewis, 2018] Lewis, S. J. *et al. Towards clinic-friendly solutions for patient trials in breast cancer phase contrast imaging* in *14th International Workshop on Breast Imaging (IWBI 2018)* **10718** (SPIE, 2018), 448–453 (Cited on pages 4, 58).

[Lindfors, 2008] Lindfors, K. K. *et al.* Dedicated Breast CT: Initial Clinical Experience. *Radiology* **246,** 725–733 (2008) (Cited on pages 2, 55).

[Long, 2014] Long, Y. & Fessler, J. A. Multi-Material Decomposition Using Statistical Image Reconstruction for Spectral CT. *IEEE Transactions on Medical Imaging* **33,** 1614–1626 (2014) (Cited on page 40).

[Longo, 2019] Longo, R. *et al.* Advancements towards the implementation of clinical phase-contrast breast computed tomography at Elettra. *Journal of Synchrotron Radiation* **26,** 1343–1353 (2019) (Cited on pages 4, 58).

[Longo, 2014] Longo, R. *et al.* Clinical study in phase- contrast mammography: image-quality analysis. *Philosophical Transactions of the Royal Society A: Mathematical, Physical and Engineering Sciences* **372,** 20130025 (2014) (Cited on pages 3, 56).

[Longo, 2020] Longo, R. *et al. Lesion visibility in phase-contrast breast CT: comparison with histological images* in *15th International Workshop on Breast Imaging (IWBI2020)* (SPIE, 2020), 68 (Cited on pages 4, 58).

[Longo, 2016] Longo, R. *et al.* Towards breast tomography with synchrotron radiation at Elettra: first images. *Physics in Medicine and Biology* **61,** 1634–1649 (2016) (Cited on pages 3, 56).

[Lusic, 2013] Lusic, H. & Grinstaff, M. W. X-ray-Computed Tomography Contrast Agents. *Chemical Reviews* **113,** 1641–1666 (2013) (Cited on page 2).

[Lyncean, 2022] Lyncean. *THE LYNCEAN COMPACT LIGHT SOURCE – A breakthrough in local, on-demand X-ray synchrotron light* Website. 2022 (Cited on page 13).

[Mandelson, 2000] Mandelson, M. T. Breast Density as a Predictor of Mammographic Detection: Comparison of Interval- and Screen-Detected Cancers. *Journal of the National Cancer Institute* **92,** 1081–1087 (2000) (Cited on page 1).

[Mechlem, 2020] Mechlem, K. *Towards low-dose spectral phase-contrast X-ray imaging.* PhD thesis (Technical University of Munich, 2020) (Cited on page 41).

[Mechlem, 2019a] Mechlem, K., Sellerer, T., Herzen, J. & Pfeiffer, F. *Statistical iterative reconstruction for spectral phase contrast CT* in *15th International Meeting on Fully Three-Dimensional Image Reconstruction in Radiology and Nuclear Medicine* (SPIE, 2019) (Cited on pages 90, 127, 131).

[Mechlem, 2020] Mechlem, K., Sellerer, T., Viermetz, M., Herzen, J. & Pfeiffer, F. A theoretical framework for comparing noise characteristics of spectral, differential phase-contrast and spectral differential phase-contrast x-ray imaging. *Physics in Medicine and Biology* **65,** 065010 (2020) (Cited on pages 5, 39, 41, 49, 50, 90, 99).

[Mechlem, 2019b] Mechlem, K., Sellerer, T., Viermetz, M., Herzen, J. & Pfeiffer, F. Spectral Differential Phase Contrast X-Ray Radiography. *IEEE Transactions on Medical Imaging* **PP,** 1–1 (2019) (Cited on pages 39–41, 90, 126).

[Mechlem, 2018a] Mechlem, K. *et al.* Joint Statistical Iterative Material Image Reconstruction for Spectral Computed Tomography Using a Semi-Empirical Forward Model. *IEEE Transactions on Medical Imaging* **37,** 68–80 (2018) (Cited on pages 5, 90).

[Mechlem, 2018b] Mechlem, K. *et al.* Spectral Angiography Material Decomposition Using an Empirical Forward Model and a Dictionary-Based Regularization. *IEEE Transactions on Medical Imaging* **37,** 2298–2309 (2018) (Cited on pages 5, 40, 90).

[Momose, 2003] Momose, A. Phase-sensitive Imaging and Phase Tomography using X-ray Interferometers. *Optics Express* **11,** 2303–2314 (2003) (Cited on pages 3, 20, 56).

[Natterer, 1986] Natterer, F. *The Mathematics of Computerized Tomography* (Vieweg + Teubner Verlag, Wiesbaden, 1986) (Cited on page 30).

[Nenot, 2009] Nenot, J.-C., Brenot, J., Laurier, D., Rannou, A. & Thierry, D. *ICRP Publication 103: The 2007 Recommendations of the International Commission on Radiological Protection* tech. rep. (2009), 417 (Cited on page 43).

[Nosratieh, 2015] Nosratieh, A. *et al.* Mean glandular dose coefficients (DgN) for x-ray spectra used in contemporary breast imaging systems. *Physics in Medicine and Biology* **60,** 7179–7190 (2015) (Cited on page 45).

[OConnell, 2017] O'Connell, A., Karellas, A., Vedantham, S. & Kawakyu-O'Connor, D. Newer Technologies in Breast Cancer Imaging: Dedicated Cone-Beam Breast CT. *Seminars in Ultrasound, CT and MRI* **39** (2017) (Cited on page 55).

[OGrady, 2018] O'Grady, S. & Morgan, M. Microcalcifications in breast cancer: From pathophysiology to diagnosis and prognosis. *Biochimica et Biophysica Acta (BBA) - Reviews on Cancer* **1869,** 310–320 (2018) (Cited on page 4).

[Olivo, 2014] Olivo, A. & Castelli, E. X-ray phase contrast imaging: From synchrotrons to conventional sources. *Rivista del Nuovo Cimento* **37,** 467–508 (2014) (Cited on pages 3, 56).

[Olivo, 2009] Olivo, A. *et al.* Phase contrast imaging of breast tumours with synchrotron radiation. *Applied Radiation and Isotopes* **67,** 1033–1041 (2009) (Cited on pages 3, 56).

[Orel, 1999] Orel, S. G. Differentiating Benign from Malignant Enhancing Lesions Identified at MR Imaging of the Breast: Are Time-Signal Intensity Curves an Accurate Predictor? *Radiology* **211,** 5–7 (1999) (Cited on page 2).

[Paap, 2011] Paap, E., Verbeek, A., Puliti, D., Paci, E. & Broeders, M. Breast cancer screening case–control study design: impact on breast cancer mortality. *Annals of Oncology* **22,** 863–869 (2011) (Cited on page 1).

[Paap, 2014] Paap, E. *et al.* Breast cancer screening halves the risk of breast cancer death: A case-referent study. *The Breast* **23,** 439–444 (2014) (Cited on page 1).

[Paci, 2014] Paci, E., Broeders, M., Hofvind, S., Puliti, D. & Duffy, S. W. European Breast Cancer Service Screening Outcomes: A First Balance Sheet of the Benefits and Harms. *Cancer Epidemiology Biomarkers & Prevention* **23,** 1159–1163 (2014) (Cited on page 1).

[Pacilè, 2018] Pacilè, S. *et al.* Advantages of breast cancer visualization and characterization using synchrotron radiation phase-contrast tomography. *Journal of Synchrotron Radiation* **25,** 1460–1466 (2018) (Cited on pages 3, 58).

[Pacilè, 2019] Pacilè, S. *et al.* Free propagation phase-contrast breast CT provides higher image quality than cone-beam breast-CT at low radiation doses: a feasibility study on human mastectomies. *Scientific Reports* **9,** 13762 (2019) (Cited on pages 4, 58).

[Pennicard, 2013] Pennicard, D. *et al.* The LAMBDA photon-counting pixel detector. *Journal of Physics: Conference Series* **425,** 062010 (2013) (Cited on page 16).

[Perry, 2006] Perry, N. *et al.* European guidelines for quality assurance in breast cancer screening and diagnosis. *European Guidelines* (2006) (Cited on pages 56, 106).

[PetoussiHenss, 2010] Petoussi-Henss, N. *et al.* ICRP Publication 116. Conversion coefficients for radiological protection quantities for external radiation exposures. *Annals of the ICRP* **40,** 1–257 (2010) (Cited on page 43).

[Pfeiffer, 2007] Pfeiffer, F., Kottler, C., Bunk, O. & David, C. Hard X-ray Phase Tomography with Low-Brilliance Sources. *Physical Review Letters* **98,** 108105 (2007) (Cited on pages 4, 21, 22, 30, 56).

[Pfeiffer, 2006] Pfeiffer, F., Weitkamp, T., Bunk, O. & David, C. Phase retrieval and differential phase-contrast imaging with low-brilliance X-ray sources. *Nature Physics* **2,** 258–261 (2006) (Cited on pages 3, 4, 22, 23, 56, 90).

[Pfeiffer, 2008] Pfeiffer, F. *et al.* Hard-X-ray Dark-Field Imaging using a Grating Interferometer. *Nature Materials* **7,** 134–137 (2008) (Cited on pages 4, 22, 23, 56).

[Piai, 2019] Piai, A. *et al.* Quantitative characterization of breast tissues with dedicated CT imaging. *Physics in Medicine and Biology* **64,** 155011 (2019) (Cited on pages 4, 58).

[Podgorsak, 2010] Podgorsak, E. B. *Radiation Physics for Medical Physicists* (Springer Berlin Heidelberg, Berlin, Heidelberg, 2010) (Cited on pages 7, 9).

[Prionas, 2010] Prionas, N. D. *et al.* Contrast-enhanced Dedicated Breast CT: Initial Clinical Experience. *Radiology* **256,** 714–723 (2010) (Cited on pages 2, 55).

[Qi, 2010] Qi, Z., Zambelli, J., Bevins, N. & Chen, G.-H. Quantitative imaging of electron density and effective atomic number using phase contrast CT. *Physics in Medicine and Biology* **55,** 2669–2677 (2010) (Cited on page 41).

[Radon, 1986] Radon, J. On the determination of functions from their integral values along certain manifolds. *IEEE Transactions on Medical Imaging* **5,** 170–176 (1986) (Cited on page 26).

[Ramachandran, 1971] Ramachandran, G. N. & Lakshminarayanan, A. V. Three-dimensional reconstruction from radiographs and electron micrographs: application of convolutions instead of Fourier transforms. *Proceedings of the National Academy of Sciences of the United States of America* **68,** 2236–40 (1971) (Cited on page 30).

[Rauch, 2020] Rauch, T. *et al.* Discrimination Analysis of Breast Calcifications using X-Ray Dark-Field Radiography. *Medical Physics* **47,** 1813–1826 (2020) (Cited on page 4).

[Resch, 2021] Resch, S. *Recent Developments in Grating-Based Phase-Contrast Breast Computed Tomography at the Munich Compact Light Source* MA thesis (Technical University of Munich, 2021) (Cited on pages 36, 55, 71, 72).

[Roessl, 2009] Roessl, E. & Herrmann, C. Cramér–Rao lower bound of basis image noise in multiple-energy x-ray imaging. *Physics in Medicine and Biology* **54,** 1307–1318 (2009) (Cited on page 50).

[Roessl, 2007] Roessl, E. & Proksa, R. K-edge imaging in x-ray computed tomography using multi-bin photon counting detectors. *Physics in Medicine and Biology* **52,** 4679–4696 (2007) (Cited on page 40).

[Russo, 2017] Russo, P. *Handbook of X-ray Imaging: Physics and Technology* (Taylor & Francis, 2017) (Cited on pages 7, 52).

[Ruth, 2020] Ruth, V., Kolditz, D., Steiding, C. & Kalender, W. Investigation of Spectral Performance for Single-Scan Contrast-Enhanced Breast-CT Using Photon-Counting Technology: A Phantom Study. *Medical Physics* **47,** 2826–2837 (2020) (Cited on page 5).

[Sankatsing, 2017] Sankatsing, V. D. *et al.* The effect of population-based mammography screening in Dutch municipalities on breast cancer mortality: 20 years of follow-up. *International Journal of Cancer* **141,** 671–677 (2017) (Cited on page 1).

[Sarno, 2015] Sarno, A., Mettivier, G. & Russo, P. Dedicated breast computed tomography: Basic aspects. *Medical Physics* **42,** 2786–2804 (2015) (Cited on page 3).

[Scherer, 2014] Scherer, K. *et al.* Bi-Directional X-Ray Phase-Contrast Mammography. *PLOS ONE* **9,** e93502 (2014) (Cited on pages 4, 56, 90).

[Scherer, 2016] Scherer, K. *et al.* Improved Diagnostics by Assessing the Micromorphology of Breast Calcifications via X-Ray Dark-Field Radiography. *Scientific Reports* **6,** 36991 (2016) (Cited on pages 4, 56, 77, 90, 126).

[Scherer, 2015] Scherer, K. *et al.* Toward Clinically Compatible Phase-Contrast Mammography. *PLOS ONE* **10,** e0130776 (2015) (Cited on pages 4, 56, 90).

[Schlegel, 1999] Schlegel, W. & Bille, J. *Medizinische Physik 2* (Springer Verlag, 1999) (Cited on page 44).

[Schlomka, 2008] Schlomka, J. P. *et al.* Experimental feasibility of multi-energy photon-counting K-edge imaging in pre-clinical computed tomography. *Physics in Medicine and Biology* **53,** 4031–4047 (2008) (Cited on pages 5, 39, 91).

[Schoonjans, 2011] Schoonjans, T. *et al.* The xraylib library for X-ray–matter interactions. Recent developments. *Spectrochimica Acta Part B: Atomic Spectroscopy* **66,** 776–784 (2011) (Cited on page 98).

[Seibert, 2006] Seibert, J. A. Flat-panel detectors: how much better are they? *Pediatric Radiology* **36,** 173 (2006) (Cited on page 16).

[Sellerer, 2016] Sellerer, T. *Projection Based Dual-energy Micro-CT with a Photon-Counting Detector* MA thesis (Technical University of Munich, 2016) (Cited on page 16).

[Sellerer, 2017] Sellerer, T. *et al. A polychromatic adaption of the Beer-Lambert model for spectral decomposition* in *Medical Imaging 2017: Physics of Medical Imaging* (2017), 101323H (Cited on pages 5, 90).

[Shikhaliev, 2011] Shikhaliev, P. M. & Fritz, S. G. Photon counting spectral CT versus conventional CT: comparative evaluation for breast imaging application. *Physics in Medicine and Biology* **56,** 1905–1930 (2011) (Cited on page 5).

[Shim, 2020] Shim, S. *et al.* Lesion Detectability and Radiation Dose in Spiral Breast CT With Photon-Counting Detector Technology: A Phantom Study. *Investigative Radiology* **55,** 515–523 (2020) (Cited on page 3).

[Snigirev, 1995] Snigirev, A., Snigireva, I., Kohn, V., Kuznetsov, S. & Schelokov, I. On the Possibilities of X-ray Phase Contrast MicroImaging by Coherent High-Energy Synchrotron Radiation. *Review of Scientific Instruments* **66,** 5486–5492 (1995) (Cited on page 20).

[Spahn, 2005] Spahn, M. Flat detectors and their clinical applications. *European Radiology* **15,** 1934–1947 (2005) (Cited on page 16).

[Spieler, 2006] Spieler, H. *Series on Semiconductor Science and Technology.* (Oxford University Press, 2006) (Cited on pages 7, 12, 16).

[Stampanoni, 2011] Stampanoni, M. *et al.* The First Analysis and Clinical Evaluation of Native Breast Tissue Using Differential Phase-Contrast Mammography. *Investigative Radiology* **46,** 801–806 (2011) (Cited on pages 4, 56, 90).

[Stampanoni, 2013] Stampanoni, M. *et al.* Toward clinical differential phase contrast mammography: Preliminary evaluations and image processing schemes. *Journal of Instrumentation* **8,** C05009 (2013) (Cited on page 90).

[Stout, 2014] Stout, N. K. *et al.* Benefits, Harms, and Costs for Breast Cancer Screening After US Implementation of Digital Mammography. *JNCI: Journal of the National Cancer Institute* **106,** dju092 (2014) (Cited on page 1).

[Sztrókay, 2013] Sztrókay, A. *et al.* Assessment of grating-based X-ray phase-contrast CT for differentiation of invasive ductal carcinoma and ductal carcinoma in situ in an experimental ex vivo setup. *European Radiology* **23,** 381–387 (2013) (Cited on pages 4, 56).

[Sztrókay, 2012] Sztrókay, A. *et al.* High-resolution breast tomography at high energy: a feasibility study of phase contrast imaging on a whole breast. *Physics in Medicine and Biology* **57,** 2931–2942 (2012) (Cited on page 56).

[Taba, 2018] Taba, S. *et al.* Toward Improving Breast Cancer Imaging: Radiological Assessment of Propagation-Based Phase-Contrast CT Technology. *Academic Radiology* **26,** e79–e89 (2018) (Cited on pages 3, 58).

[Talbot, 1836] Talbot, H. F. LXXVI. Facts relating to Optical Science. No. IV. *The London, Edinburgh, and Dublin Philosophical Magazine and Journal of Science* **9,** 401–407 (1836) (Cited on page 21).

[Taylor, 2004] Taylor, R., Morrell, S., Estoesta, J. & Brassil, A. Mammography Screening and Breast Cancer Mortality in New South Wales, Australia. *Cancer Causes & Control* **15,** 543–550 (2004) (Cited on page 1).

[Tromba, 2016] Tromba, G. *et al.* in *Lecture Notes in Computer Science (including subseries Lecture Notes in Artificial Intelligence and Lecture Notes in Bioinformatics)* 625–634 (2016) (Cited on pages 3, 58).

[Tromberg, 2005] Tromberg, B. J. *et al.* Imaging in breast cancer: Diffuse optics in breast cancer: detecting tumors in pre-menopausal women and monitoring neoadjuvant chemotherapy. *Breast Cancer Research* **7,** 279–285 (2005) (Cited on pages 37, 80).

[Vedantham, 2013] Vedantham, S. & Karellas, A. X-ray phase contrast imaging of the breast: Analysis of tissue simulating materials. *Medical Physics* **40,** 041906 (2013) (Cited on page 96).

[Venkatesan, 2009] Venkatesan, A., Chu, P., Kerlikowske, K., Sickles, E. A. & Smith-Bindman, R. Positive Predictive Value of Specific Mammographic Findings according to Reader and Patient Variables. *Radiology* **250,** 648–657 (2009) (Cited on page 1).

[vTeuffenbach, 2017] Von Teuffenbach, M. *et al.* Grating-based phase-contrast and dark-field computed tomography: A single-shot method. *Scientific Reports* **7** (2017) (Cited on page 85).

[Wadsworth, 1954] Wadsworth, G. The Blood Volume of Normal Women. *Blood* **9,** 1205–1207 (1954) (Cited on pages 62, 98).

[Wang, 2002] Wang, G. X-ray micro-CT with a displaced detector array. *Medical Physics* **29,** 1634–1636 (2002) (Cited on page 82).

[Wang, 2014] Wang, Z. *et al.* Non-invasive classification of microcalcifications with phase-contrast X-ray mammography. *Nature Communications* **5,** 3797 (2014) (Cited on pages 4, 77, 90, 126).

[Weitkamp, 2006] Weitkamp, T., David, C., Kottler, C., Bunk, O. & Pfeiffer, F. *Tomography with grating interferometers at low-brilliance sources* in *Developments in X-Ray Tomography V* **6318** (SPIE, 2006), 249–258 (Cited on pages 21, 22).

[Weitkamp, 2005] Weitkamp, T. *et al.* X-ray Phase Imaging with a Grating Interferometer. *Optics Express* **13,** 6296–6304 (2005) (Cited on pages 3, 21, 56).

[WHO, 2020a] WHO. *Breast Cancer* 2020 (Cited on page 1).

[WHO, 2020b] WHO. *Global Health Observatory (GHO) data: Women and cervical and breast cancer* 2020 (Cited on page 1).

[Wilkins, 1996] Wilkins, S., Gureyev, T. E., Gao, D., Pogany, A. & Stevenson, A. Phase-Contrast Imaging using polychromatic hard X-rays. *Nature* **384,** 335–338 (1996) (Cited on page 20).

[Willmott, 2011] Willmott, P. *An Introduction to Synchrotron Radiation: Techniques and Applications* (John Wiley and Sons, Ltd, 2011) (Cited on page 7).

[Willner, 2014] Willner, M. *et al.* Quantitative breast tissue characterization using grating-based x-ray phase-contrast imaging. *Physics in Medicine and Biology* **59,** 1557–1571 (2014) (Cited on page 98).

[Willner, 2016] Willner, M. *et al.* Quantitative Three-Dimensional Imaging of Lipid, Protein, and Water Contents via X-Ray Phase-Contrast Tomography. *PLOS ONE* **11,** e0151889 (2016) (Cited on pages 4, 36, 37, 56).

[Wirtensohn, 2022] Wirtensohn, S. *Advanced Denoising Methods in Grating-Based Phase-Contrast Breast Computed Tomography* MA thesis (Technical University of Munich, 2022) (Cited on page 85).

[Wu, 2014] Wu, J. Propagation based X-ray phase-contrast imaging technique for the microstructure analysis of biological soft tissues. *Optik – International Journal for Light and Electron Optics* **125,** 1062–1064 (2014) (Cited on pages 3, 56).

[Wu, 1991] Wu, X., Barnes, G. T. & Tucker, D. M. Spectral dependence of glandular tissue dose in screen-film mammography. *Radiology* **179,** 143–148 (1991) (Cited on page 45).

[Wu, 1994] Wu, X., Gingold, E. L., Barnes, G. T. & Tucker, D. M. Normalized average glandular dose in molybdenum target-rhodium filter and rhodium target-rhodium filter mammography. *Radiology* **193,** 83–89 (1994) (Cited on page 45).

[Xu, 2022] Xu, J. *et al.* Intensity-based iterative reconstruction for helical grating interferometry breast CT with static grating configuration. *Optics Express* **30,** 13847–13863 (2022) (Cited on pages 85, 87).

[Yagil, 2016] Yagil, Y. *et al.* Challenges in contrast-enhanced spectral mammography interpretation: Artefacts lexicon. *Clinical Radiology* **71,** 450–457 (2016) (Cited on page 89).

[Yashiro, 2015] Yashiro, W., Vagovic, P. & Momose, A. Effect of beam hardening on a visibility-contrast image obtained by X-ray grating interferometry. *Optics Express* **23,** 23462–23471 (2015) (Cited on page 90).

[Zanardo, 2019] Zanardo, M. *et al.* Technique, protocols and adverse reactions for contrast-enhanced spectral mammography (CESM): a systematic review. *Insights into Imaging* **10,** 76 (2019) (Cited on page 96).

[Zanette, 2012] Zanette, I. *et al.* Trimodal low-dose X-ray tomography. *Proceedings of the National Academy of Sciences* **109,** 10199–10204 (2012) (Cited on pages 85, 86).

List of Figures

List of Tables

Abbreviations and Symbols

ASIC	application specific integrated circuit
Au	gold
BCT	breast computed tomography
CdTe	cadmium telluride
CsI	caesium iodide
CESM	contrast-enhanced spectral mammography
CT	computed tomography
CLS	Compact Light Source
CNR	contrast-to-noise ratio
CRLB	Cramér–Rao lower bound
DBT	digital breast tomosynthesis
DFI	dark-field image
ESF	edge spread function
FBP	filtered backprojection
FOV	field of view
FPGA	field programmable gate array
FWHM	full width half maximum
GaAs	gallium arsenide
GadOx	gadolinium oxysulfide

HU Hounsfield Unit

HUp phase-contrast Hounsfield Unit

IBSIR intensity-based statistical iterative reconstruction

IAEA International Atomic Energy Agency

IP interaction point

KES K-edge subtraction

kerma kinetic energy released per unit mass

LSF line spread function

MGD mean glandular dose

MRI magnetic resonance imaging

MTF modulation transfer function

MuCLS Munich Compact Light Source

Ni nickel

NLCG nonlinear conjugate gradient algorithm

PMMA polymethyl methacrylate

PED projected electron density

PSF point spread function

ROI region of interest

Si silicon

SIR statistical iterative reconstruction

SDPC spectral differential phase contrast

TFT thin-film-transistor

THL threshold

US ultrasound

WHO World Health Organization

Acknowledgements

First of all, I would like to thank Prof. Dr. Julia Herzen for coming to the Technical University Dortmund, for introducing me there into the field of grating-based phase-contrast and spectral imaging and finally for giving me the opportunity to work in her group both as an external master student and during my doctoral studies. Thank you for accompanying me all these years, for all the constructive discussions in our bi-weekly meetings, for entrusting me with so many students and for allowing me to attend several conferences.

I would also like to thank Prof. Dr. Franz Pfeiffer for creating the working environment at our chair with all the different imaging setups, especially the MuCLS where I spent a lot of time during my experiments.

A special thanks goes to Nelly, Klaus and Veronica, who were always and mostly immediately there to help with organizational, administrative or bureaucratic issues.

During my time at the chair, I have supervised many bachelor's and master's theses. I would like to thank everyone who was a part of the breast imaging task force for the good working atmosphere during the discussions either in the office or virtually via Matrix or Zoom during the Corona lockdown. I think we could all learn a lot from each other and therefore it was a pleasure to work with you Daniel, Dominik, Franziska, Gregor, Lara, Larissa, Laurenz, Mariia, Mirko, Sandra and Rabea. I hope we will continue with our regular get-togethers in Mexican bars or beer gardens.

Many thanks goes to the *DECTRIS AG* for their support in carrying out this work and providing us with several different photon-counting detectors for conducting BCT. A special thanks goes to Spyros and Thomas for the fruitful discussions at our regular Telcos and the fun moments at the Howling at the Moon Bar in Chicago and during our visit to Baden.

I would like to thank Dr. Karin Hellerhoff and PD Dr. Susanne Grandl from the Red Cross Hospital for the successful cooperation in the dark-field mammography study and for sharing their advice from the medical perspective with us.

A big thanks goes to the whole team of the MuCLS, especially to Martin, for the support during all our beam times, for the constructive dialogues during the regular

meetings and for sharing their expertise about this X-ray source with me.

I would also like to thank the spectral island around Korbi, Thorsti and Kersti for sharing their knowledge about photon-counting detectors and spectral imaging not only with me, but with the whole breast imaging group.

A special thanks goes to the last two Reco guys left over during my PhD, Basti and Clemi, without whose help all our reconstructions and simulations would not have turned out so well.

Benedikt, Clemi, Daniel, Dominik, Johannes M., Kersti, Lego-Johnny, Manu F., Manuel V., Martin, Mirko, Rabea, Resi, Sandra, Thorsti and Wolfgang jr. - thank you all for proofreading parts of my thesis and for all your constructive comments!

Many thanks to Martin, Wolfi and Clemi for maintaining the E17 infrastructure and quickly solving any problems at any time.

Thanks to everyone I spent time with in the MIBE (formerly MSB) open office at the beginning of my PhD and in my final year in the Physics Department. I would also like to thank everyone at the chair for creating such a great working atmosphere. I enjoyed every visit to the beer garden, cooking evening, AirFit course, beach volleyball camp, seminar days week and barbecue with you.

I am very grateful for all the new friendships I made at E17. Especially for the Powerpuff girls Manu, Resi and Kersti for all the fun moments during our different activities like hiking, beer tastings, vacations and pyjama parties - thank you for being my family here in Munich, especially during the long Corona lockdown. But also for Clemi, who was by my side from day one at this chair and supported me mentally whenever needed.

Last but not least, I would like to thank my family who, despite the great distance, always stood by me unconditionally and without whose mental help, support, the many mutual visits and vacations my time here in Munich would not have been the same. With you I can always recharge my batteries for new challenges and for that I am very thankful.